Advanced Techniques for Cardiovascular Magnetic Resonance Imaging in Cases of Irregular Motion

Kolbitsch, Christoph

Awarding institution:
King's College London

Advanced Techniques for Cardiovascular Magnetic Resonance Imaging in Cases of Irregular Motion

Christoph Philipp Kolbitsch

A dissertation submitted in partial fulfillment of the requirements for the degree of

Doctor of Philosophy

of

King's College London

London, United Kingdom, 2012

Abstract

Magnetic resonance imaging (MRI) has recently been shown to provide valuable information for image-guided ablation therapy used to treat patients suffering from cardiac arrhythmia. This requires isotropic high resolution anatomical information about complex structures such as atria and pulmonary veins. In addition, the visualisation of fibrotic tissue in the myocardium can be important for treatment planning and assessment.

One of the main challenges to obtaining images with a high isotropic resolution is respiratory motion. Although a wide range of different methods to minimise respiratory motion artefacts has been presented, irregular breathing can still lead to unacceptably long scan times and scan abortions. Respiratory motion in patients must also be taken into consideration during the ablation procedure to ensure accurate image guidance. Furthermore, arrhythmia leads to pathological changes in the electrical excitation of the heart. This can cause irregular heart beat variations and result in very long scan times for the functional assessment of the heart in patients suffering from arrhythmia.

This thesis presents new MRI methods which overcome these problems and allow for the characterisation and compensation of physiological motion even in patients with highly irregular respiratory and cardiac cycles.

A new high resolution 3D whole-heart acquisition scheme is introduced. It reduces scan times by 36% in both volunteers and patients with irregular breathing motion

due to a higher respiratory navigator efficiency compared to a commonly used respiratory gating method. Furthermore, this approach not only yields anatomical information but also provides additional respiratory motion information without an increase in scan time. This information can be used to assess, and compensate for, respiratory motion during ablation procedures. This method was also modified for 3D high resolution assessment of myocardial scar tissue which led to a 60.8% increase in navigator efficiency in heart failure patients with irregular breathing.

Furthermore, a novel technique to assess cardiac function without ECG using image-based navigation is presented. This allows for a synchronised multi-slice acquisition of the heart without the need of an external ECG and could provide new methods to address arrhythmic heart beats.

In conclusion, the approaches detailed in this thesis provide imaging methods which may not only be beneficial for patients suffering from arrhythmia but also improve the accuracy, outcome and procedure time of other percutaneous procedures.

Acknowledgement

This thesis would not have been possible without the help and support of my colleagues, friends and family. I would like to thank both my supervisors, Tobias Schaeffter and Claudia Prieto, for their continued support. In addition special thanks go to my colleagues for their insight and input but also the hours spent volunteering for me in the scanner. Finally, my thanks go to my family for their patience and encouragement throughout my PhD.

Contents

1 Introduction

Magnetic resonance imaging (MRI) is a versatile medical imaging technique. It provides three dimensional (3D) high resolution images with excellent soft tissue contrast without the use of ionizing radiation. Imaging planes can be oriented freely which is especially important for complex anatomical structures. The applications of MRI include musculoskeletal, neurological and body imaging [1].

Since the introduction of MRI in 1973 [2] a wide variety of developments, such as improved signal receiver design [3], faster sequences [4, 5] and advanced signal encoding and image reconstruction techniques [6–9], have greatly enhanced speed and image quality of MRI [10]. Due to these improvements, MRI is becoming an important imaging technique to assess cardiovascular disease (CVD).

CVD is still the main cause of death in Europe with coronary artery disease (CAD) being the most common form of this disease [11–13]. Many forms of CVD lead to the build up of fibrosis in the myocardium. This tissue component has a different conductivity to the surrounding healthy myocardium which can cause pathological changes of the electrical excitation of the heart and is thought to lead to arrhythmia [14–16].

Arrhythmia describes irregularities or abnormal increase and decrease of the heart rate. Short term effects can include an alteration of the mechanical functionality of the heart but persistent arrhythmia can also lead to changes of the electrophys-

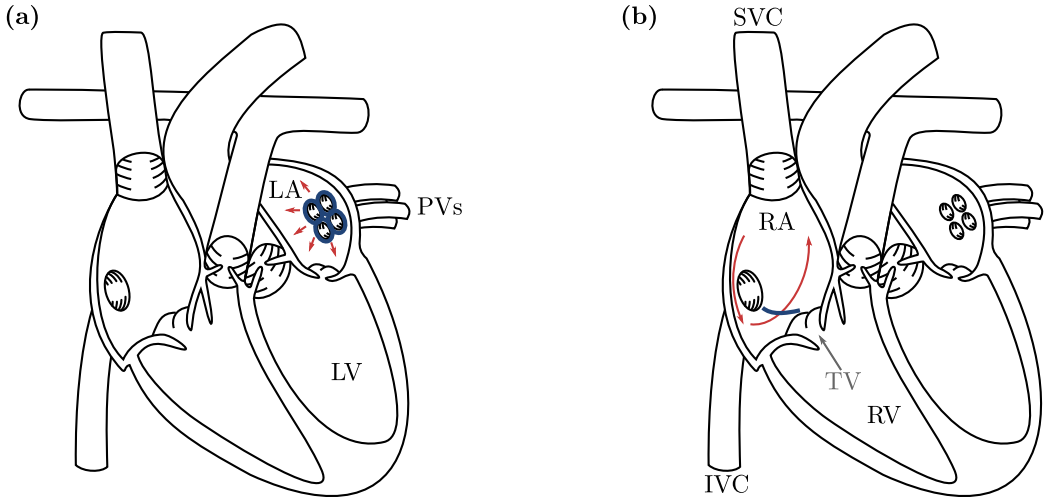

Figure 1.1: Atrial fibrillation (AF) and atrial flutter (AFL). **(a)** The origin of electrical stimuli causing AF (red arrows) lies in the area of the pulmonary veins (PVs) in the left atrium (LA). Catheter ablation of AF involves a circumferential isolation of the PVs (blue circles). **(b)** AFL is caused by a reentry signal (red arrows) circulating in the area between inferior vena cava (IVC) and tricuspid valve (TV). An insulating line of block (blue line) is created to stop these unwanted electrical signals. LV left ventricle, RV right ventricle, SVC superior vena cava, RA right atrium.

iological properties of the heart. This can in return enhance the probability of arrhythmia.

The most common forms of supraventricular (i.e. not originating from the ventricles) tachycardia are atrial fibrillation (AF) and atrial flutter (AFL). The exact mechanism behind AF is still a source of discussion but the source of AF lies most of the time in the area around the pulmonary veins in the left atrium [17]. AF is associated with a fivefold increased risk of stroke and a 2.5 times higher mortality compared to healthy subjects [18, 19]. AFL can be caused by electrical signals, so called reentry signals, circulating in the area of the tricuspid valve. This leads to abnormally fast contractions of the atrium (240 - 300 bpm) [20]. Although patients suffering from AFL have a better short time prognosis than AF patients, the long term mortality rates of AF and AFL are comparably high [19].

One important treatment to cure arrhythmia is ablation therapy. The idea is to create scars (lesions) on the inside wall of the cardiac muscle which form an insulating barrier and block the propagation of unwanted electrical stimuli. These lesions are commonly formed using radio frequency (RF) catheters but good results have also

been reported using ultrasound, laser or cryo ablation [18, 21, 22]. The common imaging modality for catheter guidance during this procedure is X-ray fluoroscopy.

RF catheter ablation therapy of AF involves a circumferential isolation of the pulmonary veins (PVs) (Fig. 1.1a) [23]. This can either be carried out guided by electrical mapping or purely based on the anatomy of the patient. The success rates for this procedure are between 60% and 80%, although a large number of patients requires repeated treatment to optimally isolate the PVs [18]. The anatomy of the PVs can vary strongly between different subjects and therefore an accurate assessment prior to the ablation can provide important information to optimally plan the procedure [24]. Furthermore, this can also help to identify complications such as PV stenosis which can be life-threatening [25].

In order to treat AFL, a linear ablation is created along the inferior vena cava and tricuspid isthmus (CTI) in order to block any reentry signals (Fig. 1.1b). The success rates for these procedures are approximately 90%. Nevertheless, studies have shown that this depends strongly on the patient's anatomy. A challenging or uncommon orientation and shape of the CTI can drastically prolong the procedure and even lead to an incomplete block and therefore unsuccessful ablation [20, 26].

For both AF and AFL detailed knowledge of the anatomy of the atria and their surrounding vessels prior to the procedure for treatment planning and during the ablation for image guidance is essential for a fast and successful ablation therapy without complications [20, 26, 27].

Although X-ray fluoroscopy offers high spatial and temporal resolution and a good catheter visualisation it suffers from low soft tissue contrast. Furthermore, it only yields two dimensional (2D) projection images making it difficult to visualise structures in 3D. Therefore, pre-acquired cardiac computer tomography (CT) data is more frequently used as a 'roadmap' to provide 3D anatomical information during the procedure. Nevertheless, cardiac CT data is obtained during breath-hold, whereas the patient is breathing during the intervention. This can result in misalignments between the roadmap and the actual position of the anatomy [28]. These alignment errors can be minimised using dynamic 3D CT data but it involves a significant radiation dose for the patient.

MRI has recently been reported to be able to provide roadmaps for percutaneous procedures with excellent soft tissue contrast [29–33]. Furthermore, it can provide additional information about cardiac function, blood flow and myocardial scar tissue [34–39].

The lesions created during catheter ablation are approximately five to eight millimetres wide but can be several centimetres long. As already discussed a successful ablation therapy requires complete blocks, i.e. continuous lesions without any gaps [22, 40]. Atria are highly complex structures and the atrial wall thickness can vary significantly between different areas in the atrium and also between subjects [41]. Therefore, roadmaps should be acquired with a high isotropic resolution to accurately depict atrial structures and avoid any image degradation due to partial volume effects.

A major challenge to obtain MR images with a high isotropic spatial resolution is respiratory motion. Although a single breath-hold whole-heart acquisition using parallel imaging extensively has been proposed [42], these long breath-holds are usually not applicable for the majority of patients and the spatial resolution is limited. In order to improve spatial resolution, MR data acquisition has to be carried out during free-breathing. This requires a robust approach to minimise artefacts due to respiratory motion and to obtain all necessary data in the shortest possible time. Although a wide range of different methods to minimise respiratory motion artefacts have been presented, patients exhibiting irregular breathing patterns still lead to long scan times, poor image quality scores and even scan abortions affecting up to 20% of patients [43–45]

During the ablation procedure respiratory motion leads to misalignments between the roadmap and the X-ray fluoroscopy images [31]. As mentioned above the thickness of the atrial wall and the size of the ablation lesions are in the range of millimetres. Therefore, it is important to ensure that any misalignments due to respiration are well below this value. ‘Dynamic roadmaps’ have been proposed to minimise these alignment errors [46–48]. The shape and position of the roadmap is updated according to a pre-acquired motion model and a motion surrogate recorded during the interventional procedure. In order to create such 3D affine motion models dynamic

MR data has to be acquired in addition to the 3D anatomical data, which increases the overall scan time [47].

Fibrotic tissue both in the atria and ventricles is currently under investigation as a source for tachyarrhythmia [14–16]. Initial results of ablation therapy carried out at locations of fibrosis have shown promising results to treat arrhythmia [49]. This shows that for the planning of ablation therapy not just anatomical but also additional 3D high resolution information about scar tissue can provide valuable information. Furthermore, visualisation of scar tissue can also be important to assess the outcome of the ablation procedure [14, 50].

A commonly used technique to assess ventricular function with MRI is retrospectively reordered cine imaging. Data is acquired over multiple cardiac cycles during breath-hold. For the final image reconstruction data from different cardiac cycles but the same cardiac phase are combined retrospectively to achieve both high temporal and high spatial resolution [34, 51–53]. The necessary information about the different cardiac phases is usually provided by an external electrocardiogram (ECG). Data from cardiac cycles with different cycle lengths are scaled linearly prior to data combination [54].

Nevertheless, this only leads to good results for moderate variations of the heart rate. In order to ensure a high image quality even for strong changes of the heart rate 'arrhythmia rejection' techniques are commonly applied [55]. Data acquired during cardiac cycles with a cycle length which is more than 20 - 30% shorter or longer than the average cycle length are rejected and reacquired.

As mentioned above arrhythmia leads to changes in the electrical excitation of the heart. This can present multiple problems for cine imaging. ECG signals might not necessarily provide reliable information for MR data acquisition. Furthermore, patients suffering from arrhythmia can show strong variations in their heart rate and even exhibit additional ('ectopic') heart beats. Although arrhythmia rejection techniques provide a robust and straight forward approach to avoid image degradation due to a varying heart rate, they can lead to excessively long scan times or even scan abortions for patients suffering from arrhythmia.

Therefore, novel techniques providing reliable information on the cardiac cycle without the need for an external ECG could potentially improve the assessment

of patients with arrhythmia. These methods might also allow for more advanced approaches to utilise rather than reject data obtained during arrhythmic heart beats. Furthermore, assessment of arrhythmic patients might also profit from cine imaging during free breathing rather than breath-holds which puts additional strain on the patient and might trigger arrhythmic heart beats.

This thesis presents novel MR methods to characterise and compensate for irregular motion of the heart. The following gives a brief summary of each chapter:

Chapter 2 The main principles of MR physics such as interaction of nuclear magnetic moments with static and time dependent magnetic fields, magnetic relaxation effects and MR echo acquisitions are discussed. In addition different MR sampling schemes and reconstruction techniques are compared.

Chapter 3 An overview of anatomy and function of the heart is given. MR imaging techniques to diagnose and assess CVD are presented. The effect of physiological motion on MR images and techniques to minimise motion artefacts are discussed.

Chapter 4 A Scan Simulation Environment (SSE) is developed to evaluate image quality and scan efficiency of novel MRI acquisition schemes which minimise respiratory motion artefacts and provide respiratory motion information.

Chapter 5 To verify the obtained results in-vivo, the most promising technique is implemented on an MR scanner. Volunteer studies are carried out to obtain high resolution anatomical images and additional respiratory motion information. The novel method is compared to a standard Cartesian MR approach in terms of image quality and navigator efficiency, especially for subjects with irregular breathing patterns.

Chapter 6 The novel acquisition scheme used in the volunteer study does not just yield one high resolution 3D image obtained in a certain breathing phase but also additional respiratory motion information without an increase in scan time. This additional data is utilised to assess respiratory motion in different regions of the heart. Furthermore, the use of the respiratory information to build respiratory motion models for image guidance during percutaneous procedures is explored. The accuracy of these motion models is determined in both volunteer and patient data.

Chapter 7 The use of a highly efficient acquisition scheme presented in chapter 4 for 3D high resolution assessment of myocardial scar tissue is explored. The approach is evaluated in patients and compared to a standard Cartesian reference method.

Chapter 8 A new image-based navigator technique for cardiac function assessment without the need of an external ECG is presented. The accuracy of the obtained cardiac navigator signal is compared to an external ECG signal.

Chapter 9 In order to allow for a 3D functional assessment of the entire ventricle the proposed image-based cardiac navigator is combined with a dual-slice excitation approach. This yields a reliable cardiac gating signal at a static location in the ventricle independent of the image slice.

2 MRI: An Overview

The following chapter discusses the principles of nuclear magnetic resonance (NMR), methods to spatially encode NMR signals and reconstruction techniques to obtain the final image information. Although NMR requires a quantum mechanical description, a classical approach leads to the same results. Here a semiclassical overview will be given. A more detailed discussion can be found in [56].

2.1 Nuclear Magnetic Resonance

Nuclear magnetic resonance (NMR) is based on aligning nuclear spins in an external static magnetic field $\vec{B}_0$ and their excitation by a rotating field $\vec{B}_1$ perpendicular to $\vec{B}_0$. The response of nuclear spins to this external stimulus can be measured and can provide image information.

2.1.1 Nuclear Spin and Magnetic Moment

The nuclear spin $\vec{I}$ is a quantum mechanic characteristic of nuclei with absolute value and z-component given by

$$\begin{aligned} |\vec{I}| &= \sqrt{I(I+1)}\hbar \quad \text{with} \quad I = 0, \frac{1}{2}, 1, \frac{2}{3}, \dots \\ I_z &= m\hbar \quad \text{with} \quad m = -I \dots I \quad . \end{aligned} \tag{2.1}$$

The quantum number I depends on the atomic number of the nucleus and has a value larger than zero only for odd atomic numbers and/or odd mass numbers.

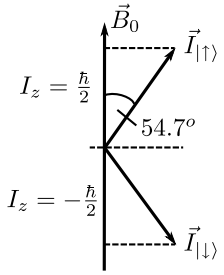

Figure 2.1: In a static external magnetic field $\vec{B}_0$ nuclear spins with $I = \frac{1}{2}$ are either oriented in the same direction as $\vec{B}_0$ ($|\uparrow\rangle$) or opposite to it ($|\downarrow\rangle$). The angle between $\vec{I}$ and $\vec{B}_0$ is given by $\cos\left(\frac{I_z}{|\vec{I}|}\right)$ and according to equation (2.1) this leads to either 54.7° ($|\uparrow\rangle$) or −54.7° ($|\downarrow\rangle$).

Nucleons consist of charged quarks and this inner structure leads to a magnetic moment $\vec{\mu}$ proportional to the nuclear spin

$$\vec{\mu} = \gamma \vec{I} \quad \gamma \ldots \text{gyromagnetic ratio} \quad . \tag{2.2}$$

Without any external force the orientation of $\vec{I}$ and therefore of $\vec{\mu}$ is indiscriminate. In an static external magnetic field $\vec{B}_0$ nuclear spins take up quantised orientations relative to $\vec{B}_0$ which is referred to as Zeeman effect.

MRI in medicine mainly uses hydrogen (^1H) nuclei for imaging purposes due to its natural abundance in the human body and high sensitivity to magnetic fields, i.e. large gyromagnetic ratio

$$\bar{\gamma}(^1H) = \frac{\gamma}{2\pi} = 42.58 \frac{MHz}{T} \quad . \tag{2.3}$$

The spin quantum number for ^1H is $\frac{1}{2}$ and therefore hydrogen nuclei can have two different orientations $|\uparrow\rangle$ (spin up) and $|\downarrow\rangle$ (spin down) relative to $\vec{B}_0$ (Fig. 2.1). Each of these states has different energy eigenvalues which are separated by

$$\Delta E = \gamma \hbar |\vec{B}_0| = \hbar |\vec{\omega}_0| \quad . \tag{2.4}$$

The frequency $\vec{\omega}_0$ is called Lamor frequency and it depends both on the strength of the external magnetic field and on the element specific gyromagnetic ratio.

A system of nuclear spins has a total magnetisation

$$\vec{M} = \frac{1}{V} \sum_{\substack{\text{protons} \\ \text{in V}}} \vec{\mu}_i \tag{2.5}$$

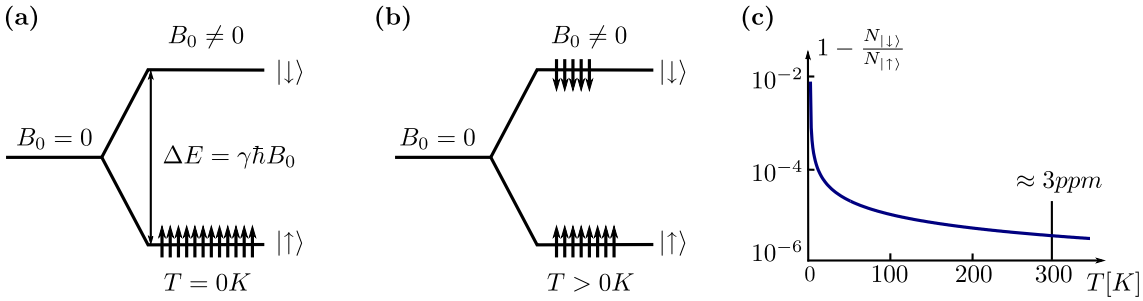

Figure 2.2: Population numbers of nuclear spin states. **(a)** At T = 0K only the lower energy state $|\uparrow\rangle$ is occupied. **(b)** With increasing temperature also the higher energy level $|\downarrow\rangle$ is filled. **(c)** The difference between the population of $|\uparrow\rangle$ and $|\downarrow\rangle$ depending on the temperature follows a Boltzmann distribution and reaches a few ppm at room temperature.

which is a macroscopic parameter describing the sum over all $\vec{\mu}_i$ per unit volume.

The population numbers $N_{|\downarrow\rangle}$ and $N_{|\uparrow\rangle}$ of the two spin states $|\downarrow\rangle$ and $|\uparrow\rangle$ follow a Boltzmann distribution

$$\frac{N_{|\downarrow\rangle}}{N_{|\uparrow\rangle}} = e^{-\frac{\Delta E}{k_B T}} = e^{-\frac{\gamma\hbar B_0}{k_B T}} \quad k_B \ldots \text{Boltzmann constant} \quad . \tag{2.6}$$

At T = 0K only the lower energy level with $E_{|\uparrow\rangle}$ is occupied which leads to a large $\vec{M}$ but for T $\approx$ 300K the spin surplus of $|\uparrow\rangle$ is only a few ppm (Fig. 2.2).

For $N_{|\uparrow\rangle} \neq N_{|\downarrow\rangle}$ there is a surplus of magnetic moments in one direction which leads to a net magnetisation $\vec{M}$ according to equation (2.5). Its amplitude is proportional to the field strength B_0, gyromagnetic ratio and the density of magnetic moments ρ (e.g. proton density for ^1H) and inverse proportional to the temperature T

$$M_0 \approx \frac{\hbar\rho\gamma^2 B_0}{4kT} \quad . \tag{2.7}$$

M_0 is referred to as longitudinal equilibrium magnetisation or average magnetic dipole density.

The magnetic moments precede around $\vec{B}_0$ with random phases and therefore, only their components parallel or antiparallel to $\vec{B}_0$ but not perpendicular to the external magnetic field contribute to a net magnetisation.

Once nuclear spins are exposed to $\vec{B}_0$, they orient themselves following equation (2.6) which yields $\vec{M}$ parallel to $\vec{B}_0$ and the nuclear spins reach thermal equilibrium. In order to obtain information about the spin system, their equilibrium state has to be perturbed. This can be achieved by changing the population of $|\uparrow\rangle$ and $|\downarrow\rangle$ which will be discussed in the next chapter.

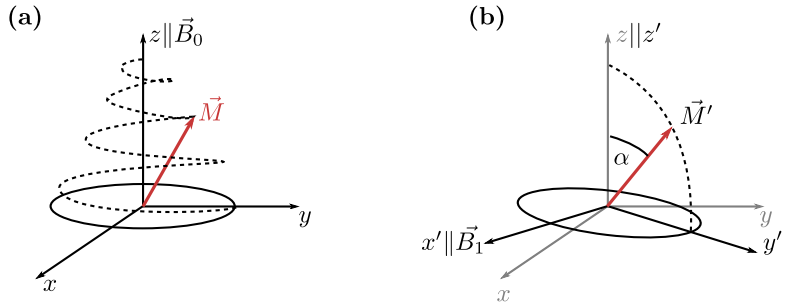

Figure 2.3: Change of magnetisation $\vec{M}$ due to an external radio frequency (RF) field $\vec{B}_1$. **(a)** In the laboratory frame $\vec{M}$ describes a complex spiral trajectory when the spin system is exposed to a RF field $\vec{B}_1(t)$. **(b)** In a rotating frame of reference (indicated by $'$) the equation of motion can be simplified and $\vec{M}'$ is turned by an angle θ from the z-axis to the y-axis when $\vec{B}_1$ is applied.

2.1.2 Time Varying Magnetic Fields

According to equation (2.4) the difference between the energy levels $|\uparrow\rangle$ and $|\downarrow\rangle$ is $\hbar\omega_0$. For Hydrogen in a magnetic field of several Tesla ω_0 is in the order of 100 MHz and therefore transitions between nuclear spin states can be induced with a radio frequency (RF) field $\vec{B}_1(t)$.

Applying a RF field $\vec{B}_1(t)$ leads to the following equation of motion for the magnetisation

$$\frac{d\vec{M}(t)}{dt} = \gamma \vec{M}(t) \times \vec{B}(t) \quad \text{with} \quad \vec{B}(t) = \vec{B}_0 + \vec{B}_1(t) \quad . \tag{2.8}$$

In a frame revolving with $\vec{\omega}$ relative to the static laboratory frame this transforms to

$$\frac{d\vec{M}(t)}{dt} = \left(\frac{d\vec{M}(t)}{dt}\right)' + \left(\vec{\omega} \times \vec{M}(t)'\right) = \gamma \left(\vec{M}(t)' \times \left(\vec{B}(t)' - \frac{\omega}{\gamma}\right)\right) \tag{2.9}$$

where primed quantities indicate a variable in the rotating frame. Assuming a static magnetic field oriented along the z-direction ($\vec{B}_0 = B_0\hat{z}$) and the RF field aligned with the x'-direction of the rotating frame of reference ($\vec{B}_1 = B_1\hat{x}' = \gamma\omega_1\hat{x}'$) the magnetisation can be described as

$$\left(\frac{d\vec{M}(t)}{dt}\right)' = \vec{M} \times ((\omega_0 - \omega)\hat{z} + \omega_1\hat{x}') \quad . \tag{2.10}$$

For $\omega = \omega_0$, the term $\vec{B}_0 - \frac{\omega}{\gamma}$ is zero and $\vec{B}'(t)$ has only one component perpendicular to the static magnetic field. This causes the vector of the magnetization $\vec{M}$ to

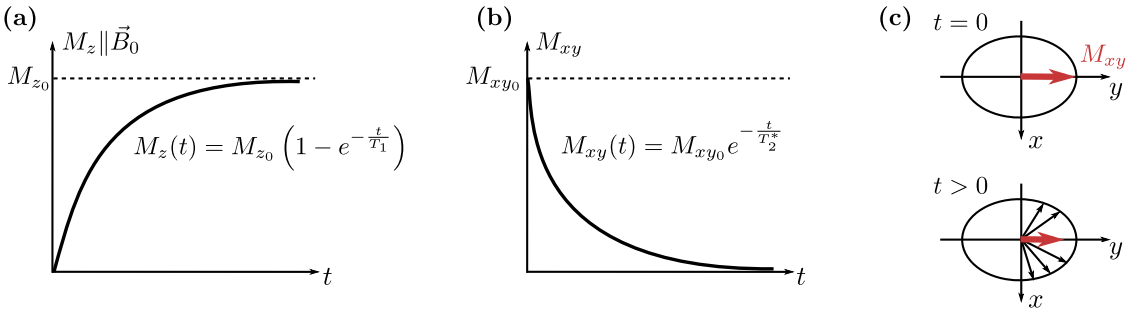

Figure 2.4: Spin relaxation. **(a,b)** Due to longitudinal and transversal relaxation processes $M_z(t)$ increases (a) and $M_{xy}(t)$ decreases (b) exponentially over time after the RF field is switched off. **(c)** Decay of $M_{xy}(t)$ due to field inhomogeneities.

be turned from the z-direction parallel to $\vec{B}_0$ to the transversal x'-y'-plane by a so called flip angle α. For small flip angles α is determined by the strength and time τ for which the RF field is applied

$$\alpha(\tau) = -\gamma \int_0^\tau B_1(t')dt' \quad . \tag{2.11}$$

Figure 2.3 depicts the magnetisation in both the laboratory and the rotational frame. $\vec{M}$ can be described by a longitudinal component M_z parallel to to $\vec{B}_0$ and a transversal component $\vec{M}_{xy} = M_x\hat{x} + M_y\hat{y}$ perpendicular to the static magnetic field.

2.1.3 Longitudinal and Transversal Relaxation

When the RF field is switched off the spin system relaxes back into its equilibrium state. During this process nuclear spins can exchange energy with the surrounding lattice resulting in transitions from $|\downarrow\rangle$ to $|\uparrow\rangle$. This causes an increase of M_z

$$M_z(t) = M_{z_0}\left(1 - Ae^{-\frac{t}{T_1}}\right) \tag{2.12}$$

where M_{z_0} describes the initial magnetisation in equilibrium and A depends on the flip angle (e.g. $A = 1$ for a 90° pulse). This is referred to as T_1 or longitudinal relaxation process.

The nuclear spins also interact and exchange energy with each other which is called transversal relaxation and decreases M_{xy}. It is caused partly by field inhomogeneities due to imperfections of the magnet. In addition nucleons and electrons are always in motion due to their thermal energy which causes local fluctuations of the magnetic

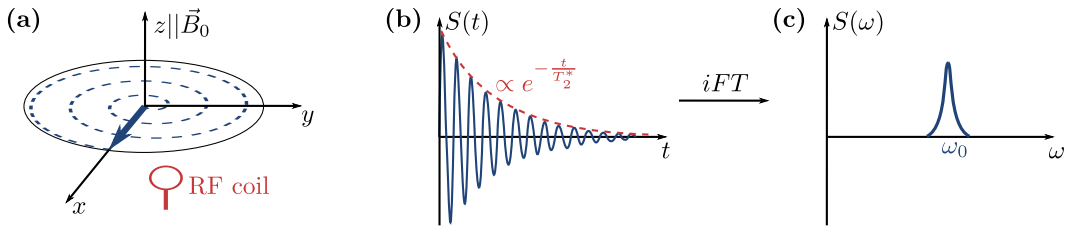

Figure 2.5: Free induction decay (FID) signal. **(a)** The transversal magnetisation ($\vec{M}_{xy}$, blue arrow) rotates around $\vec{B}_0$ with the Lamor frequency ω_0 and an amplitude decreased by transversal relaxation. $\vec{M}_{xy}$ induces a voltage in a RF receiver coil. **(b)** The signal $S(t)$ induced in the receiver coil by $\vec{M}_{xy}$ oscillates with ω_0 and is attenuated over time due to transversal relaxation. **(c)** The inverse Fourier transformation (iFT) of $S(t)$ yields a peak at the Lamor frequency with a width inverse proportional to the transversal relaxation time.

field. The contribution of these two effects to transversal relaxation is described by T_2' and T_2, respectively which leads to

$$M_{xy}(t) = M_{xy_0} e^{-\frac{t}{T_2^*}} \quad \text{with} \quad \frac{1}{T_2^*} = \frac{1}{T_2} + \frac{1}{T_2'} \quad . \tag{2.13}$$

Both longitudinal and transversal relaxation are depicted in Fig. 2.4.

The relaxation times T_1 and T_2' and M_0 depend on the properties of the investigated sample and can therefore provide physical information.

2.1.4 Signal Measurements

RF fields can be applied as short (200μs - 5ms[1]) pulses which rotate $\vec{M}$ by a certain flip angle according to equation (2.11). This leads to a measurable transversal magnetisation $\vec{M}_{xy}$ which decreases over time due to the above discussed relaxation processes. In a nearby receiver coil $\vec{M}_{xy}$ induces a voltage according to Faraday's Law of electromagnetic induction (Fig. 2.5a) yielding a so called free induction decay (FID) signal $S(t)$ (Fig. 2.5b). The Fourier transform of $S(t)$ yields a peak at the Lamor frequency with an amplitude proportional to $|\vec{M}_{xy}|$.

Depending on the preparation of the spin system prior to data acquisition the obtained signal can be dependent on a multitude of different parameters such as proton spin density, T_1 and T_2. This provides a wide range of information making MRI a highly versatile imaging technique.

[1] One exception are adiabatic pulses which can be significantly longer. They are used for example to achieve inversion which is insensitive to B_1 inhomogeneities. For more details please see [57].

2.1.5 Applications of NMR

The principles of NMR are applied in different techniques. In magnetic resonance spectroscopy (MRS) nuclear spins of certain elements are excited and their response is measured as a function of the Lamor frequency. As the Lamor frequency does not just depend on $\vec{B_0}$ but also on the chemical environment of each nuclear spin, the obtained spectrum yields biochemical information [58].

In nuclear magnetic resonance tomography, often abbreviated as MRI the spatial distribution of nuclear spins is encoded in the Lamor frequency which will be discussed in the next section.

2.2 Magnetic Resonance Imaging

2.2.1 Signal Echo Formation

Data acquisition in magnetic resonance imaging (MRI) is commonly carried out during the formation of echo signals created either by RF pulses (spin echo (SE)) or gradients with opposite polarity (gradient echo (GE)).

SE sequences use a 90° RF pulse to flip the magnetisation into the transversal plane. Due to T_2 and T_2^* relaxation processes spins start to dephase. If a 180^o pulse is applied at the time $\frac{T_E}{2}$ relative to the first RF pulse, the dephasing of the spins due to static field inhomogeneities is reversed and the spins refocus or rephase at the echo time T_E producing a spin echo (Fig. 2.6a). The signal intensity and therefore the image contrast is determined by T_2 relaxation. Instead of using a combination of a 90° and 180° pulse, also two 90° pulses can produce a spin echo which is referred to as Hahn echo. Furthermore, multiple 90° pulses can yield so called stimulated echoes [59, 60].

Since the introduction of faster, more powerful and more accurate magnetic field gradient systems, gradient echo (GE) techniques have become increasingly used especially in cardiac MRI. In contrast to SE sequences a RF pulse with an arbitrary flip angle α can be used and no 180° pulse is required which allows for very fast imaging. After the excitation pulse a dephasing gradient G_D is used to enhance

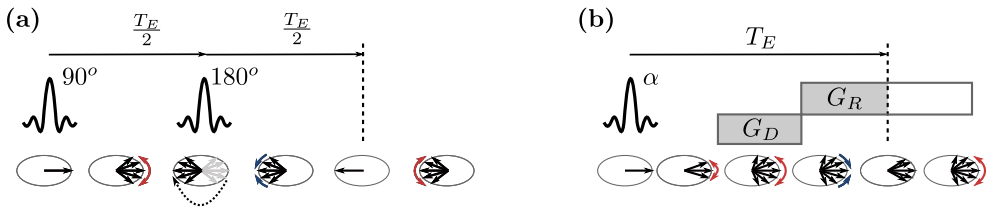

Figure 2.6: Signal echo formation. **(a)** Spin echo sequence. After the 90^o RF pulse the nuclear spins (black arrows) dephase due to transversal relaxation. A 180^o RF pulse inverts the dephasing of the spins (dotted arrow) which results in a spin echo at the echo time T_E. **(b)** Gradient echo sequence. After the RF pulse α a dephasing gradient (G_D) is used to enhance the dephasing of spins. In order to create a signal echo, a rephasing gradient (G_R) with opposite polarity to G_D is applied. A gradient echo is formed once the zeroth moment of G_D and G_R (grey areas) compensate each other. Dephasing/rephasing red/blue arrows

the dephasing of spins in addition to T_2^* relaxation. A gradient echo is formed by applying a rephasing gradient G_R with opposite polarity to G_D which leads to a signal intensity dependent upon T_2^* (Fig. 2.6b). The echo time T_E is chosen such that

$$\int_0^{T_E} G(t)dt = \int_0^{T_E} \left(G_D(t) + G_R(t)\right) dt = 0 \quad . \tag{2.14}$$

2.2.2 Spatial Encoding - *K*-Space

In order to obtain image data information from spin and gradient echo signals the location of nuclear spins is encoded in frequency and phase of the obtained echo signals.

The Lamor frequency of nuclear spins can be spatially varied using linear magnetic field gradients ($G_{x,y,z}$)

$$\omega(x, y, z) = \gamma(B_0 + xG_x + yG_y + zG_z) \tag{2.15}$$

with

$$G_n = \frac{\partial (B_0)_z}{\partial n}, \quad n \ldots x, y, z \quad . \tag{2.16}$$

In the presence of field gradients spins accumulate an additional phase $\phi(\tau)$ depending on their location (x, y, z)

$$\phi(n, \tau_n) = \gamma \int_0^{\tau_n} nG_n(t)dt, \quad n \ldots x, y, z \tag{2.17}$$

where τ_n describes the time the gradients are applied for.

$\vec{M}_{xy}$ can be described as a complex vector rotating in the transversal plane. The amplitude and phase of $S(t)$ induced in the receiver coils are then given by

$$S(G_n, \tau_n) = \int \rho(n) e^{-2\pi i \gamma \int_0^{\tau_n} G_n(t) n dt} dn, \quad n \ldots x, y, z \quad . \tag{2.18}$$

The spatially encoded signal from the nuclear spin system is described here as the effective proton density ρ which describes not just the density of proton spins but also includes all other effects which influence the obtained signal such as tissue relaxation effects. Introducing new variables k_x, k_y and k_z with

$$k_n = \gamma \int_0^{\tau_n} G_n(t) t dt, \quad n \ldots x, y, z \tag{2.19}$$

leads to

$$S(k_x, k_y, k_z) = \int \rho(x, y, z) e^{-2\pi i (k_x x + k_y y + k_z z)} \quad . \tag{2.20}$$

According to the above equation the signal S is obtained in a spatial frequency space or k-space. The k-space encoding is determined by the gradient strength and/or duration of gradients which yield different spatial harmonics of ρ. The aim of a MRI scan is to obtain a complete k-space by applying a succession of different gradient settings. The image information given by ρ can then be obtained by inverse Fourier transforming the obtained signal.

So far S and ρ have been described as continuous functions but during a MR scan only discretised and truncated signals are acquired. This can lead to image artefacts, i.e. deviation between the reconstructed image and the true effective spin density which will be discussed in chapter 2.3.

2.2.3 Pulse Sequence Diagrams

The temporal order of RF pulses, field gradients and data acquisition necessary for image formation can be described with so called pulse sequence diagrams. One example of a gradient echo sequence is shown in Fig. 2.7.

During the RF pulse a slice selection gradient (G_z) is applied to restrict the excitation of spins to a thin 2D slice or a well defined 3D region. G_z changes the Lamor frequency according to equation (2.15)

$$\omega(z) = \gamma(B_0 + z G_z) \quad . \tag{2.21}$$

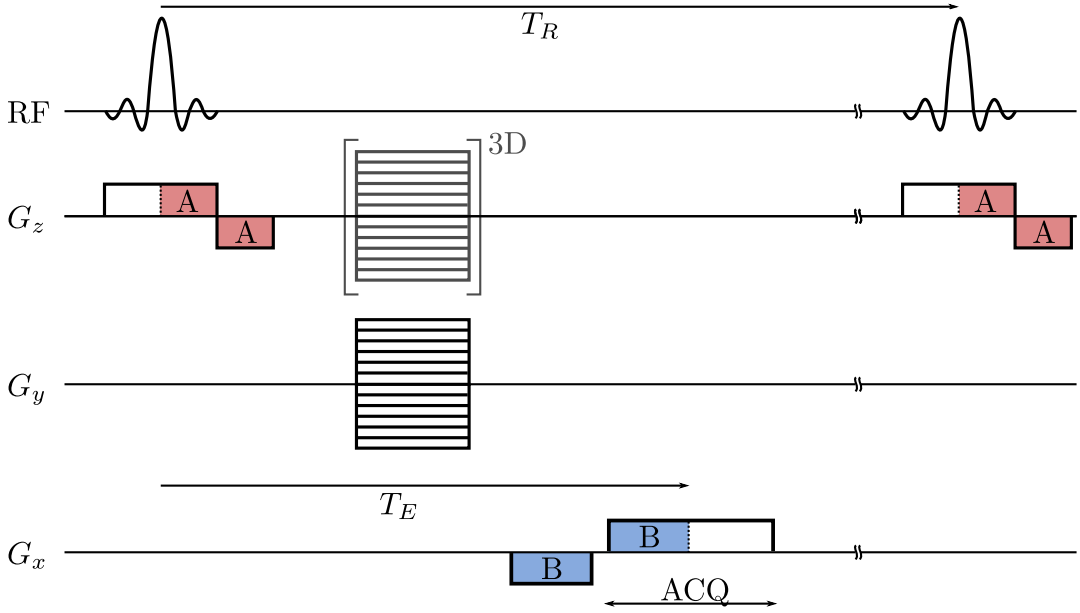

Figure 2.7: Sequence diagram of MRI acquisition. A slice encoding gradient G_z and a RF pulse with a finite bandwidth is used to spatially restrict the spin excitation. The dephasing caused be G_z is compensated for with a gradient with opposite polarity and half the gradient area of G_z (red, A). A phase encoding gradient G_y and for 3D imaging also G_z is used to spatially encode the signal in the y and $y-z$ plane respectively. Applying a dephasing gradient prior to the frequency encoding gradient G_x leads to gradient echo at the echo time (T_E) once the area of the dephasing gradient (blue, B) has been compensated for by G_x. Data acquisition (ACQ) is carried out such that the gradient echo occurs in the centre of k-space. The time between subsequent RF excitation pulses used for data acquisition of an image is referred to as repetition time (T_R).

Therefore, a RF pulse centred at ω_0 with a bandwidth of $\Delta\omega = \gamma\Delta z G_z$ only excites nuclear spins located within Δz centred at $z = 0$. The Lamor frequency of all other spins is either too high or too low and they are not affected by the RF excitation. The centre of the slice depends on the centre frequency of the RF pulse. According to equation (2.17) G_z also leads to dephasing of spins along the slice encoding direction. This has to be compensated for by applying a gradient with opposite polarity after the excitation.

A RF pulse with a true rectangular frequency response would require an infinite *sinc* pulse in the time domain. In practice time truncated *sinc* or Gauss-shaped pulses are used. This can lead to excitation of nuclear spins outside of the desired FOV which may lead to slice crosstalk when acquiring multiple slices using an interleaved acquisition scheme [61].

After spin excitation the phase encoding gradient G_y (and for 3D imaging also the slice encoding gradient G_z) is used for spatial encoding. A gradient echo is formed by applying a dephasing gradient prior to the frequency encoding gradient. The timing and strength of the dephasing gradient is selected such that the gradient echo occurs when the central k_x position (i.e. lowest spatial frequency) is acquired.

A 2D image with N_x x N_y pixels requires N_y different settings of the phase encoding gradient. Therefore, the above described sequence has to be repeated N_y times with the repetition time T_R to obtain all necessary information.

2.2.4 Incoherent and Coherent Gradient Echo sequences

The signal available at each T_R depends on the previous RF pulses and field gradients. In order to achieve a reproducible magnetisation for each T_R and avoid image artefacts, steady-state free-precession (SSFP) GE sequences are commonly used [62]. A steady-state of the magnetisation is reached after a certain number of startup cycles if the flip angle, T_R and dephasing due to field gradients are kept constant for each T_R. Different values of these parameters lead to different steady-states and therefore to different image contrasts [63,64].

If the spin system is completely dephased before each excitation only the longitudinal magnetisation is affected by previous data acquisitions. This is referred to

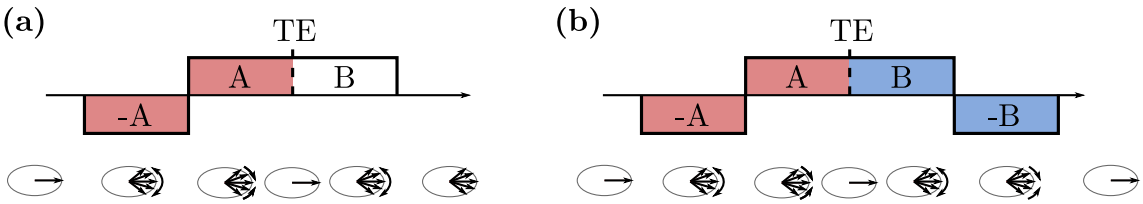

Figure 2.8: Frequency encoding gradient (FE) and transversal magnetisation (M_{xy}) for **(a)** steady-state free precession (SSFP) and **(b)** balanced SSFP (bSSFP) sequences. For both sequences a succession of gradients with opposite polarity (red) is used to form a gradient echo at the echo time T_E. The second part of the readout gradient (B) after T_E leads to further dephasing. For bSSFP sequences a refocusing gradient is therefore applied after data acquisition to compensate for this dephasing (blue). Any dephasing of spins due to transversal relaxation and off-resonance effects is neglected in this figure.

as incoherent SSFP and can be achieved using $T_R \gg T_2$ or additional dephasing of transversal magnetisation using RF and gradient spoiling after each T_R. For coherent SSFP methods, the transversal magnetisation can be refocused which leads to the formation of additional echoes.

A special case of SSFP methods are balanced SSFP (bSSFP) techniques where the dephasing due to the gradients within each T_R is zero. This maximises the amplitude of the transversal magnetisation M_{xy} which leads to

$$M_{xy} = \frac{1}{2} M_0 \sqrt{\frac{T_2}{T_1}} \tag{2.22}$$

for an optimised flip angle. This is the highest signal intensity achieved by any GE sequence and therefore bSSFP methods provide the best signal to noise ratio. More details on the derivation of the above formula can be found in [65]. Figure 2.8 compares a SSFP and a bSSFP sequence. Balanced SSFP techniques are sometimes also know as TrueFISP, balanced FFE, or FIESTA [63].

For bSSFP sequences each RF pulse applied once the magnetisation is in a steady-state leads to a mirroring of $\vec{M}$ around the z-axis. Therefore the phase Φ_B of the RF excitation pulse has to be alternated between 0 and π for successive excitations in order to ensure constructive interference of successive echoes.

Field inhomogeneities, eddy currents and susceptibility effects also cause dephasing of magnetic moments. These off-resonance effects can lead to severe artefacts for bSSFP sequences as the additional dephasing violates the assumption that all magnetic moments are in phase before each RF pulse [66]. The dephasing ϕ after the

time T_R is given by

$$\phi = 2\pi\nu T_R \tag{2.23}$$

where ν describes the frequency offset between the RF pulse and the resonance frequency of the tissue. For tissue with $\nu = \pm\frac{1}{2T_R}$ this leads to $\phi = \pi$ and is visible as dark bands in images (banding artefacts).

2.3 Sampling Schemes

The signal S which is obtained with the receiver coils is not measured continuously but as a function of a finite number of discrete k-space positions (Fig. 2.9a,b). A signal $\hat{S}$ sampled at N discrete sampling positions which are separated by Δk can be described by

$$\hat{S}(p\Delta k) = S(k)c(k)r\left(\frac{k+\frac{\Delta k}{2}}{W}\right) \quad \text{with} \quad W = N\Delta k \quad . \tag{2.24}$$

$S(k)$ describes the Fourier transform of the effective spin density $\rho(x)$, $c(k)$ is a 'comb' function

$$c(k) = \Delta k \sum_{p=-\infty}^{\infty} \delta(k - p\Delta k) \tag{2.25}$$

and r(k) a rect function

$$r(|k| \leq \frac{1}{2}) = 1 \quad \text{and} \quad r(|k| > \frac{1}{2}) = 0 \quad . \tag{2.26}$$

For the reconstructed signal $\hat{\rho}$ this leads to

$$\hat{\rho}(x) = \rho(x) * C(x) * Wsinc(\pi Wx)e^{-i\pi x\Delta k} \tag{2.27}$$

with

$$C(x) = \sum_{q=-\infty}^{\infty} \delta\left(x - \frac{q}{\Delta k}\right) \quad . \tag{2.28}$$

This means the discrete sampling in k-space leads to multiple copies of the imaged object shifted by $\frac{1}{\Delta k}$ in image space. In order to avoid aliasing or backfolding artefacts the extend of the imaged object has to be smaller than $\frac{1}{\Delta k}$. This is also referred to as the Nyquist-Shannon sampling theorem which states that for a bandlimited function f with the bandwidth b, a sampling frequency f_s of $\frac{1}{2b}$ is required.

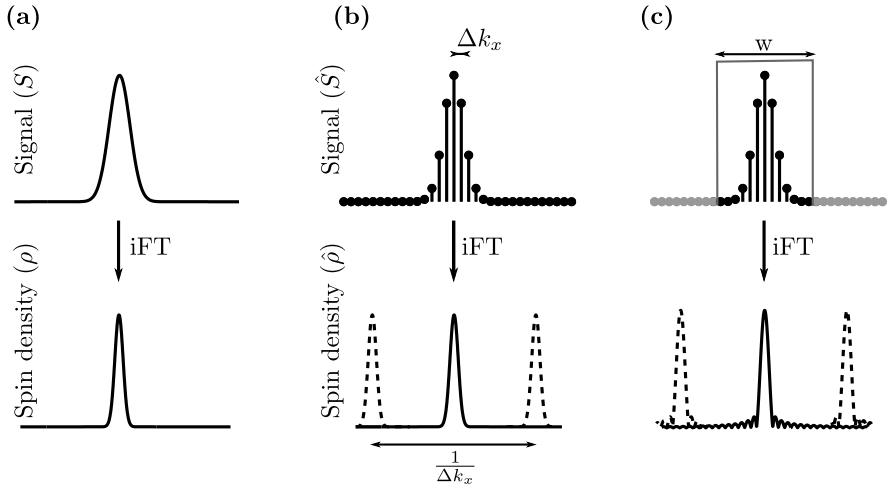

Figure 2.9: Effect of discrete and finite acquisition on reconstructed data. **(a)** Ideally the spin density ρ (bottom row) would be determined as a continuous and infinite signal S (top row). **(b)** The discrete sampling of S at positions separated by Δk_x leads to copies of ρ at $\frac{1}{\Delta k_x}$. **(c)** The finite sampling of S within $W = N\Delta k$ leads to Gibb's ringing artefacts.

The *sinc* functions can cause Gibbs ringing artefacts (Fig. 2.9c) [61]. They occur close to strong signal intensity changes (i.e. edges) and their frequency is proportional to the number of samples N but their amplitude of $\approx 9\%$ is constant. They can be reduced by applying a low-pass filter with the tradeoff of additional blurring.

Not just the k-space signal is discrete and truncated but also the image information is obtained on a finite and discrete grid. Applying the above also for $\rho(x)$ and assuming that $\hat{\rho}(x)$ and $\hat{S}(k)$ have the same number of samples N leads to

$$\Delta x \Delta k = \frac{1}{N} \quad . \tag{2.29}$$

Therefore, for an image with a desired resolution of Δx and a field of view of F the k-space has to be sampled from $-k_x^{max}$ to $k_x^{max} - 1$ on discrete sampling points separated by Δk with

$$\Delta k = \frac{1}{F} \quad \text{and} \quad k_x^{max} = \frac{1}{2\Delta x} \quad . \tag{2.30}$$

Location and temporal order of the measured k-space positions (k_x, k_y, k_z) are referred to as sampling scheme, acquisition scheme, encoding scheme, sampling pattern or k-space trajectory. Basically any sampling scheme can be used to record $\hat{S}$ within the restrictions of the physical properties of the gradient coils. Figure 2.10

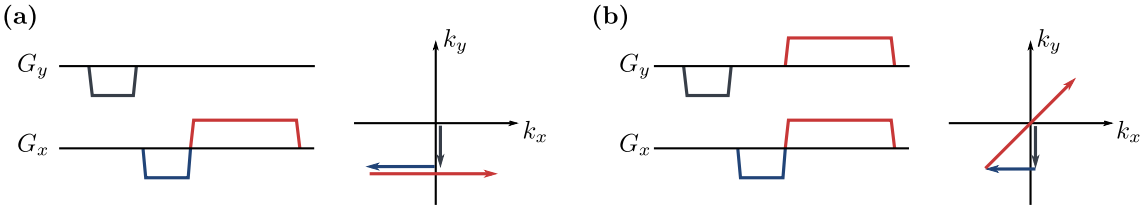

Figure 2.10: Temporal order of frequency and phase encoding gradients G_x and G_y to sample k-space data along a horizontal **(a)** or a diagonal line **(b)**.

shows two examples how the gradients G_x and G_y can be used to record data along a horizontal and diagonal line in k-space.

A useful tool to analyse how different sampling schemes influence the final image data are point spread functions (PSFs). They provide a method to study the effect of imaging systems on arbitrary input data. A PSF is the response of an imaging system to the input of a single point, i.e. a discrete delta function. Once the PSF is known, the effect of the imaging system on arbitrary input can be calculated as the convolution of the PSF with the input data. Figure 2.11 depicts the PSF of two different imaging systems and their effect on image data.

The following sections explain different acquisition schemes in MRI and discuss their advantages and disadvantages.

2.3.1 Cartesian Sampling Schemes

A 3D Cartesian sampling pattern consists of N_{k_x} x N_{k_y} x N_{k_z} k-space sampling positions located on a grid with the uniform spacings Δk_x, Δk_y and Δk_z (Fig. 2.12a). Therefore, equation (2.30) can be directly applied which leads to

$$FOV_n = N_n \Delta n = \frac{1}{\Delta k_n} \quad \text{and} \quad \Delta n = \frac{1}{N_{k_n} \Delta k_n} \quad \text{with} \quad n = x, y, z \tag{2.31}$$

for a reconstructed image with N_x x N_y x N_z pixels and resolution $\Delta x, y, z$.

If the Nyquist-Shannon sampling theorem is not met, aliasing artefacts appear as copies of the imaged object shifted along the undersampled k-space direction which is referred to as ghosting (Fig. 2.12). For 3D sampling the k_y-k_z plane is sometimes also referred to as 2D phase encoding (PE) plane with the axis PE_1 and PE_2.

Cartesian sampling is the most widely used acquisition scheme both for 2D and 3D imaging in clinical practise mainly because it yields a very high signal to noise

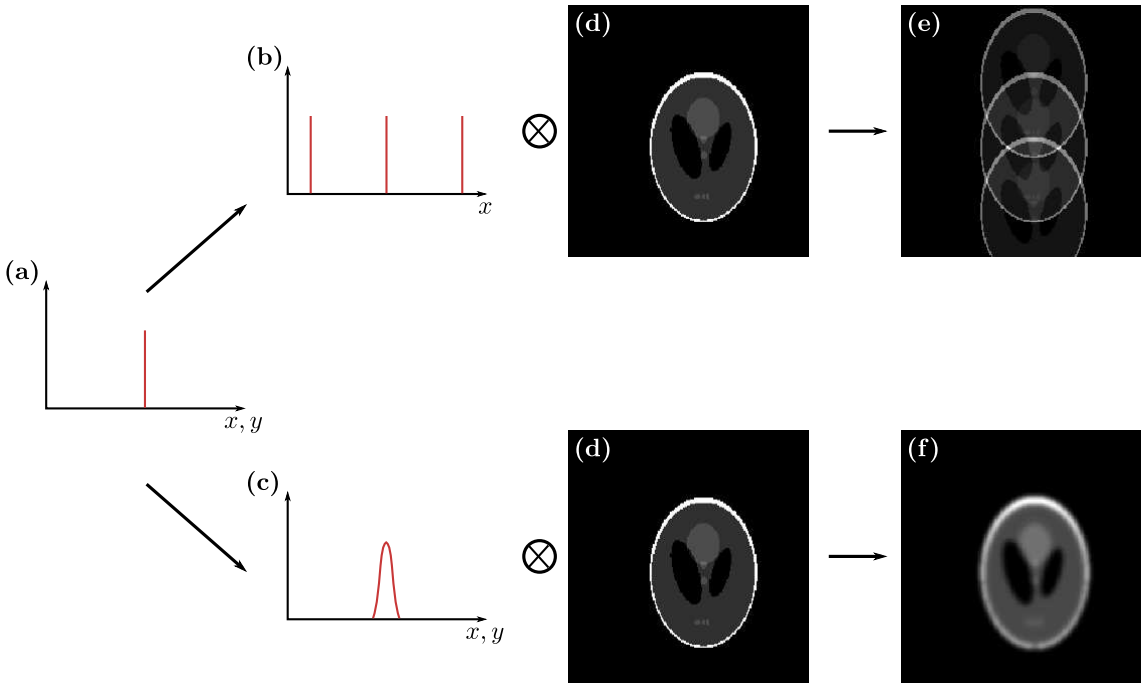

Figure 2.11: Analysis of imaging systems using point spread functions (PSF). The PSF describes the response of an imaging system to an input of a delta function **(a)**. Two imaging systems are shown which create a PSF with multiple delta peaks **(b)** and a broadening of the delta peak (i.e. blurring) **c)**. The effect of these imaging systems on arbitrary input data **(d)** can be calculated by convolving the PSF with the input data (**(e)** and **(f)**).

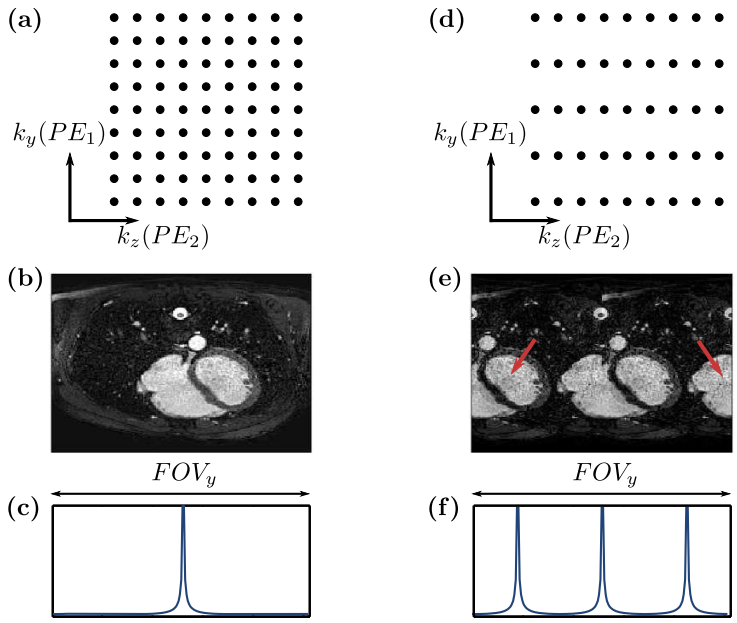

Figure 2.12: 3D Cartesian sampling. **(a)** Fully sampled Cartesian 2D phase encoding plane (k_y-k_z or PE_1-PE_2) leads to **(b)** an aliasing artefact free image and **(c)** a point spread function (PSF) with a single peak in the centre of the FOV. **(d)** Undersampling by a factor of 2 in one phase encoding direction (k_y or PE_1) causes **(e)** ghosting artefacts, i.e. copies of the image shifted by $\frac{\text{FOV}}{2}$ (red arrows). **(f)** The PSF of this sampling pattern exhibits therefore multiple peaks within the FOV along the undersampled direction.

ratio (SNR) compared to other sampling patterns [67]. Furthermore, image data can be obtained with an inverse fast Fourier transform (iFFT) providing fast image reconstruction [67].

The temporal order which is used to sample k-space data in the 2D phase encoding PE_1 - PE_2 can strongly effect the quality of the obtained image. The central part of k-space describes low spatial frequencies which determine the contrast of the image. Any errors during the acquisition of these k-space positions can lead to very pronounced artefacts.

One possibility to acquire 3D high resolution anatomical information is to use a hybrid Cartesian sampling pattern (Fig. 2.13). Each of the Cartesian k-space positions in the 2D PE plane is assigned a radius (i.e. distance from the k-space centre) and an angle. Data is acquired for a certain range of angles starting with the lowest radius value and moving to the periphery of k-space. Then the next range of angles is obtained in the same way until all M angular ranges are acquired.

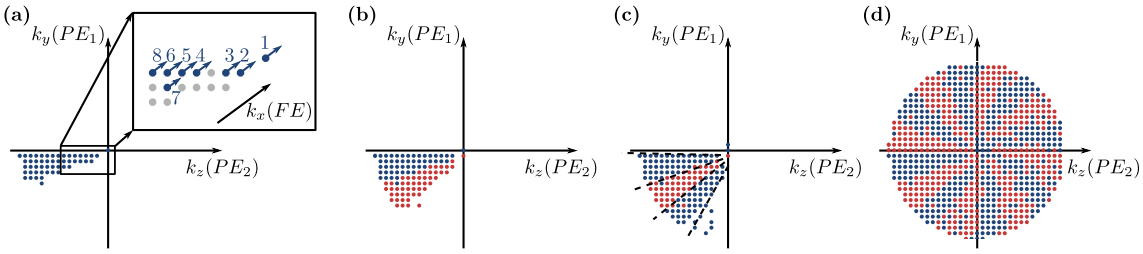

Figure 2.13: 3D Hybrid Cartesian sampling scheme. **(a)** Sampling starts in the centre and progresses towards the periphery of k-space. The numbers indicate the order of the first eight phase encoding (PE) positions. For each sampling point in the 2D PE plane (k_y-k_z or PE_1-PE_2) a fully frequency (FE) encoded k-space line is obtained. **(b,c)** Sampling continues for sampling points within adjacent angular ranges (indicated by dashed black lines) until **(d)** the entire 2D PE plane is acquired.

To ensure a covering of low frequency data even for acquisitions which are terminated before the successful end of the scan, data within the central region of k-space is obtained independent of their angle. A central region with M points (i.e. same number as number of angular ranges) is defined and for each range of angles the first k-space position is sampled from this central region starting in the k-space centre.

Cartesian sampling is usually restricted to k-space points within a circular region in the 2D phase encoding plane leaving the highest spatial frequencies unsampled. This application of a so called elliptic shutter leads to a decrease in scan time by approximately 21.5%, an increase in SNR and an isotropic spatial resolution [68].

2.3.2 Radial Sampling Scheme

As already mentioned previously 2D k-space data can also be sampled along radial lines at different angles α_{k_i} with frequency encoding in radial and phase encoding along the angular direction. This is referred to as polar sampling, radial sampling or radial frequency encoding (Fig. 2.14a) [2,69].

A common method to define α_{k_i} is an uniform radial sampling pattern (Fig. 2.15a)

$$\alpha_{k_i} = i\Delta\alpha_k \quad \text{with} \quad i = 0, 1, \ldots N_a - 1 \quad \text{and} \quad \Delta\alpha_k = \frac{\pi}{N_\alpha} \tag{2.32}$$

which leads to uniform angular gaps $\Delta\alpha^{(max)} = \Delta\alpha_k$ after sampling N_α radial lines (Fig. 2.14c). For a high number of radial sampling lines $\Delta\alpha_k$ is very small which leads to a slow covering of k-space over time. This can be avoided with a segmented

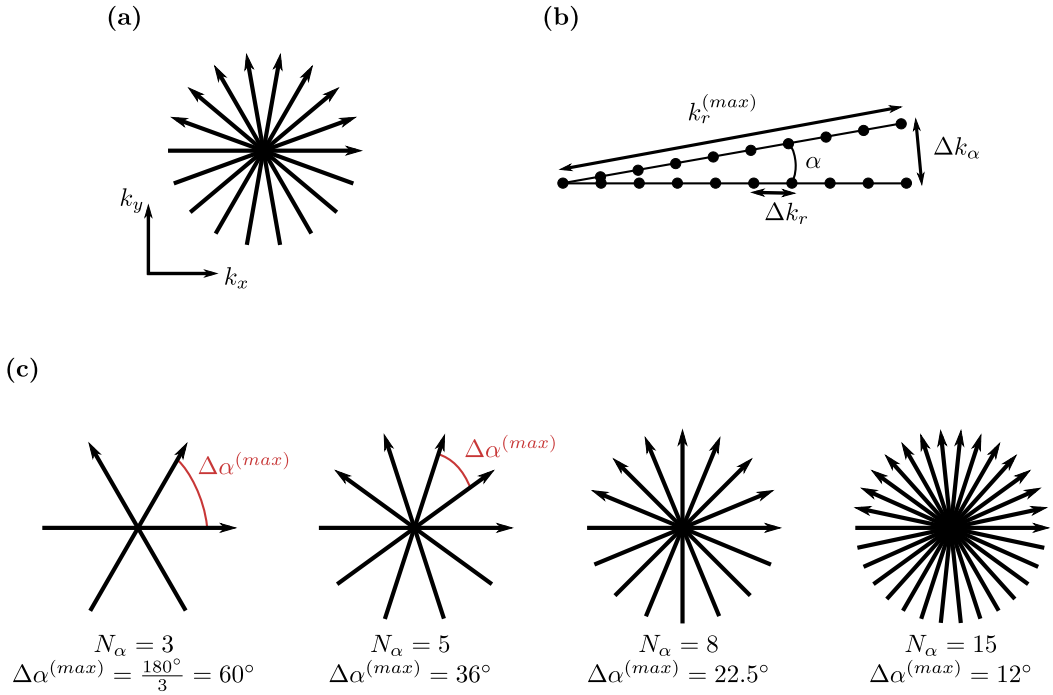

Figure 2.14: 2D uniform radial sampling pattern. **(a)** For a 2D uniform radial sampling scheme data is sampled along radial spokes. **(b)** The distance between sampling points Δk_a is a function of $k_r^{(max)}$ and angle α. **(c)** Sampling N_α radial lines leads to uniform angular gaps given by $\Delta\alpha^{(max)} = \frac{180°}{N_\alpha}$

approach (Fig. 2.15b). Here radial spokes are divided into N_s segments, each covering 0 to π but with larger angular gaps $\Delta\alpha_k = \frac{\pi}{N_\alpha}N_s$. Several of these segments with different starting angles α_s are acquired successively to achieve the same $\Delta\alpha^{(max)} = \frac{\pi}{N_\alpha}$ as above. Therefore, the sampling order of angles is given by

$$\alpha_{k_i} = \alpha_s + i\Delta\alpha_k \quad \text{with} \quad i = 0, 1, \ldots \left(\frac{N_\alpha}{N_s} - 1\right) \quad \text{and} \quad j = 0 \ldots (N_s - 1) \quad . \tag{2.33}$$

The starting angles α_s can be defined in a bit reversed order to make the covering of k-space even more homogeneous over time.

The distance between radial sampling positions is a function of the radius (Fig. 2.14b) and in order to fulfill the Nyquist theorem and avoid undersampling artefacts the number of angular views N_a should equal $\frac{\pi}{2}N_r$, where N_r is the number of k-space samples along each radial trajectory. This ensures that the maximum distance between spokes Δk_a is equal to the spacing Δk_r between the sampling points along radial lines. Compared to a Cartesian sampling scheme this means that $(\frac{\pi}{2} - 1)N_r$

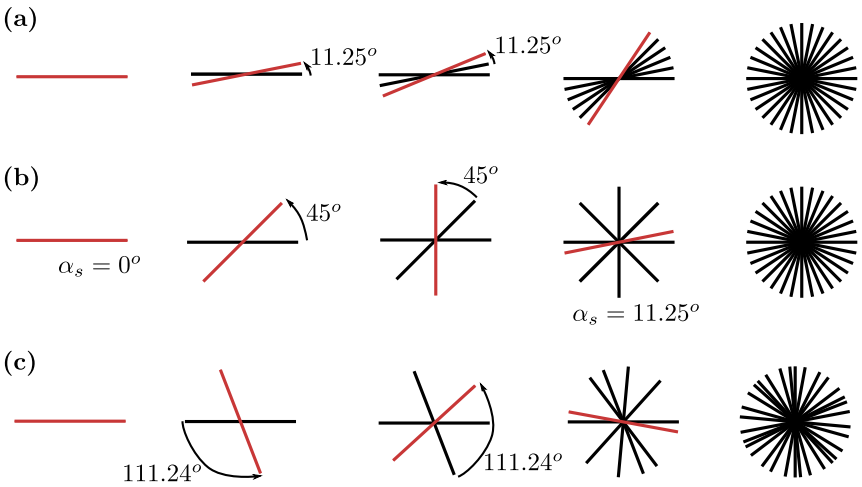

Figure 2.15: First 16 spokes for three different radial sampling patterns. **(a)** For a uniform radial sampling scheme the $N_a = 16$ radial lines are tilted by $\frac{180°}{16} = 11.25°$ to each other. **(b)** For the segmented approach with four segments ($N_s = 4$) the angles for each segment are tilted by $4\frac{180°}{16} = 45°$ and the starting angles α_s for the segments are 0°, 11.25°, 22.5°, and 33.75° respectively. **(c)** Using the Golden Angle (GA) approach leads to successive spokes tilted by $0.618\pi \approx 111.24°$ which leads to a homogeneous distribution of radial lines for any number N_a. For the same number of spokes the GA approach can lead to larger angular gaps than the uniform sampling schemes.

more k-space samples are required to obtain a fully sampled k-space for the same FOV and resolution.

A different approach to set α_{k_i} uses the idea of the Golden Ratio g, which is defined as

$$g = \frac{\sqrt{5}-1}{2} \approx 0.618 \quad . \tag{2.34}$$

It is the solution of an optimisation problem trying to distribute an arbitrary number of points on a circle as homogeneous as possible [70]. Furthermore, it ensures that any number of points can be added without impairing the homogeneous distribution. For radial lines this leads to [71]

$$\alpha_{k_i} = \alpha_{k_{i-1}} + 0.618\pi \quad \text{with} \quad \alpha_0 = 0 \tag{2.35}$$

which is also referred to as Golden Angle (GA) or Golden Ratio (GR) radial sampling.

Figure 2.15 compares the first 16 profiles of a uniform and GA radial sampling scheme. A disadvantage of the GA sampling pattern is that it can result in larger angular gaps $\Delta\alpha^{(max)}$ than the uniform radial sampling scheme for the same number

of radial k-space lines. These larger gaps can cause more pronounced sampling artefacts. Winkelmann et al. compared a uniform radial sampling scheme to the Golden Ratio approach analytically with the result that the image quality is comparable but the signal to noise ratio (SNR) is 0.5 - 2.5% lower for the GA scheme [71].

The inhomogeneous sampling density of uniform radial trajectories decreases the SNR to 86 - 87% of the SNR of an image acquired with a Cartesian sampling scheme for the same number of k-space points [72, 73]. Nevertheless, as the k-space centre is highly oversampled and each spoke samples both high and low frequencies radial acquisitions can exhibit better undersampling properties [74, 75].

For radial encoding schemes aliasing artefacts do not occur as discrete copies of the main peak of the PSF as for homogeneous Cartesian sampling patterns. Undersampling in the angular direction leads to streaking whereas undersampling in the radial direction causes ghosting artefacts [76]. In contrast to Cartesian sampling these ghosting artefacts are not located at certain positions but smeared along a ring at a distance $r_j = \frac{j}{\Delta k_r}$ from the centre of the FOV. Both radial and angular undersampling lead to non-coherent undersampling artefacts [72].

Figure 2.16 compares angular and radial undersampling artefacts for both uniform and GA sampling. The GA scheme leads to less coherent angular aliasing artefacts than the uniform scheme but they can be more pronounced due to the larger angular gaps between spokes.

For 3D data acquisition the radial sampling can be carried out in all three dimensions by tilting the radial lines by two angles or a combination of a 2D radial k-space pattern with Cartesian slice encoding (Fig. 2.17) [74, 77].

Each radial spoke of a polar trajectory passes through the k-space centre. Nevertheless, eddy currents and field inhomogeneities can cause distortion of the k-space trajectory which leads to additional artefacts. These distortions can be corrected for either by optimizing field gradients or by correcting the phase of the acquired data [78–81].

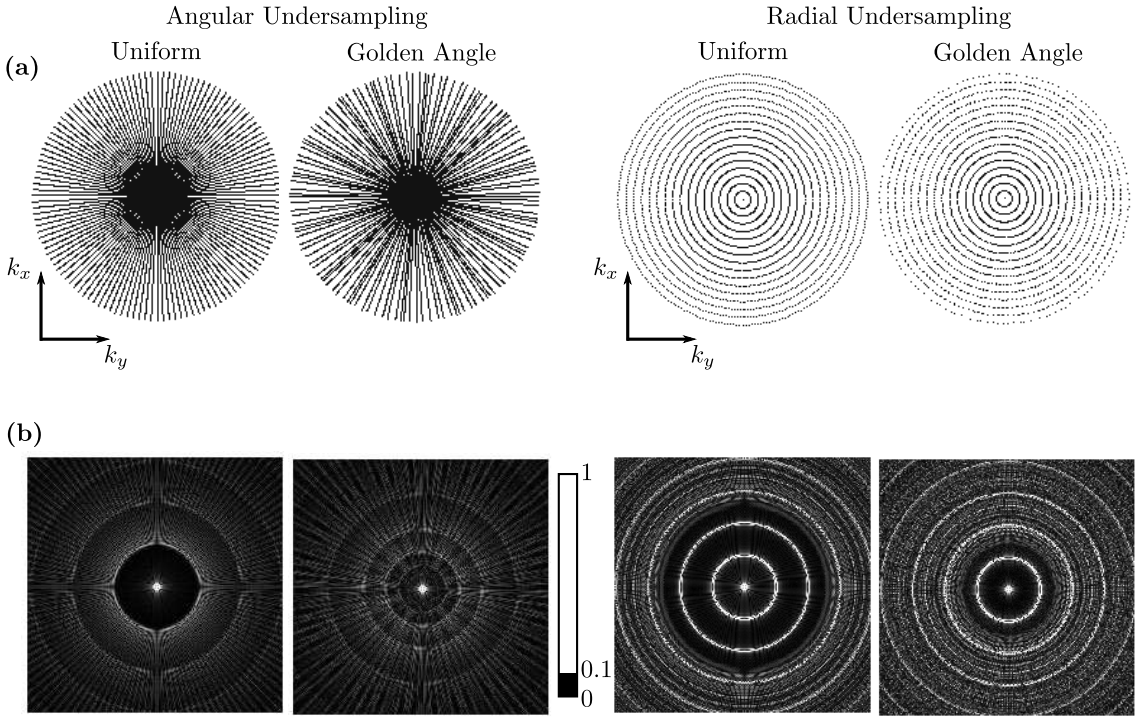

Figure 2.16: Angular and radial undersampling. **(a)** Angular undersampling ($\Delta k_a > \Delta k_r$) causes streaking artefacts. The Golden Ratio approach yields angular gaps with varying sizes which causes more pronounced but also more incoherent undersampling artefacts. **(b)** Radial undersampling leads to ring like aliasing artefacts. The varying spaces between neighbouring radial spokes of GA yields less pronounced ring like artefacts but an overall higher background noise level.

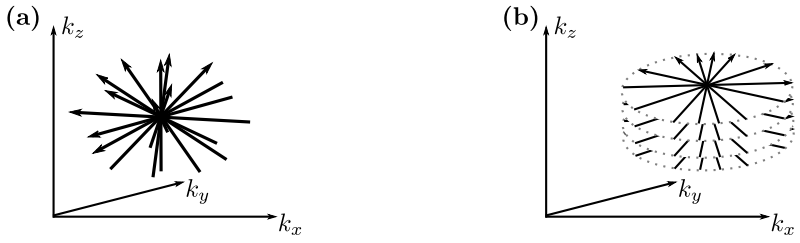

Figure 2.17: 3D k-space sampling schemes. Frequency encoding is carried out along black arrows. **(a)** Radial sampling schemes can be expanded to 3D by rotating the radial spokes about two angles (Koosh ball). **(b)** Another possibility is to combine a 2D radial acquisition with Cartesian slice encoding along k_z (stack-of-stars).

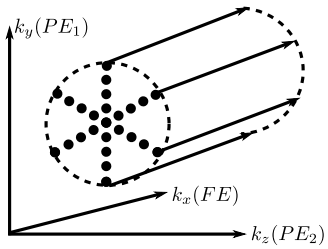

Figure 2.18: Radial Phase Encoding (RPE). For RPE phase encoding is carried out along a radial like pattern in the 2D phase encoding plane (PE_1 - PE_2). FE frequency encoding

2.3.3 Radial Phase Encoding (RPE)

As already discussed 3D Cartesian sampling uses Cartesian frequency encoding on a Cartesian two-dimensional phase encoding (PE) grid (Fig. 2.18a). Radial phase encoding (RPE) combines Cartesian frequency encoding with phase encoding along a radial-like sampling pattern in the 2D PE plane (PE_1 - PE_2) (Fig. 2.18). This results in similar undersampling properties as radial frequency encoding without its drawbacks such as the requirement of large FOVs and sensitivity to eddy currents. Furthermore, both radial and angular undersampling as well as a partial Fourier acquisition along the spokes are possible. Boubertakh et al. show that with an interleaved radial RPE scheme much higher undersampling factors are achievable than with Cartesian sampling using a non-Cartesian sensitivity encoding reconstruction[2]. Furthermore, the superior properties of interleaved undersampling along the radial direction are demonstrated. K-space positions along radial lines with the spacing Δk_r are shifted by a fraction of Δk_r along the radial direction for successive spokes in order to achieve more incoherent undersampling artefacts [82]. Figure 2.19 demonstrates the advantageous undersampling properties of an interleaved radially undersampled RPE acquisition.

The superiour undersampling properties of RPE schemes in combination with advanced reconstruction techniques has also been used in other applications such as temporally resolved imaging [83].

[2]Non-Cartesian sensitivity encoding reconstructing is an iterative reconstruction scheme which uses the information from multiple receiver coils to reduce undersampling artefacts. Chapter 2.5 discusses this technique in more detail.

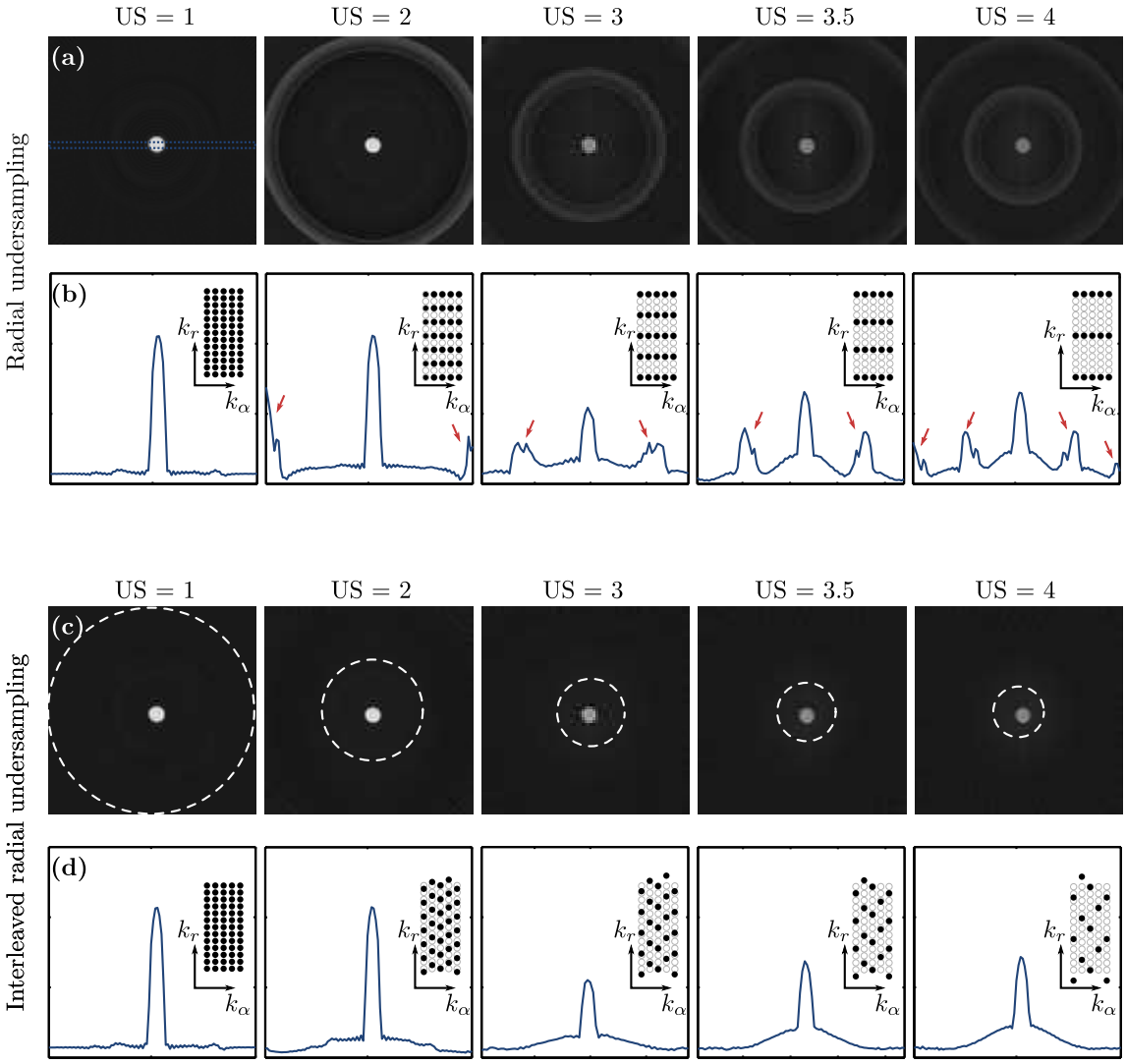

Figure 2.19: Non-interleaved **(a-b)** and interleaved **(c-d)** radially undersampled RPE scheme. Each column shows a different undersampling factor (US = 1, 2, 3, 3.5 and 4). (a) and (c) show an image of a phantom and (b) and (d) depict a projection of the dotted region marked in (a). The dashed circles indicated the aliasing artefact free FOV according to the Shannon-Nyquist sampling theorem. The interleaved radial undersampling avoids any coherent undersampling artefacts (red arrows).

2.4 Image Reconstruction

In MRI information is encoded as a function of spatial frequencies and the corresponding image data is obtained using different reconstruction techniques. The methods and algorithms used for image reconstruction depend on multiple parameters such as acquisition scheme, image content and application, some of which shall be discussed in the following.

As already mentioned data acquired on a Cartesian grid can be reconstructed with a discrete inverse fast Fourier transform (iFFT) which only requires $N \log N$ operations for N^2 recorded k-space positions. Nevertheless, the iFFT cannot be applied for trajectories with a inhomogeneous distribution of k-space positions, such as radial or RPE trajectories, and therefore different methods are required.

One approach is to interpolate the k-space data S first onto an equispaced rectilinear grid using a convolution kernel K and then to apply the iFFT to obtain the image information ρ. This technique is referred to as gridding and can be described as

$$\rho = \left(iFFT\left([(SD) * K]C\right)\right)\frac{R}{k} \quad \text{with} \quad k = iFFT(K) \quad . \tag{2.36}$$

The density compensation function (DCF) D is applied to the sampled k-space positions S to compensate for their inhomogeneous distribution by weighting them according to their sampling density. The DCF can be calculated either analytically or numerically using a Voronoi approach [84]. Jackson et al. suggests to use

$$D = \frac{1}{P * K} \tag{2.37}$$

with the sampling function P to compensate for different sampling densities [85]. This approach can be extended to a technique which iteratively improves the DCF [86]. The accuracy of D has a strong effect on image quality and SNR increases of up to 30% are reported in phantom experiments by optimising the density compensation function [87].

The convolution of the weighted k-space data with the kernel K shall decrease errors due to the discretisation of the data onto a rectilinear grid [88]. O'Sullivan shows that a perfect image reconstruction can be obtained if K is an infinite *sinc* function. This is computationally impracticable and therefore he suggests to use a

Kaiser-Bessel window instead [89]. Jackson et al. investigate several different window functions with the result that a Kaiser-Bessel function with

$$K(u) = \frac{\beta}{W}\sqrt{1-\left(\frac{2u}{W}\right)^2} \quad \text{for} \quad |u| \leqslant \frac{W}{2} \tag{2.38}$$

leads to the smallest aliasing energy within the region of interest [85]. A window width W of 4 with $\beta = 18.5547$ is reported to yield good results. Furthermore, an oversampling factor of two is usually used for the convoluted k-space to reduce aliasing artefacts. These parameters can also be further optimised to reduce computational demands without compromising image quality [90].

The data is sampled onto a discrete rectilinear grid by multiplying it with a *comb* function C and the iFFT can be applied to obtain image information. Afterwards dividing the image by the inverse Fourier transform of the gridding kernel K compensates for the convolution. A multiplication with the rect function R limits the image to the desired region of interest.

An alternative to the gridding approach is the inverse nonequispaced fast Fourier transform (iNFFT) which can directly Fourier transform the non-Cartesian k-space data. The obtained image information has to be interpolated onto an equispaced rectilinear grid afterwards [91].

Radially acquired k-space data can also be reconstructed by Fourier transforming each radial spoke individually and then applying a filtered backprojection method to obtain the image information on a rectilinear grid. No significant difference in image quality between filtered backprojection and gridding are reported [92]. In this thesis all images acquired at inhomogeneously distributed k-space positions were reconstructed either using gridding or iNFFT.

2.5 Acceleration of Data Acquisition

Compared to other medical imaging techniques such as computed tomography or ultrasound, MRI data acquisition takes considerably more time. Therefore, numerous methods have been proposed to accelerate MR imaging. One possibility is to reduce the number of acquired k-space samples. In order to avoid negative effects on the FOV, resolution or image quality, the missing data can be retrieved during re-

construction by making assumptions on the acquired k-space, on the imaged object and/or by using additional hardware.

2.5.1 Partial *K*-Space Reconstruction

The objects imaged in MRI are described by real values. Therefore, k-space data of these objects should be hermitian, i.e. the real part of the k-space signal should be symmetric and the imaginary part should be antisymmetric round the centre of k-space

$$S(k_x, k_y) = S^{\star}(-k_x, -k_y) \quad . \tag{2.39}$$

Instead of acquiring data from $-k^{max}$ to k^{max} it should therefore be sufficient to acquire 0 to k^{max} and retrieve missing sampling positions from their complex conjugate counterpart (conjugate synthesis, Fig. 2.20b) or by applying a weighting function to the k-space data (homodyne approach, Fig. 2.20c). Nevertheless, susceptibility artefacts caused for example by air/tissue borders or B_0 inhomogeneities can lead to complex image information and violate the assumption in equation (2.39). One possibility to overcome this problem is to estimate the phase $\phi_L(x)$ of the image from a low resolution image ρ_L using the fully sampled centre of k-space

$$e^{-i\phi_L(x)} = \frac{\rho_L^*(x)}{|\rho_L(x)|} \quad . \tag{2.40}$$

This phase map can then be used to make all image information real again. To increase the image quality further the homodyne approach can also be repeated iteratively [93].

2.5.2 Constraint Reconstruction

MR image reconstruction can be seen as a matrix inversion problem. The encoding matrix (given by the k-space trajectory) applied to the imaged object is known. Reconstruction of image data ρ is equivalent to finding the inverse of the encoding matrix E in order to transform the acquired k-space S to image space. Equation (2.20) can be rewritten as

$$S = E\rho = PF\rho \tag{2.41}$$

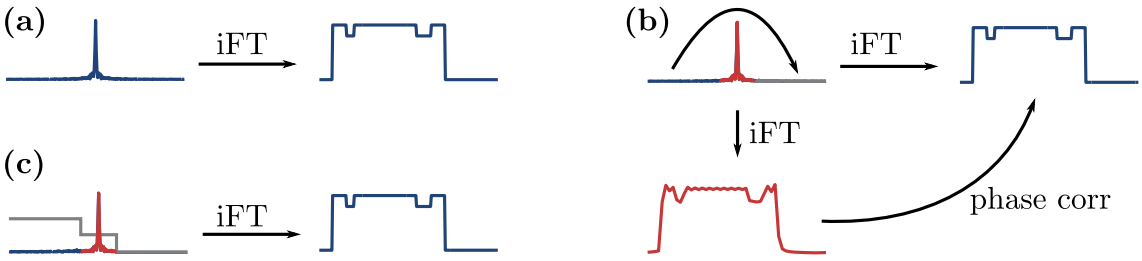

Figure 2.20: Partial k-space reconstruction. **(a)** Image information is obtained by applying an inverse Fourier transform (iFT) to a fully sampled k-space data. **(b)** In order to compensate for data which have not been acquired (gray) unsampled data can be replaced by their complex conjugate counterpart (blue). Phase errors are compensated with a low resolution image reconstructed from the symmetrically sampled centre of k-space (red). **(c)** Instead of replacing the unsampled data a weighting function can be applied to the k-space. The same phase correction as in (b) is also required for this method.

with the Fourier matrix F and sampling pattern P. The image can be retrieved by inverting the above equation to $\rho = E^{\dagger}S$. The exact solution of the reconstruction matrix $R = E^{\dagger}$ is the Moore-Penrose inverse of E

$$R = (E^H E)^{-1} E^H \tag{2.42}$$

with ^{H} referring to the complex conjugate of a matrix. For an N x N image this requires N^6 operations and is usually not applicable for standard image reconstruction.

A computationally less demanding approach minimises the squared difference (L_2-norm) between acquired and reconstructed data according to

$$min\|R^{-1}E\rho - S\|_2^2 \quad . \tag{2.43}$$

This minimisation problem can be solved using a conjugate gradient approach [94] or similar iterative techniques. If the k-space data is undersampled the above equation is ill posed. One possibility to increase image quality is to add further constraints to the minimisation problem such as the L_1 norm for sparse data [9] or a total variation (TV) constraint for piecewise constant images [95]

$$min\|R^{-1}E\rho - S\|_2^2 + \lambda_{L1} min\|R^{-1}E\rho - S\|_1^2 + \lambda_{TV} TV(\rho) \quad . \tag{2.44}$$

These additional constraints can improve the conditioning of the inversion problem and lead to a better image quality. Nevertheless, the constraints can also negatively impair image quality if their weighting factors λ_{L1} and λ_{TV} are not chosen appropriately.

2.5.3 Parallel Imaging

Phased array receiver coils provide another possibility to improve the conditioning of equation (2.41) for undersampled k-space acquisitions. Each coil has a characteristic sensitivity which is restricted to a small area of the FOV and therefore provides additional spatial information about the acquired signal. There are several so called parallel imaging techniques which use this additional information either to retrieve unsampled k-space data (SMASH [6], GRAPPA [8]) or to remove aliasing artefacts in image space (SENSE [7]). Here, only sensitivity encoding (SENSE) shall be discussed in more detail as this technique was used in this thesis.

Equation (2.20) describes the relationship between magnetisation of excited nuclear spins located at $\vec{r} = (x, y, z)$ and measured k-space values S. Due to the measurement (i.e. sum over all excited spins) the spatial information is lost and only the movement of nuclear spins in the magnetic field B_0 over time is obtained.

Parallel imaging techniques recover some of the spatial information by using multiple receiver coils with locally restricted sensitivities $a_\gamma(\vec{r})$ ($\gamma = 1 \ldots$ number of receiver coils). This transforms equation (2.20) to

$$S(\vec{k}, \gamma) = \int \rho(\vec{r}) e^{i\vec{k}\vec{r}} a_\gamma(\vec{r}) d\vec{r} \quad \text{or} \quad S = PFA\rho \quad . \tag{2.45}$$

where the encoding matrix E of equation (2.41) is extended by the coil sensitivity matrix A.

For k-space data sampled along a Cartesian grid the number of entries of the encoding matrix can be reduced, thus allowing for directly solving the matrix inversion of equation (2.42). Fourier transforming $E_{\vec{r},(\vec{k},\gamma)}$ to $E_{\vec{r},(\vec{r}',\gamma)}$ makes the encoding matrix sparse and a reconstruction matrix with only one entry per coil and row is required (sensitivity encoding (SENSE) [7]).

For non-Cartesian sampling schemes like radial or spiral sampling the encoding matrix cannot be made sparse. One possibility to reduce the number of operations required to obtain image data is using an iterative conjugate gradient (CG) approach [94]. Equation (2.45) can be rewritten to

$$(IE^H DEI)b = c \quad \text{with} \quad b = I^{-1}\rho \quad \text{and} \quad c = IE^H DS \tag{2.46}$$

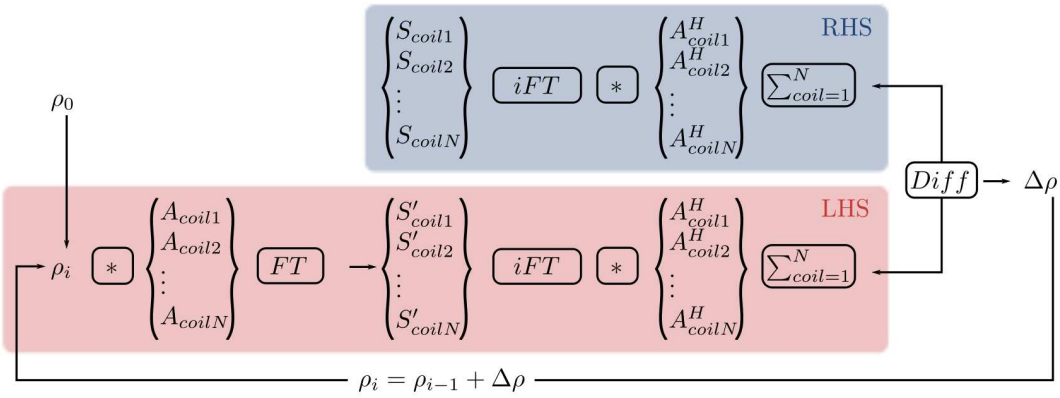

Figure 2.21: Iterative non-Cartesian SENSE reconstruction using a conjugate gradient approach. For the right hand side (RHS) of equation (2.46) k-space data from each coil ($S_{coil_{1\ldots N}}$) is inverse Fourier transformed (iFT) and then multiplied with the corresponding complex conjugate of the coil sensitivities $A^H_{coil_{1\ldots N}}$. The sum over all coils yields the value for c in equation (2.46). For the left hand side (LHS) of this equation an initial guess of the image data ρ_0 is required, which is then multiplied with $A_{coil_{1\ldots N}}$ and Fourier transformed (FT) to k-space. Then the same transformations as for RHS are applied which leads to b in equation (2.46). Finally, the difference $\Delta\rho$ between RHS and LHS is calculated and used to update the image data. These steps are repeated until $\Delta\rho$ is below a threshold or a certain number of iterations has been reached.

which leads to a formulation solvable by the CG method. The density compensation function D takes the inhomogeneous sampling density of the non-Cartesian trajectory into account. Furthermore, the multiplication with coil sensitivities is compensated for with $I = \frac{1}{\sqrt{\sum_\gamma |a_\gamma(\vec{r})|^2}}$.

Applying E^H is equivalent to an inverse Fourier transform (FT), a multiplication with the complex conjugate of the coil sensitivity maps and a sum over all coils. Therefore the right side of the above equation is equivalent to reconstructing an image from k-space data. E equals a multiplication with the coil sensitivity maps and an FT providing the inverse operation to E^H (i.e. transformation from image space to k-space). Figure 2.21 depicts the different CG steps necessary to obtain the image data. The required number of iterations depends strongly on the initial k-space data [96] and is usually determined visually.

One disadvantage of this approach is that data consistency evaluations are only carried out at sampled k-space positions. For radial sampling scheme this means data consistency is only ensured along the individual spokes which can lead to reconstruction artefacts. Additional regularisation terms, such as total variation, can be added in order to obtain an improved solution of the iterative approach [95].

The coil sensitivity matrix or coil sensitivity map A required for the reconstruction can either be estimated from the image data itself [3, 97] or from separately acquired reference scans [7].

A drawback of parallel imaging is that the SNR is locally reduced to

$$SNR_{para} = \frac{SNR_{full}}{\sqrt{R}g} \tag{2.47}$$

where R describes the acceleration of the acquisition (i.e. the undersampling factor) and g depends on several parameters such as coil geometry and sampling pattern. A low g factor is obtained if coil sensitivity maps lead to a well conditioned matrix (i.e. sensitivity value of each coil for aliased pixels vary strongly). In order to also take the effect of the reconstruction algorithm into account, 'noise amplification maps' can be calculated to assess inhomogeneous noise amplification of parallel imaging techniques [82].

3 Cardiac MRI

Cardiac MRI has only recently started to become part of clinical practice. It can be used in the broadest range of applications and therefore has great potential to improve health care.

The following sections discuss anatomy and function of the heart and how they can be visualised and assessed using MRI. The main focus lies on MRI sequences which were used in this thesis. A more detailed and comprehensive description of cardiac MRI can be found in [98].

3.1 Heart Anatomy

The four main chambers of the heart are the right atrium and right ventricle, where deoxygenated blood is collected and pumped into the lungs via the pulmonary arteries, and the left atrium and left ventricle where the oxygenated blood arrives from the lungs and is pumped to the body via the aorta. Figure 3.1 depicts a human heart and the main veins and arteries connected to it.

Cardiac MRI was first introduced using spin echo sequences yielding black-blood images (i.e. low signal intensity from inflowing blood, high signal intensity from myocardium and vessel walls). The development of advanced field gradient systems led to the more frequent use of gradient echo (GE) sequences to image cardiac anatomy. GE yields high signals from blood and lower intensities from myocardium

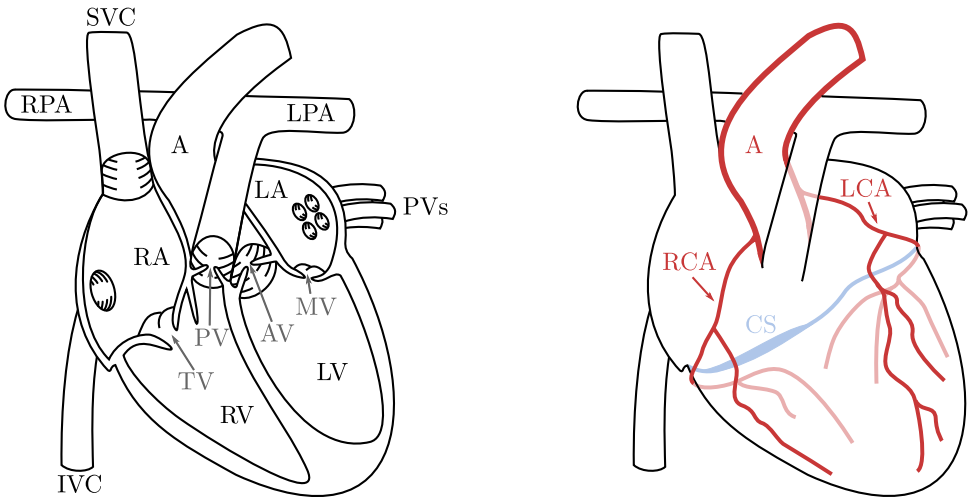

Figure 3.1: Anatomy of the heart. A aorta, AV aortic valve, CS coronary sinus, IVC inferior vena cava, LA left atrium, LCA left coronary artery, LPA left pulmonary artery, LV left ventricle, MV mitral valve, PV pulmonary valve, PVs pulmonary veins, RA right atrium, RCA right coronary artery, RPA right pulmonary artery, RV right ventricle, SVC superior vena cava, TV tricuspid valve.

and vessel walls (bright-blood images) [99]. Nevertheless, a wide variety of techniques is available to adapt tissue contrast for different applications.

As already discussed the image contrast of bSSFP sequences is proportional to the ratio between T_2 and T_1. In cardiac MRI this leads to a high contrast between myocardium and blood pool. Furthermore, especially for 2D imaging, inflow effects of the blood further enhance the contrast between myocardium and blood pool.

Due to the high SNR, bSSFP yields an excellent image quality and also allows for acceleration techniques such as parallel imaging which yields fast 3D whole-heart imaging with high spatial resolution [100]. As mentioned before high isotropic resolution is especially important to visualise complex structures, such as atria and pulmonary veins, in patients suffering from arrhythmia for treatment planning and for image guidance during ablation procedures. Recent studies have shown that MRI is able to provide this information not just for ablation therapy but also for other image guided percutaneous procedures [29–31].

The bSSFP techniques are also used to detect coronary artery disease [12, 45] and asses congenital heart disease [101]. The main limitation of 3D high resolution whole-heart MR imaging is respiratory motion of the heart which will be discussed in chapter 3.3.

Figure 3.2 shows MR images of the heart in different image orientations acquired with a bSSFP sequence using fat suppression and a T_2 prep-pulse to enhance the contrast between coronary arteries and myocardium [102].

Fibrosis in the myocardium can be visualised using delayed enhancement (DE) sequences [39] . A contrast agent such as Gd-DTPA (Gadopentetate-Dimeglumine) is administered with a dose of 0.02 mmol/kg and imaging is carried out 10 to 20 minutes after in injection, although dose and timing can be adapted for different scan protocols. By this time the contrast agent is washed out of the healthy myocardium but remains in the inter-cellular space of the fibrotic tissue. The contrast agent shortens the T_1 time of the surrounding tissue and can be visualised using inversion recovery (IR) sequences. A 180° RF pulse is used to invert the longitudinal magnetisation (M_z). Imaging is carried out after the inversion time (T_I) such that M_z of the healthy myocardium is zero. Due to the shorter T_1 time of the contrast enhanced fibrotic tissue, this yields an optimal contrast between healthy and scarred myocardium (Fig. 3.3).

Myocardial fibrosis is being investigated as the source of tachyarrhythmia [14–16]. Ashikaga et al. present animal studies which suggest that RF ablation therapy targeting fibrotic tissue could provide a highly efficient treatment of arrhythmia [49]. This makes DE-MRI a very important technique for treatment planning of ablation therapy. Furthermore, it can also be used to assess the outcome of RF ablation therapies in patients suffering from arrhythmia (Fig. 3.4) [103].

3.2 Cardiac Function

The heart acts as a ‘mechanical pump’ which maintains the circulation of blood in the body. A succession of one contraction (systole) and relaxation (diastole) of the heart is referred to as cardiac cycle. During this process deoxygenated blood from the body gets to the right atrium through inferior and superior vena cava. From the right atrium it passes through the tricuspid valve to the right ventricle. Then it is pumped via the pulmonary arteries to the lungs. Oxygenated blood is transported back through the pulmonary veins into the left atrium and through the mitral valve into the left ventricle. Finally the blood is pumped to the body via

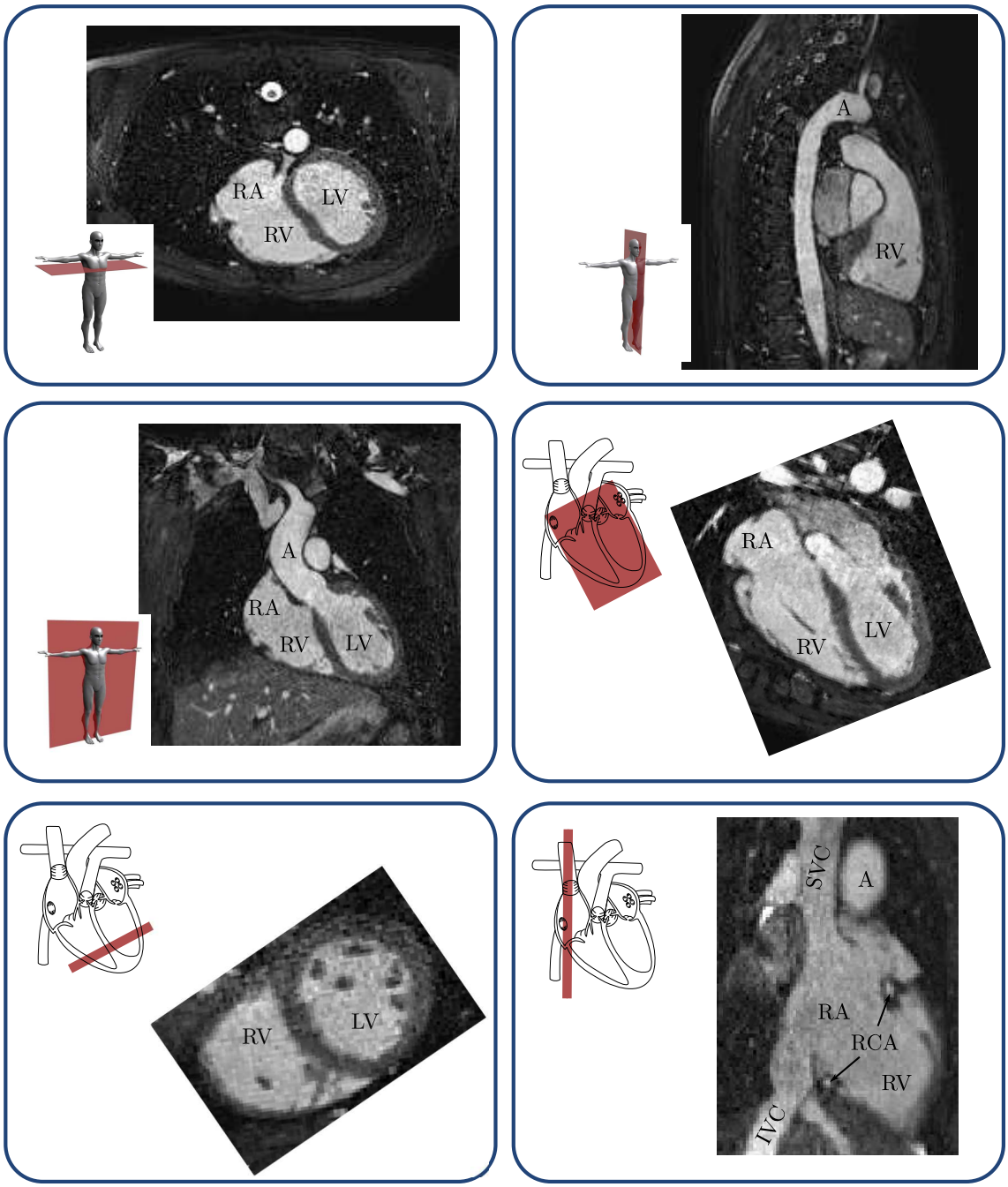

Figure 3.2: Cardiac MR images using a balanced steady-state free-precession (bSSFP) sequence with fat suppression and a T_2 preparation pulse acquired at different imaging planes (indicated by red planes). A aorta, IVC inferior vena cava, LA left atrium, LV left ventricle, RA right atrium, RCA right coronary artery, RV right ventricle, SVC superior vena cava.

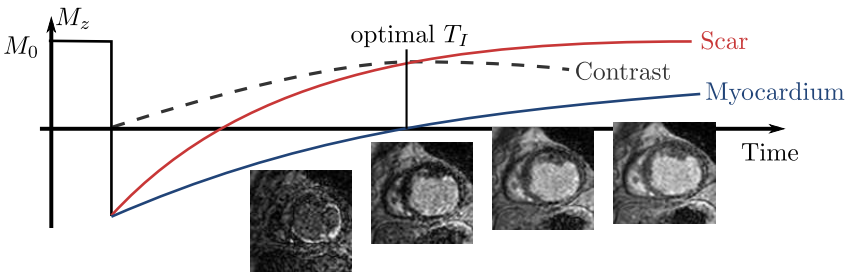

Figure 3.3: Inversion recovery sequence for delayed enhancement imaging. A RF pulse is used to invert longitudinal magnetisation (M_z). Due to the administered contrast agent, M_z relaxes differently for healthy myocardium (blue curve) and scar tissue (red line). If imaging is carried out when M_z of the healthy myocardium reaches 0 (optimal inversion time T_I) the highest contrast between scar tissue and healthy myocardium is achieved.

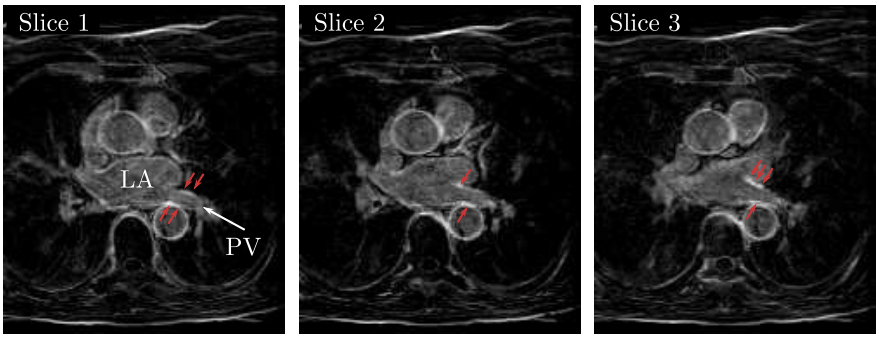

Figure 3.4: Three transverse slices showing the enhancement of scar tissue (red arrows) created by RF catheter ablation around the pulmonary veins (PV). Due to the age of the patient fibrotic tissue is also present in vessel walls and leads to signal enhancement which is especially visible in the wall of the aorta [104]. LA left atrium.

the aorta and a new cardiac cycle starts. The oxygen supply for the heart muscle is ensured through the left and right coronary arteries and blood is drained by the coronary sinus (Fig. 3.1).

The electrical activity controlling each cardiac cycle starts in the sino-atrial (SA) node in the right atrium, first causing contraction of the atria. The stimulus then propagates via the atrio-ventricular node to the ventricles and causes them to contract. This predefined excitation path is ensured by protein junctions between adjacent cells which provide low resistive pathways (gap junctions).

The electrical excitation of the heart creates an electric field. Its strength and orientation varies during the cardiac cycle which can be measured externally using an ECG. This technique provides information about the heart function and can be used non-invasively to detect irregularities in the cardiac cycle.

Blood flow of the heart, propagation of the electrical stimuli and corresponding ECG signals are depicted in Fig. 3.5.

The function of the heart can be assessed visually by comparing the timing and magnitude of contraction for different segments of the heart. Furthermore, quantitative functional parameters such as ejection fraction (EF) can be determined

$$\mathrm{EF} = \frac{\mathrm{SV}}{\mathrm{EDV}} \tag{3.1}$$

with the stroke volume (SV) given as the difference between end-diastolic (EDV) and end-systolic (ESV) volume.

To study the contraction of the heart, bSSFP sequences are widely used due to their excellent contrast between myocardium and blood pool, and high SNR. Real-time MRI has been proposed to provide reliable functional assessment [105]. Nevertheless, both spatial and temporal resolution of real-time MRI is strongly limited. Therefore, cine MRI is commonly used [34–37]. Data are acquired over several cardiac cycles and retrospectively combined to achieve excellent temporal and spatial resolution. This approach will be discussed in more detail in chapter 3.3.1. Figure 3.6 shows a series of short axis images depicting the contraction of the ventricles during a cardiac cycle.

Quantitative blood-flow measurements with velocity encoded MRI [38] and myocardial wall motion measurements using MR tagging can provide further infor-

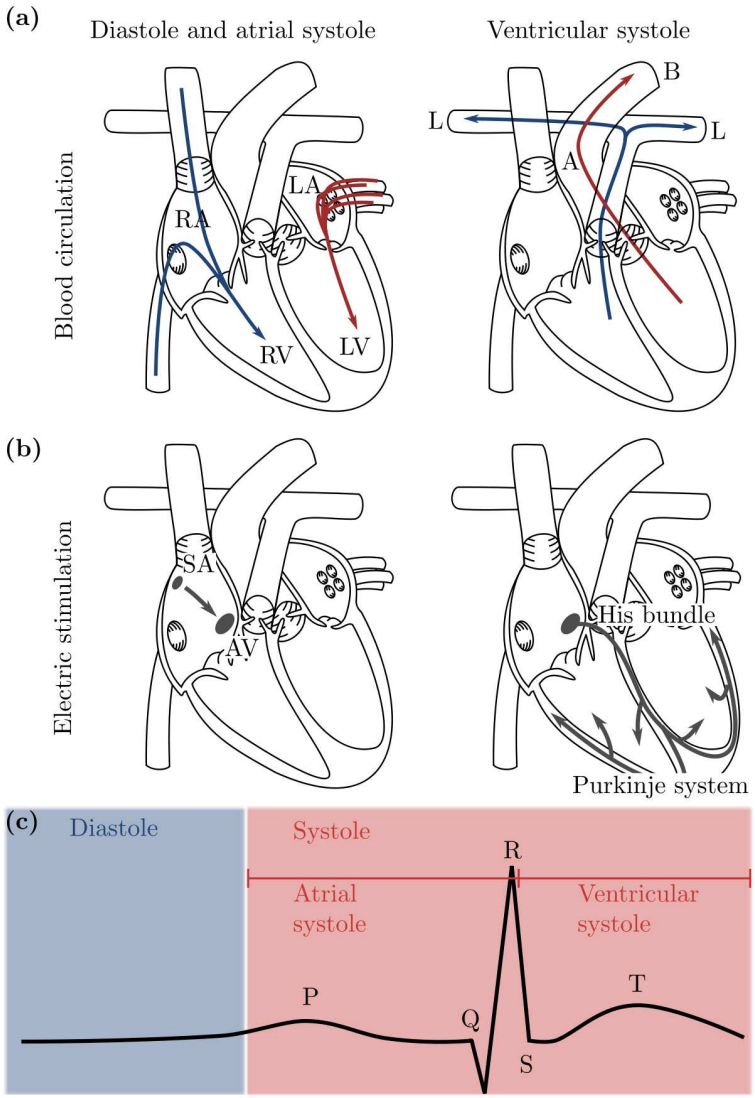

Figure 3.5: Cardiac cycle **(a)** During diastole blood flows into left and right atrium (LA and RA) which pump it into the left and right ventricle (LV and RV) during atrial systole. Ventricular systole causes both ventricles to contract which pumps deoxygenated blood into the lungs (L) and oxygenated blood via the aorta (A) into the body (B). Blue/red arrows: deoxygenated/oxygenated blood. **(b)** The electrical stimulus of atrial systole starts in the sino-atrial (SA) node and propagates to the atrio-ventricular (AV) node. Ventricular systole is stimulated by an electric signal travelling from the AV node via the bundle of His into the Purkinje system. **(c)** In an ECG signal the beginning of atrial systole is indicated by the P-wave and its end by the beginning of the QRS complex. The ventricular systole extends from the R-wave to the end of the T-wave.

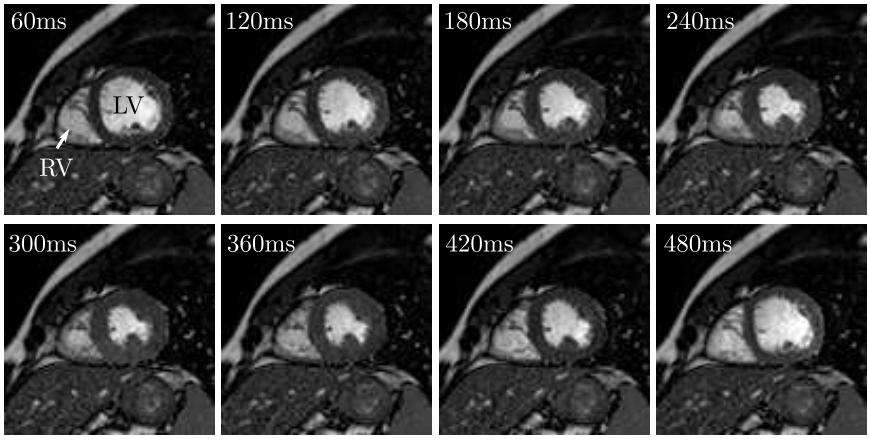

Figure 3.6: Cine MRI short axis views showing the contraction of the ventricles during systolic contraction and diastolic relaxation. Data was acquired with a bSSFP sequence yielding an excellent contrast between blood pool and myocardium, and high SNR. The time in milliseconds is relative to the previous R-peak. LV/RV left/right ventricle

mation about cardiac function [106]. MRI can also be used to assess myocardial perfusion [107] which is especially important in ischemic heart disease.

As already mentioned, respiratory and cardiac motion are the main limiting factors in cardiac MRI which will be discussed in more detail in the following sections.

3.3 Physiological Motion of the Heart

Acquiring MR images of moving objects such as the heart can lead to various motion artefacts and even signal cancellation (Fig. 3.7) which can severely impair image quality. Therefore, motion has to be avoided (e.g. breath-hold imaging), minimised to a tolerable level (motion gating/triggering) and/or compensated for (motion correction).

In cardiac MRI motion due to blood flow and physiological movement (i.e. respiratory and cardiac motion) have to be considered [53]. This section focuses on the latter and discusses commonly used techniques to overcome artefacts caused by the movement of the heart.

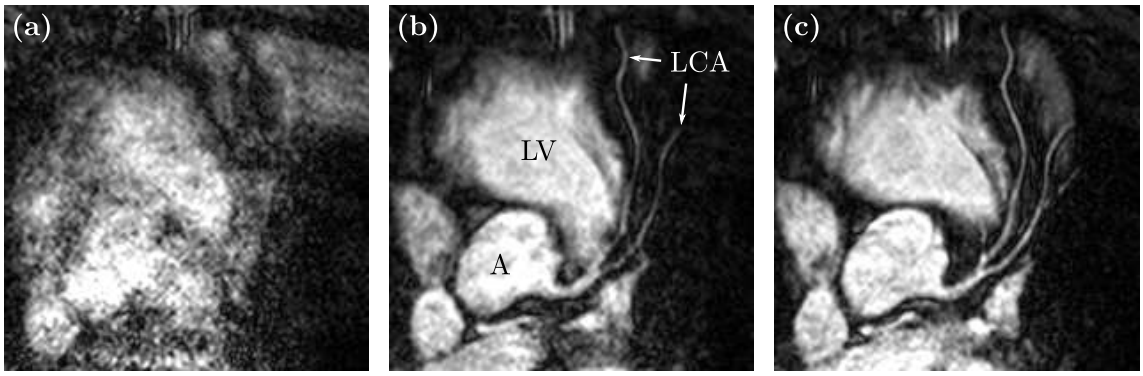

Figure 3.7: Magnetic resonance angiography of the left coronary artery (LCA) with **(a)** no motion compensation, **(b)** compensation of cardiac motion and **(c)** compensation of both cardiac and respiratory motion of the heart. Both cardiac and respiratory motion cause image artefacts and need to be compensated for to achieve an optimal image quality.

3.3.1 Cardiac Motion

Compared to other medical imaging techniques such as computer tomography or echocardiography MR data acquisition is considerable slower. Although real-time MRI has been demonstrated for functional and flow studies of the heart [108], angiography of coronary vessels [109], assessment of functional cardiac parameters [110] and visualisation of interventional devices [111] it imposes strong restrictions on the achievable resolution, field of view (FOV) and signal to noise ratio (SNR). The temporal resolution of real-time MRI is in the range of 20 to 30 ms while providing a spatial resolution of 3 millimetres [105].

In order to avoid any of these limitations and minimise the negative effect of cardiac motion data have to be acquired within a time window (acquisition window) which is short compared to the cardiac cycle length. Data from the same cardiac phase but different cardiac cycles can be combined retrospectively to achieve a higher resolution and cover a larger FOV. Image data can be acquired using either cardiac triggering or cardiac gating.

Information about cardiac cycles is commonly obtained from external ECG devices. The R-peaks of the ECG signal can be detected and are used as reference points during MR data acquisition. Cardiac movement can also be monitored using additionally recorded MR data [112] or by determining the position of the heart directly from the acquired image data [113].

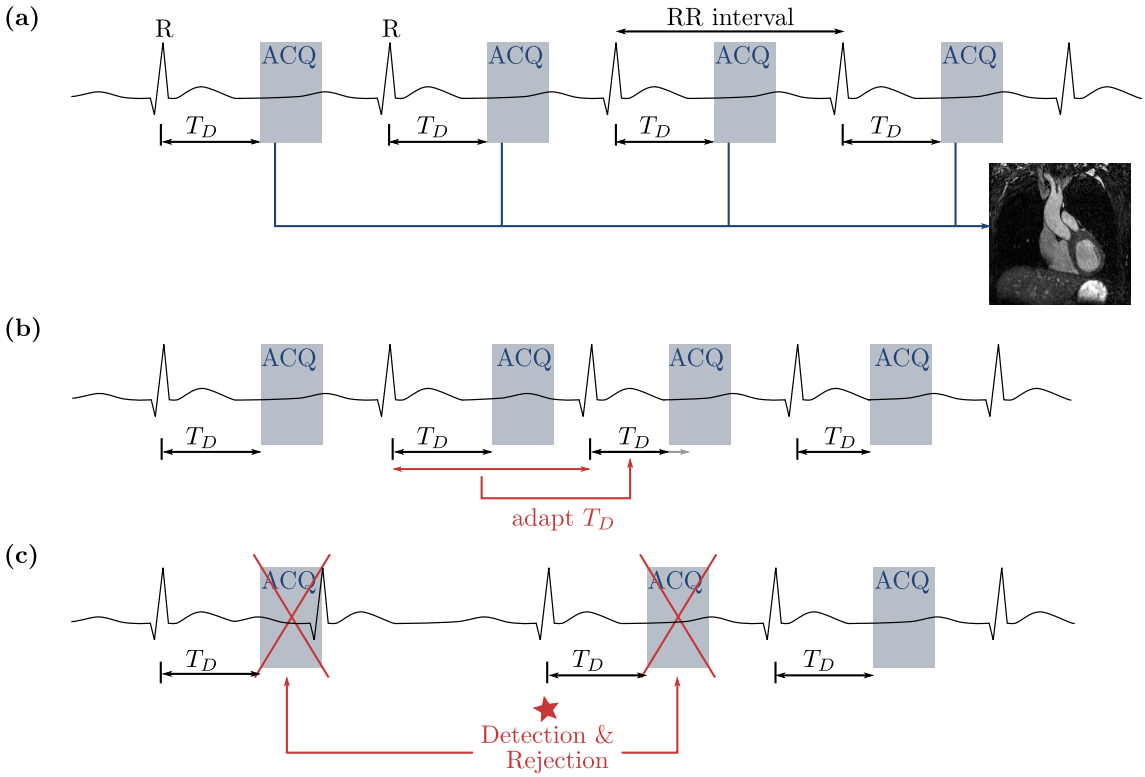

Figure 3.8: Minimisation of cardiac motion using cardiac triggering. **(a)** Data are recorded within a predefined time window (ACQ) in the same cardiac phase over several heart cycles. Data acquisition is started after a constant time delay (T_D) after the detection of the R-wave. Data are combined for final image reconstruction. **(b)** In order to adapt the acquisition to changes in the heart rate T_D can be modified according to the length of the previous RR intervals. **(c)** Arrhythmias can be detected retrospectively and data acquired during these cardiac cycles can be rejected and reacquired to maintain high image quality.

For cardiac triggering data acquisition is carried out within a certain acquisition window at a predefined temporal trigger delay T_D from the R-peak (Fig. 3.8a). It is mainly used for high resolution anatomical imaging.

For strong variations of the heart rate during MR scans a constant T_D does not lead to the optimal image quality [44]. Roes et al. present an approach which adapts T_D during the acquisition according to the latest RR intervals lengths based on a physiological model (Fig. 3.8b) [114].

This approach assumes that the length of the cardiac cycle is a slow varying function and that the heart rate stays constant for several consecutive cardiac cycles. In order to avoid image artefacts due to sudden changes of the cardiac cycle Leiner et al. propose an arrhythmia rejection technique [55]. Their method compares the current length of the RR interval to the average heart rate. If this value is outside

of a certain range (usually ± 20-30% of the average heart rate), data are rejected and reaquired (Fig. 3.8c). Although this method avoids image degradation due to irregularities of the cardiac cycle it can lead to a significantly longer overall acquisition time. Especially for patients suffering from arrhythmia this approach can lead to unacceptably long scan times or even scan abortions.

Functional assessment of the heart is commonly carried out using cardiac gating also referred to as retrospectively reordered cine MRI. Data is acquired throughout the entire cardiac cycle. Each data point is assigned a time stamp indicating the time since the last detected R-peak. For the final image reconstruction data with similar time stamps are combined which yields images of different cardiac phases [34, 51–53]. In order to combine data from cardiac cycles with different lengths, each cardiac cycle is oversampled by 20% or data are interpolated to a certain heart rate. Data acquired during systole and diastole are scaled differently as a function of the length of the RR interval

$$\begin{aligned} \text{systolic period} &= 546\text{ms} - 2.1\frac{60000}{\text{RR interval}} \\ \text{diastolic period} &= \text{RR interval} - \text{systolic period} \quad . \end{aligned} \tag{3.2}$$

This formula is based on a study comparing different systolic time intervals for different heart rates [54, 115]. It is shown that the duration of systole is almost constant for a wide range of heart rates for both healthy volunteers and patients suffering from CVD. Nevertheless, equation (3.2) only provides a simple model for the scaling of systole and diastole which might not lead to an accurate description for each individual subject. Figure 3.9 depicts retrospective cardiac gating.

3.3.2 Respiratory Motion

Breathing leads to a shift and deformation of the heart mainly in the foot-head direction [116] but also additional 3D affine motion components which differ strongly between different subjects [117–120].

One possibility to reduce the negative impact of respiratory motion on the image quality is to acquire data during breath-hold sequences. Even though parallel imaging techniques make whole heart scans during one breath-hold possible [42] it limits FOV and resolution. Furthermore, studies have shown that more than 30%

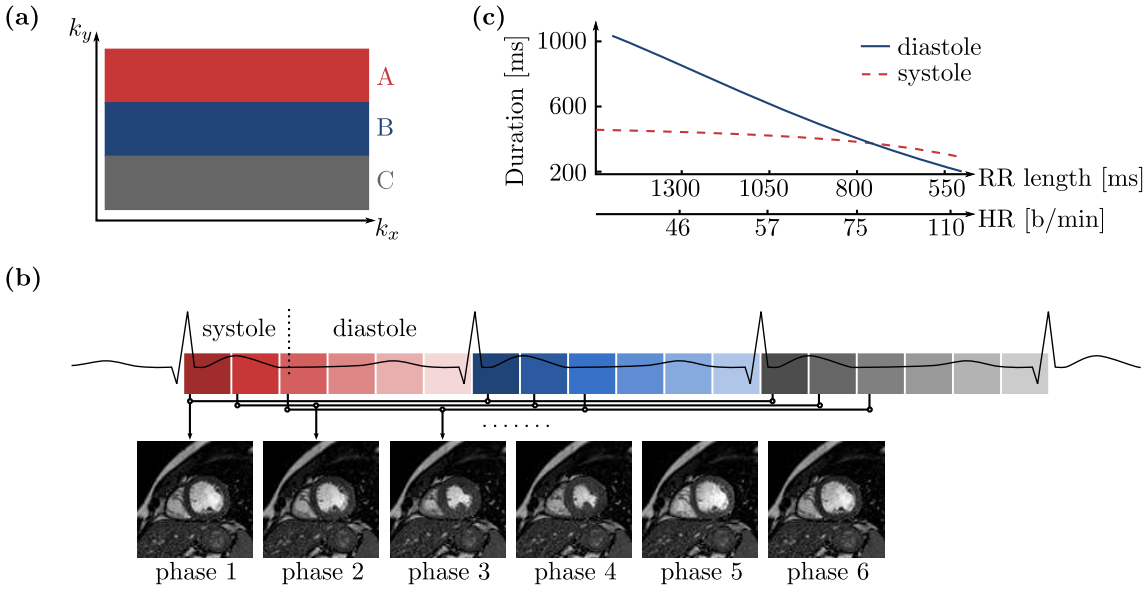

Figure 3.9: Retrospective cardiac gating **(a)** Depending on the number of cardiac phases to be imaged, the desired k-space is separated into different complementary sections (A,B,C). **(b)** Data from each section is acquired for one cardiac cycle. Each data point is assigned a time stamp relative to last detected R-peak. Data from the same cardiac phase but different cardiac cycles are combined for final image reconstruction of high resolution images of different cardiac phases (phase 1, phase 2,...). **(c)** In order to be able to combine data from cardiac cycles with different lengths the assigned time stamps are scaled to a reference cardiac cycle length according to equation (3.2). This formula is based on the observation that for healthy volunteer the length of the systolic period hardly changes for varying heart rates. A change in the length of the cardiac cycle mainly affects the diastolic length. The scaling yields time stamps as a percentage of a normalised systolic and diastolic length.

of patients can have problems to hold their breath in a reliable and reproducible way [121].

Similar to cardiac motion compensation data acquired in the same respiratory phase from multiple breathing cycles can be combined. In contrast to the heart beat respiratory motion is highly variable and can be influenced consciously by the subject. Therefore, it is necessary to obtain a surrogate which can be directly related to the respiratory motion of the heart.

Motion Surrogate

A commonly used surrogate is the position of the right hemi-diaphragm (a muscle between lung and liver) measured by a navigator pencil-beam placed in the foot-head direction. This navigator beam yields a 1D projection of the ROI where the diaphragm is visible as a border between the bright liver and dark lung. Monitoring this reference point yields a navigator signal corresponding to the breathing motion of the diaphragm in the foot-head direction. Techniques to predict information about 2D motion and rotation from respiratory navigators have also been proposed [122–124].

In order to avoid additional scan time for the navigator signal and to minimise the time gap between estimating the navigator position and data acquisition, a motion surrogate can be obtained from echoes of the image data acquisition which is referred to as respiratory self-navigation [125, 126]. Respiratory motion can also be monitored using external devices such as respiratory bellows [127] or ultrasound probes [128].

Motion Minimisation

One method to minimise respiratory motion artefacts in cardiac MRI is to restrict data acquisition to a certain breathing phase (e.g. end of expiration). Image data is only recorded if the obtained navigator signal is within a predefined range, so called gating window (accept/reject or gating method) (Fig. 3.10) [127]. Figure 3.11 shows the combination of respiratory gating with ECG triggering to acquired cardiac MR images.

The position of the diaphragm is recorded over several breathing cycles prior to the image data acquisition during a preparation or training phase. From this

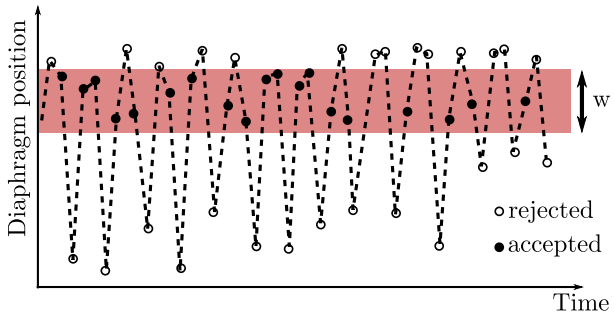

Figure 3.10: Respiratory navigator method. Acquired image data is only accepted if the current displacement of a reference point such as the right hemi-diaphragm is within a predefined navigator window (red).

information the most frequent breathing position which is usually towards end-expiration is determined and a gating window is placed accordingly.

Nevertheless, this might not be the choice leading to the shortest scan time, as the breathing pattern and therefore the most frequent navigator position can change during data acquisition. In order to compensate for these effects the gating window can be shifted within a certain range. This can however lead to a larger overall gating window and therefore to more pronounced motion artefacts.

The navigator efficiency, a value describing the ratio between navigator positions used for data acquisition and total number of acquired respiratory navigators, of the accept/reject method depends strongly on the initial training phase and the steadiness of the respiratory cycle. If breathing patterns change significantly after the preparation phase or if breathing is irregular in general this approach can lead to a very low scan efficiency. This is confirmed by a study using the accept/reject approach for whole heart MR angiography. The MR scan could not be completed in approximately 14% of the patients due to the above mentioned reasons [45]. Therefore, methods which are more flexible and adapt to different breathing patterns can lead to shorter scan times and more reliable results.

The Diminishing Variance Algorithm (DVA) tries to overcome the problem of incomplete scans and low scan efficiency by initially acquiring a fully sampled k-space regardless of the navigator signal. Afterwards k-space positions which were recorded at navigator positions furthest away from the currently most frequent respiratory position are resampled to reduce motion artefacts [129]. This causes a convergence

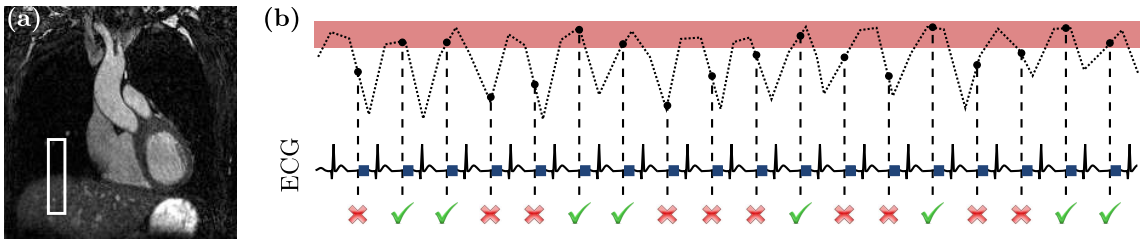

Figure 3.11: Respiratory gating with cardiac triggering. **(a)** A respiratory surrogate is acquired using a pencil beam (white rectangle) placed over the hemi diaphragm. **(b)** Data acquisition (blue box) is carried out using cardiac triggering. Prior to acquisition of image data, respiratory navigator information is obtained. If the respiratory navigator is within a predefined gating window (red rectangle), data is accepted (green tick) other rejected (red cross) and reacquired.

to a k-space with all values sampled in a certain navigator range. Nevertheless, if the most frequent respiratory position changes strongly over time the DVA might not converge to the desired window width and only an image with an insufficient quality can be reconstructed.

Another approach tries to deal with this problem by recording data continuously and labeling it with the navigator position it was sampled at. The Phase Ordering with Automatic Window Selection (PAWS) method uses several gating windows also referred to as bins covering the entire range of the navigator signal. The final image can be reconstructed from the k-space data from one bin or from the combination of several contiguous bins. In order to avoid the collection of superfluous data the sampling scheme has to be defined such that k-space information from neighbouring bins is complementary. The window width Δw does not have to be equal for all windows but can be adjusted to minimise motion artefacts [130].

Jhooti et al. show that the most efficient results can be achieved with images reconstructed from a combination of data from two bins. Nevertheless, they present PAWS with a 2D Cartesian sampling scheme using a combination of three bins in order to minimise residual motion artefacts (Fig. 3.12). One bin is used to record the left hand side, one the right hand side and the third the centre of k_y-space (phase encoding direction). The sampling direction of the first two bins is predefined and for the third k_y values are sampled either towards $-k_y^{(max)}$ or $k_y^{(max)}$ depending which side still has the largest unsampled region. For each k_y value a complete frequency-

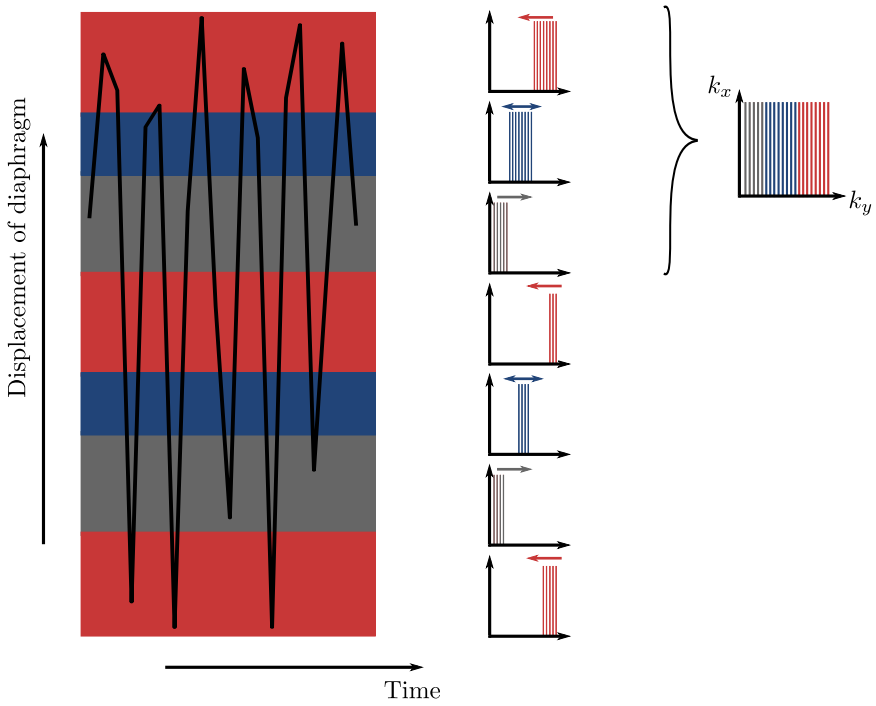

Figure 3.12: Principle of Cartesian PAWS. The entire range of the navigator displacement signal is divided into multiple bins. K-space data from three consecutive bins is used to reconstruct the final image. The frequency encoding is carried out in k_x direction and the phase encoding in k_y direction as indicated by arrows. One bin is used to sample the right hand side (red), one the left hand side (grey) and one the centre (blue) of k-space such that a combination of three bins leads to a fully sampled k-space. Data acquisition is finished if a combination of three adjacent bins leads to a fully sampled k-space. The width of the central bins (blue) is set narrower to achieve a stronger motion minimisation for the central part of k-space.

encoded k_x-line is recorded. The data acquisition is finished when one combination of three consecutive bins leads to a fully sampled k-space.

A recent study shows that the PAWS algorithm exhibits the highest scan efficiency with the best image quality compared to the accept/reject method and DVA [43]. Nevertheless, it still suffers from several limitations. In order to ensure a high image quality, the width of the central bin is set narrower than the other two bins (Fig. 3.12). Although this minimises respiratory motion for the central k-space values it can also cause distinct displacement discontinuities close to the centre of k-space and therefore can lead to strong motion artefacts. Nuval et al. present an adaption of PAWS to overcome this problem which leads to an improvement of image quality but also to an increase in scan time [131].

With 3D MAG the ideas of PAWS have also been extended to 3D Cartesian acquisition schemes but only with data binning along one phase encoding direction [132, 133]. This strongly limits the motion minimisation achieved with PAWS and can again lead to distinct displacement discontinuities in k-space.

The PAWS algorithm is further used to acquire multiple volumes within one scan in order to increase navigator efficiency [134, 135]. Also an extension of PAWS to avoid incomplete data sets similar to DVA and increase navigator efficiency further has been presented [136].

Respiratory gating does not avoid motion artefacts due to breathing altogether but it reduces them to an acceptable level. One approach to minimize these residual artefacts is based on the idea that artefacts are more severe if motion occurs during the sampling of the k-space centre rather than during recording of higher spatial frequencies. Thus several methods use a window width w depending on the currently sampled k-space position [137–139].

Motion Correction

Motion correction can either be used to reduce artefacts of a gated scan even further or to increase image quality of an ungated scan. A possibility to correct motion prospectively is to adapt the ROI for the image data acquisition according to the information from the navigator beam to compensate for linear translations due to breathing [140].

A variety of different methods to carry out motion correction retrospectively has been proposed. They range from phase corrections of k-space data [141, 142] to affine motion correction in image space [143].

Both motion minimisation and motion correction only lead to a good image quality if the relationship between respiratory motion of the heart and the diaphragm is constant over time. Studies have shown that the relationship between the left coronary artery and both hemidiaphragms can in general be described with a constant ratio of 0.6 [116], but can vary strongly between subjects (0.17 - 1.21) and also between exams of the same subject (0.17 - 0.55) [120]. Furthermore for some patients even a hysteresis effect between inspiration and expiration has been observed [117].

3.3.3 Motion Artefacts

The effect of physiological motion during data acquisition on images strongly depends on the used k-space sampling pattern (Fig. 3.13).

2D Cartesian Sampling Scheme

For Cartesian sampling periodic motion leads to ghosting artefacts (i.e. shifted copies of the moving object) along the phase encoding direction [144]. The frequency of the motion determines the spacing of the ghosts and the motion amplitude their intensity which decreases with the distance from the centre of the moving object. In addition blurring is visible parallel to the direction of the motion. Therefore, adapting k-space sampling to the expected motion can improve image quality. Nguyen et al. show that the best image quality for both 2D and 3D images can be obtained with the readout direction parallel to motion and an edge-centre-edge view ordering, which reduces motion in the k-space centre and minimises the frequency of the motion [145].

2D Radial Sampling Scheme

Radial sampling leads to streaking and blurring rather than coherent artefacts from periodic motion. Glover and Pauly analyse motion artefacts origination from a circular object performing a linear periodic motion. Their findings show a region free from motion artefacts with a radius proportional to the frequency of the movement. Furthermore, the energy of the artefacts increases with the distance from the object, which is in contrast to Cartesian sampling where the energy of the artefacts is highest closest to the moving object [146].

As discussed earlier PAWS provides a highly efficient approach to minimise respiratory motion artefacts but still suffers from limitations especially for 3D imaging. The next chapter discusses novel acquisition schemes which extend the ideas of PAWS to an interleaved phase encoding scheme to overcome these problems.

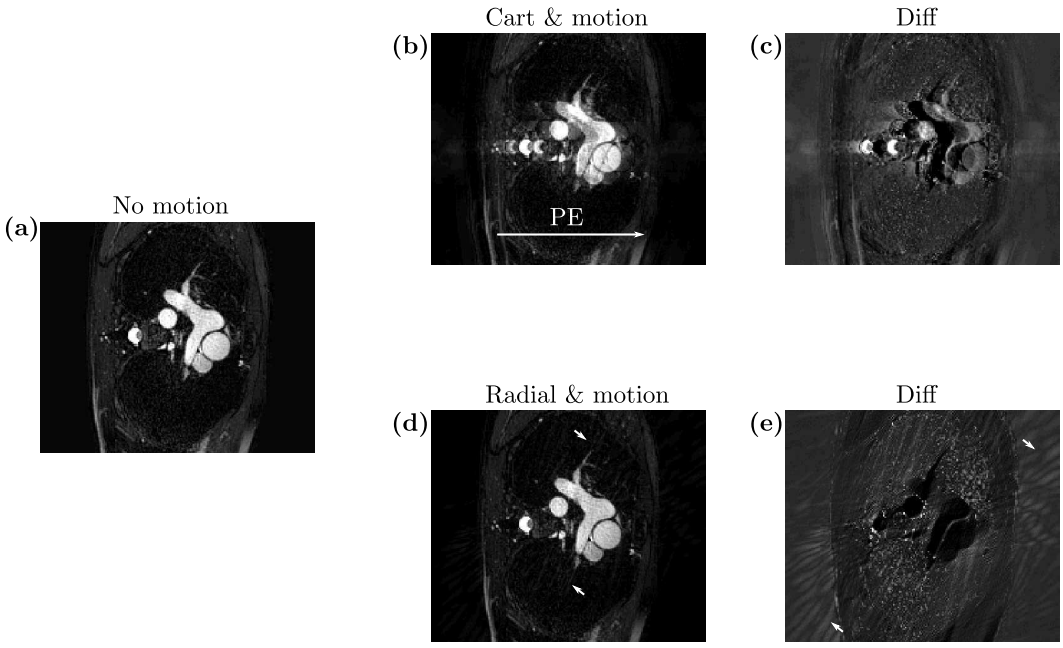

Figure 3.13: Comparison of the effect of periodic motion on image quality for a Cartesian and a radial 2D sampling scheme. **(a)** Image without motion. **(b)** Motion corrupted image obtained with a 2D Cartesian sampling scheme. Periodic motion leads to coherent motion artefacts which are visible as copies of the main image content shifted along the phase encoding (PE) direction. The shift and intensity of these ghost artefacts depends on the frequency and periodicity of the motion. **(c)** Difference between images shown in (a) and (b). **(d)** For a radial sampling scheme, periodic motion leads to streaking artefacts (white arrows) but no coherent artefacts are visible. **(e)** Difference between (a) and (d).

4 | Evaluation of PAWS with Different Interleaved Phase Encoding Schemes to Minimise Respiratory Motion Artefacts

4.1 Introduction

In the previous chapter Phase Ordering with Automatic Window Selection (PAWS) has been discussed as a highly efficient technique to minimise respiratory motion artefacts. Despite its high efficiency, PAWS still presents some disadvantages:

- In spite that a combination of two bins to reconstruct the final image has been reported as the most efficient approach [130], PAWS has only been presented using combinations of three bins to avoid image quality degradation with the Cartesian sampling approach.

- The width of the central bin is set narrower than the other two bins. Although this can lead to a enhanced motion minimisation for the central k-space it can also cause distinct displacement discontinuities in the k-space centre leading to strong motion artefacts. It has been shown that the only way to overcome this problem is an increase in scan time [131].

- For 3D imaging binning of data occurs along just one phase encoding (PE) direction which strongly limits the achieved minimisation of motion artefacts.
- Image reconstruction is usually not possible before the scan has finished.
- The final image is reconstructed at a certain breathing position using data from only one combination of bins while all other acquired data is discarded.

To overcome these problems we propose to extend the ideas of PAWS to a 3D acquisition scheme using an interleaved phase encoding (PE) scheme. This method allows for the combination of data from two bins for image reconstruction in the most optimal way. It carries out a homogeneous acquisition of data in the 2D PE plane, which leads to a reduction of motion artefacts [146]. Furthermore, our approach does not just yield one high quality image but also additional motion information is obtained without an increase in scan time. This maximises the amount of data utilised from each scan (Fig. 4.1). Therefore, this novel method provides a highly efficient approach to obtain high isotropic resolution images and additional motion information which can be used for treatment planning and for image guidance during ablation procedures.

In order to select a k-space trajectory which yields the best image quality in combination with PAWS, different PAWS sampling schemes need to be compared. An in-vivo comparison of different acquisition schemes in a dynamic environment (e.g. temporal changes due to respiratory motion) is challenging because the same scan conditions cannot be ensured for successive scans. Therefore, a large number of subjects and a randomised order of different acquisition methods is required. Nevertheless, the long scan times of high resolution 3D whole-heart scans strongly restricts the number of techniques which can be compared in each subject.

Therefore, a Scan Simulation Environment (SSE) was developed in Matlab (MathWorks, Inc., Natich MA, USA). It provides a framework to evaluate and compare different acquisition schemes and reconstruction techniques using a numerical phantom. This phantom is analytically described in k-space, and thus avoids any errors or inaccuracies due to data interpolation. Respiratory motion of heart and diaphragm can be simulated using navigator signals recorded during in-vivo MR scans.

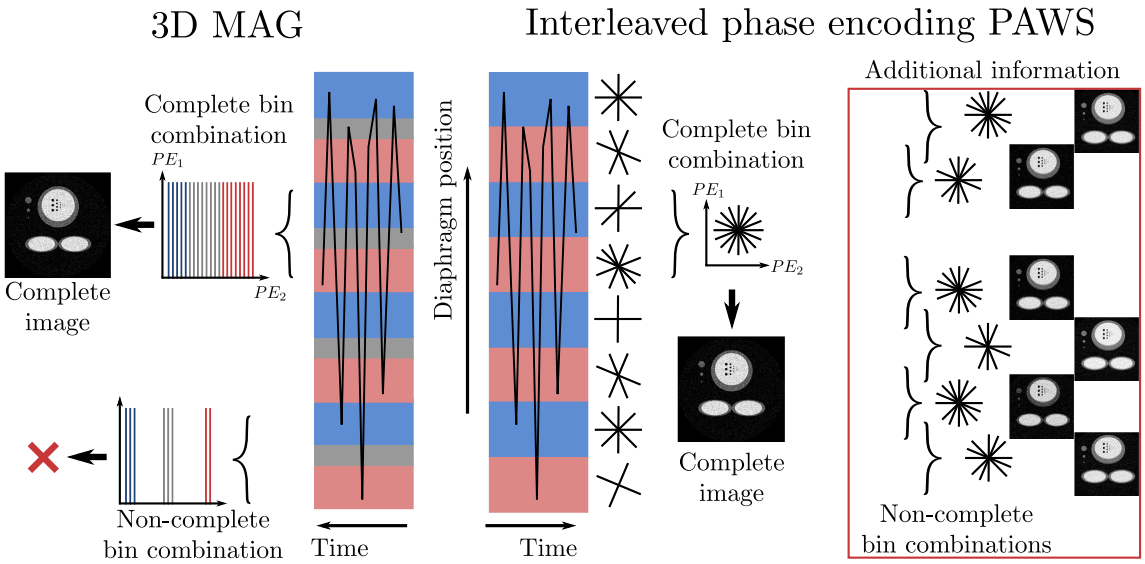

Figure 4.1: Comparison between 3D MAG and the proposed interleaved phase encoding PAWS technique. Both techniques acquire complimentary data in multiple respiratory bins covering the entire navigator amplitude. The scan is successfully finished if a combination of adjacent bins leads to the required k-space information and a complete image can be reconstructed. In contrast to 3D MAG, the sampling trajectory of our proposed method ensures a homogeneous covering k-space during the entire scan. Therefore, not just one high quality complete image but also further images from non-complete bin combinations with good image quality can be obtained which can provide additional data, such as respiratory motion information.

The following chapter describes the components of the SSE and presents a comparison between a commonly used respiratory gated Cartesian acquisition scheme (gated Cartesian) [43], a 3D Cartesian PAWS technique (3D MAG) [132, 133] and three novel PAWS methods using radial phase encoding (GRPE-PAWS and bitrevRPE-PAWS) and hybrid Cartesian trajectories (hybridPAWS). It is shown that these new techniques lead to a better depiction of small image features such as vessel structures and an improved navigator efficiency compared to 3D MAG and the gated Cartesian technique. In contrast to hybridPAWS, the radial phase encoding sampling schemes require iterative reconstruction techniques which are computationally demanding. Nevertheless, GRPE-PAWS and bitrevRPE-PAWS allow for the reconstruction of respiratory resolved 3D data and therefore yield not just high resolution anatomical but also dynamic respiratory information without an increase in scan time.

4.2 Scan Simulation Environment (SSE)

The main component of the Scan Simulation Environment is a dynamic numerical phantom which allows for the simulation of respiratory motion of the heart and diaphragm. It is defined analytically in k-space. Therefore, data can be obtained along arbitrary k-space trajectories without introducing errors due to data interpolation. Data acquisition and image reconstruction are highly flexible and can be easily adapted to different scan parameters. Figure 4.2 shows a block diagramm of the SSE.

4.2.1 Numerical Phantom

The numerical phantom used for this study represented diaphragm and heart. It included a resolution grid in the centre of the heart model to study the effect of different sampling trajectories and motion artefacts on small structures. The size of the circles of the resolution grid were 6, 4, 2, 1 and 0.5 pixel for a phantom consisting of 256 x 256 pixels. Figure 4.3 shows the image space representation of this phantom.

Respiratory motion was simulated as translation and expansion/compression in the foot-head direction using respiratory signals recorded during in-vivo 3D SSFP

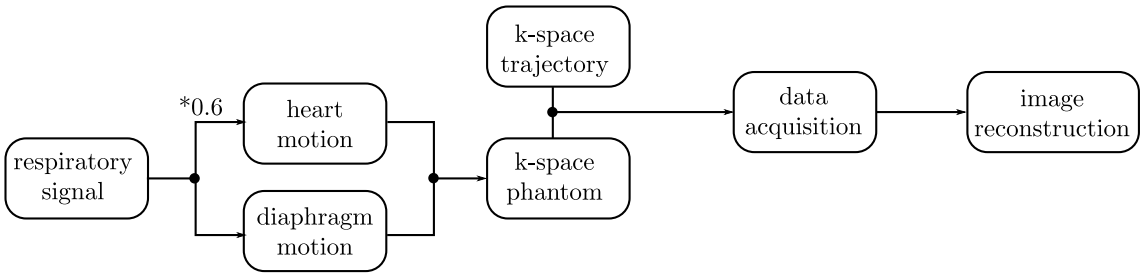

Figure 4.2: Block diagram of the Scan Simulation Environment (SSE). The main component of the SSE is a numerical phantom which allows for the simulation of respiratory motion of both heart and diaphragm and for data acquisition along arbitrary k-space sampling patterns. Both data acquisition and image reconstruction can be customized to allow for a variety of simulations. The same respiratory signal is used for heart and diaphragm but the amplitude of the heart motion was scaled to 60% relative to the diaphragm according to [116].

whole-heart scans (Fig. 4.3). The amplitude of motion of the heart was scaled to 60% of the diaphragm movement [116]. Noise was introduced to the k-space data, such that the signal to noise ratio (SNR) of an image reconstructed from a fully-sampled Cartesian trajectory without respiratory motion was approximately 16 dB. This value for the SNR was chosen according to previous studies on high-resolution 3D cardiac MR images [102, 114].

The sampling schemes compared in this study all carried out data acquisition along the frequency encoding direction in the same way. Any differences in image quality are shown in the 2D phase encoding (PE) plane. Therefore, data acquisition was simulated along the two PE directions which were chosen as the two image axis of the 2D numerical phantom (i.e. along FH and RL in Fig. 4.3). For each respiratory navigator value half the number of values required for a fully encoded line in the 2D PE plane are obtained.

4.2.2 PAWS Combined with RPE Sampling Schemes

As already discussed in chapter 2.3.3 radial phase encoding (RPE) is a Cartesian acquisition scheme with PE along radial lines (Fig. 4.4a).

At each respiratory navigator position only half the number of PE values required for a fully sampled radial PE line are obtained. Therefore, in our implementation of the RPE trajectory the phase encoding positions along each radial line are acquired with an interleaved low-high profile order as shown in Fig. 4.4b. The numbers

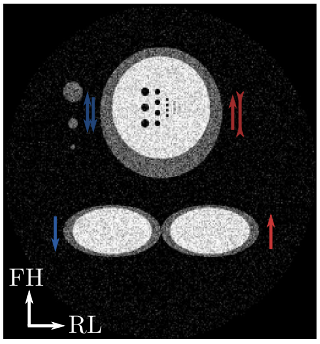

Figure 4.3: Numerical phantom representing heart and diaphragm. The coloured arrows indicate the simulated respiratory motion during expiration (blue arrows) and inspiration (red arrows). FH foot-head and RL right-left direction.

indicate the order in which the phase encoding steps are recorded at each respiratory navigator position. All k-space values along one radial line are sampled before acquiring the next radial line at a certain angle α. Therefore, the sampling patterns can be expressed as an array of α

$$\alpha(n) = i_{\Delta\alpha}(n)\Delta\alpha \quad \text{with} \quad n = 0 \ldots (N_\alpha - 1) \tag{4.1}$$

The following two RPE sampling patterns were compared

- bit reversed order (bitrev) of radial phase encoding lines (bitrevRPE)

$$i_{\Delta\alpha}(n) = bitrev(\{0, 1, \ldots (N_\alpha - 1)\}) \quad \text{and} \quad \Delta\alpha = \frac{\pi}{N_\alpha} \tag{4.2}$$

  The bit reversed sampling scheme leads to an evenly distributed k-space data acquisition over time but it requires the number of radial PE lines to be of a power of two.

- Golden Angle between successive radial phase encoding lines (GRPE)

$$i_{\Delta\alpha}(n) = \{0, 1, \ldots (N_\alpha - 1)\} \quad \text{and} \quad \Delta\alpha = 111.24^\circ \quad . \tag{4.3}$$

  As already discussed in chapter 2.3.2 the Golden Angle leads to a homogeneous distribution of radial profiles during the entire acquisition. Compared to the bit reversed order of phase encoding lines, it leads to larger maximum angular gaps between neighbouring k-space sampling positions for the same number of acquired radial lines and therefore, to stronger streaking artefacts. Nevertheless, in contrast to bitrevRPE it can be used for an arbitrary number of radial PE lines.

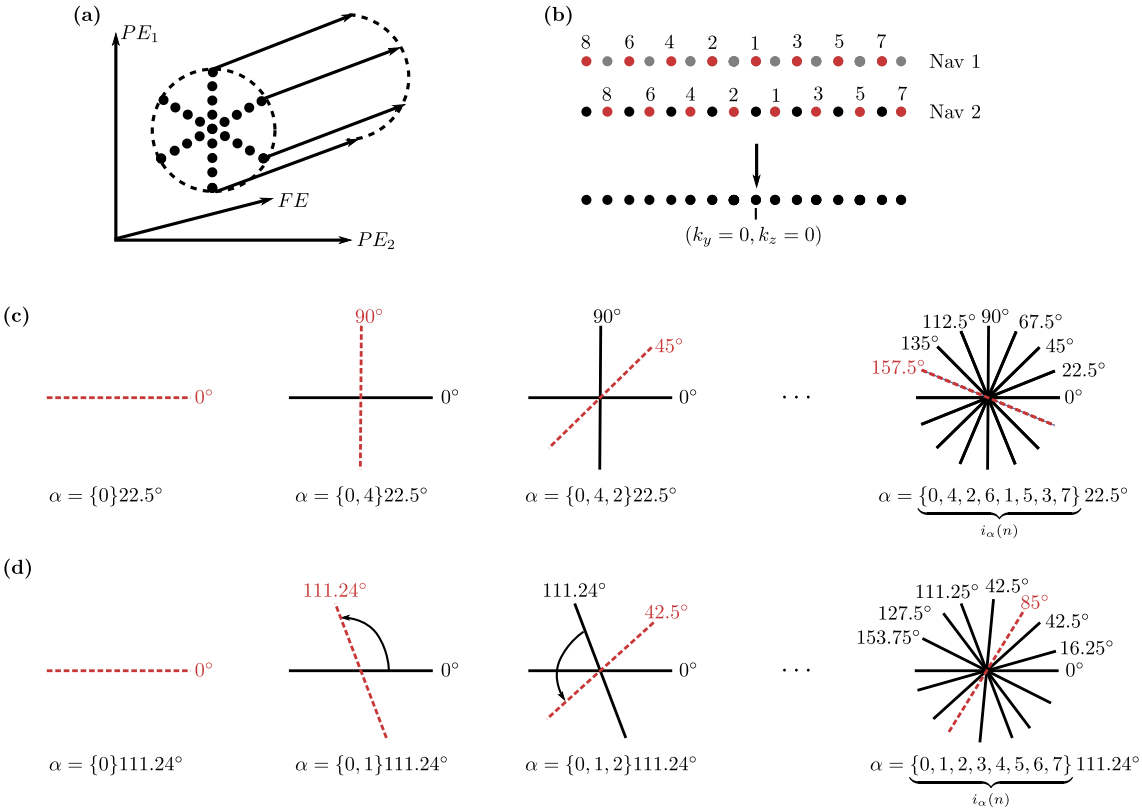

Figure 4.4: (a) Radial Phase Encoding (RPE) is a Cartesian sampling scheme where phase encoding points (black dots) are acquired along radial lines in a 2D phase encoding plane (PE_1 - PE_2). FE frequency encoding. **(b)** Data acquisition along each radial line is carried out with an interleaved low-high profile order. The numbers indicate the order of the recorded phase encoding positions at each respiratory navigator position (Nav). **(c,d)** The sampling order of eight radial phase encoding (PE) lines for (c) bit reversed RPE (bitrevRPE) with $\Delta\alpha = 22.25°$ and (d) Golden Angle RPE (GRPE) with $\Delta\alpha = 111.24°$. For the same number of radial PE lines GRPE leads to larger angular gaps than bitrevRPE.

The sampling of eight radial lines for bitrevRPE and GRPE is depicted in Fig. 4.4c and d.

In order to combine these trajectories with the ideas of PAWS, the k-space sampling schemes were defined such that data from two adjacent respiratory bins were complementary and could be combined in the most optimal way. Here we propose to apply two RPE trajectories s1 and s2 with two different angular sampling directions. In order to ensure complementary data along each radial line, s2 uses an inverted order of the interleaved low-high profile order of s1.

Both s1 and s2 include the same radial lines but sampling for s1 starts at 0^o and continues towards the largest angle $i_\alpha((N_\alpha - 1)\Delta\alpha)$ and conversely for s2. The

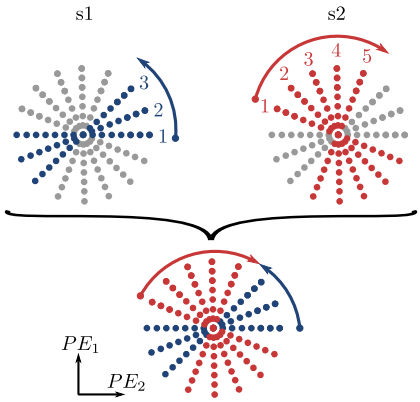

Figure 4.5: Complementary interleaved radial phase encoding schemes s1 and s2. Both schemes sample the same PE positions but the s1 starts at 0° (blue dot) and continues anticlockwise and conversely for s2. Once the two sampling schemes 'meet', a completed k-space can be obtained.

sampling of s1 and s2 and the combination of the two sampling patterns are depicted in Fig. 4.5.

A combination of data from two consecutive bins A and B leads to a completed k-space if $nA = N_\alpha - nB$ where nA and nB describe the currently sampled angle of these bins. In the following the case $nA = N_\alpha - nB$ shall be referred to as 'complete bin combination' and $nA < N_\alpha - nB$ as 'non-complete bin combination'. If a percentage of acquired data is given for a certain combination of bins, then it is always in relation to the complete bin combination with $nA = N_\alpha - nB$.

The sampling patterns of bitrevRPE and GRPE then transform to

$$s1(n) = \{i_\alpha(0)\Delta\alpha, i_\alpha(1)\Delta\alpha \ldots i_\alpha(N_\alpha - 1)\Delta\alpha\} = \{i_\alpha(0), i_\alpha(1), \ldots i_\alpha(N_\alpha - 1)\}\Delta\alpha \tag{4.4}$$

$$s2(n) = \{i_\alpha(N_\alpha - 1)\Delta\alpha, i_\alpha(N_\alpha - 2)\Delta\alpha, \ldots i_\alpha(0)\Delta\alpha\} = \{i_\alpha(N_\alpha - 1), i_\alpha(N_\alpha - 2), \ldots i_\alpha(0)\}\Delta\alpha. \tag{4.5}$$

The two sampling patterns are also depicted in Fig. 4.6a and b.

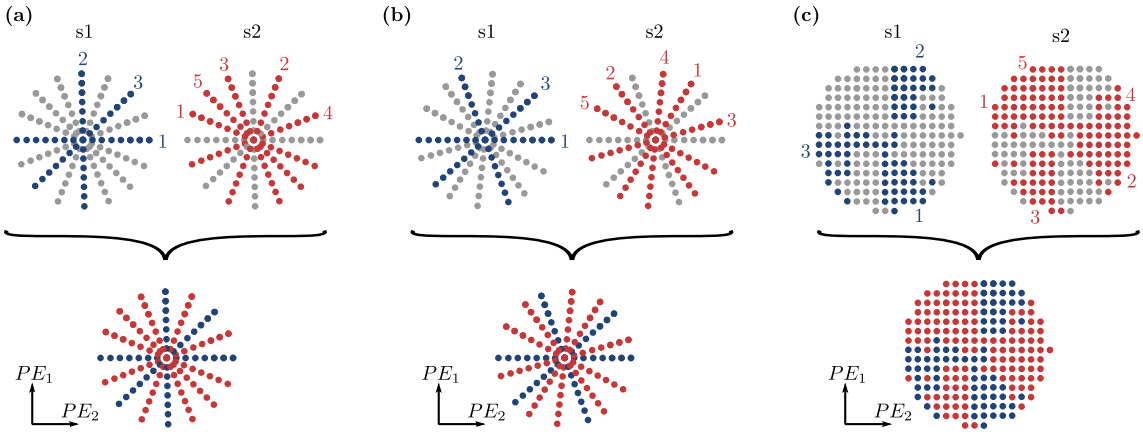

Figure 4.6: Combination of data from adjacent respiratory bins for final image reconstruction. Numbers indicate temporal order of sampling in the 2D phase encoding plane (PE_1-PE_2). **(a)** bitrevRPE-PAWS. **(b)** GRPE-PAWS. **(c)** HybridPAWS. The definition of the complimentary sampling schemes s1 and s2 in equation (4.4) and (4.5) ensures a combination of data in the most optimal way.

4.2.3 PAWS Combined with Hybrid Cartesian Sampling Scheme

Hybrid Cartesian sampling was already described in chapter 2.3.1. All the phase encoding positions are located on a rectilinear grid but they are sampled in a radial way. This means at every navigator position k-space data covering both low and high spatial frequencies are obtained.

Each of these angular k-space segments can be assigned an angle index similar to the above discussed RPE trajectories. In order to obtain a homogeneous covering of the 2D phase encoding plane over time, the angle indices of these k-space segments are acquired in a random order. Furthermore, the sampling patterns s1 and s2 from equation (4.4) and (4.5) are used to ensure interleaved complimentary data acquisition in adjacent respiratory bins (Fig. 4.6c). This method will be referred to as HybridPAWS in the following.

4.2.4 3D MAG and Gated Cartesian Sampling Scheme

3D MAG is implemented according to [130, 132, 133]. The respiratory gated Cartesian method uses a hybrid Cartesian sampling pattern but in contrast to Hybrid-

PAWS with a linear sampling order of the angular k-space segments in the 2D PE plane. Respiratory gating is carried out as described in chapter 3.3.2.

4.2.5 Data Acquisition and Reconstruction

For GRPE-PAWS and bitrevRPE-PAWS $N_\alpha = 256$ radial lines with $N_r = 256$ phase encoding steps each were recorded to satisfy Nyquist in the corresponding Cartesian image. For all other acquisitions the acquisition matrix was 256 x 256. At each respiratory navigator position 128 phase encoding samples were recorded. In this study the different acquisition schemes were compared for 62 different respiratory navigator signals. They were recorded during 3D whole-heart SSFP scans of volunteers (29 signals, mean age 29.9 years), congenital heart disease patients (28 signals, mean age 28.6 years) and patients with atrial fibrillation (5 signals, mean age 59.2 years).

GRPE-PAWS, bitrevRPE-PAWS and HybridPAWS used the combination of data from two adjacent bins for the final image reconstruction. The width of the navigator window for each bin was 3 millimetres. For 3D MAG data from three consecutive bins was combined. The respiratory bins sampling high frequencies had a width of 2.5 millimetres and the bin obtaining the low frequencies a width of one millimeter. For the gated Cartesian acquisition a 6 millimeters navigator window was used. This ensured that for all acquisition methods images were reconstructed from data acquired over a respiratory motion range of 6 millimetres.

Data acquired with a RPE trajectory were reconstructed using a non-uniform fast Fourier transform (NUFFT) [91]. For all other sampling schemes a fast Fourier transform (FFT) was applied.

Parallel imaging was not included in the simulation to avoid any negative effects on image quality due to inaccuracies in the coil design. Furthermore, non-homogeneous noise enhancement of parallel imaging techniques can impair signal to noise comparisons.

4.2.6 Data Analysis

The quality of the reconstructed images was assessed according to apparent signal to noise ratio (aSNR), peak to sidelobe ratio (PSR) and structure sharpness (SS). The aSNR was determined as the ratio between the mean signal within a region of interest (ROI) exhibiting high signal intensity (I_S) and the standard deviation of the background signal (SD_N)

$$aSNR = \frac{I_S}{SD_N} \quad . \tag{4.6}$$

The PSR describes the ratio of the peak value (I_P) of the point spread function (PSF) to the maximum artefact value (I_A) in one of the sidelobes. The more coherent and pronounced the motion and sampling artefacts are the lower the PSR with a minimum value of one

$$PSR = \frac{I_P}{I_A} \quad . \tag{4.7}$$

The PSF was calculated by replacing the numerical k-space phantom of the SSE with a constant k-space.

The structure sharpness (SS) was defined similar to the vessel sharpness in [147] as the mean value along the edge (IE) of the resolution grid in the centre of the phantom relative to the mean value in a ROI excluding the circles of the resolution grid (IR)

$$SS = \frac{IE}{IR} \quad . \tag{4.8}$$

The edges of the resolution grid were determined with a Canny edge detection algorithm [148]. Figure 4.7 depicts how these image quality parameters were calculated. All image quality parameters are given relative to the gated Cartesian reference method.

Paired student t-tests were used to compare the results and the Holm-Bonferroni method with a p value of 0.05 was applied to determine if results were statistically significant [149].

As discussed before 3D MAG and other previously presented PAWS techniques do not allow for the reconstruction of incomplete data sets due to large gaps which can occur in k-space. GRPE-PAWS, bitrevRPE-PAWS and HybridPAWS use trajectories which ensures a homogeneous distribution of acquired k-space data over

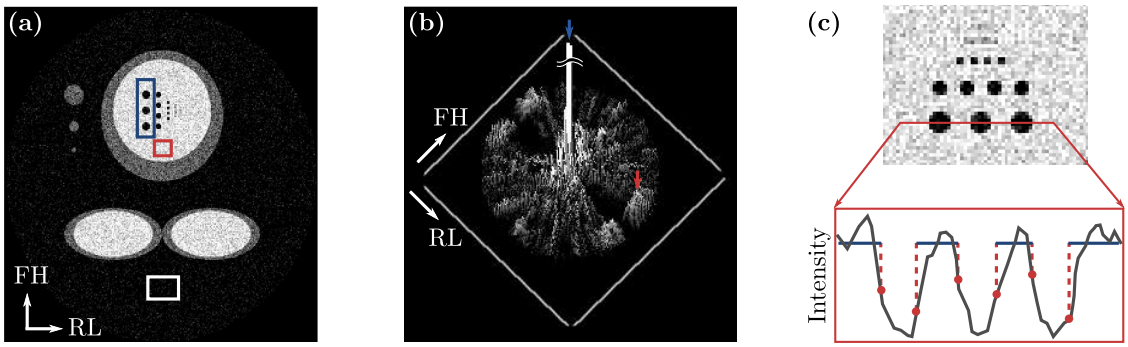

Figure 4.7: Calculation of image quality parameters. **(a)** The apparent signal to noise ratio (aSNR) was calculated as the ratio between the mean value of an area exhibiting high signal intensity (red rectangle) and the standard deviation of background signal (white rectangle). The structure sharpness (SS) was determined from the resolution grid in the centre of the phantom (blue rectangle). **(b)** The peak to sidelobe ratio (PSR) was defined as the ratio between the maximum value of the point spread function (PSF) (blue arrow) and the highest artefact value (red arrow) in one of the side lobes of the PSF. The PSF was calculated by simulating data acquisition of a constant k-space. FH foot-head and RL right-left direction. **(c)** The structure sharpness (SS) was obtained using the resolution grid in the centre of the phantom. The edges of the resolution grid (red dots) were determined with an edge detection algorithm. SS was calculated as the mean value along the edges relative to the mean value of the signal surrounding the circles of the resolution grid (blue lines).

the 2D phase encoding plane during the entire scan. Therefore, images from non-complete bin combinations were additionally reconstructed for one regular and one irregular breathing pattern using a sliding window approach. This yields multiple 3D images from the same data set showing the phantom at different stages in the respiratory cycle. An analysis of aSNR and SS for non-complete images having different undersampling factors was carried out.

4.3 Results

Figure 4.8 shows reconstructed images for each of the simulated acquisition schemes. The overall image quality for the different sampling methods was comparable. Nevertheless, in contrast to the other techniques artefacts close to the edges of the resolution grid were visible in several images obtained with 3D MAG (Fig. 4.8).

The mean value and standard deviation over all 62 respiratory signals of aSNR, SS and PSR for the different sampling schemes are depicted in Fig. 4.9a-d relative to the gated Cartesian reference method. All image quality parameters for 3D

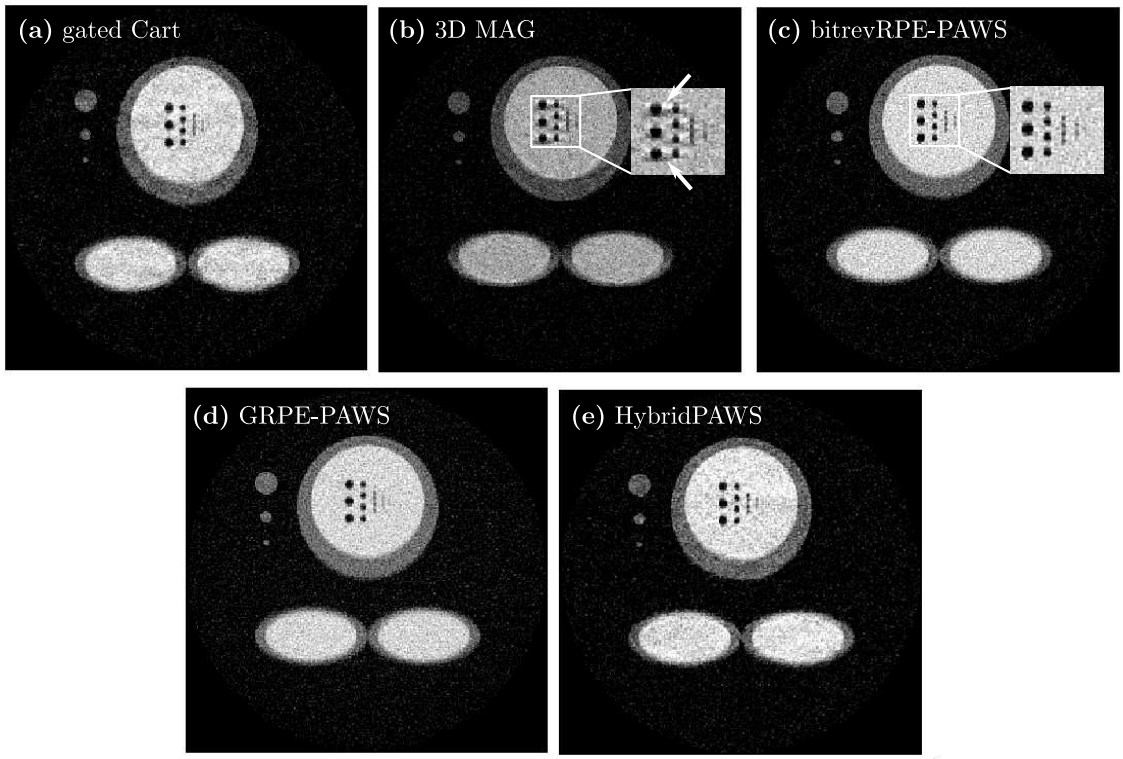

Figure 4.8: Reconstructed phantom images acquired with **(a)** respiratory gated Cartesian approach, **(b)** 3D MAG, **(c)** bitrevRPE-PAWS, **(d)** GRPE-PAWS and **(e)** HybridPAWS. Distortions of the resolution grid were visible only for 3D MAG (white arrows).

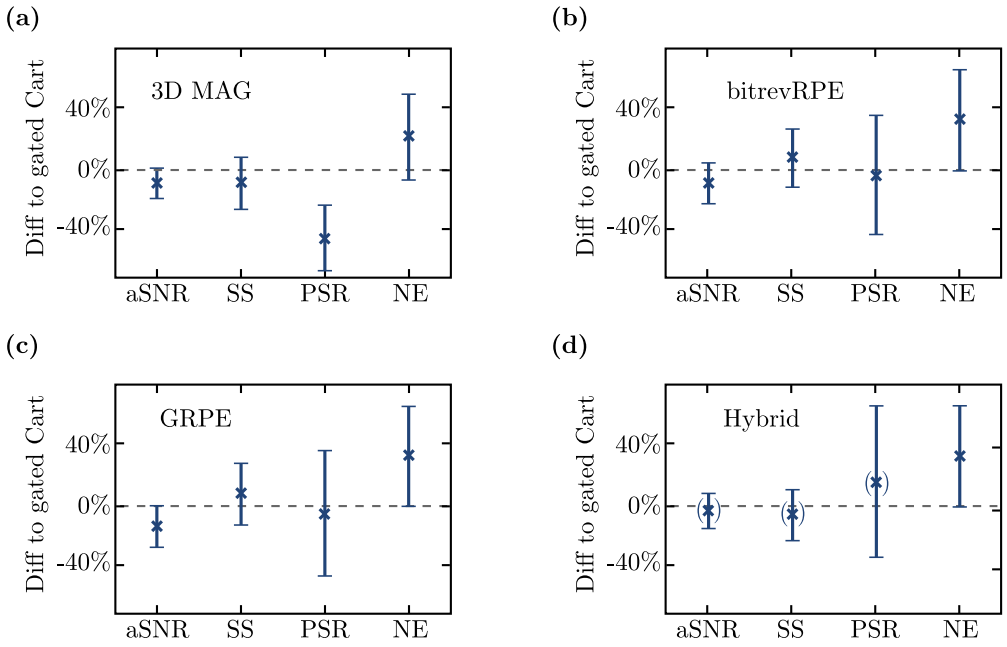

Figure 4.9: Comparison of image quality parameters and navigator efficiency for **(a)** 3D MAG, **(b)** bit reversed RPE-PAWS (bitrevRPE), **(c)** Golden Angle RPE-PAWS (GRPE) and **(d)** hybrid Cartesian PAWS (Hybrid). All values are given as the mean and standard deviation (error bars) over 62 simulations using different respiratory signals recorded during in-vivo 3D whole-heart MR scans relative to the gated Cartesian reference method (gated Cart). Navigator efficiency (NE) is shown for respiratory patterns which have a NE below 50% for the gated Cartesian reference method. aSNR apparent signal to noise ratio, SS structure sharpness and PSR peak to sidelobe ratio. All values are statistically significant except for differences in aSNR, SS and PSR for HybridPAWS (brackets).

MAG are lower than for the reference method, especially the PSR. GRPE-PAWS and bitrevRPE-PAWS lead to lower aSNR and PSR but higher SS than the gated Cartesian approach with slightly higher values for bitrevRPE-PAWS. HybridPAWS yields similar image quality values than the gated Cartesian method. All four methods yield a higher navigator efficiency than the reference method.

The navigator efficiency (NE) is the same for GRPE-PAWS, bitrevRPE-PAWS and HybridPAWS because all three use two bins for the final image reconstruction and same sampling schemes s1 and s2. Therefore, in the following NE of these three techniques will be discussed together as NE of general 2-bin PAWS methods.

Figure 4.10 depicts the improvement in NE between respiratory gated method and 2-bin PAWS. It shows that for subjects with irregular respiratory patterns (i.e. NE below 50% for the respiratory gated Cartesian method) 2-bin PAWS improves NE by 35.6% on average with a maximum increase of more than 180%. The average

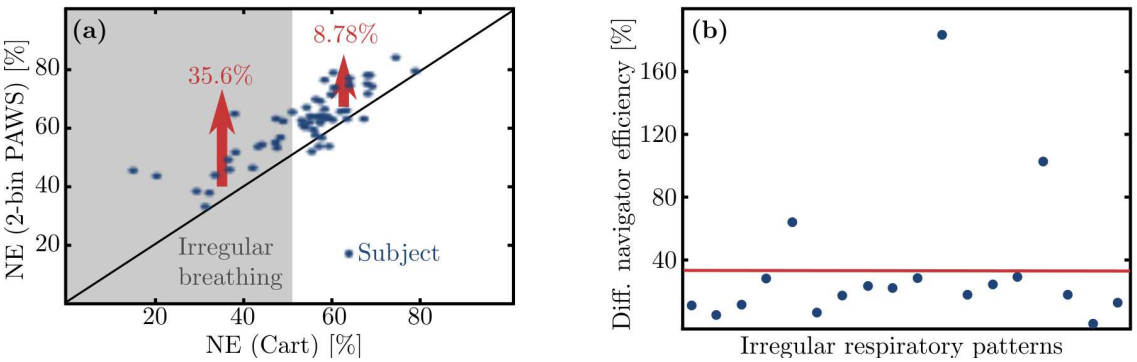

Figure 4.10: Comparison of navigator efficiency (NE) between between respiratory gated Cartesian scan (Cart) and the proposed 2-bin PAWS approach. **(a)** On average 2-bin PAWS improves NE by 35.6% and 8.7% for subjects with irregular (i.e. NE below 50% for the respiratory gated Cartesian method) and regular respiratory patterns, respectively. **(b)** For subjects with irregular breathing patterns 2-bin PAWS always led to an improvement in NE with a mean increase of 35.6% (solid red line) and a maximum improvement of more than 180%.

increase of NE was shown to be statistically significant by a paired student t-test resulting in a p value lower than 0.0001.

Images reconstructed from all complete and non-complete bin combinations are shown in Fig. 4.11a for a regular breathing pattern (i.e NE $>$ 50%) and in Fig. 4.11b for an irregular breathing pattern (i.e. NE $<$ 50%) comparing bitrevRPE-PAWS and HybridPAWS. Images obtained with GRPE-PAWS are not shown here, because there is no visible difference between images acquired with bitrevRPE-PAWS and GRPE-PAWS. The aSNR and SS as a function of sampled k-space data are shown in Fig. 4.11c and Fig. 4.11d for the images reconstructed from the bitrevRPE-PAWS acquisition. Both parameters were normalized to their maximum value obtained from the complete bin combination. With increasing undersampling aSNR is strongly reduced due to increase of incoherent undersampling artefacts. SS remains almost constant for a wide range of different undersampling factors.

SS as well as aSNR are not necessarily proportional to the undersampling, which shows that these parameters are strongly influenced by motion artefacts. Depending on the residual motion and its distribution in k-space for different bin combinations images can exhibit higher aSNR and SS values despite higher undersampling factors.

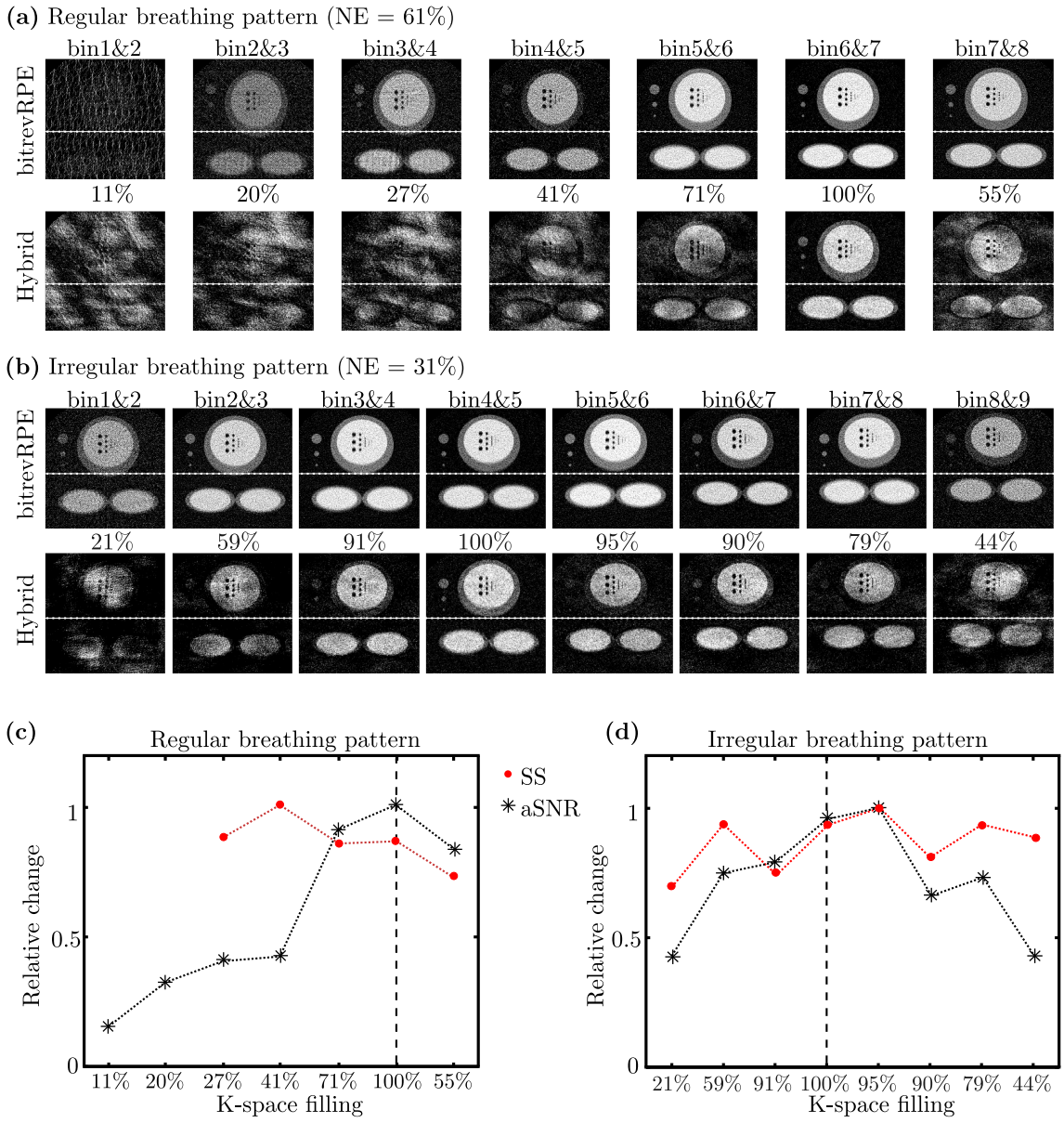

Figure 4.11: Respiratory resolved images reconstructed from complete and non-complete bin combinations obtained with bit reversed RPE-PAWS (bitrevRPE) and hybrid Cartesian PAWS (Hybrid). **(a)** A regular breathing pattern (navigator efficiency (NE) = 61%) has a clearly defined most frequent breathing phase usually towards end-expiration which leads to one complete bin combination and highly undersampled non-complete bin combinations. **(b)** An irregular breathing pattern (NE = 31%) results in several almost complete bin combinations. Although several high quality non-complete images can be reconstructed with hybridPAWS for irregular breathing patterns, only bitrevRPE-PAWS ensures a high image quality even for non-complete images obtained from as little as 20% compared to complete bin combinations **(c-d)** Structure sharpness (SS) and apparent signal to noise ratio (aSNR) determined in the images obtained with bitrevRPE-PAWS in (a) and (b). For the regular breathing pattern, SS could not be determined for non-complete images reconstructed from 11% and 20%.

4.4 Discussion

The presented 2-bin PAWS approaches with an interleaved phase encoding scheme lead to significant improvements in navigator efficiency compared to a commonly used respiratory gating method and 3D MAG, especially for subject with irregular breathing patterns. PAWS combined with interleaved RPE trajectories yield a better depiction of small structures than standard Cartesian sampling, especially for undersampled data.

Previous studies by Nguyen et al. show only a small difference in image quality between Cartesian PAWS (i.e. 3D MAG) and a respiratory gated Cartesian approach [43]. Nevertheless, the authors do not provide detailed information about the sampling scheme of the gated Cartesian method. The hybrid Cartesian sampling scheme of the gated Cartesian approach used here leads to incoherent motion artefacts. 3D MAG leads to coherent and pronounced motion artefacts because data binning is carried out only in one phase encoding direction rather than over the entire 2D phase encoding plane as the presented interleaved PAWS techniques.

Figure 4.12 depicts a 1D PSF for the different sampling schemes which also emphasises the higher artefact level of 3D MAG compared to the other approaches. Furthermore, it shows that bitrevRPE-PAWS and GRPE-PAWS can exhibit streaking artefacts similar to a 2D radial trajectory which leads to a decreased PSR. Nevertheless, the two RPE methods yield the narrowest main lobe of the PSF and thus the least blurring and highest SS value.

The slight decrease in aSNR for bitrevRPE-PAWS and GRPE-PAWS compared to gated Cart and hybridPAWS was to be expected due to the inhomogeneous k-space sampling density of RPE similar to radial frequency encoding (see chapter 2.3.2). Furthermore, in order to meet Nyquist for the RPE trajectories $256 * \pi\backslash 2$ radial phase encoding lines would have been necessary. Here, N_α was only 256. This led to undersampling artefacts which increase the background signal and thus decrease aSNR.

As already suggested by Jhooti et al [130] the 2-bin PAWS approach leads to a significantly higher NE than the respiratory gated method (+31%) and even than 3D MAG (+10%).

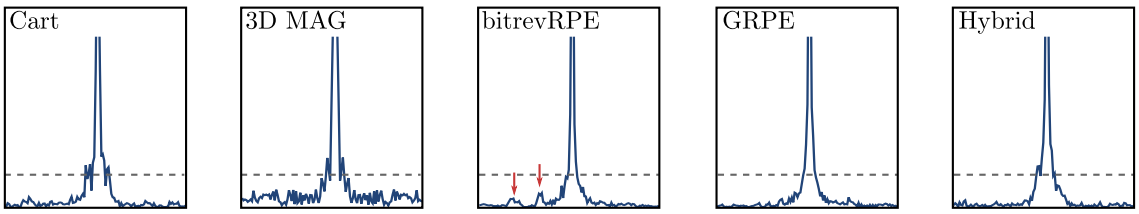

Figure 4.12: 1D point spread function (PSF) along one phase encoding direction obtained with respiratory gated Cartesian scan (Cart), 3D MAG, bit reversed RPE-PAWS (bitrevRPE), Golden Angle RPE-PAWS (GRPE) and hybridPAWS (Hybrid). The sampling pattern of 3D MAG leads to the most pronounced motion artefacts. The hybrid Cartesian sampling scheme of Cart and HybridPAWS lead to highly incoherent motion artefacts but also to a broadening of the main lobe of the PSF. For GRPE and bitrevRPE motion can cause streaking artefacts (red arrows) and a lower PSR. Nevertheless, both RPE sampling schemes show the narrowest main peak of the PSF and thus the least blurring and highest SS.

In order to compensate for irregular breathing pattern, the position of the gating window for a standard respiratory gating method is updated for each acquired respiratory navigator as already discussed in chapter 3.3.2. Although this maximum shift between two successively obtained navigators is only a small fraction of the gating window width, this update can lead to an effective gating window which is much larger than the initially anticipated one and therefore to more pronounced image artefacts (Fig. 4.13). For regular breathing patterns the standard respiratory gating method leads to a similar image quality than a 2-bin PAWS approach. Nevertheless, for irregular breathing patterns the image quality achieved with gated Cartesian can be strongly decreased due to the larger gating window. Our 2-bin PAWS methods lead to a reliable image quality even for highly irregular breathing patterns.

There is no significant difference in image quality between bitrevRPE-PAWS and GRPE-PAWS. Nevertheless, as discussed previously bitrevRPE-PAWS leads to smaller angular gaps for the same number of radial PE lines than GRPE-PAWS. This is probably the reason of higher aSNR and SS for bitrevRPE-PAWS compared to GRPE-PAWS. Therefore, bitrevRPE-PAWS was used for further in-vivo evaluations which are presented in the following chapter.

The undersampling properties of RPE trajectories discussed in chapter 2.3.3 allow for the reconstruction of high quality images even for highly undersampeld non-complete bin combinations. The phantom is only slightly impaired even though the image is reconstructed using as little as 20% of k-space data. Furthermore, the

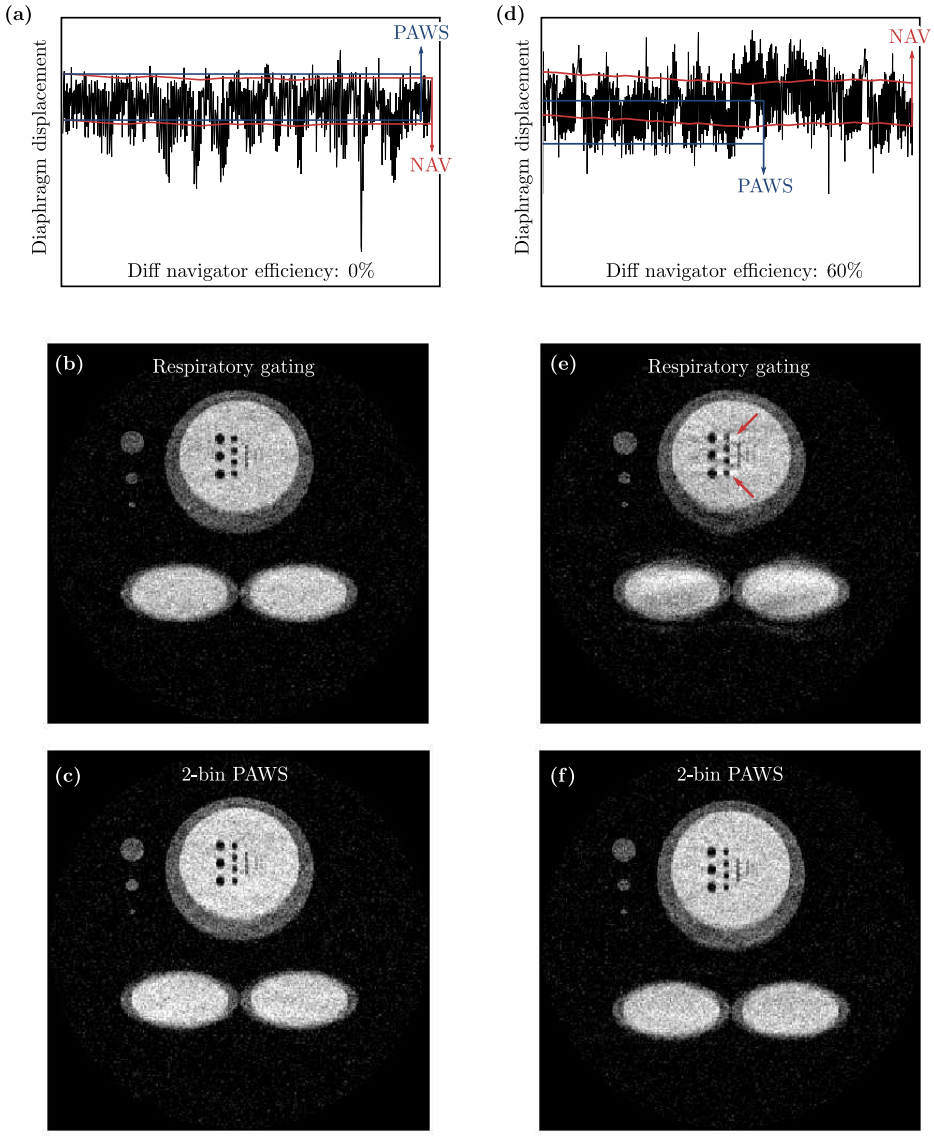

Figure 4.13: Effect on image quality of a varying position of the navigator window for a regular (a-c) and irregular (d-f) breathing pattern. **(a,d)** Respiratory gating window of a standard respiratory gating approach (NAV, red) and respiratory bin combination used for the final image reconstruction for a 2-bin PAWS approach. Images acquired with a **(b,e)** standard Cartesian respiratory gating approach and a **(c,f)** 2-bin PAWS approach. For a regular breathing pattern both respiratory gating and a 2-bin PAWS method acquire data at similar respiratory positions and lead to similar image quality. Irregular breathing patterns lead to a larger gating window for respiratory gating, longer overall scan time (i.e. navigator decreased by 40%) and stronger image artefacts than HybridPAWS.

behaviour of SS in Fig. 4.11c and d indicates that despite a decrease in aSNR, small structures such as vessels are only slightly impaired by high undersampling factors. Therefore, bitrevRPE-PAWS and GRPE-PAWS provide not just one high resolution data set at a certain respiratory phase but additional images with high quality can be obtained showing the ROI at different breathing positions. These non-complete images yield further information such as respiratory motion. Chapter 6 discusses how this additional information can be used to create respiratory motion models of the heart for cardiovascular interventions.

For MR applications which do not just require anatomical but also respiratory motion information bitrevRPE-PAWS and GRPE-PAWS provide useful techniques to obtain all necessary information within one 3D high resolution scan without an increase in scan time. Nevertheless, data acquired with RPE cannot be reconstructed using standard fast Fourier transformation. Especially for MR scans accelerated with parallel imaging approaches such as SENSE, RPE requires reconstruction techniques which are computationally demanding such as iterative non-Cartesian techniques.

In contrast to bitrevRPE-PAWS, quality of non-complete images for hybridPAWS is strongly dependent on the amount of k-space data available in the non-complete bins. The phantom is hardly visible even for non-complete bin combinations containing more than half the k-space data of the complete bin combination obtained with hybridPAWS. Nevertheless, for scans which do not require additional motion information and the computational resources do not allow for iterative non-Cartesian SENSE reconstruction HybridPAWS provides an alternative to bitrevRPE-PAWS and GRPE-PAWS without a decrease in navigator efficiency or image quality. A patient study using HybridPAWS for DE-MRI is also presented in chapter 7.

4.5 Conclusion

We presented a Scan Simulation Environment (SSE) which allowed for a comprehensive evaluation of different PAWS sampling schemes. It has been shown that PAWS with an interleaved phase encoding sampling scheme yields a superior image quality and a significant increase in navigator efficiency compared to other previously presented PAWS techniques.

BitrevRPE-PAWS allows for the reconstruction of respiratory resolved 3D data sets with a high image quality providing not just high isotropic resolution anatomical data but also additional respiratory motion information. A volunteer study to evaluate bitrevRPE-PAWS is presented in the following chapter. The assessment of the motion information obtained with bitrevRPE-PAWS is shown for volunteer and patient scans in chapter 6.

HybridPAWS yields the same navigator efficiency but does not provide the same high quality respiratory motion information as bitrevRPE-PAWS. For applications where this additional information is less important, HybridPAWS provides a highly efficient acquisition scheme to minimise respiratory motion artefacts without the high computational demand of image reconstruction for RPE. Therefore, for a study evaluating high resolution 3D inversion recovery images obtained in heart failure patients HybridPAWS was used to visualise late gadolinium enhancement (LGE) which is presented in chapter 7.

5 Highly Efficient Whole-Heart Imaging with High Isotropic Resolution Using RPE-PAWS

5.1 Introduction

As discussed previously ablation therapy can be greatly improved with high resolution 3D MR images. The main challenges are long acquisition times required to achieve high isotropic spatial resolution and artefacts due to physiological motion. Niendorf et al. have proposed a single breath-hold whole-heart acquisition using parallel imaging extensively [42]. Nevertheless, these long breath-holds are usually not applicable for the majority of patients and the spatial resolution is limited. In order to improve spatial resolution, MR data acquisition has to be carried out during free-breathing using a robust approach to minimise artefacts due to respiratory motion.

The results of the previous chapter have shown that bitrevRPE-PAWS leads to a strong increase in navigator efficiency. Furthermore, the undersampling properties of

Some of the following results have already been presented in Kolbitsch *et al.*, "Highly efficient whole-heart imaging using radial phase encoding - phase ordering with automatic window selection", *Magn Reson Med*, vol. 66, pp. 1008-18, 2011.

RPE trajectories allows for very high acceleration factors (e.g. 10) by exploiting the undersampling properties of radial encoding and reducing undersampling artefacts with an iterative reconstruction scheme [82, 83]. This makes bitrevRPE-PAWS an ideal acquisition scheme for 3D whole-heart MRI with high isotropic resolution.

A volunteer study was carried out using bitrevRPE-PAWS for isotropic 3D whole-heart imaging. The experimental results show the advantages in scan time and image quality of the proposed approach in comparison with a commonly used respiratory gating method using a Cartesian k-space trajectory (gated Cartesian). BitrevRPE-PAWS allows for fast acquisition of 3D datasets due to high acceleration factors possible with RPE and reconstruction of respiratory resolved 3D images visualising the heart from inspiration to expiration.

5.2 Volunteer Study

5.2.1 RPE-PAWS

Based on the results of the previous chapter bitrevRPE-PAWS (in the following referred to as RPE-PAWS) was implemented on a 1.5T MR scanner (Philips Medical System, Best, The Netherlands). The same k-space trajectory described in the previous chapter was used here but with an additional partial Fourier acquisition along the radial direction in order to reduce the overall scan time (Fig. 5.1a). In contrast to the simulations carried out previously, here a complete image does not necessarily have to be fully sampled to provide a high resolution image with an iterative reconstruction method.

5.2.2 Experiments

Whole-heart MR data were obtained from eight healthy volunteers (seven male, one female, mean age 31 years) with RPE-PAWS and a respiratory gated Cartesian acquisition using a FOV of 288 x 288 x 288 mm at isotropic resolution (1.5 x 1.5 x 1.5 mm) (Fig. 5.1b). Written informed consent was obtained from all participants and the study was carried out following an approved protocol from our local hospital. A 32-channel cardiac phased array coil was used for signal reception and parallel

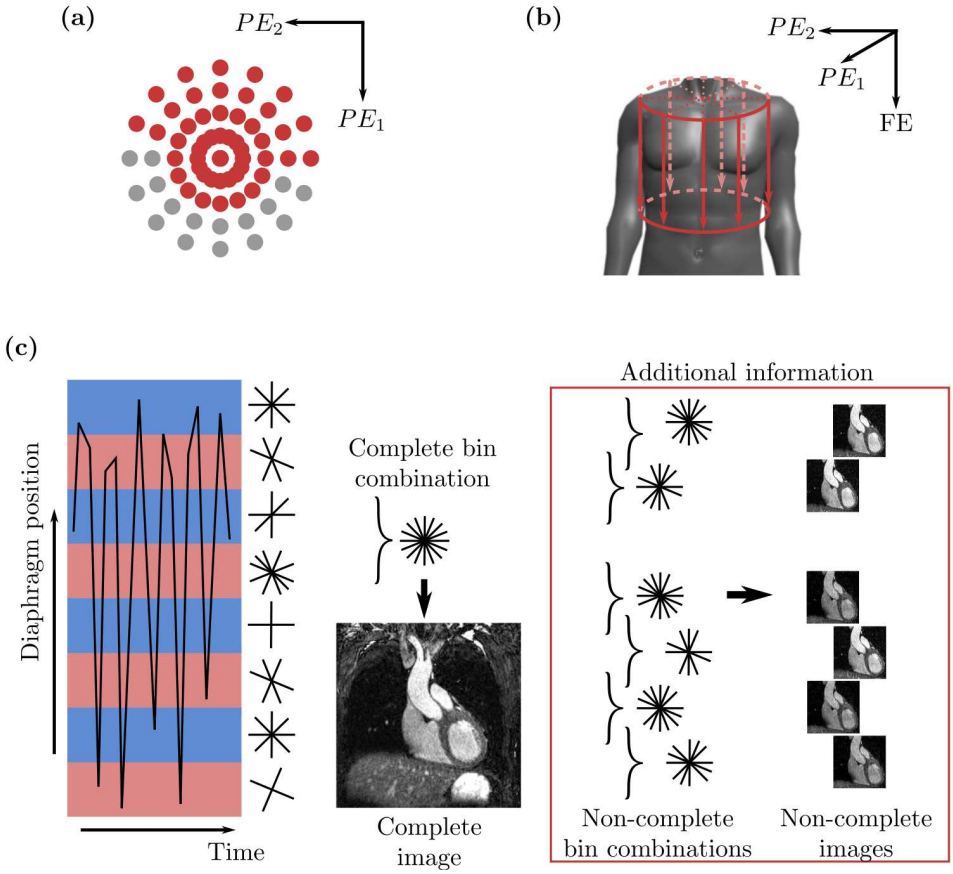

Figure 5.1: Data acquisition using RPE-PAWS **(a)** RPE-PAWS acquires data along radial spokes in the 2D phase encoding plane (PE_1-PE_2). A partial Fourier factor is used for each spoke to decrease scan time (red: sampled data, gray: unsampled data). **(b)** 3D whole-heart data is acquired with frequency encoding along the foot-head direction and a transversal orientation of the 2D phase encoding plane. **(c)** Several bins are placed to cover the entire amplitude of the respiratory navigator signal. The sampling schemes s1 (blue) and s2 (red) are alternately assigned to these bins (see Fig. 4.6 and equation (4.4) and (4.5)). Data is acquired until one combination of two adjacent bins contains all the desired k-space information and a high resolution image at a certain breathing position can be reconstructed (complete image). Nevertheless, two neighbouring bins always contain complementary k-space data and therefore additional information can be obtained.

imaging. An ECG triggered (end-diastole) balanced steady-state free-precession sequence with a T_2 preparation pulse ($T_E = 50$ ms) and fat suppression were used with the following parameters: flip angle of 90°, T_R/T_E of 4.3/2.2 ms, segmented approach (TFE factor = 24) with low-high profile order. A schematic of this pulse sequence is shown in Fig. 5.2.

For RPE-PAWS, $N_\alpha = 64$ radial lines each with $N_r = 192$ samples were acquired with partial Fourier encoding (factor 0.75) along the radial direction, which resulted in an undersampling factor of 4 compared to the fully sampled Cartesian case.

Scans using the respiratory-gated Cartesian acquisition were carried out for comparison purposes with the same imaging settings as listed above except for the sampling parameters. Sensitivity encoding (SENSE, [7]) with a factor 2 was applied in the anterior-posterior (AP) direction and a partial Fourier value of 0.6 in the left-right (LR) direction. Furthermore, a circular shutter was applied which restricts the obtained k-space data to an elliptic region leaving the highest spatial frequencies unsampled. Therefore, the number of acquired k-space points are reduced by a factor of $\frac{\pi}{4}$. This resulted in the same number phase encoding steps and a compareable k-space coverage as the above described RPE scheme. The imaging time for an acquisition with the isotropic resolution was 6.25 min assuming a navigator efficiency of 100% and a heartbeat of 60 beats per minute. The necessary image information to determine the coil sensitivity maps for the SENSE reconstruction was acquired between the Cartesian and RPE-PAWS scans.

For respiratory gating, a navigator beam was placed on the dome of the right hemi diaphragm using a navigator window of 6 mm for the Cartesian scan. Since the proposed RPE-PAWS scheme combines data from two respiratory bins for the image reconstruction, a navigator window of 3 mm was applied for the individual respiratory bins of the RPE-PAWS scan.

Multiple bins are placed to cover the diaphragm displacement (Fig. 5.1c). Prior to data acquisition a navigator training phase is carried out to determine the most common diaphragm position and the range of the displacement. In order to take shifts of the respiratory pattern into account and make sure that data is acquired at every occurring navigator position the bins are placed over a range twice the breathing amplitude.

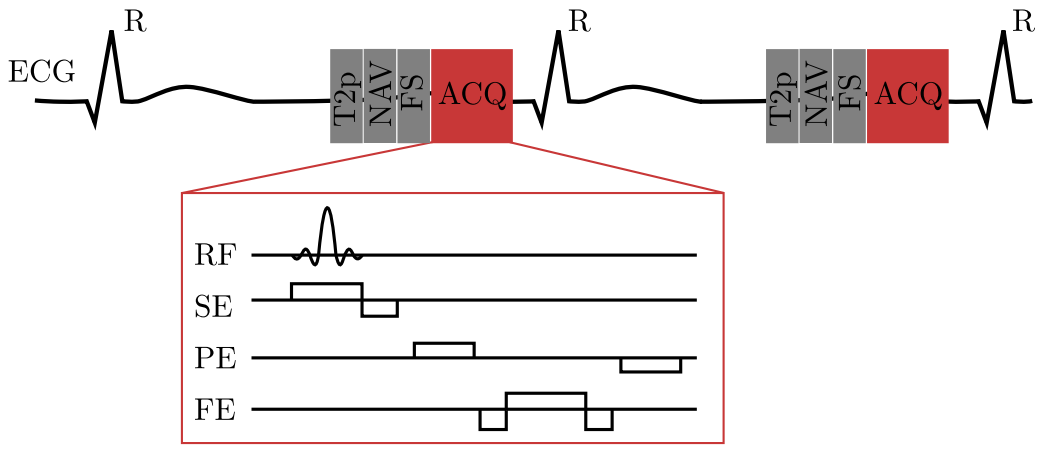

Figure 5.2: Schematic of pulse sequence. Data acquisition (ACQ) is carried out after a predefined trigger delay following each R-wave. Prior to ACQ, a T_2 preparation pulse (T2p) and fat suppression (FS) is applied. In addition a respiratory navigator (NAV) is obtained. Tissue excitation is achieved using an RF-pulse (RF) combined with a slice encoding gradient (SE). The obtained signal is encoded using phase (PE) and frequency (FE) encoding gradients.

In order to investigate further scan time reductions due to the advantageous undersampling properties of RPE, images were also reconstructed from 80% and 50% of k -space compared to the complete image.

5.2.3 Image Reconstruction

All images were reconstructed offline using Matlab (The MathWorks, Inc., Natich, MA, USA). To compensate for the missing data due to the partial Fourier acquisition a homodyne reconstruction was employed for both acquisition schemes. Image data from the 3D Cartesian data sets was obtained with the SENSE method [7]. The images acquired with the RPE-PAWS approach were reconstructed using a non-Cartesian iterative SENSE algorithm using the number of iterations as the only user input [94]. Nevertheless, in this study the same number of iterations (3) was used for all data sets. The phase errors due to the homodyne reconstruction were corrected using a low resolution image obtained from the centre of k-space using the SENSE and iterative SENSE method, respectively. Figure 5.3 gives a schematic overview of the image reconstruction.

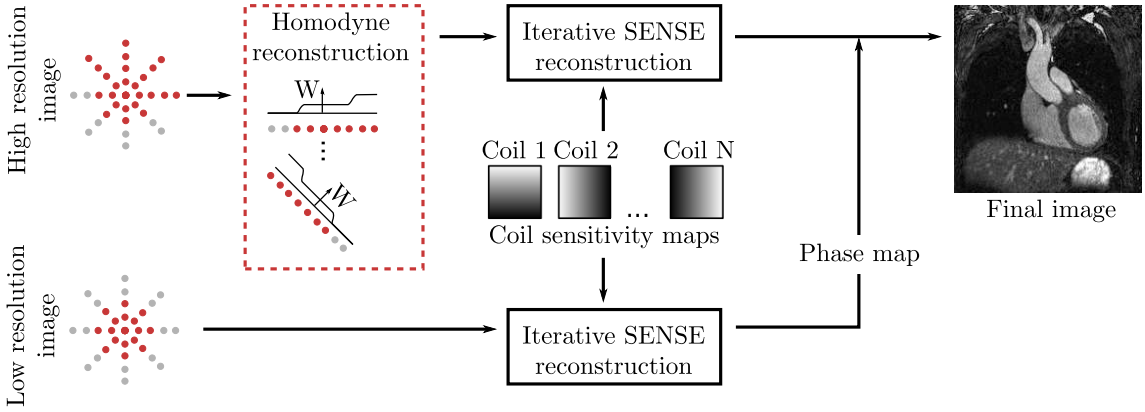

Figure 5.3: Schematic overview of the image reconstruction. To compensate for the missing data due to the partial Fourier acquisition, each radial line is multiplied with a weighting function (homodyne reconstruction). In addition to the high resolution image, also a low resolution image using only the symmetrically sampled centre of k-space is reconstructed using a iterative SENSE approach. The low resolution image is used to correct any phase errors due to the homodyne reconstruction.

5.2.4 Data Analysis

The images obtained with the respiratory gated Cartesian method and from the complete bin combination (100% k-space data) with RPE-PAWS were compared with respect to navigator efficiency and image quality. The breathing patterns between two succeeding scans can vary quite strongly. Therefore, the navigator information was recorded during the gated Cartesian and RPE-PAWS acquisition and the scans were later repeated in a virtual scan environment to determine the gating efficiency using the same respiratory information for both methods.

In addition the quality of images reconstructed from non-complete bin combinations containing approximately 75% of k-space data was compared to images obtained from the complete bin combination (i.e. 100% of k-space data) for all volunteers.

For assessment of the image quality the apparent signal to noise ratio (aSNR) and the apparent contrast to noise ratio (aCNR) were used. To evaluate the influence of the acquisition schemes on small structures the vessel sharpness (VS) of the left (LCA) and right coronary artery (RCA) were determined although the presented scan protocol is not intended for coronary MRA in particular.

All image quality parameters were derived using 'soap-bubble' [147]. In particular, the aSNR and aCNR were calculated as the relationship between the mean signal within a circular ROI of the blood (IB) and the myocardium (IM) and the standard deviation of the background signal in the lungs (SDL)

$$\text{aSNR} = \frac{\text{IB}}{\text{SDL}} \quad \text{and} \quad \text{aCNR} = \frac{\text{(IB - IM)}}{\text{SDL}} \quad . \tag{5.1}$$

The absolute values for aSNR and aCNR are user dependent and are strongly influenced by the reconstruction schemes (e.g. regularization) due to their inhomogeneous noise amplification [7]. However, in this study the same reconstruction (iterations and regularization) was performed allowing to use aSNR and aCNR as means of a relative comparison.

The vessel sharpness (VS) was also determined using 'soap-bubble' and it is defined as the mean intensity value of the vessel borders along part of the vessel [102]. It is normalised with the average maximum intensity in the centre of the vessel and the higher the value the sharper the vessel. VS is defined similar to the structure sharpness in the previous chapter (see also Fig. 4.7c).

Paired student t-tests were used to compare the results considering a p value smaller than 0.05 as statistically significant.

Similar to the previous chapter aSNR and VS for complete and non-complete images were compared for volunteers with regular and irregular breathing patterns, respectively.

5.2.5 Results

Data acquisition was successfully finished in all eight volunteers with an average scan time of 14.5min (gated Cartesian) and 10.9min (RPE-PAWS). Figure 5.4 shows reformatted images of the LCA and RCA obtained from two volunteers. In addition to the images from the complete bin combination, reformatted views of the LCA and RCA are also shown for non-complete bin combinations including approximately 80% and 50% of k-space data. Table 5.1 summarises the obtained image quality parameters from the gated Cartesian and the complete bin combination acquired with RPE-PAWS. The difference between image parameters is given as a relative value compared to the results from the Cartesian scan. The apparent signal to

Table 5.1: Result of the comparison of a respiratory gated 3D Cartesian approach (Cart) and images reconstructed from complete bin combinations (i.e. 100% k-space data) obtained with the proposed RPE-PAWS method. All values (apparent signal to noise ratio (aSNR), apparent contrast to noise ratio (aCNR), vessel sharpness (VS) for left (LCA) and right (RCA) coronary arteries and navigator efficiency (NE)) are mean values of eight measurements with the standard deviation in brackets. For comparison, the p value from a paired student t-test is also given.

	aSNR			**VS**		
	muscle	**blood**	**aCNR**	**LCA**	**RCA**	**NE**
Cart	113.09 (±26.95)	217.02 (±69.74)	103.93 (±48.04)	39.82 (±5.59)	31.04 (±9.34)	45.26% (±14.63%)
RPE - PAWS	88.17 (±15.86)	196.75 (±53.23)	108.45 (±38.75)	46.62 (±4.82)	36.27 (±6.30)	54.57% (±11.11%)
Difference	-22.03% p<.05	-9.34% p>.05	4.35% p>.05	17.07% p<.05	16.82% p>.05	20.57% p<.001

noise ratio (aSNR) measured in the muscle was reduced by -22%, (p=0.02) due to the inhomogeneous sampling density of the radial-like PE trajectory. The vessel sharpness of the left coronary arteries was improved (17.1%, p=0.005). The increase in vessel sharpness for the right coronary artery is not statistically significant, which is probably due to the orientation of the scan geometry causing partial volume effects for RCA.

The results of the comparison between RPE-PAWS images reconstructed using 100% and 75% of k-space data are summarised in Tab 5.2. No significant difference was observed for aSNR, aCNR or VS which suggests, that the images exhibit comparable image quality.

In all eight volunteers, the RPE-PAWS approach led to an average increase in NE of 20.5% compared to the gated Cartesian scan.

The increase in NE and the amount of additional information from the non-complete bin combinations depends strongly on the individual breathing pattern. The results for two volunteers exhibiting regular and irregular respiratory cycles

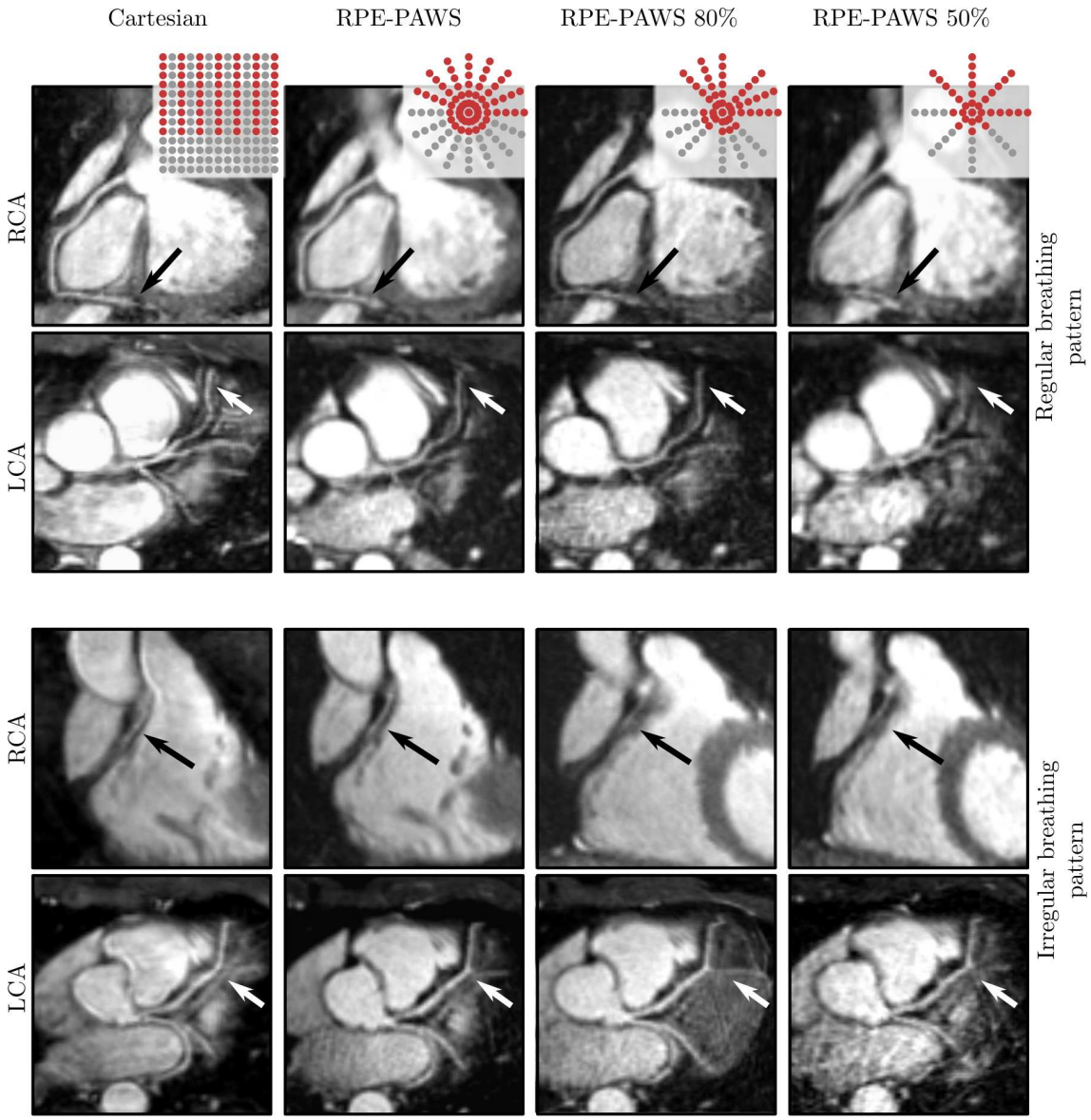

Figure 5.4: Reformatted images showing the right (RCA) and left (LCA) coronary arteries obtained from the 3D Cartesian and the RPE-PAWS scans (undersampling factor of 4 compared to fully sampled Cartesian case) for a volunteer with a regular and one with an irregular breathing pattern. For RPE-PAWS, images reconstructed from the complete bin combination and from non-complete bin combinations (≈80% and ≈50% k-space data compared to filled case) are shown. RCA and LCA are indicated with black and white arrows, respectively.

Table 5.2: Result of the comparison between images obtained with RPE-PAWS using data from a complete (100% k-space data) and non-complete (75% k-space data) bin combination. All values (apparent signal to noise ratio (aSNR), apparent contrast to noise ratio (aCNR) and vessel sharpness (VS) for left (LCA) and right (RCA) coronary arteries) are mean values of eight measurements with the standard deviation in brackets. For comparison, the p value from a paired student t-test is also given.

	aSNR			**VS**	
	muscle	**blood**	**aCNR**	**LCA**	**RCA**
RPE - PAWS	88.17	196.75	108.45	46.62	36.27
100%	(±15.86)	(±53.23)	(±38.75)	(±4.82)	(±6.30)
RPE - PAWS	81.06	201.09	117.45	43.30	38.57
75%	(±23.47)	(±63.63)	(±49.18)	(±5.08)	(±9.32)
Difference	-8.06%	-2.20%	8.30%	-7.12%	6.35%
	p>.05	p>.05	p>.05	p<.05	p>.05

are shown in Fig 5.5. The recorded navigator signals are shown in Fig. 5.5a,c and the corresponding histograms of the occurred diaphragm positions are plotted in Fig. 5.5b,d. Each bin of the histogram includes the same diaphragm positions as the navigator bins used during the data acquisition. The gray bars comprise only data recorded during the initial training phase (e.g. before the gating window is positioned) and the blue bars contain the entire respiratory signal.

The histogram of the regular breathing pattern (Fig. 5.5b) exhibits a clear maximum e.g. a clear most probable breathing state throughout the entire data acquisition. In this case, the navigator window positioned by the gating method leads to a reasonable scan efficiency (37.7%) and only a moderate improvement can be achieved with the PAWS approach (+20.4%). The second histogram (Fig. 5.5d) does not show a well defined most frequent breathing position. Here NE for the standard gating method was 15.9% and it was increased to 45.1% by RPE-PAWS.

In Fig. 5.5e and f for two volunteers eight images each are displayed which were obtained from different combinations of bins using a sliding window reconstruction showing the ROI over a range of more than 90% of the extent of the respiratory

cycle. The anatomy of the heart is still clearly visible for all images shown. VS of the coronary arteries and aSNR are depicted as a function of different bin combinations in Fig. 5.5g and h. Similar to the simulations presented in the previous chapter aSNR decreases faster than VS with increasing undersampling.

5.2.6 Discussion

RPE-PAWS provides fast and highly efficient 3D whole-heart scans and in addition yields dynamical information. The images obtained with RPE-PAWS show a higher value for VS that indicates that our proposed method visualises small structures such as the coronary arteries more accurately than the gated Cartesian method. This is in good agreement with earlier studies, comparing radial and Cartesian sampling patterns for coronary magnetic resonance angiography [150] and supports the results from the simulations carried out in the previous chapter.

The lower aSNR was expected for RPE-PAWS due to the inhomogeneous sampling density of the radial-like PE trajectory. Nevertheless, the two sampling methods lead to entirely different undersampling and motion artefacts and in addition the noise amplification due to the SENSE and iterative SENSE reconstruction is also different. Therefore, a comparison of aSNR and aCNR between Cartesian and RPE-PAWS scans is difficult.

The presented scan protocol for the in-vivo experiments leads to very long scan times which would not be feasible for clinical scans. Usually a lower resolution along

Figure 5.5 ***(following page)*****: (a-d)** Plot of the recorded navigator signals and corresponding histograms for a volunteer with regular (a-b) and irregular (c-d) breathing. The most frequent breathing position is the same for the training phase (gray bars) and the data acquisition period (blue bars) for the regular breathing pattern (b) but not for the irregular one (d). The values of the training phase were multiplied with a factor of 10 for better visibility. **(e-f)** RPE-PAWS yields one high resolution image at a certain stage in the respiratory cycle reconstructed from the complete bin combination (i.e. 100% k-space data). In addition images can also be reconstructed from non-complete bin combinations showing the ROI at different stages in the breathing cycle. The white dashed line indicates the position of the diaphragm in end-expiration ((e) regular and (f) irregular breathing pattern). **(g-h)** Vessel sharpness (VS) and apparent signal to noise ratio (aSNR) assessed in the images shown in e and f, respectively. The dashed lines mark values for the filled bin combinations. The percentage values in (c-h) indicate the amount of k-space data sampled in the bin combinations used to reconstruct the images.

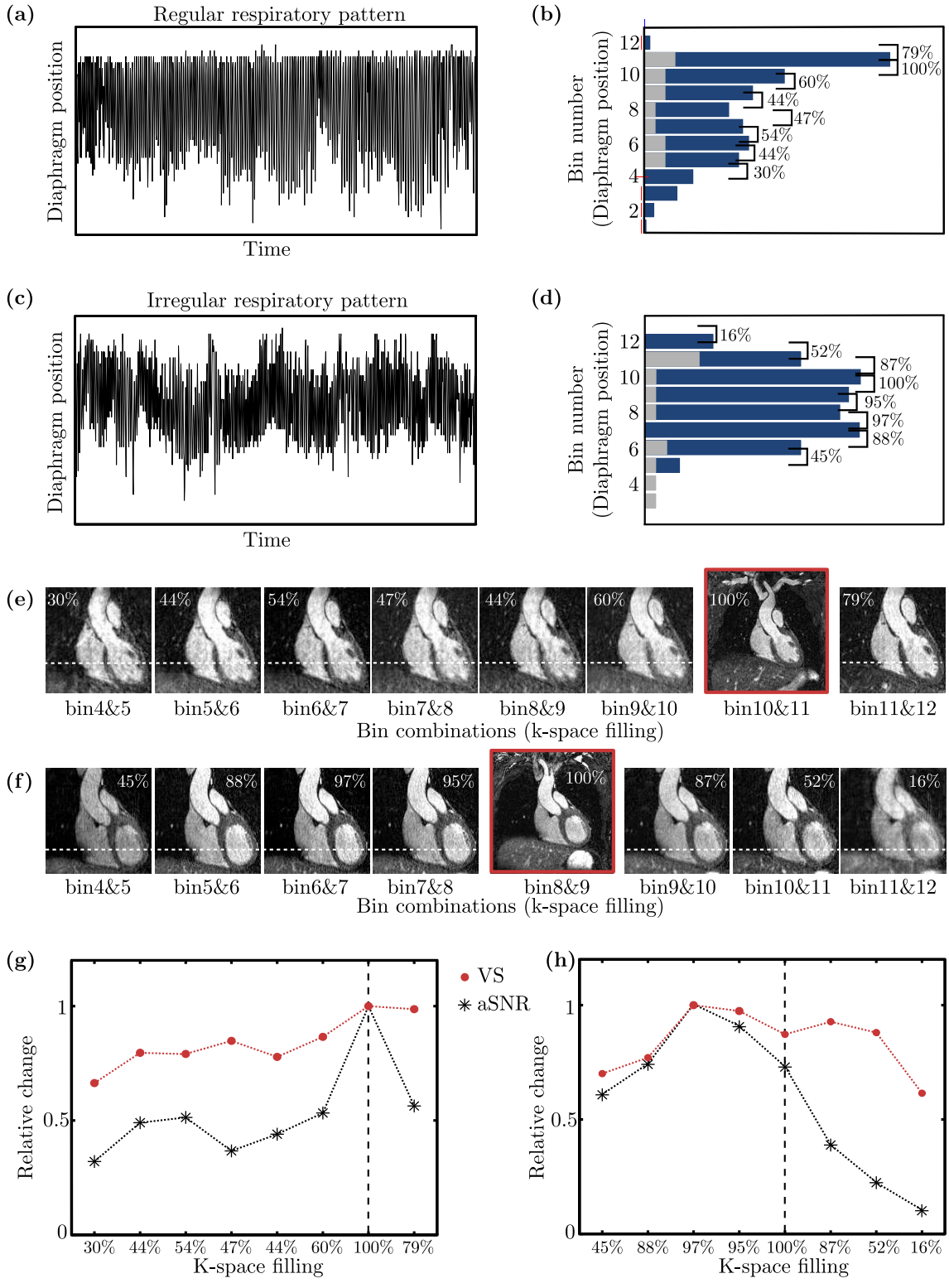
(a)
Regular respiratory pattern
Diaphragm position
Time
(b)
Bin number (Diaphragm position)
12
10
8
6
4
2
79%
100%
60%
44%
47%
54%
44%
30%
(c)
Irregular respiratory pattern
Diaphragm position
Time
(d)
Bin number (Diaphragm position)
12
10
8
6
4
16%
52%
87%
100%
95%
97%
88%
45%
(e)
30%
44%
54%
47%
44%
60%
100%
79%
bin4&5
bin5&6
bin6&7
bin7&8
bin8&9
bin9&10
bin10&11
bin11&12
Bin combinations (k-space filling)
(f)
45%
88%
97%
95%
100%
87%
52%
16%
bin4&5
bin5&6
bin6&7
bin7&8
bin8&9
bin9&10
bin10&11
bin11&12
Bin combinations (k-space filling)
(g)
Relative change
1
0.5
0
VS
aSNR
30% 44% 54% 47% 44% 60% 100% 79%
K-space filling
(h)
Relative change
1
0.5
0
45% 88% 97% 95% 100% 87% 52% 16%
K-space filling

one phase-encoding direction is used ('overcontiguous slices') resulting in shorter scan time. However, the high resolution and large FOV were chosen for comparison purposes only. The scan time could be reduced by using an anisotropic FOV similar to [151] and adapted resolution settings. Furthermore, higher acceleration factors should also be possible by introducing undersampling in the radial direction for example.

RPE-PAWS always led to a statistically significant higher navigator efficiency compared to the respiratory gated Cartesian method, which is in good agreement to earlier studies [132,133]. For one subject, RPE-PAWS only led to a slight increase of NE, which indicates that the respiratory gated Cartesian method already yields the highest navigator efficiency and no further improvements are possible. Further improvements can be achieved by stopping the RPE-PAWS scan before one complete bin combination is available. This is only possible because for RPE-PAWS the binning of data affects the entire 2D phase encoding plane and not just one PE direction as with PAWS using a 3D Cartesian sampling scheme. This means the operator has more freedom when to end the scan and can interactively optimise NE. For example terminating the scan if the most complete bin combination includes 80% (Fig. 5.4) of k-space data can increase NE further by more than 70%. According to the results shown in Tab. 5.2 an RPE-PAWS scan could be stopped even if 25% of k-space data are still missing without a significant decrease in image quality. This threshold of 25% was chosen arbitrarily and a sufficient image quality could probably be achieved with less data.

One limitation of this study is that it does not involve a comparison between Cartesian PAWS and RPE-PAWS. Nevertheless, the obtained VS, aSNR and NE for both the gated Cartesian scan and RPE-PAWS are in good agreement with the results of the scan simulation shown in the previous chapter. This suggests that the improvement in image quality and NE of our approach compared to 3D MAG predicted by the scan simulation would be confirmed by an in-vivo study.

A sound analysis of the image quality between the two methods is only possible for a large number of subjects to avoid bias due to changes of the respiratory pattern in successive scans, which would go beyond the scope of this thesis.

For a standard respiratory gating approach data acquisition is carried out in a navigator window located at end-expiratory. For regular breathing patterns this is a respiratory rest period which means that the velocity of tissue moving due to breathing is low. This is advantageous for the obtained image quality. The complete image obtained with RPE-PAWS is always reconstructed at the most frequent respiratory phase. For subjects with regular respiratory patterns it is most likely at end-expiratory. It is usually not the case for irregular breathing patterns which can yield a complete image at an arbitrary respiratory phase. This can lead to a higher artefact level due to the higher breathing velocity of the heart in this phase compared to the end-expiratory phase. Nevertheless, also the standard respiratory gating approach cannot ensure that all data is acquired in end-expiration and therefore suffers from the same limitation (see also Fig. 4.13).

A further benefit of the proposed acquisition scheme is that it allows for the reconstruction of additional images from partially filled bin combinations showing the ROI at different respiratory motion stages. As discussed previously the quality of these images depends not just on the undersampling ratio but also on the distribution of motion over k-space. Both parameters depend entirely on the individual breathing pattern and cannot be predicted. Therefore, a general systematic comparison of all images is not possible. A quantitative comparison of these images has to be adapted depending on the further application of these images and will be discussed in the following chapter.

The bit reversed order of the radial phase encoding lines restricts the number of radial lines N_α to a power of two. Nevertheless, this limitation of the number of phase encoding steps can be overcome by using different partial Fourier factors. Furthermore, using a 3D Golden-Radial Phase Encoding trajectory would offer a continuous choice of N_α while maintaining a homogeneous covering of k-space [83].

In the past one drawback of non-Cartesian SENSE have been long reconstruction times, as image data are obtained iteratively. Nevertheless, it has been shown recently that the iterative SENSE approach can be implemented on a graphical processor unit (GPU) and this enables image reconstruction in real time [152].

5.3 Conclusion

We presented two methods which combine interleaved phase encoding schemes with the ideas of PAWS in order to achieve fast 3D imaging with a high isotropic resolution and high navigator efficiency even for highly irregular breathing. The interleaved sampling scheme ensures that data from two bins can be combined optimally for image reconstruction and it maintains a smooth distribution of motion over the entire 2D phase encoding plane.

The RPE-PAWS approach leads to a significant increase in navigator efficiency and a superior depiction of small structures compared to a respiratory gated 3D Cartesian approach. The acquisition can be stopped before the scan has finished in order to optimise the navigator efficiency without compromising image quality. Furthermore, a sliding window approach can be used to reconstruct images showing the ROI at different respiratory stages providing additional information from the same scan data. This can be of benefit for image-guided interventions where the influence of respiratory motion needs to be addressed which will be discussed in the next chapter.

6 | Prospective High Resolution Respiratory-Resolved Whole-Heart MRI for Image-Guided Percutaneous Procedures

6.1 Introduction

Image guided percutaneous procedures are commonly used to assess and treat cardiovascular diseases. Their applications include diagnosis and treatment of ischemic and congenital heart disease [29] as well as cardiac arrhythmia [18,27,153] and heart failure [154]. All these procedures benefit from high quality 3D anatomical images for an accurate diagnosis, accurate treatment planning and reliable guidance during the interventional procedure. In particular, the treatment of cardiac arrhythmias requires detailed anatomical information about the atria, ventricles, pulmonary veins and coronary sinus. In order to ensure optimal depiction of the complex geometries

Some of the following results have already been presented in Kolbitsch *et al.*, "Prospective high-resolution respiratory-resolved whole-heart MRI for image-guided cardiovascular interventions", *Magn Reson Med*, vol. 68, pp. 205-13, 2011.

this image data should be acquired with a high isotropic resolution to avoid image degradation such as partial volume effects.

As discussed previously MRI has recently been reported to be able to provide 3D anatomical information ('roadmaps') during percutaneous procedures with excellent soft tissue contrast [29–33]. It also yields additional information about cardiac function, blood flow and myocardial scar tissue. In order to avoid any alignment errors between the roadmap and the X-ray fluoroscopy images due to the breathing motion of the patient during the procedure, 'dynamic roadmaps' have been proposed [46–48]. The shape and position of the roadmap is updated according to a pre-acquired motion model and a motion surrogate recorded during the interventional procedure.

The complexity of respiratory motion models has been studied by several groups using X-ray angiography [118], multiple MR pencil beams [117] and cardiac 3D MR images [119, 155]. It has been shown that patient specific 3D affine motion models can describe the respiratory motion of the heart with a satisfactory degree of accuracy [47, 118, 119]. In order to create such 3D affine motion models dynamic MR data has to be acquired in addition to the 3D anatomical data, which prolongs the overall scan time [47].

Here we show that RPE-PAWS yields all necessary information for a high resolution dynamic roadmap from one highly efficient 3D whole-heart MR scan. The results of the previous chapter have shown that RPE-PAWS leads to an efficient acquisition of a high resolution 3D whole-heart image while providing also undersampled 3D data sets at different stages in the breathing cycle. These respiratory resolved 3D image datasets are used to create a 3D affine motion model without the need for any additional data acquisition. Affine motion is determined between the different image data sets and a motion model is created by polynomial fitting of the affine parameters over time. In contrast to previous methods [47], high resolution data sets are used both to obtain the anatomical information for the roadmap and to determine the respiratory motion information. The images available for the motion estimation can be impaired by undersampling artefacts. Therefore, the effect of image quality on the results of the motion estimation is assessed. The 3D affine motion models are evaluated using data from ten healthy volunteers, which has been acquired with RPE-PAWS. The motion of important anatomical landmarks of the

heart is determined and differences between volunteers are reported. The accuracy of the affine model is quantitatively assessed. An analysis of the respiratory motion and results of the 3D dynamic roadmap from a patient before catheter ablation for atrial fibrillation treatment are presented.

6.2 Methods

6.2.1 Data Acquisition and Reconstruction

Data acquisition was carried out using (bit reversed) RPE-PAWS presented in chapters 4 and 5.

As already mentioned the interleaved bit reversed RPE scheme ensures a homogeneous distribution of acquired k-space data over the 2D phase encoding plane for undersampled data sets. Data from two adjacent bins are complementary and can be combined for image reconstruction using a sliding window approach to improve the sampling density (Fig. 6.1a-b). After the scan is successfully finished, one complete and multiple non-complete images can be obtained showing the ROI at different stages in the respiratory cycle.

The image data is reconstructed off-line by performing a homodyne reconstruction along the radial direction and a subsequent non-Cartesian SENSE reconstruction (see also Fig. 5.3) [94]. This ensures reconstruction of complete images with excellent quality and isotropic resolution as well as good image quality for non-complete data sets.

6.2.2 3D Affine Motion Model

The respiratory motion of the heart was modelled using a subject specific 3D affine motion model M, which describes the temporal behaviour of translation, rotation, shearing and scaling. The main steps of this registration process are summarised in Fig. 6.1c-d. The 12 affine parameters were obtained using a 3D affine registration algorithm with one registration level, which was applied to a 3D rectangular region of interest (ROI) around the heart [156]. A normalised cross-correlation function was used as a similarity measure. The complete image was registered to the different

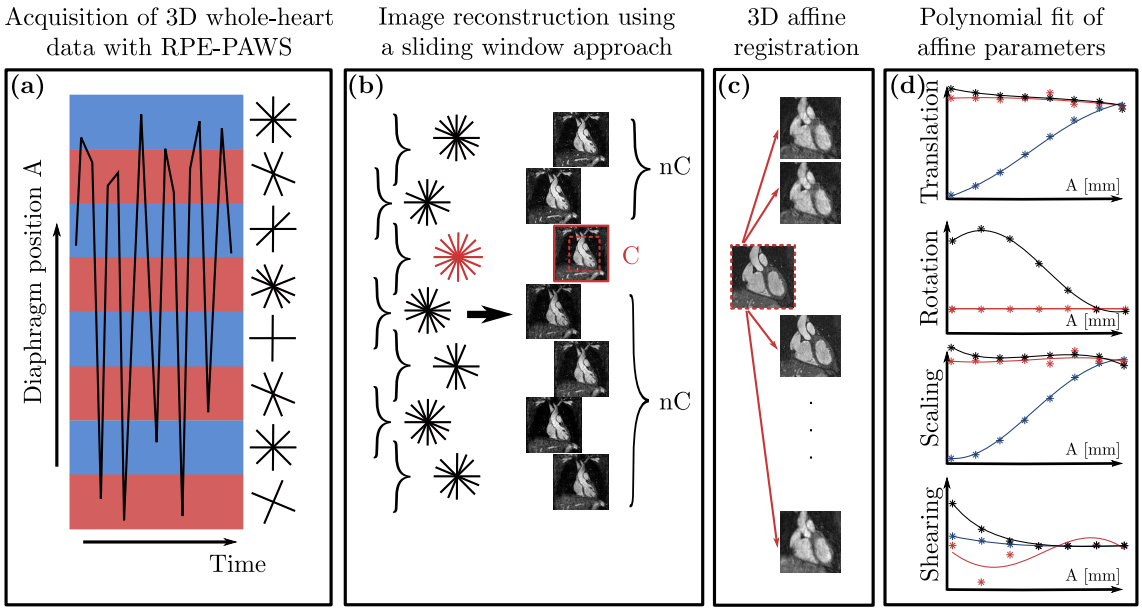

Figure 6.1: (a) RPE-PAWS acquires data with an interleaved bit reversed Radial Phase Encoding (RPE) trajectory which leads to a homogeneous covering of k-space during the entire scan and allows for the optimal combination of k-space data from adjacent respiratory bins (red/blue area). **(b)** The scan is successfully finished if one combination of two bins yields the desired k-space information and a complete image (C) can be reconstructed. Additional images can be reconstructed from the non-complete (nC) bin combinations. **(c)** After selecting a ROI around the heart, the complete image (C) is registered to the non-complete images (nC) using a 3D affine registration. **(d)** This yields 12 affine parameters (stars) which are fitted with a 3rd order polynomial (line) for the final motion model. The graphs show the affine parameters for translation, rotation, scaling and shearing as a function of A for foot-head (blue), left-right (black) and anterior-posterior (red).

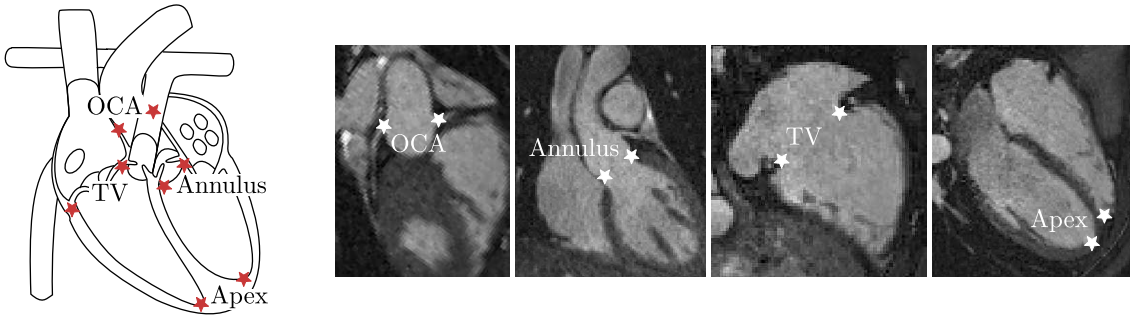

Figure 6.2: Anatomical landmarks to assess accuracy of respiratory motion models. Eight landmarks were selected at anatomically well defined positions in the heart: lateral/medial apex, lateral/medial tricuspid valve (TV), lateral/medial aortic valve annulus and origin of left/right coronary arteries (OCA).

non-complete images, which represent the different respiratory phases. This yielded a set of 12 affine parameters $\phi_{1...12}$ for each registration, i.e. N-1 different respiratory phases rph_n

$$\phi_i(rph_1, rph_2, ...rph_{N-1}) \quad \text{with} \quad i = 1 \ldots 12. \tag{6.1}$$

To create a motion model M, each of the 12 parameters $\phi_i(rph_1, rph_2, \ldots rph_{N-1})$ were fitted by a third order polynomial as a function of the diaphragm position in millimetres. Therefore, the affine parameters are not just defined at discrete positions of the diaphragm given by the respiratory bins but can be interpolated for a continuous range of breathing stages. The fitted ϕ_i were then used to create a matrix defining the 3D affine transformation between the complete and the non-complete images.

6.2.3 Evaluation of Heart Motion

The effect of respiratory motion was evaluated for different areas in the heart, i.e. ventricles, atria and coronary arteries. For that, eight anatomical landmarks (LMs) were selected manually as lateral/medial apex, lateral/medial tricuspid valve, lateral/medial aortic valve annulus and origin of the left/right coronary artery (Fig. 6.2).

6.2.4 Effect of Undersampling on Motion Estimation

All 3D image sets, which were reconstructed from the RPE-PAWS data, had the same high isotropic resolution. However, the non-complete images, which were used to form the motion model, could be impaired by undersampling artefacts. Therefore, their quality depended mainly on the amount of acquired k-space data in each bin, which was determined by the individual breathing pattern and thus cannot generally be predicted. The influence of image quality on the accuracy of the motion model was assessed on data that was retrospectively undersampled. For this, non-complete sets of images containing 40%, 30%, 20%, 15%, 10% and 5% of k-space data were generated (100% corresponds to the complete image) in one specific volunteer exhibiting an irregular breathing pattern allowing for this analysis which will be discussed in more detail in the 'Results' section. The k-space data was undersampled such that it was distributed the same as if the scan had originally been stopped at 40%, 30%,... 5%.

In the previous chapters image quality parameters were analysed as functions of k-space undersampling (Fig. 4.11 and Fig. 5.5). Here the effect of undersampling was analysed with respect to the accuracy of motion models. For this six motion models ($M_{40\%}$, $M_{30\%}$,..) were derived from the undersampled data sets and were applied to the landmarks determined in the complete image. This led to six sets of predicted landmarks $LM_{40\%}$, $LM_{30\%}$,.. which were then compared to the landmark positions predicted by the motion model M_{ref} created from the original data. As a means of comparison the maximum and root mean square (RMS) error of the distance between the positions of the landmark points LM_{ref} and $LM_{40\%}$, $LM_{30\%}$,.. were calculated

$$E_{US}(i) = \sqrt{\frac{1}{8N}\sum_{lm=1}^{8}\sum_{rph=1}^{N}|M_{ref}(rph)LM(lm,rph=C) - M_i(rph)LM(lm,rph=C)|^2} \tag{6.2}$$

with i = 40%, 30%, 20%, 15%, 10% and 5%, with $rph = C$ referring to the complete image and with lm and rph describing the different landmarks and respiratory phases, respectively.

The value of the RMS error (E_{US}) is an average over all landmarks and all respiratory phases. An increase in E_{US} for individual targets might not be immediately obvious from that value. The maximum error is, however, sensitive to the behaviour of single landmarks. Therefore, a different behaviour of the RMS and the maximum error as a function of undersampling would be a good indicator that E_{US} did not change evenly but showed a dependency on the landmark position.

It is important to note that for this analysis the landmark positions predicted by M_{ref} were compared to the ones predicted by $M_{40\%}$, $M_{30\%}$,.. $M_{5\%}$. Therefore, any errors introduced by inaccurate selection of the position of LM were avoided and could not distort the result.

6.2.5 Model Accuracy

The accuracy of motion models is usually assessed using the target registration error (TRE), which describes the distance between different pairs of landmarks [157]. For this study the 3D TRE was determined for eight landmark points LM by measuring their position in each of the non-complete images and the position of the LMs predicted by applying the motion model M to the landmark positions determined in the complete image ($rph = C$). In addition to the mean value and standard deviation the root mean square (RMS) error of the model accuracy E_{MA} is given as the RMS error over all N_v volunteers and all N respiratory phases

$$E_{MA}(lm) = \sqrt{\frac{1}{N_V N} \sum_{v=1}^{N_V} \sum_{rph=1}^{N} |LM(lm, v, rph) - M(v, rph) LM(lm, v, rph = C)|^2} \tag{6.3}$$

where $lm = 1...8$ described the different landmarks. The landmark points were visually selected and therefore, the intra- and inter-observer variability of the model accuracy were determined in order to assess the reproducibility of the evaluation.

6.2.6 Motion Model Application

For the final roadmap five regions of interest for cardiac catheterisation (left/right ventricle, left/right atrium, coronary arteries) were segmented in the complete images using a semiautomatic approach (ITK-SNAP, www.itksnap.org) [158]. The mo-

tion model M was applied to this roadmap and the position and shape of it were analysed qualitatively for different respiratory phases.

6.3 Experiments

6.3.1 Volunteer and Patient Studies

In addition to the 3D whole-heart data acquired for the previous study presented in chapter 5, two additional healthy volunteers and one patient (43 years, due to undergo catheter ablation for paroxysmal atrial fibrillation treatment) were imaged on a 1.5T MRI scanner (Philips Medical Systems, Best, The Netherlands) with the same scan protocol as before: balanced steady-state free precession sequence, T2-prep pulse (TE = 50 ms), isotropic FOV: 288 x 288 x 288 mm, isotropic resolution: 1.5 mm^3, fat supression, 90^o flip angle, TR/TE = 4.3/2.2 ms, segmented approach (TFE factor = 24) with low-high profile order.

The images of the volunteers were obtained with a 32-channel cardiac phased array coil and patient data was acquired with a 5-channel cardiac phased array coil. The data was undersampled in the angular direction and a partial Fourier factor of 0.75 was used along the radial direction which resulted in an overall undersampling factor of 4 for the complete image. The acquisition matrix consisted of 144 phase encoding points in the radial direction and 64 radial lines. Mid-diastolic triggering was applied and each respiratory bin covered a diaphragm displacement of 3 mm. Therefore, an image for each three millimetres of the respiratory cycle is available. Written informed consent was obtained from all participants and the study was carried out following an approved protocol from our local hospital.

The effect of undersampling on the motion estimation was analysed using data from a volunteer exhibiting a highly irregular breathing pattern. This led to a homogeneous distribution of k-space data in a wide range of bin combinations rather than a clear most probable breathing state (e.g. end-expiration) as with regular breathing patterns. For this volunteer also the behaviour of the individual affine parameters describing the motion models were studied as a function of undersampling. The motion of the landmarks LM was studied for different volunteers and mean

motion between end-inspiration and end-expiration was calculated and standard deviation was given. Furthermore, the intra-observer and inter-observer variability were assessed in one volunteer by determining the model accuracy E_{MA} for the eight landmarks in all respiratory phases by the same observer twice and by two different observers, respectively. The mean and standard deviation of E_{MA} over the landmark positions were used as a quantitative parameter.

In the data set acquired from the patient before catheter ablation treatment the respiratory motion and the model accuracy were assessed for landmarks close to the atrium (origin of coronary arteries, tricuspid valve and aortic valve annulus). Furthermore, 3D roadmaps from both volunteer and patient were segmented from the complete image data and the motion model was applied.

6.4 Results

The scan was successfully finished in all volunteers. The total acquisition time ranged from 8.4 - 14.8 min with a mean navigator efficiency of 52%. The number of obtained bins/respiratory phases was between 4 and 9 (mean 6.3) depending on the individual breathing patterns, i.e. the amplitude of the respiratory movement of the diaphragm in foot-head direction. A summary of the individual breathing parameters is given in Table 6.1.

The majority of volunteers showed regular breathing patterns, which led to a well-defined most probable breathing state in end-expiration and therefore one highly populated bin combination and several other bins with considerably less data (Fig. 6.3a). Data from these subjects was not suitable for the analysis of the effect of undersampling on the motion model, because only a few respiratory phases were available due to the small amount of data in the non-complete bins and only a small range of undersampling factors could have been analysed. Therefore, for the assessment of the effect of undersampling on the motion model a volunteer exhibiting a highly irregular breathing pattern was selected (Fig. 6.3b). For this subject a large number of respiratory bins with a high amount of acquired data in each of them were available. This data set consisted of one complete bin combination (100% k-space data) and eight non-complete bin combinations containing 9.6%, 45%, 88%,

Table 6.1: Summary of volunteer study. Navigator efficiency (NE), total number of respiratory bin combinations (# Bins), number of bin combinations containing more than 40% and 10% of k-space data compared to the complete bin combination (# Bins $\geq$ 40%, # Bins $\geq$ 10%), number of rejected bins (# Bins rejected) and the maximum of respiratory motion amplitude over all landmarks in each volunteer. The data from volunteer 5 was used to study the effect of undersampling on the accuracy of the motion estimation.

Volunteer	**NE**	**# Bins**	**# Bins $\geq$ 40%**	**# Bins $\geq$ 10%**	**# Bins rejected**	**Resp. amp [mm]**
1	0.63	5	3	5	0	7.65
2	0.49	10	4	8	2	18.00
3	0.64	4	3	4	0	6.71
4	0.49	6	4	6	0	9.49
5	**0.34**	**9**	**7**	**9**	**0**	**13.58**
6	0.41	8	7	8	0	11.05
7	0.33	7	6	7	0	9.12
8	0.62	3	3	3	0	6.18
9	0.50	9	5	7	2	14.15
10	0.63	5	4	5	0	9.00

97%, 95%, 87%, 52% and 16% of k-space data. The percentage values describe the amount of k-space data in each combination of bins relative to the complete image. The first and the last bin combinations were not included in this analysis in order to achieve more homogeneously distributed data with at least 45% of k-space data. Figure 6.3c shows one slice of the reference image and one of each of the data sets, which were retrospectively undersampled to 40%, 30%, 20%, 15%, 10% and 5%. The outline of the heart is still visible for a wide range of undersampling ratios but image quality decreases strongly for the 5% case as it contains as few as three sampled radial phase encoding lines.

Figure 6.4a shows the 4 (translation, rotation, scaling and shearing) x 3 (anterior-posterior (AP), foot-head (FH) and right-left (RL)) affine parameters as functions of undersampling for different respiratory phases. Each column describes the results of the registration of one of the non-complete images (nC1, nC2,...) to the complete image. The complete image describes a respiratory phase between nC4 and nC6. The different columns visualise the behaviour of the affine parameters for different respiratory phases. Relative to the complete data set, nC6 and nC7 show increasing translation in FH but no scaling or shearing. Moving from the complete image towards end-inspiration, translation in the opposite direction and additional scaling and shearing occurs. All parameters reach a maximum change relative to the complete data set at end inspiration.

The affine parameters show little variation for images using at least 10% of k-space data. For higher undersampling factors some parameters change strongly which suggests that the image quality is not sufficient for a reliable image registration.

The RMS and maximum error of the motion model due to undersampling (E_{US}) over all seven respiratory phases and over all eight landmarks for the different motion models are depicted in Fig. 6.4b. Both errors are well below the image resolution and show a similar behaviour which suggests that the motion models describe the respiratory motion of the heart for all eight landmarks equally well and the errors do not depend on the position of the landmarks. The assessment of the effect of undersampling is also summarized in Fig 6.3c.

The behaviour of both the individual affine parameters and of E_{US} suggests that a threshold of 10% of k-space data is sufficient to ensure accurate motion estima-

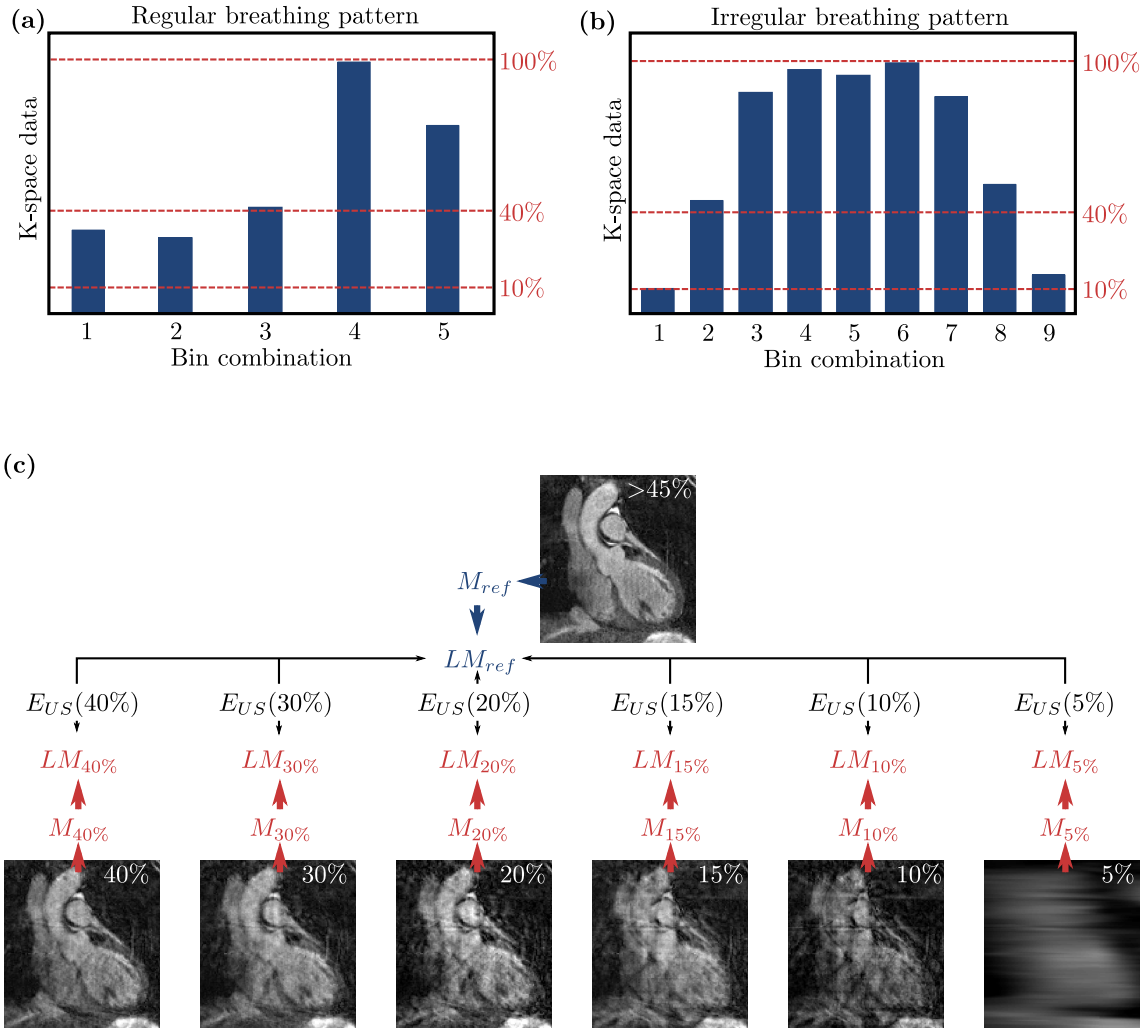

Figure 6.3: Assessment of the effect of undersampling on the motion model accuracy. **(a-b)**: Histogram showing the amount of k-space data acquired in different respiratory bin combinations for a regular (a) and irregular (b) breathing pattern. Only an irregular breathing pattern leads to a high number of bins with a large amount of acquired k-space data sufficient for this analysis. **(c)** The non-complete bin combinations (>45%) of one volunteer with an irregular breathing pattern were retrospectively undersampled to 40%, 30%,5% of k-space data (100% correspond to the complete image). The prediction of the six motion models $M_{40\%}, M_{30\%}, \dots M_{5\%}$ of the position of the landmarks LM were compared to the original model M_{ref}.

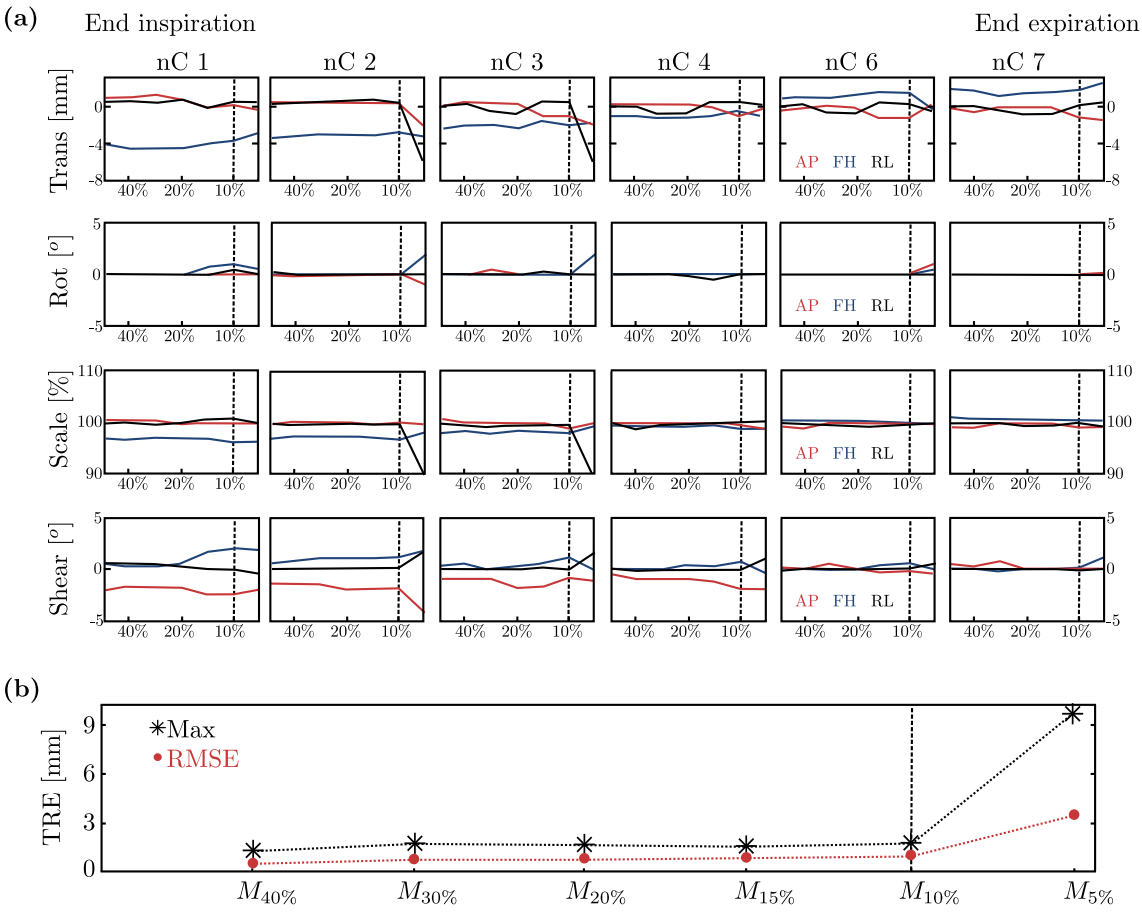

Figure 6.4: Effect of undersampling on motion model accuracy. **(a)** Behavior of 4 x 3 affine parameters for different undersampling factors. Each column represents the results of the registration of one of the non-complete images (nC1, nC2,) to the complete image. The complete image represents a respiratory phase between nC4 and nC6. Each individual image shows either translation (transl), rotation (rot), scaling (scale) or shearing (shear) in anterior-posterior (AP, red), foot-head (FH, blue) and right-left (RL , black) as a function of the undersampled motion models (>45%, 40%, 30%,5%). The scaling of the figures was set to visualize significant changes of the parameters. **(b)** The RMS and maximum error for different motion models. The latter were obtained from retrospectively undersampled images and compared to the motion model determined from the original data. The amount of k-space data used for the non-complete images is given in percent relative to the complete image.

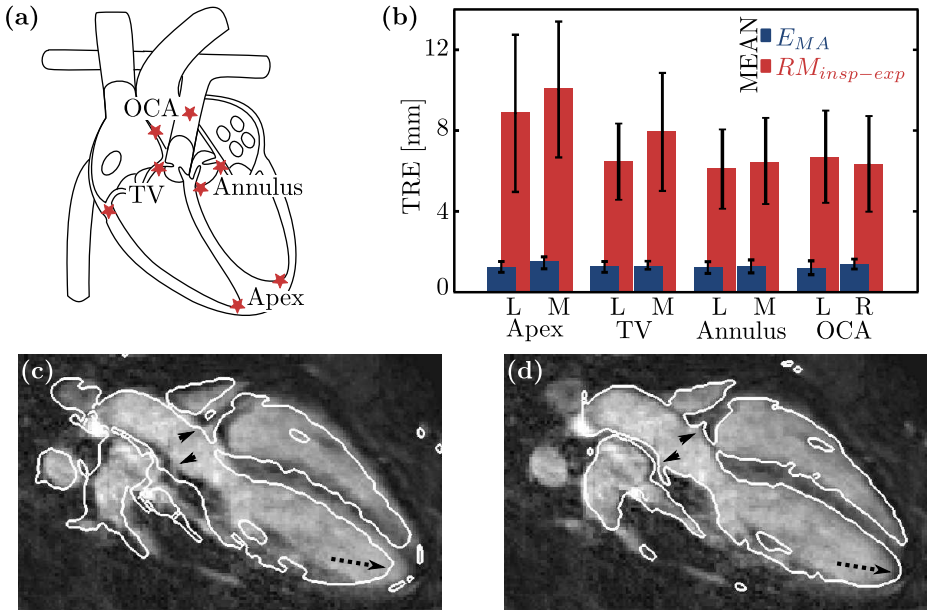

Figure 6.5: (a) Eight landmarks were selected at anatomically well defined positions in the heart: lateral/medial apex, lateral/medial tricuspid valve (TV), lateral/medial aortic valve annulus and origin of left/right coronary arteries (OCA). **(b)** Mean values and standard deviation (error bars) of the displacement of landmarks between end-inspiration and end-expiration ($RM_{insp-exp}$) and the model accuracy (E_{MA}). **(c-d)** The greyscale image shows an oblique plane through the heart at end-inspiration. (c) The white contours were obtained from the same plane but in end-expiration exhibiting significant displacements not just in the apex (dashed arrow) but also in the area of the origin of the coronary arteries (arrow heads). (d) Applying the obtained 3D affine transformation to the end-expiration image corrects for these displacements with an accuracy below the image resolution.

tion. Therefore, this threshold was applied to all volunteer data, which meant that for two volunteers two bins each were discarded. The quantitative analysis of the motion between end-expiration and end-inspiration of the eight landmark points and the model accuracy for the different landmarks was carried out on the data after excluding four bins as mentioned above. Eight landmarks were selected in each respiratory phase from all 10 volunteers with a mean number of 6.3 respiratory bins leading to a total of 504 landmarks. Eight points had to be removed because their visibility was strongly impaired by undersampling artefacts. The results of the analysis of the remaining 496 landmarks are shown in Fig. 6.5b. The motion decreases with increasing distance from the diaphragm but it is still in the range of 6 mm even for the origin of the coronary arteries. In addition, there is a considerable standard deviation between different volunteers. The mean error of E_{MA} lies below the voxel size (1.5 mm) for all landmarks with a standard deviation between 0.22 and 0.41 mm (Tab. 6.2). Table 6.2 also includes the RMS and maximum error of E_{MA}. All values do not exhibit an explicit dependency on the position of the landmarks.

The intra-observer and inter-observer variability of E_{MA} was found to be -0.13 ($\pm$ 0.34) mm and -0.13 mm ($\pm$ 0.33) mm, respectively.

Figures 6.5c and d depict an oblique plane of the 3D whole-heart data in end-inspiration. The white contour in Fig. 6.5c is obtained from the corresponding end-expiration image showing misalignments at the apex and also at the origin of the coronary arteries. Figure 6.5d shows the contour of the end-expiration image which was transformed to end-inspiration with the obtained 3D affine motion model. Snapshots of the final segmented roadmap at different respiratory positions for one volunteer are shown in Fig. 6.6.

The acquisition of the patient data took 9.3 min with a respiratory gating efficiency of 59%. All of the six bin combinations contained more than 10% of k-space data and no data had to be discarded. Figure 6.7 summarizes the results of the patient scan. The obtained affine parameters for translation and scaling are displayed in Fig. 6.7a,b and snapshots of the final dynamic roadmap are shown in Fig. 6.8 for multiple breathing stages. The dominant breathing motion is scaling and translation in foot-head direction. Figure 6.7c shows the left and right atrium and the measured

Table 6.2: Mean, standard deviation (std), minimum (Min) and maximum (Max) value of the respiratory motion ($RM_{insp-exp}$) between end-inspiration and end-expiration of eight landmarks. Root mean square error (RMSE), maximum error (Max), mean value (Mean) and standard deviation (Std) of the model accuracy E_{MA} for eight landmarks. All values in [mm]. (CA coronary arteries, AV aortic valve)

		Apex		**Tricuspid valve**		**AV Annulus**		**Origin of CA**	
		L	**M**	**L**	**M**	**L**	**M**	**L**	**M**
$RM_{insp-exp}$	**Mean**	8.85	10.01	6.43	7.93	6.10	6.46	6.69	6.33
	Std	±3.89	±3.34	±1.90	±2.95	±1.98	±2.14	±2.29	±2.39
	Min	4.97	6.18	3.67	3.35	3.00	3.67	3.00	3.00
	Max	18.00	15.00	9.12	13.83	9.60	11.02	10.61	11.32
E_{MA}	**Mean**	1.24	1.48	1.28	1.30	1.20	1.28	1.22	1.38
	Std	±0.27	±0.36	±0.30	±0.22	±0.32	±0.36	±0.41	±0.30
	RMSE	1.47	1.70	1.52	1.52	1.44	1.52	1.43	1.61
	Max	2.78	2.73	2.77	2.71	2.76	2.75	2.50	2.70

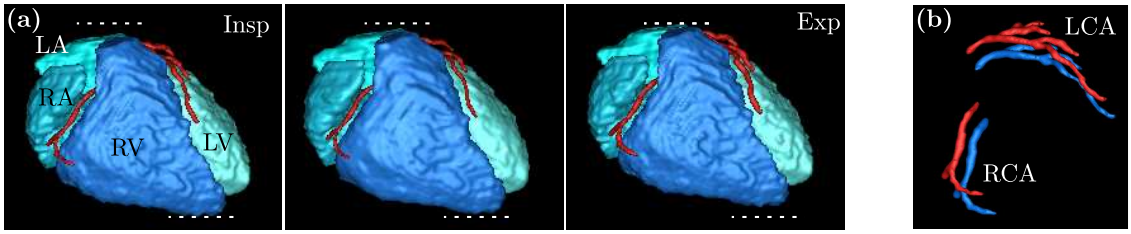

Figure 6.6: Segmented roadmap from volunteer data. **(a)** Roadmap at different respiratory positions. **(b)** Segmented left (LCA) and right (RCA) coronary artery at inspiration (blue) and expiration (red).

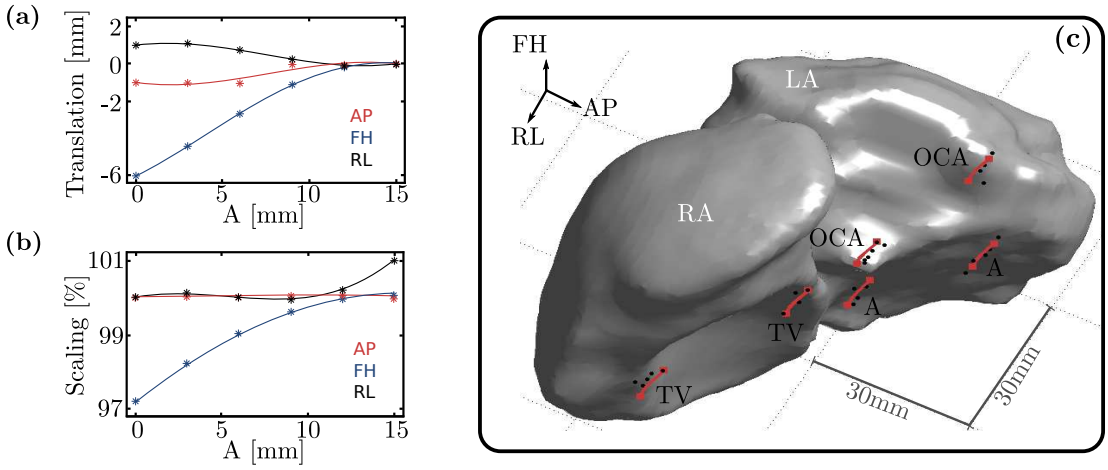

Figure 6.7: Results of the patient scan. **(a-b)** Affine parameters describing translation and scaling in anterior-posterior (AP), foot-head (FH) and right-left (RL) direction (star: measured, line: 3rd polynomial fit). **(c)** The measured positions (black dots) and the positions predicted by the obtained motion model (red line) of the selected landmarks displayed on the segmented RA and LA.

and predicted positions of 33 landmarks. The amplitude of respiratory motion was more than 9 mm and the model accuracy E_{MA} was 1.17 mm $\pm$ 0.36 mm which is below the image resolution.

6.5 Discussion

The dynamic information provided by RPE-PAWS can be used to create an accurate 3D affine motion model from a single scan describing the respiratory motion of the heart in order to minimise alignment errors due to breathing. A qualitative and quantitative analysis of respiratory heart motion shows significant displacements not just at the apex of the heart but also in the area of the atria. Furthermore, a

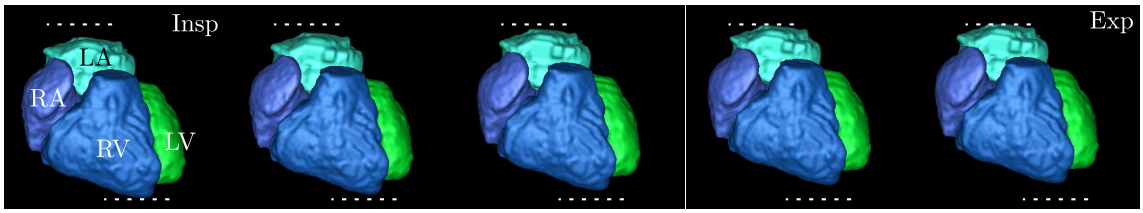

Figure 6.8: Segmented respiratory resolved roadmap obtained from patient data at different breathing positions. (LA/RA left/right atrium, LV/RV left/right ventricle, Insp end-inspiration, Exp end-expiration). The dominant motion components are a translation and scaling in FH.

strong variability between different subjects is reported. Both results are in good agreement with earlier studies [118,119,155] and emphasise the importance of patient specific dynamic roadmaps.

The mean error of the accuracy of the motion model E_{MA} lies below the acquired resolution of 1.5 mm. This suggests, that E_{MA} is limited by how accurate the landmark points can be defined by the observer rather than how well the affine motion model describes the respiratory motion of the heart.

The effect of undersampling on the motion model accuracy was studied on only one volunteer. Nevertheless, the obtained threshold value of 10% of k-space data has been verified in the analysis of the model accuracy on 11 subjects as it led to an accurate motion model for all volunteers and one patient.

The threshold value of 10% corresponds to a k-space coverage leading to an image resolution which is approximately 8 mm^3. Images with a similar resolution have been used successfully in previous studies for prospective 3D affine motion correction for high resolution imaging of coronary arteries [155].

The number of respiratory bins and therefore the number of acquired respiratory phases depends on the individual breathing pattern, the amplitude of the diaphragm movement A and the predefined bin width w. Some volunteers exhibit small A which can lead to as few as four acquired respiratory phases. This could be overcome using a 3D Golden RPE trajectory which would allow for a retrospective definition of different widths w [159].

For several volunteers bin combinations had to be excluded from the registration and motion modelling because they did not contain enough data for reliable motion estimation. This was due to the current stopping criteria of RPE-PAWS, which has

been defined for the shortest possible scan time of the complete data set rather than obtaining all non-complete images with a certain amount of k-space data. In order to optimise the data acquisition for motion modelling a new stopping criteria based on the results from the analysis of the motion model stability could be defined. The results of Fig. 6.4a and b suggest that a threshold of 10% of k-space data would be enough to ensure a sufficient image quality in each bin combination for accurate affine motion estimation. Therefore, the RPE-PAWS acquisition could also be carried out until each bin combination contains at least 10% of k-space data. In this case the k-space trajectory for complete bin combinations could be rotated by half of the angular gap between adjacent lines in order to increase the sampling density and therefore the image quality of the complete images and avoid the acquisition of redundant data. This would lead to a more predictable population of the respiratory bins and to an accurate motion model for the entire extent of the respiratory cycle with only a slight increase in scan time. An additional scan time of about two minutes would have halved the number of excluded bins in our volunteer study. To increase the accuracy of the motion estimation further, the iterative SENSE reconstruction could be extended with additional constraints such as total variation [160].

The reported total scan time of our whole-heart acquisition is higher than commonly used respiratory gated Cartesian 3D acquisitions. This is due to the fact that RPE-PAWS provides an acquired isotropic resolution in contrast to the majority of 3D Cartesian trajectories, which use retrospective interpolation methods usually in the slice encoding direction to achieve a reconstructed isotropic resolution.

The annulus of the aortic valve and the tricuspid valve are two dimensional structures. This makes an accurate selection of these anatomical structures as landmark points challenging. In order to ensure a reliable and reproducible landmark selection the position of these landmark points was determined in a plane which included other unique anatomical features in close proximity. For the aortic valve annulus for example a plane was chosen which showed the aortic valve and the offspring of the left coronary artery. A similar approach was taken for the tricuspid valve. This ensured both low inter- and intra-observer variability.

Previous studies have reported hysteresis effects in respiratory cycles, i.e. translation differences between inspiration and expiration of up to 6 mm [155]. Our presented approach does not model the inspiration and expiration cycle separately. In principle, this is possible, but would require the acquisition of more k-space data and thus a longer scan time. In addition, the positive effect of modelling the inspiration and expiration cycle separately has so far not been shown for cardiac roadmaps [47].

The motion model is obtained as a function of the diaphragm movement but this information is not always available during interventional procedures. Nevertheless, the 3D affine motion model also allows the use of different surrogates such as the position of a catheter at a certain anatomical location in the heart.

Previous studies carried out in our department have presented a framework to use pre-acquired MR data during image guided catheterisation procedures [31, 161]. The motion models obtained with RPE-PAWS can be directly implemented into this framework in order to be applied during clinical studies. Further collaboration with Philips Medical System (Best, The Netherlands) involves the implementation of this framework into a commercial project.

The non-Cartesian reconstruction of the image data is carried out iteratively which is computationally demanding. For this study reconstruction times for one respiratory resolved data set were longer than one hour. An implementation of the iterative SENSE algorithm on a graphical processor unit (GPU) is possible and can strongly reduce reconstruction times [162]. Nevertheless, in order to utilise a highly efficient acquisition scheme to minimise respiratory motion artefacts in patient studies without the requirements of additional hardware such as GPUs, HybridPAWS was used for the assessment of myocardial scar which is explained in the following chapter.

6.6 Conclusion

We have shown that RPE-PAWS yields all the necessary information to obtain accurate dynamic cardiac roadmaps with high isotropic resolution using a highly efficient 3D whole-heart scan without the need of additional data acquisition. The motion of the heart during the respiratory cycle can lead to misalignment errors of more than 10 mm. The 3D affine motion models obtained from the RPE-PAWS data

reduce this error to less than the acquired resolution (1.5 mm). The accuracy of the motion models is influenced by image quality and the results suggest that at least 10% of k-space data compared to the complete image is required for reliable motion estimation. Nevertheless, the beneficial undersampling properties in combination with flexible stopping criteria of RPE-PAWS can ensure an accurate motion model for all breathing phases. Finally, results from a patient scan emphasize the importance of respiratory-resolved roadmaps for cardiovascular interventions targeting thin structures such as the atrial wall and demonstrate the accuracy of our 3D dynamic roadmaps.

7 High Resolution 3D Assessment of Myocardial Scar Using Highly Efficient HybridPAWS

7.1 Introduction

Delayed enhancement (DE) MRI yields images with a high contrast between viable and fibrotic myocardial tissue as already discussed in chapter 3.2 [39]. Recent studies have highlighted the connection between fibrotic tissue and cardiac arrhythmia. Therefore, visualisation of myocardial fibrosis can provide important information for the planning of ablation therapy. Furthermore, DE-MRI can also be used to assess the outcome of ablation procedures [14, 50]. In addition it can help to diagnose heart failure patients [163] and improve cardiac resynchronisation procedures [154].

Standard DE techniques acquire multiple 2D slices (M2D) covering the ROI over several breath-holds. The obtained images provide an excellent spatial resolution in-plane but poor scar visualisation along the slice encoding direction. Furthermore, data are acquired over multiple breath-holds which can be strenuous for patients. It can also lead to misregistration along the slice encoding direction due to varying breath-hold positions.

Recently, Peters et al. have shown that high resolution respiratory gated 3D DE images can overcome these problems and lead to a better image quality than 2D

breath-hold images [164]. Nevertheless, patients with myocardial scar often exhibit irregular breathing. As discussed previously this can lead to excessively long scan times which makes these MR scans clinical impracticable. Furthermore, long scan times have a negative effect on image quality due to contrast agent wash-out which changes the concentration of the contrast agent in the myocardium. For data acquired towards the end of the scan the initially determined inversion time T_I does not lead to optimal nulling of the healthy myocardium anymore which can cause image artefacts. Scan times around five minutes are recommended to avoid this effect [165]. Nguyen et al. propose to combine respiratory gated 3D DE imaging with the ideas of PAWS to achieve scan times below this limit [130, 166]. Nevertheless, they acquire images with a similar slice resolution as M2D breath-hold images and do not use the advantages offered by 3D high resolution scans.

Here we propose to acquire 3D high resolution DE data with HybridPAWS (see also chapter 4.2.3). A study of 38 patients suffering from heart failure shows, that HybridPAWS leads to a strong increase of navigator efficiency especially for patients with irregular breathing patterns. This ensures that 3D high resolution DE data can be obtained fast and without artefacts due to contrast agent washout. Our presented approach yields a similar in-plane image quality compared to a standard DE-M2D acquisition but with highly superior visualisation of scar tissue along the slice encoding direction.

7.2 Methods

7.2.1 HybridPAWS

The interleaved phase encoding scheme of HybridPAWS shown in Fig. 4.6 was combined with a 3D DE inversion sequence. An inversion pulse is applied to invert longitudinal magnetisation. The inversion time T_I between the inversion pulse and data acquisition is selected to optimally null signal from healthy myocardium. A pencil beam navigator signal is obtained prior to data acquisition as a respiratory surrogate. In order to ensure sufficient signal intensity of the diaphragm the signal at the location of the navigator is restored right after the inversion pulse. Data acqui-

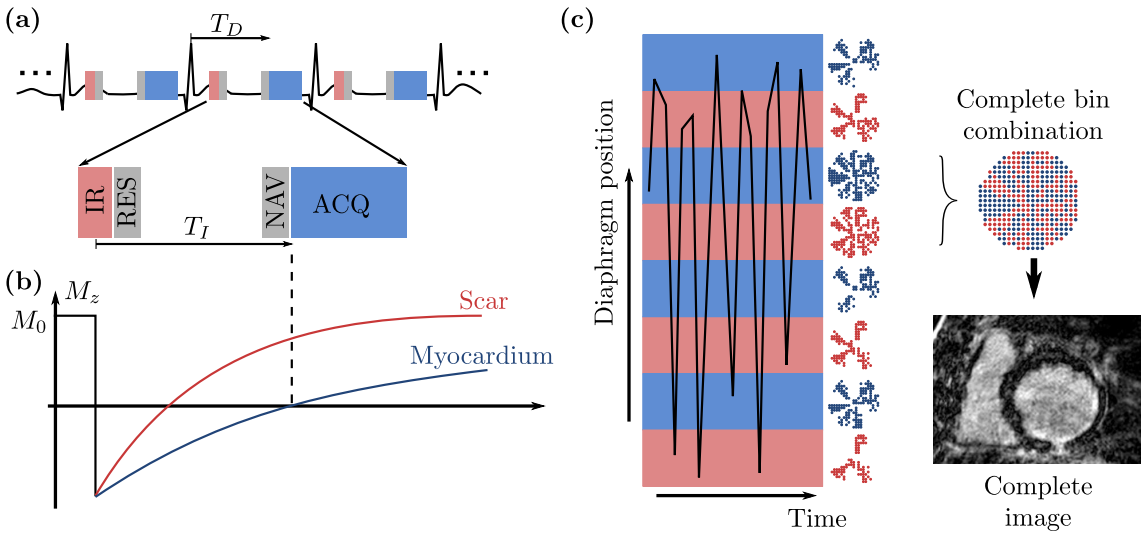

Figure 7.1: 3D delayed enhancement sequence combined with HybridPAWS. **(a)** Data acquisition is cardiac triggered with the trigger delay T_D. An inversion pulse (IR) inverts the longitudinal magnetisation. Signal at the location of the respiratory navigator (NAV) is restored (RES). Data is obtained after an inversion time T_I which is selected to optimally null healthy myocardium. **(b)** IR inverts the longitudinal magnetisation M_z. The administered contrast agent leads to a shortening of the T_1 time of scar tissue. Therefore, M_z of scar tissue (red) recovers faster than the longitudinal magnetisation of viable myocardium (blue). The inversion time T_I is set to optimally null signal from healthy myocardium. **(c)** HybridPAWS acquires data in multiple respiratory bins (red/blue bars) covering the entire amplitude of diaphragm movement. An interleaved phase encoding scheme is used which allows for the combination of data from two adjacent bins. Data acquisition is successfully finished if one combination of two bins leads to the desired k-space information and a complete image can be reconstructed.

sition is ECG triggered. Figure 7.1a,b depict the acquisition scheme and behaviour of the longitudinal magnetisation for healthy and fibrotic myocardium.

Similar to RPE-PAWS, HybridPAWS acquires data in multiple respiratory bins covering the entire amplitude of the respiratory signal. Data acquisition is successfully finished if one bin combination contains leads to the desired k-space information and a complete image is reconstructed (Fig. 7.1c).

7.2.2 Experiments

3D DE images were acquired in 38 heart failure patients using HybridPAWS with a resolution of 1.3 x 1.3 x 2.6 mm and a FOV of approximately 300 x 300 x 100 mm. Further parameters include flip angle of 25° and T_R/T_E of 5.4/2.6 ms. Parallel imaging was used with SENSE factors of 2 and 1.3 in phase and slice encoding

direction, respectively. The inversion time T_I for the inversion recovery sequences was selected individually for each patient based on a Look-Locker scan to ensure optimal nulling of the myocardium [167]. The total scan time was 3.8 min assuming a heart rate of 60 beats per minute and 100% navigator efficiency.

The 3D images obtained with HybridPAWS were compared to a standard M2D DE sequence. Data for each slice are acquired within one breath-hold using a FOV of 300 x 300 mm with a resolution of 1.56 x 1.87 mm and a slice thickness of 8 mm. The flip angle was 25° with T_R/T_E of 5.0/2.0 ms. A SENSE factor of 2 was applied in phase encoding direction. Both M2D and 3D data were acquired in a short-axis orientation during end-diastole.

A 32-channel cardiac phased array coil was used for signal reception and parallel imaging. All image data were reconstructed using a sensitivity encoding (SENSE) approach [7]. The necessary coil sensitivity information was obtained prior to the data acquisition.

Written informed consent was obtained from all participants and the study was carried out following an approved protocol from our local hospital.

7.2.3 Analysis

The navigator efficiency (NE) achieved with HybridPAWS was compared to a standard respiratory gating approach in real-time during data acquisition. NE was also analysed for patients with regular and irregular breathing separately. Patients with a NE below 40% for standard respiratory gating were considered to have irregular breathing patterns. Paired student t-tests were used to compare the results considering a p value smaller than 0.05 as statistically significant.

7.2.4 Results

Data acquisition was successfully finished in all patients. Look-Locker images were obtained prior to all DE acquisitions. Images acquired with a Look-Locker sequence are shown in Fig. 7.2.

Data acquisition with HybridPAWS led to an average respiratory navigator efficiency (NE) of 45% compared to 37.34% for a standard respiratory gating. The

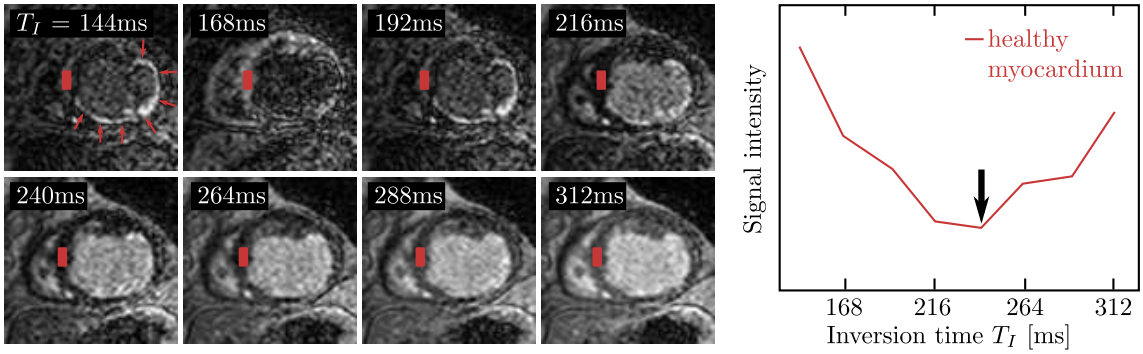

Figure 7.2: Results from a Look-Locker acquisition. **(a)** 2D Short axis images acquired with a Look-Locker sequence showing the change in contrast between healthy myocardium and scar tissue (red arrows). **(b)** Signal intensity from a ROI of viable myocardium (red rectangle in (a)) as a function of T_I. The inversion time was selected to minimize the signal from healthy myocardium (black arrow).

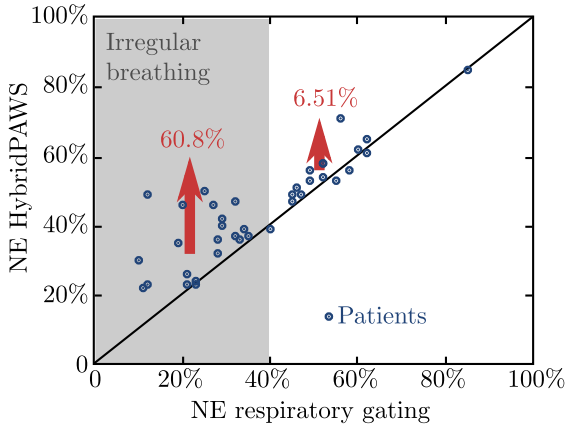

Figure 7.3: Comparison of navigator efficiency (NE) achieved with HybridPAWS and standard respiratory gating. HybridPAWS improves NE by 60.8% for patients with irregular (n = 22) and by 6.51% for patients with regular (n = 16) breathing patterns. Patients with NE below 40% for respiratory gating were considered to have irregular breathing.

main improvement is achieved for patients with low NE. Here NE was increased by 60.8% using HybridPAWS. Improvements of NE were shown to be statistically significant by a paired student t-test. A comparison of NE between HybridPAWS and the standard gating technique is shown in Fig. 7.3 and the results are also summarised in Tab. 8.1.

Figure 7.4 shows short-axis and reformatted images of M2D and 3D DE images for three patients with different respiratory patterns (i.e. different NE).

Table 7.1: Results of the patient study. HR: heart rate, bpm: beats per minute, ST: scan time, NE: navigator efficiency, ΔNE: difference of NE between HybridPAWS and Cartesian reference method (Cart).

		HybridPAWS		**Cart**		
	HR [bpm]	**ST [s]**	**NE [%]**	**ST [s]**	**NE [%]**	**ΔNE**[%]
1	84	8.93	0.35	16.45	0.19	84.21
2	56	8.79	0.46	20.22	0.2	130.00
3	72	14.02	0.26	17.36	0.21	23.81
5	56	11.16	0.42	16.16	0.29	44.83
6	57	18.42	0.30	55.26	0.1	200.00
7	57	11.76	0.47	17.27	0.32	46.88
8	85	6.58	0.39	6.42	0.4	-2.50
9	62	9.96	0.51	11.04	0.46	10.87
10	75	7.14	0.49	7.45	0.47	4.26
11	75	6.07	0.56	6.94	0.49	14.29
12	75	6.42	0.53	6.94	0.49	8.16
13	62	9.41	0.54	9.77	0.52	3.85
14	73	5.85	0.53	5.64	0.55	-3.64
15	68	5.44	0.71	6.89	0.56	26.79
16	85	4.59	0.56	4.43	0.58	-3.45
17	69	6.24	0.61	6.14	0.62	-1.61
18	93	6.77	0.50	13.55	0.25	100.00
19	48	29.83	0.22	59.66	0.11	100.00
20	64	15.38	0.32	17.58	0.28	14.29
21	74	9.85	0.36	12.67	0.28	28.57
22	48	20.83	0.39	23.90	0.34	14.71
23	54	12.15	0.40	16.76	0.29	37.93
24	57	12.45	0.37	14.39	0.32	15.63
25	63	10.62	0.36	11.58	0.33	9.09
26	58	9.24	0.49	37.72	0.12	308.33
27	60	8.57	0.49	9.33	0.45	8.89
28	56	9.54	0.58	10.64	0.52	11.54

Table 7.1: Results of the patient study. HR: heart rate, bpm: beats per minute, ST: scan time, NE: navigator efficiency, ΔNE: difference of NE between HybridPAWS and Cartesian reference method (Cart).

		HybridPAWS		**Cart**		
	HR [bpm]	**ST [s]**	**NE [%]**	**ST [s]**	**NE [%]**	**ΔNE**[%]
29	55	24.90	0.23	24.90	0.23	0.00
30	112	10.19	0.23	19.53	0.12	91.67
31	67	7.65	0.47	7.99	0.45	4.44
32	60	7.59	0.58	8.46	0.52	11.54
33	85	3.49	0.65	3.66	0.62	4.84
34	57	6.50	0.85	6.50	0.85	0.00
35	65	16.83	0.24	17.56	0.23	4.35
36	87	2.87	0.46	4.89	0.27	70.37
37	66	5.87	0.62	6.06	0.6	3.33
38	68	10.02	0.37	10.59	0.35	5.71

7.2.5 Discussion

HybridPAWS leads to a significant improvement in scan efficiency especially for patients with irregular breathing. This allows for a fast and reliable acquisition of 3D high resolution DE images. The in-plane image quality of these 3D data sets is comparable to a standard multi-slice 2D acquisition but with superior visualisation of scar tissue along the slice encoding direction.

Compared to the M2D images the 3D high resolution scan leads to a similar depiction of myocardial fibrosis in the acquired short axis orientation for patients with both regular (NE $>$ 40%) and irregular (NE $\leq$ 40%) breathing patterns.

Nevertheless, the poor spatial resolution along the slice encoding direction of the M2D images and possible misregistration between adjacent slices due to inconsistencies in the breath-hold positions strongly impairs the visualisation of scar tissue for images perpendicular to the SA orientation. The 3D high resolution scans do

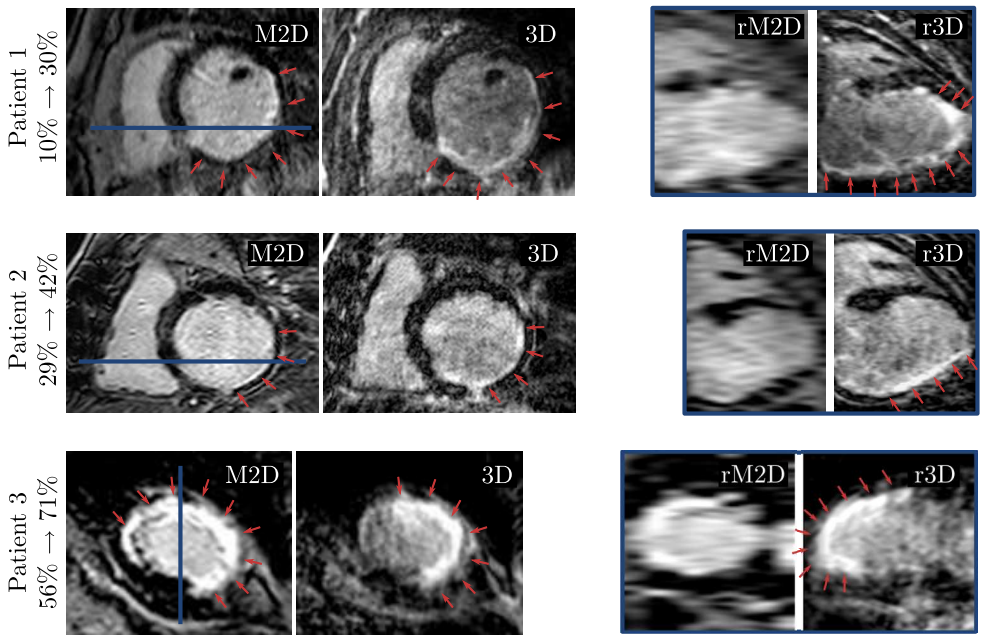

Figure 7.4: Multi-slice 2D (M2D) and 3D short axis images of three patients with different navigator efficiencies (NE). For patient 1 HybridPAWS led to an improvement in NE from 10% to 30%, for patient 2 from 29% to 42% and for patient 3 from 56% to 71%. Myocardial scar tissue (red arrows) is clearly depicted with both acquisitions. M2D and 3D data were reformatted (r) to long axis (LA) views. The blue line in M2D indicates the orientation of the reformatted data. The high resolution 3D images yield a superior depiction of scar tissue along the reformatted direction than the M2D data.

not suffer from such effects. Reformatted images show a similar image quality independent of the image orientation.

One limitation of this study is that the temporal order of DE 3D and M2D scans was not randomized. The M2D scan was part of a standard clinical protocol and therefore it was always acquired before the 3D images which could lead to a systematic difference in scar visualisation which was not accounted for.

Due to their smaller voxel size and higher acceleration factors the 3D high resolution images can exhibit lower SNR than the M2D images. Nevertheless, the 3D data sets allow for the retrospective averaging of adjacent slices to improve SNR without losing the ability to reformat data.

SNR could also be improved by retrospectively combining data from different respiratory phases. Here only one complete image was reconstructed from data obtained with HybridPAWS. Especially for patients with irregular breathing, a high amount of data is acquired in all non-complete bins. Results from the scan simulation in chapter 4 suggest that these non-complete bins yield images with very poor image quality. Nevertheless, a more advanced reconstruction approach such as compressed sensing could strongly improve the quality of these non-complete images [9]. This could allow for motion estimation and correction between images from different respiratory bins. Complete and non-complete images could then be combined to enhance image quality even further [168].

7.3 Conclusion

In this patient study we have shown that HybridPAWS reduces scan times on average by 60% for patients with irregular breathing compared to a standard respiratory gating method. More than 60% of patients showed irregular breathing patterns which emphasises how important an efficient method to minimize respiratory motion artefacts is especially for patients suffering from cardiovascular disease.

Our method ensures fast and reliable 3D high resolution assessment of myocardial scar. Images are reconstructed with FFT and therefore long reconstruction times not applicable in patient scans or the requirement of additional reconstruction hardware are avoided.

8 | Image-Based Self-Navigator using Cardiac Functional Parameters for Cine Imaging

8.1 Introduction

MRI can provide important functional cardiac information such as ventricular volume or ejection fraction [37]. Real-time imaging has been proposed for ventricular assessment [105] but it suffers from low SNR and strongly restricts spatial and temporal resolution. Therefore, cine imaging is more commonly used which acquires data in a segmented retrospectively gated approach using an external ECG signal (see also chapter 3.3.1). Data are obtained over multiple cardiac cycles and for the final image reconstruction data from different cardiac cycles but same cardiac phase are combined.

As discussed previously certain medical conditions of patients, such as arrhythmia, can lead to altered and weakened ECG signals which can sometimes make it difficult to accurately detect the necessary R-waves [169]. Cardiac self-navigators have been proposed to overcome this problem [113].

The majority of these techniques relies on the change of the overall signal intensity due to increases and decreases of the blood volume during the cardiac cycle [112,170–172]. This leads to amplitude modulations of central k-space values which can be measured and provide a cardiac navigator signal. Other approaches extend this idea and monitor changes of 1D projection images during the cardiac

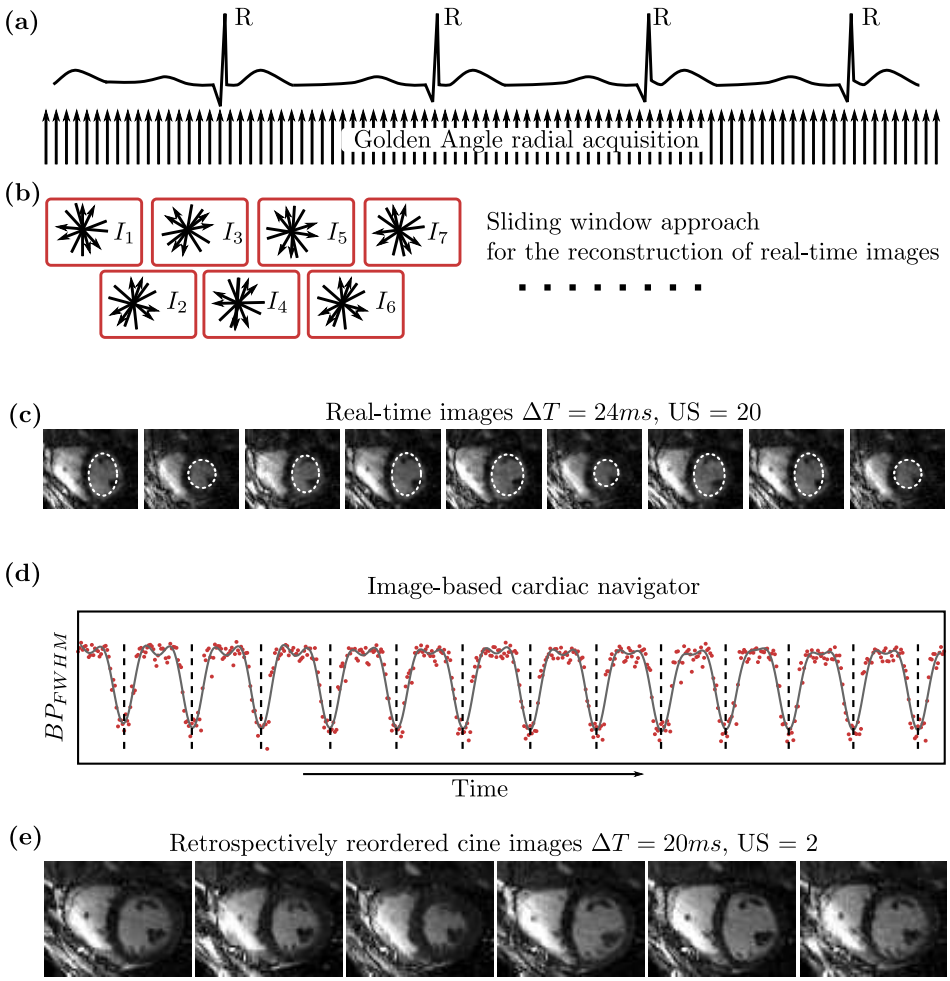

Figure 8.1: Overview of the presented image-based cardiac navigator approach. **(a)** Data are acquired over multiple cardiac cycles with a 2D Golden Angle radial sampling scheme. **(b)** A sliding window approach is used to reconstruct undersampled real-time images (I_n) with a high temporal resolution (ΔT). **(c)** In each of the real-time images the full-width at half-maximum (FWHM) of the LV blood pool (white dotted circles) is determined. **(d)** This yields a quantitative functional cardiac gating signal (red dots) which provides information about the timing of the different cardiac cycles (dashed lines). **(e)** Based on the image-based cardiac navigator the obtained k-space data can be retrospectively reordered and cine images with high temporal and high spatial resolution without noticeable undersampling artefacts can be reconstructed. US undersampling factor. BP_{FWHM} mean temporal change of the full-width at half-maximum of the LV blood pool.

cycle [173]. The main limitation of these techniques is that they cannot accurately distinguish between changes of the blood pool due to cardiac motion and other effects which lead to signal variations such as inflow effects.

Furthermore, both ECG and cardiac self-navigators derive gating signals from signal changes which are correlated with cardiac motion but do not measure the movements of the ventricles directly.

Here we present a new method which derives an image-based cardiac navigator signal directly from cardiac function using 2D real-time images obtained with a Golden Angle radial sampling scheme. The navigator signal allows for the retrospective combination of data from different cardiac cycles and the reconstruction of MR cine images with high temporal resolution without noticeable undersampling artefacts (Fig. 8.1). In contrast to standard cine imaging, data acquisition with this approach is highly flexible and does not require a prospective setting of cardiac phases or prospective arrhythmia rejection techniques.

8.2 Methods

8.2.1 Data Acquisition Scheme

Data is acquired with a Golden Angle (GA) radial trajectory (Fig. 8.2a, see also chapter 2.3.2) which leads to a homogeneous covering of k-space over time. It allows for the retrospective combination of arbitrary radial lines and offers great flexibility for retrospectively gated cine imaging (Fig. 8.2b) [71]. In contrast to Winkelmann et al. [71] data obtained with our approach were retrospectively reordered, i.e. data from different cardiac cycles but the same cardiac phase are retrospectively combined for the final image reconstruction.

8.2.2 Image Reconstruction

All images were reconstructed offline using Matlab (The MathWorks, Inc., Natich, MA, USA) with a non-Cartesian iterative SENSE reconstruction scheme [94]. The necessary coil sensitivity information was obtained from the data itself. Due to the sampling properties of the GA trajectory, all radial lines acquired for each slice

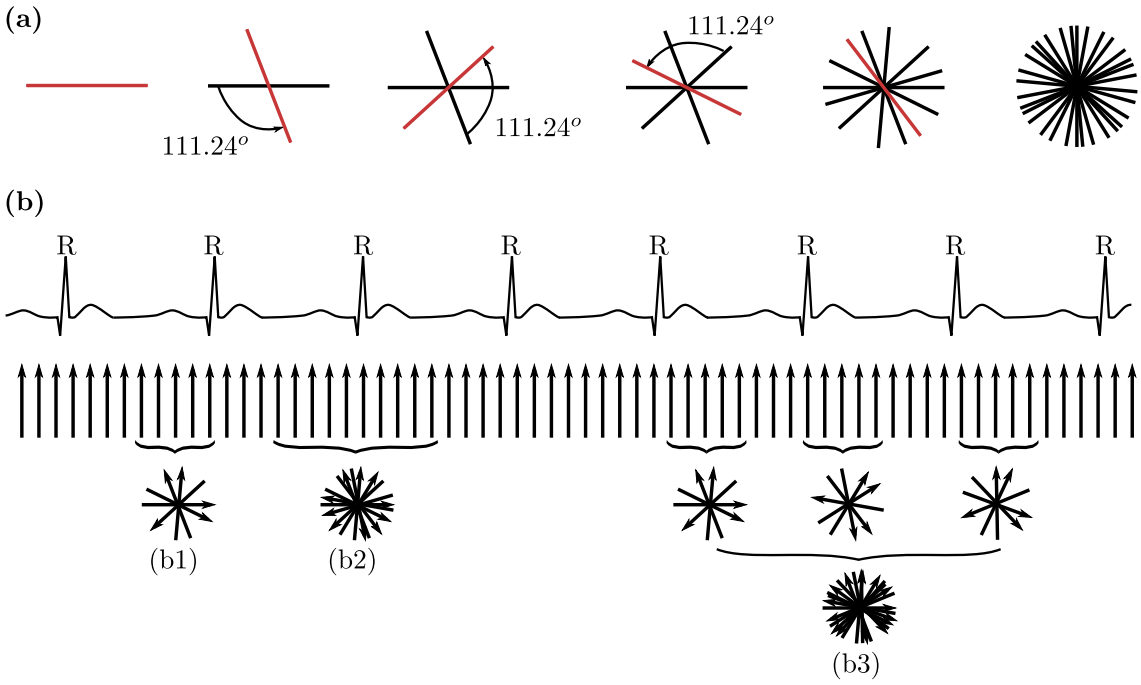

Figure 8.2: 2D Golden Angle (GA) radial sampling scheme. **(a)** For a 2D GA radial k-space trajectory successive radial lines are tilted by 111.24°. This leads to a homogeneous filling of k-space over time. **(b)** As already discussed by Winkelman et al., the 2D GA sampling schemes allows for the combination of an arbitrary number of radial lines (b1 and b2) [71]. Furthermore, data obtained at different time points are complimentary and can be combined (b3) for image reconstruction.

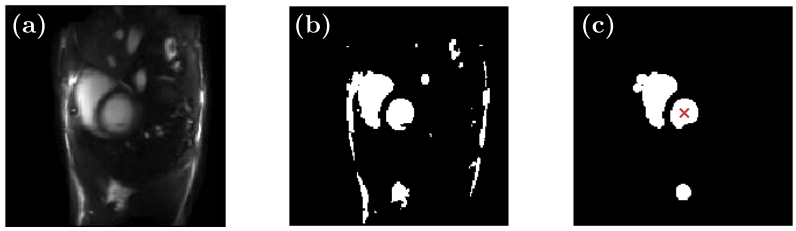

Figure 8.3: Automatic identification of the left ventricular blood pool. **(a)** Temporal mean of all real-time images. **(b)** A binary image is created based on a greyvalue threshhold. **(c)** After applying morpholigical opening and closing operations the LV blood pool is identified (red cross).

are complimentary and can be combined in the most optimal way. This yields a highly oversampled temporal average of the ROI. This image data can be used to determine high quality coil sensitivity information without the need of additional data acquisition.

8.2.3 Image-based Cardiac Navigator (IBCN)

The image-based cardiac navigator (IBCN) signal is determined in image space as the temporal change of the LV blood pool diameter. Real-time images are reconstructed with high temporal resolution using a sliding window approach. These images show the heart during multiple cardiac cycles at discrete time points t.

The centre of the LV is determined in a composite image caculated as the temporal mean of all real-time images. Morphological operations are applied to identify the blood pool of the LV and its centre is calculated as the centre of mass of the LV blood pool (Fig. 8.3).

In each of the real-time images the image intensity values are determined along diagonal lines through the centre of the LV blood pool. This is carried out for NP lines rotated by $\frac{\pi}{NP}$ to each other in order to cover the entire LV homogeneously (Fig 8.4a,b). In this study NP was set to 60.

The data describing the blood pool of the LV is determined automatically and any impairing signals from the RV or other surrounding tissue are removed. In all NP profiles the full-width at half-maximum (FWHM) of the LV blood pool is determined (Fig 8.4c). The final image-based cardiac navigator BP_{FWHM} is calculated as the

mean over all NP FWHM values (Fig 8.4d)

$$BP_{FWHM}(t) = \frac{1}{NP} \sum_{n=1}^{NP} FWHM(NP, t) \tag{8.1}$$

and describes the mean temporal changes of the FWHM of the LV blood pool as a function of time.

8.2.4 Retrospective Reordering of *K*-Space Data

In order to achieve both high spatial and high temporal resolution and avoid any undersampling artefacts, data for the final image reconstruction are retrospectively reordered. For this reference points S_n for each cardiac cycle are determined as the maximum of systolic contraction (i.e. smallest FWHM of the LV blood pool). A low-pass filter with a cutoff frequency of 3.72 Hz is applied to the image-based navigator signal and S_n are calculated as the local minima of this fit (Fig. 8.5a).

Each acquired radial profile is assigned a time stamp relative to S_n similar to a standard cine scan using an external ECG signal (see also chapter 3.3.1). In order to compensate for heart rate variations the time stamps are scaled according to equation (3.2).

The acquired data are resorted according to their time stamp and the final images are reconstructed from these reordered k-space data (Fig. 8.5b-d). To ensure constant time intervals between successive cine images Cartesian k-space data is interpolated in the time domain for a standard retrospective reorderding approach. This is not possible in the same way for the Golden Angle radial acquisition scheme used in this study because a different radial profile is obtained at each time point. Therefore, a temporal interpolation could only be carried out using data at neighbouring but not the same k-space points as for the Cartesian cine acquisition. Nevertheless, the number of radial lines used for each cine image can be adapted in order to obtain cine images at regular time intervals.

Due to the sampling properties of the Golden Angle acquisition, the number of cardiac phases does not have to be chosen prior to the data acquisition.

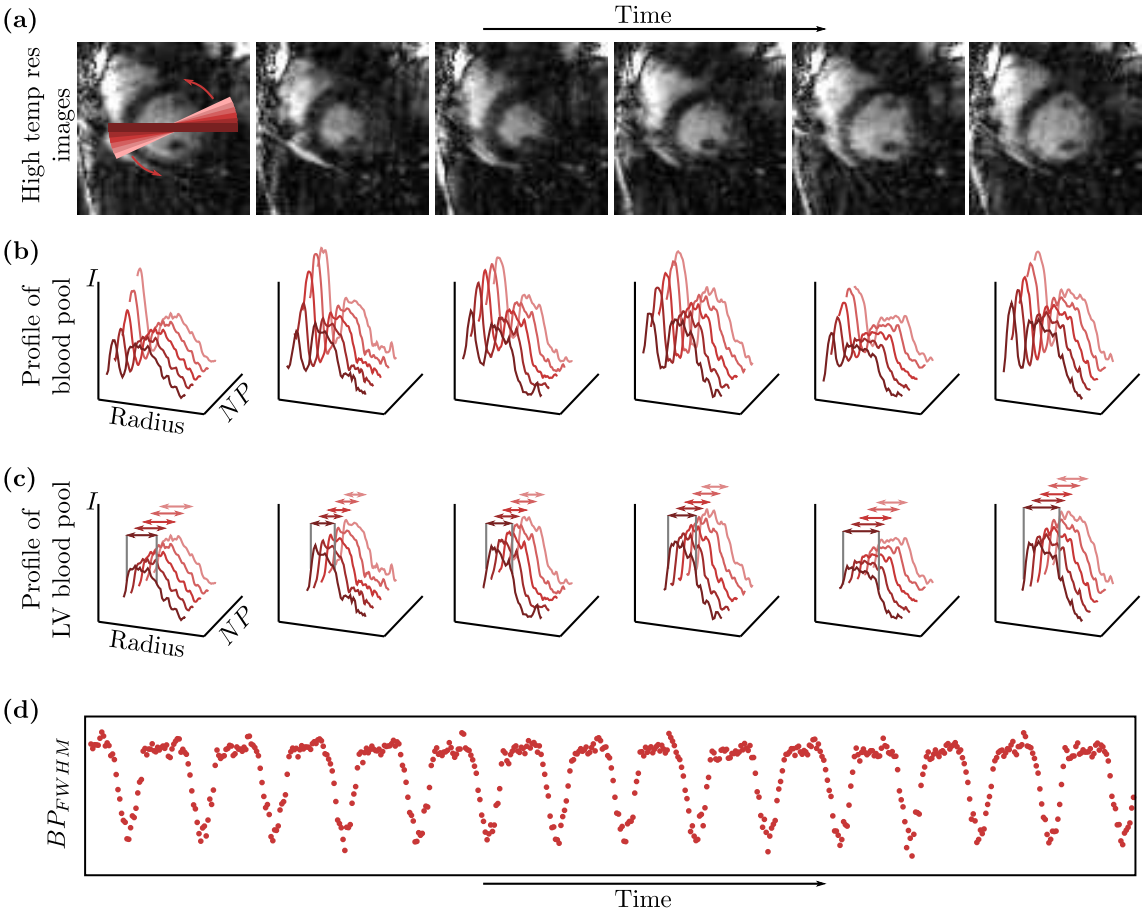

Figure 8.4: Image-based cardiac navigator. **(a)** The image intensity values (I) along lines through the centre of the LV (red bars) are obtained for NP different lines in each of the high temporal resolution real-time images. **(b)** This yields NP profiles of the blood pool as a function of the radius for each time point. **(c)** The blood pool of the LV is detected automatically and any other impairing signal is removed. The full-width at half-maximum (FWHM) of each profile is determined and represents the change of the blood pool over time due to cardiac contraction and relaxation. **(d)** The final image-based cardiac navigator signal is calculated as the mean FWHM of the LV blood pool (BP_{FWHM}) over all NP FWHM values for each time point. This leads to a image-based cardiac navigator signal describing the mean temporal changes of the FWHM of the LV blood pool.

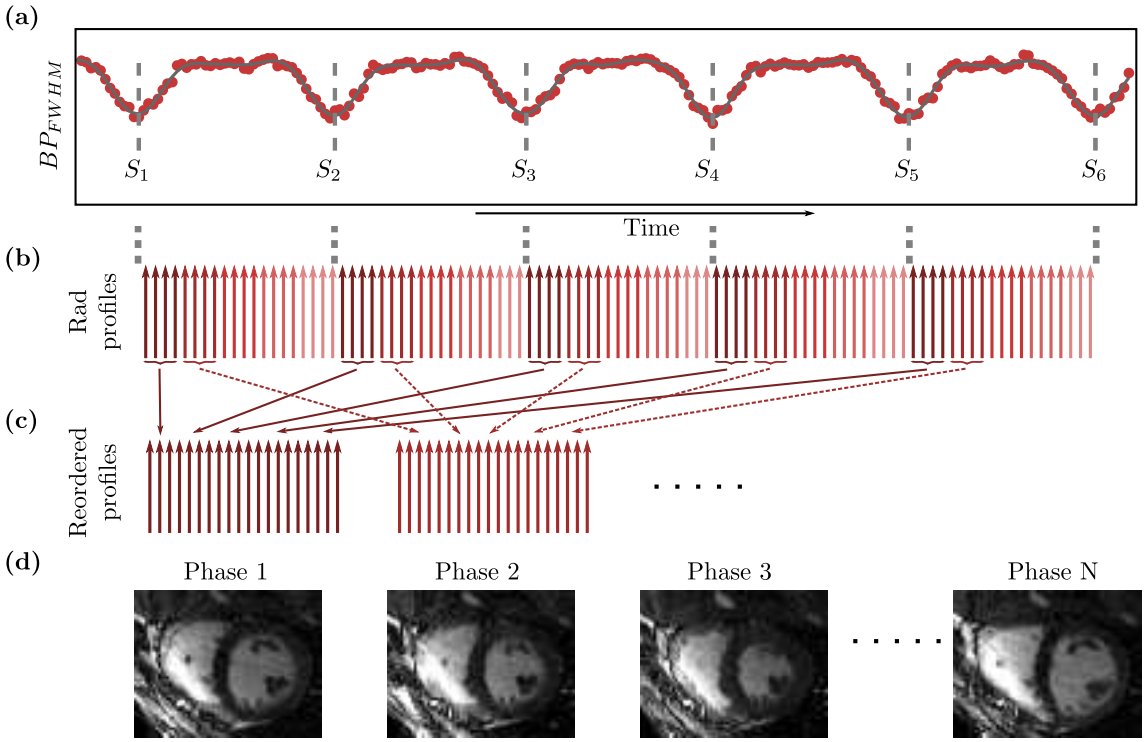

Figure 8.5: Retrospective reordering of k-space data and final image reconstruction. **(a)** The obtained IBCN signal describing the mean FWHM of the blood pool over time (red dots) is low-pass filtered (grey line) and the local minima describing the maximum of systolic contraction (grey dashed lines, S_n) are identified as reference points for each cardiac cycle. **(b)** According to S_n each obtained radial line is assigned a timestamp depending on its temporal position within each cardiac cycle (i.e. its cardiac phase). **(c)** Radial profiles from different cardiac cycles but same cardiac phase are retrospectively combined. **(d)** Final image with high temporal and high spatial resolution without any visible undersampling artefacts are reconstructed. BP_{FWHM} mean temporal change of FWHM of the LV blood pool.

8.3 Experiments

A 2D Golden Angle radial sampling scheme was implemented on a 1.5T MRI scanner (Philips Medical System, Best, The Netherlands). With this method short axis images at three different positions in the LV were acquired in five healthy volunteers: bSSFP sequence, FOV: 320 x 320 mm, 2 mm^2 in plane resolution, 8 mm slice thickness, 60° flip angle, TR/TE = 3.0/1.49 ms. Each slice was acquired over a 18 seconds breath-hold in order to have a large number of cardiac cycles available for analysis. A 32-channel cardiac phased array coil was used for signal reception and parallel imaging. Written informed consent was obtained from all participants and the study was carried out following an approved protocol from our local hospital.

The quality of the real-time images is expected to affect the accuracy of the IBCN signal. For real-time images with a very high temporal resolution undersampling artefacts might negatively impair the IBCN. Real-time images with a low temporal resolution show very few undersampling artefacts but their temporal resolution might not be sufficient to accurately describe rapid changes of the ventricle.

In order to optimise the trade off between high temporal resolution and low undersampling artefacts for the accuracy of the IBCN, real-time data sets with temporal resolutions ranging from 12 ms (i.e. 8 radial lines, sliding window approach, window shift of 4 radial lines) to 48 ms (i.e. 32 radial lines, sliding window approach, window shift of 16 radial lines) were obtained in two volunteers with different heart rates. The temporal resolution leading to the highest accuracy of IBCN was then applied to all further experiments.

The IBCN signals were used to retrospectively reorder the obtained k-space data. This allowed for the reconstruction of 50 cardiac phases each from 240 radial lines (sliding window approach, window shift of 120 radial lines) which have a similarly high temporal resolution as the real-time images but without noticeable undersampling artefacts. The final temporal resolution of the cine data depends on the mean heart rate of the subject which also applies to a standard ECG gated approach.

8.4 Analysis

The accuracy of the image-based navigator was calculated by comparing the obtained S_n to the R-peaks (R_n) determined by the MR scanner from a standard ECG signal which was recorded parallel to the data acquisition.

As discussed in chapter 3.2 the R-peak occurs prior to the minimum of systolic contraction. This temporal delay M_{IBCN} can be described by the temporal difference between R_n and S_n

$$M_{IBCN} = \frac{1}{N_R} \sum_{r=1}^{N_R} (S_r - R_r) \tag{8.2}$$

where N_R is the number of RR intervals for each slice. In order to assess the reproducibility of the IBCN signal for different slice locations M_{IBCN} was compared between different slices for each volunteer.

The accuracy of the IBCN signal was calculated as the standard deviation E_{IBCN} between R_n and S_n for each slice

$$E_{IBCN} = \sqrt{\frac{1}{N_R} \sum_{r=1}^{N_R} \left((S_r - R_r) - M_{IBCN} \right)^2} \quad . \tag{8.3}$$

Furthermore, the largest difference MAX_{IBCN} between S_n and M_{IBCN} was also determined to estimate the maximum error between IBCN and the standard ECG signal.

The quality of the final retrospectively reordered images was assessed using spatial-temporal plots of the blood pool.

8.5 Results

Data was acquired successfully in all volunteers and a reliable IBCN signal could be obtained from all data sets.

Figures 8.6a and 8.6b show M_{IBCN}, E_{IBCN} and MAX_{IBCN} as a function of different temporal resolutions of the real-time images for two volunteers with a low (55 bpm) and a high heart rate (76 bpm), respectively. In both cases real-time images with a temporal resolution ΔT below 20 ms start to show significant undersampling artefacts which obscure the blood pool signal and therefore negatively impair the

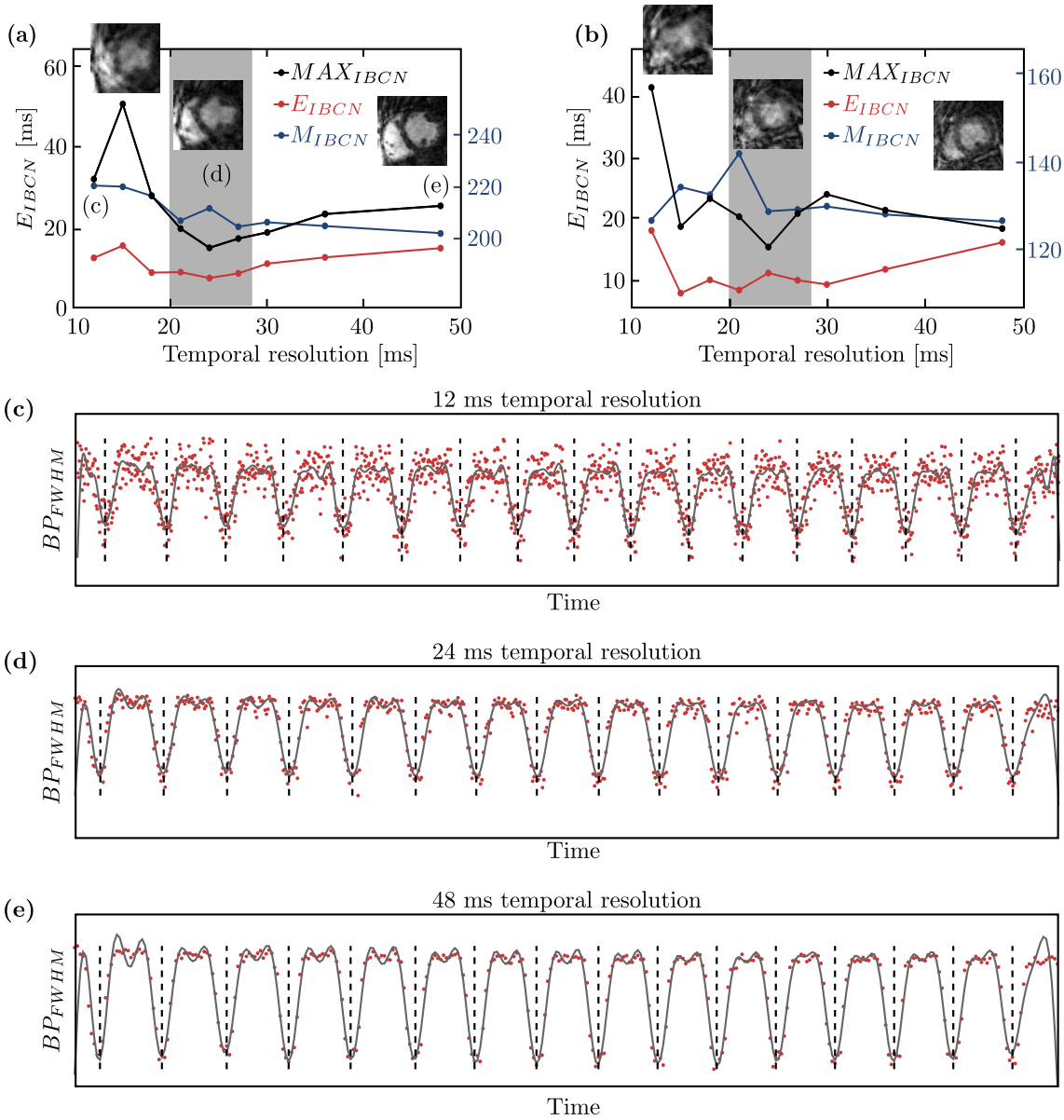

Figure 8.6: Accuracy of the IBCN compared to a standard ECG signal for different temporal resolutions of the real-time data for a volunteer with heart rate of **(a)** 55 bpm and **(b)** 76 bmp. The temporal delay (M_{IBCN}), the standard deviation (E_{IBCN}) and maximum error (MAX_{IBCN}) between the IBCN and ECG signal are plotted. Furthermore, real-time images with a temporal resolution ΔT of 12, 24 and 48 ms are shown. For the volunteer in (a) three different IBCN signals are depicted (red dots) including their low-pass filtered signals (grey line) and the determined minima of systolic contraction (dashed lines) for temporal resolutions of **(c)** 12, **(d)** 24 and **(e)** 48 ms. For ΔT lower than 20 ms undersampling artefacts strongly impair the image-quality which leads to strong noise in the IBCN signals. Although real-time images obtained with ΔT larger than 40 ms show a very good image quality, fast systolic changes of the LV cannot be described accurately anymore which decreases the accuracy of IBCN. A temporal resolution between 20 and 30 ms provides a good trade off between high temporal resolution and low undersampling artefacts (grey area). M_{IBCN} shows very little variation for different temporal resolutions. BP_{FWHM} mean temporal change of FWHM of the LV blood pool.

obtained IBNC. This leads to very noisy IBNC signals (Fig.8.6c). A ΔT larger than 40 ms leads to high quality real-time images and a smooth IBNC signal (Fig.8.6e). Nevertheless, this temporal resolution does not seem to be sufficient anymore to accurately describe fast systolic contraction and therefore leads to an increase of E_{IBCN}. The delay between S_n and M_{IBCN} does not seem to be affected by the different temporal resolutions. Real-time images with ΔT between 20 and 30 ms provide a good trade off between high temporal resolution and low undersampling artefacts. Figure 8.6d depicts IBCN for a temporal resolution of 24 ms where fast systolic contraction and a flattening of diastolic expansion towards end-diastole are clearly visible.

For all further image reconstruction a temporal resolution of 24 ms was chosen for the real-time data. This led to an average value of E_{IBCN} over all subjects of 15.9 ($\pm$ 5.3) ms, which is below the temporal resolution of IBCN. The mean delay M_{IBCN} between the R-peaks detected by the scanner using an external ECG device and S_n obtained in the IBCN signal varied by up to 74 ms for different slice locations in the same volunteer. The results for each of the volunteers is summarised in Tab. 8.1.

Retrospectively gated cine images using the IBCN signals for three volunteers are depicted in Fig. 8.7 for three different volunteers. In addition temporal-spatial plots are also shown.

8.6 Discussion

We have presented an image-based navigator technique which yields a cardiac gating signal directly from the motion of the LV during the cardiac cycle. The obtained IBCN signal is shown to have an accuracy below 20 ms. It allows for the retrospective reordering of the acquired data which yields high quality cine images.

The accuracy of the IBCN signals depends on the temporal resolution of the real-time images. Nevertheless, the results shown in Fig. 8.6 suggest that the accuracy of IBCN changes very slowly with increasing or decreasing temporal resolution. Therefore, the selection of a certain temporal resolution has only little effect on the accuracy of the IBCN signal and even a suboptimal temporal resolution leads to a

Table 8.1: Results of the volunteer study. The RR cycle length (mean±standard deviation), temporal delay (M_{IBCN}), the standard deviation (E_{IBCN}) and maximum error (MAX_{IBCN}) between the ECG and the proposed image based cardiac navigator are shown for three slices in each volunteer. All values are given in milliseconds.

		RR length	$\mathbf{M_{IBCN}}$	$\mathbf{E_{IBCN}}$	$\mathbf{MAX_{IBCN}}$
Volunteer 1	1	1089 ±10	254 .2	16.5	34.2
	2	1037 ±35	194.9	16.3	27.4
	3	987 ±21	178.7	10.67	22.53
Volunteer 2	1	928 ±81	114.6	9.8	17.5
	2	987 ±122	86.4	13.2	21.7
	3	960 ±89	95.6	9.5	18.5
Volunteer 3	1	881 ±66	137.5	11.4	21.7
	2	948 ±30	148.3	13.0	23
	3	922 ±45	160.8	16.3	31.5
Volunteer 4	1	803 ±39	187.2	18.2	35.1
	2	911 ±31	165.5	11.3	17.8
	3	916 ±48	156.5	16.1	50.8
Volunteer 5	1	863 ±47	122.7	22.4	36.5
	2	856 ±75	128.7	26.8	56.5
	3	835 ±50	128.0	13.7	28.2
Volunteer 6	1	782 ±20	135.2	13.4	24.0
	2	733 ±23	149.1	26.8	46.2
	3	771 ±29	166.0	20.8	38.6

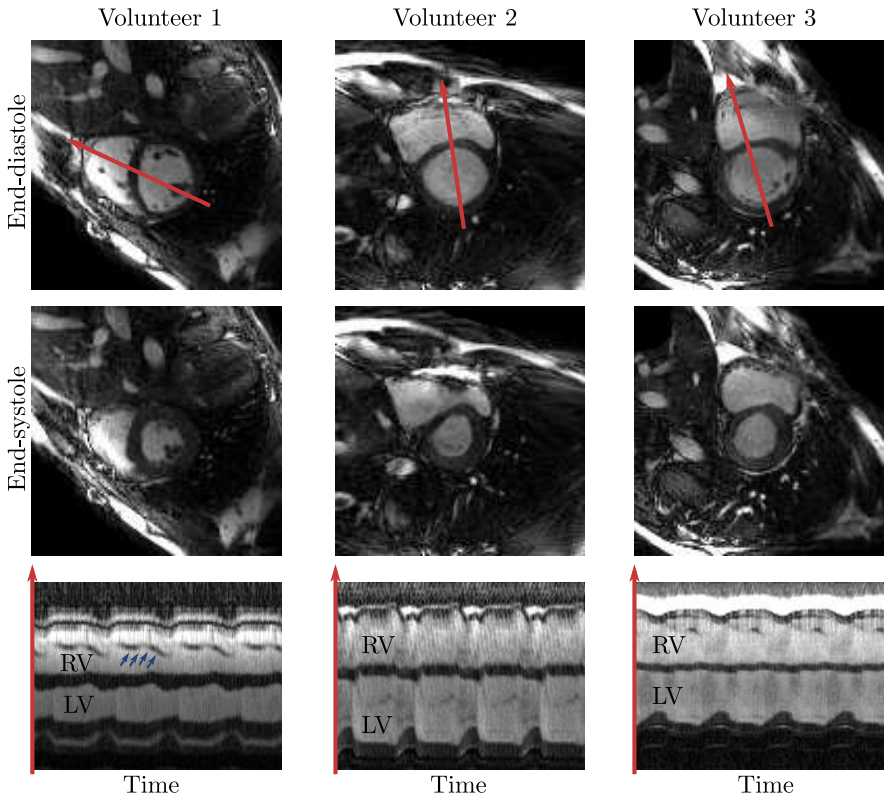

Figure 8.7: Retrospectively reordered images of diastole and systole for three different volunteers at different locations in the ventricle. In addition spatial-temporal plots are shown which depict the behaviour of a lineplot (red arrow in end-diastole images) over time. They clearly show the contraction and expansion of the RV and LV during cardiac cycles. Furthermore, small structures such as papillary muscles (blue arrows) are accurately depicted without any visible blurring.

very accurate IBCN. Furthermore, due to the undersampling properties of the GA radial sampling scheme, the temporal resolution does not have to be selected prior to the data acquisition. This allows for a retrospective optimisation of the IBCN signal.

The heart rate variability varied strongly between different subjects (Tab. 8.1). For volunteer 2 the heart rate variability is almost four times larger than for volunteer 1. Nevertheless, both E_{IBCN} and MAX_{IBCN} were slightly lower vor volunteer 2 which suggests that the accuracy of the IBCN is not influenced by the heart rate variability.

Here we have only used a short axis orientation of the obtained images as this is the most common image orientation for functional assessment. Nevertheless, our approach could be applied to any image orientation which shows the behaviour of the blood pool during the cardiac cycle.

The scan times used for the in-vivo studies are longer than for standard cine MRI. The length of each acquisition was selected to achieve a larger number of cardiac cycles for the evaluation of the IBCN signal rather than to optimise scan time. Furthermore, from the data presented in this chapter 50 cardiac phases were reconstructed for each slice. For patient scans usually only 30 cardiac phases are used. Reducing the number of obtained cardiac phases to 30 without changing the number of radial k-space lines for each phase would lead to a scan time of 10.8 seconds per slice which is similar to standard cine MRI scans.

As discussed before the most common approach to compensate for arrhythmic heart beats during data acquisition is to reject and reacquire data if the length of the cardiac cycle is outside a predefined window. Although this provides a reliable, robust and easy to implement approach to deal with arrhythmic heartbeats, it can lead to unacceptable long scan times or even scan abortions.

The functional information obtained with our method could provide new approaches to address arrhythmic heart beats. So far the minimum of systolic contraction was used as a reference point for each cardiac cycle. This allowed for an accurate and reliable reordering of acquired k-space data. Nevertheless, the image-based cardiac navigator signal provides real-time functional information of the heart which has the potential for much more advanced data reordering schemes. It could

be used to form a cardiac motion model which would allow for the correction of irregularities in the cardiac cycle instead of a simple data rejection. Furthermore, our presented approach is not limited to the reconstruction of a single series of cine images. Reconstructing data acquired during regular and arrhythmic heart beats separately could provide important information about pathological changes of the cardiac cycles.

One limitation of the GA sampling scheme is that after the retrospective ordering the homogeneous distribution of the k-space cannot be ensured anymore. Nevertheless, due to the high number of radial lines used for the reconstruction of the cine images this only leads to streaking artefacst which seem hardly visible and are not likely to impair the diagnostic quality of our images. Furthermore, we believe that the highly advantageous sampling properties of GA radial trajectories outweigh this limitation.

The mean delay between R-peaks determined from the external ECG and the systolic minima obtained from the image-based navigator signals varies strongly between different slice locations. This indicates that although our approach yields a highly accuracy cardiac gating signal it does not provide a global gating signal which allows for the synchronised combination of multiple slices. Nevertheless, this is a general problem of every self-navigation technique used for M2D scans.

One possibility to overcome this limitation would be to use a dual-slice excitation pulse to obtain data from two independent slices in parallel. An IBCN signal can be obtained from one slice which is kept at a constant location in the centre of the ventricle. This is then used to retrospectively reorder the data acquired in the second slice which can be moved to cover the entire ventricle. This approach will be discussed in more detail in the following chapter.

In addition to a cardiac gating signal also respiratory motion information can be obtained from the real-time images. This would allow for a free-breathing data acquisition using respiratory gating and motion compensation to minimise motion artefacts. Figure 8.8 shows examples of real-time images obtained with our presented method during free-breathing. These images were reconstructed with a temporal resolution of 210 ms. Registering images from the same cardiac phase and different cardiac cycles would yield a respiratory navigator signal which could be used for

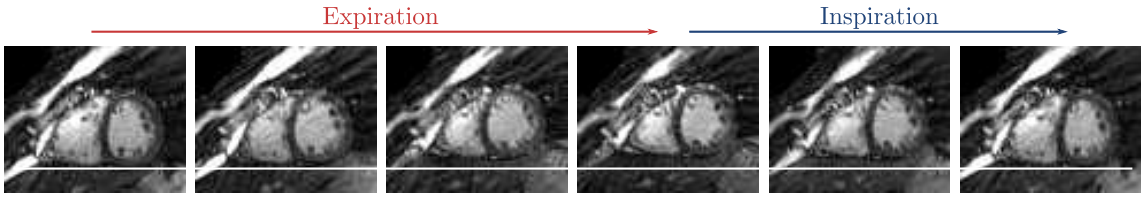

Figure 8.8: Real-time images depicting the ventricles during one respiratory cycle. This shows that with our presented method both a cardiac and respiratory image-based self-navigator signal can be obtained. Data were acquired with the same scan parameters as the breath-hold data described in the 'Experiments' section of this chapter. Images were reconstructed with a temporal resolution of about 200 ms and for each cardiac cycle only one image at mid-diastole is displayed similar to [174].

respiratory gating and/or motion compensation similar to the approach detailed by Hansen et al. in [174].

8.7 Conclusion

We have presented a method which derives a cardiac gating signal directly from the motion of the left ventricle with accuracies below the temporal resolution of the real-time data. High quality retrospectively reordered cine images are reconstructed based on the IBCN signals.

Our approach does not require any arrhythmia rejection techniques during data acquisition. The obtained IBCN signal would allow not just for the detection of cardiac arrhythmias but also for their quantification. Furthermore, the highly flexible data acquisition yields not just retrospectively gated cine images from data acquired in regular cardiac cycles but also high quality real-time images showing irregular heartbeats could be obtained. This could yield further information to characterise the heart functionality of arrhythmia patients.

In order to extend the presented approach to a multi-slice 2D acquisition covering the entire ventricle it is combined with a dual slice excitation scheme which is discussed in the following chapter.

9 Cardiac Function Assessment without ECG Using Image-Based Navigation

9.1 Introduction

As already discussed in the previous chapter cardiac self-navigation techniques have been proposed to avoid the need of external ECG signals [113]. They mainly rely on signal changes of central k-space points or variations of the cross-correlation values in selected region of interests.

Therefore, they require a detectable periodic signal change in each image slice. This requirement is not necessarily fulfilled for apical slices where the blood pool can only be visible during late diastole. In addition, the complex blood flow close to the valve plane could also lead to inaccuracies of the self-navigator signal. Furthermore, these techniques obtain the gating signal from each slice individually and therefore, it is not guaranteed that the self-navigator signals are synchronised between different slices. This limitation has also been emphasised by the results of the previous chapter. The proposed image-based cardiac navigator (IBCN) signal provided a highly accurate alternative to ECG signals. Nevertheless, although the accuracy of the IBCN did not vary according to the current slice position, the relative shift between IBCN and an external ECG signal showed a dependency on the slice location. This

would prevent the synchronisation of slices of an M2D acquisitions required for a functional assessment of the heart.

Here we overcome this limitation by acquiring an image and a navigator slice simultaneously using radial CAIPIRINHA (radCaipi) [175] with a Golden Angle sampling order [71]. During a M2D acquisition, the navigator slice is kept at a constant position centred between apex and valve plane and the image slice is moved to cover the entire ventricle. From the navigator slice the IBCN signal is obtained directly from cardiac function as shown in chapter 8. This approach guarantees that the same accurate navigator signal is available for all slices which avoids any position dependent variations. The navigator signal allows for the retrospective combination of data from different cardiac cycles and the reconstruction of high temporal and spatial resolution MR cine images acquired from the image slice. An overview of the proposed method is given in Fig. 9.1.

9.2 Methods

The technique presented here is a combination of a dual-slice RF excitation using the ideas of radial CAIPIRINHA [175] to separate the signal from the two excited slices, and the image-based cardiac navigator (IBCN) approach presented in the previous chapter. It can be separated into five main steps

- simultaneous excitation of a navigator and an image slices
- 2D Golden Angle radial data acquisition
- signal separation of navigator and image slice
- obtaining an image-based cardiac navigator (IBCN) based on functional information of the LV from the navigator slice
- retrospective reordering of k-space data from the image slice and reconstruction of final cine images with high temporal resolution

which will be discussed in the following in more detail.

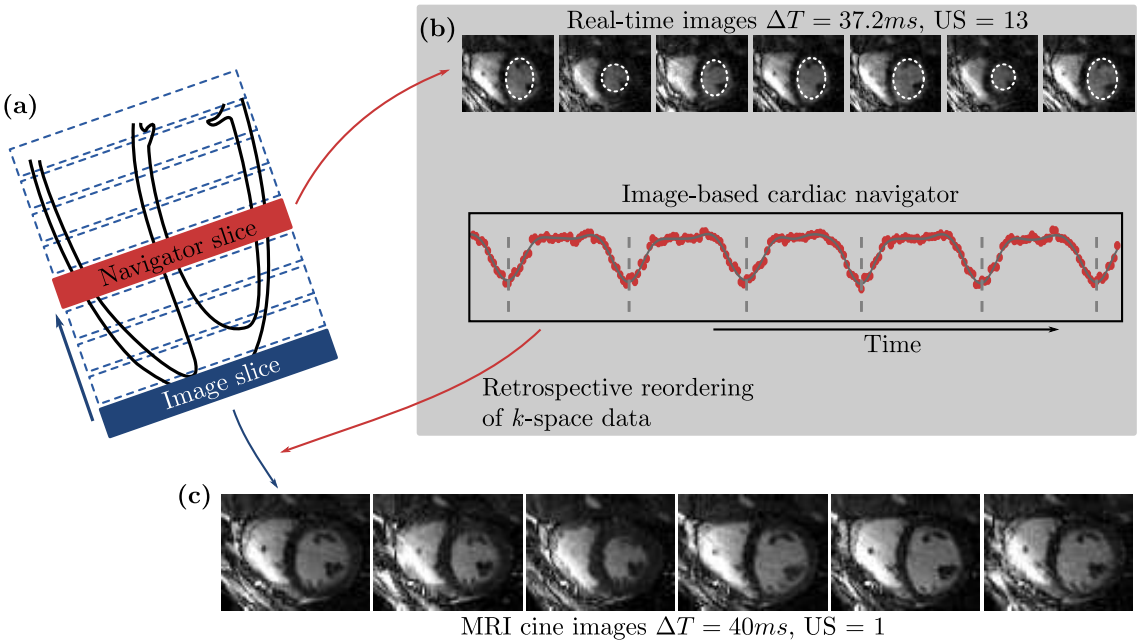

Figure 9.1: Overview. **(a)** A dual-slice excitation pulse is used to obtain data both from a navigator slice and an image slice simultaneously. While the image slice is moved over the entire left ventricle, the position of the navigator slice is kept constant. **(b)** A image-based cardiac navigator (IBCN) signal is obtained from the navigator slice as discussed in the previous chapter. For this real-time images with a high temporal resolution (ΔT) are reconstructed from the navigator slice. In each image the area of the LV is assessed (white circles). The IBCN signal is obtained from the temporal change of the size of the blood-pool in the LV. **(c)** The cardiac gating signal is used to retrospectively combine data from different cardiac cycles but same cardiac phase for the image reconstruction of the image slice in order to achieve high temporal resolution without visible undersampling artefacts. US undersampling factor.

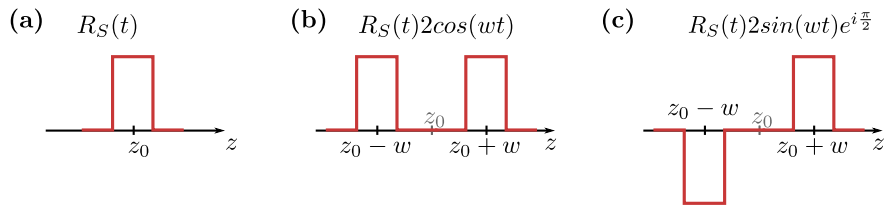

Figure 9.2: Slice profiles for **(a)** single-slice and **(b-c)** dual-slice excitation. The modulation of an single-slice RF pulse ($RF_S(t)$) with a cosine function $2cos(wt)$ leads to the excitation of two slices separated by $2w$. The same results but with an additional phase shift of π for the slice located at $z_0 - w$ are achieved with a sine modulation $2sin(wt)e^{-i\frac{\pi}{2}}$.

9.2.1 Dual-Slice Excitation

The excitation of a navigator and image slice simultaneously is achieved with dual-slice excitation pulses. They are created by modulating a RF pulse used for single slice excitation ($RF_S(t)$) with cosine and sine functions [176,177]. Assuming $RF_S(t)$ excites a slice located at z_0, then the modulated pulse $RF_S(t)2cos(wt)$ leads to the excitation of two slices located at $z_0 - w$ and $z_0 + w$, respectively. A similar excitation pattern is achieved if $RF_S(t)$ is modulated with $2sin(wt)e^{-i\frac{\pi}{2}}$. The slice at $z_0 + w$ is excited identically as before but the phase of slice located at $z_0 - w$ is shifted by π relative to the slice at $z_0 + w$ (Fig. 9.2). The factor $e^{-i\frac{\pi}{2}}$ compensates for the phase difference between sine and cosine. This modulation does not change thickness or orientation of the excited slices. In the following the pulse obtained by modulating $RF_S(t)$ with $2cos(wt)$ and $2sin(wt)e^{-i\frac{\pi}{2}}$ will be referred to as RF_0 and RF_π, respectively.

9.2.2 Golden Angle radial CAIPIRINHA (GCaipi)

Both RF pulses RF_0 and RF_π lead to the simultaneous excitation of two slices (slice 1 at $z_0 + w$ and slice 2 at $z_0 - w$). During data acquisition spins from both slices contribute equally to the recorded k-space data. Several methods have been proposed to separate the image information from slice 1 and slice 2 [176–178]. For a uniform radial sampling scheme Yutzy et al. suggest to alternate the phase of the RF pulse for one slice in order to achieve destructive interference and therefore signal cancellation for this slice [175]. This radial CAIPIRINHA (radCaipi) approach will be discussed in the following.

The alternation of the RF phase is achieved using RF_0 prior to the acquisition of every odd and RF_π prior to every even radial line. Both RF pulses lead to the same excitation for slice 1. For slice 2 every odd radial line is obtained with RF phase 0 and every even with RF phase π (Fig. 9.3a-b). This leads to two subsets of k-space data, one subset acquired with an RF phase of 0 and the other one with π. If these two subsets are interleaved, they interfere destructively. Therefore, data acquisition with radCaipi yields only image information from slice 1 and any image content from slice 2 cancels to zero.

In order to retrieve image information from slice 2, the alternation of the RF phase has to be compensated for by retrospectively multiplying every even radial spoke with $e^{-i\pi}$. This leads to the same RF phase for all spokes of slice 2 but to alternating RF phases for slice 1. Therefore, k-space data of slice 1 interferes destructively and image reconstruction only yields information from slice 2.

Here we extend this method to Golden Angle radial trajectories. In contrast to the uniform radial approach, the RF pulse is alternated for successively acquired radial lines, rather than for even and odd radial lines. Due to the sampling properties of the Golden Angle this also leads to two interleaved subsets of k-space data with phase 0 and π, respectively (Fig. 9.3c). Therefore, the image information from slice 1 and slice 2 can be separated in the same way as for radCaipi.

9.2.3 Limitations of radCaipi and GCaipi using bSSFP Sequences

As discussed in chapter 2.2.4 for bSSFP sequences the phase of the RF pulse has to be increased linearly by Φ_B in order to achieve a constructive interference of the signal from subsequent echoes. Commonly Φ_B is set to π in order to ensure an optimal signal intensity. Nevertheless, off-resonance effects can still lead to signal cancellation and banding artefacts described by equation (2.23). Figure 9.4a shows the signal intensity as a function of dephasing θ due to off-resonance effects.

For radCaipi and GCaipi the RF phase also changes between 0 and π for slice 2 due to the alternation between RF_0 and RF_π which is required to separate the image information of the two excited slices. This counteracts the increase of the

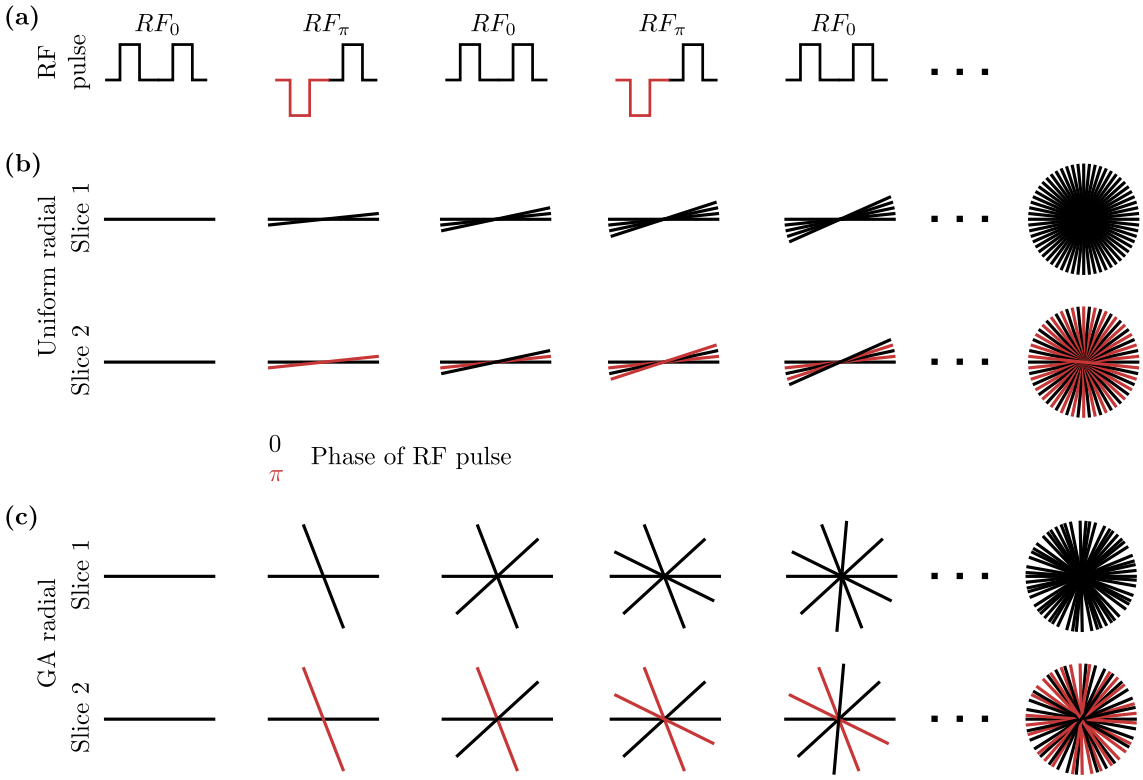

Figure 9.3: Radial CAIPIRINHA. **(a)** In order to be able to separate the image content of the two simultaneously excited slices, spin excitation is carried out with RF_0 and RF_π alternatingly. **(b)** This leads to an excitation with a constant RF phase for slice 1 but two subsets of k-space for slice 2, one with RF phase 0 and one with RF phase π. **(c)** The sampling properties of a Golden Angle (GA) radial acquisition also lead to a constant RF phase for slice 1 and alternating RF phase for slice 2, if every second dual-slice excitation is carried out with RF_π.

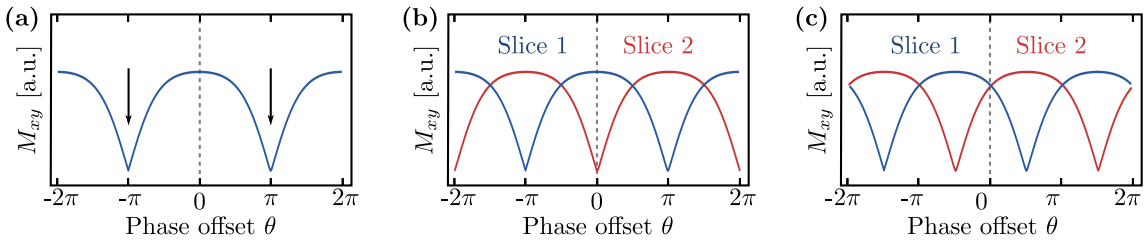

Figure 9.4: Signal intensity (M_{xy}) for a bSSFP acquisition as a function of dephasing θ due to off-resonance effects. **(a)** Banding artefacts (black arrows) occur when $\theta = \pi$. **(b)** The phase alternation of the RF pulse for the CAIPIRINHA encoding counteracts Φ_B and leads to banding artefacts for $\theta = 0$. **(c)** Setting Φ_B to $\frac{\pi}{2}$ avoids this signal cancellation for slice 2 and leads to high image quality for both excited slices.

RF phase by $\Phi_B = \pi$ and results in a constant RF phase for slice 2 which leads to strong artefacts and signal cancellation (Fig. 9.4b). Staeb et al. suggest to avoid this strong signal decrease for slice 2 by setting Φ_B to $\frac{\pi}{2}$ [179]. The RF phase for slice 1 is then increased by $\frac{\pi}{2}$ and for slice 2 by -$\frac{\pi}{2}$ for successive excitations which ensures high image quality for both slices (Fig. 9.4c).

9.2.4 Image Reconstruction

All images were reconstructed offline using Matlab (The MathWorks, Inc., Natich, MA, USA) with a non-Cartesian iterative SENSE reconstruction scheme [94]. The necessary coil sensitivity information was obtained from the data itself.

9.2.5 Image-Based Cardiac Navigator and Retrospective Ordering of *K*-Space Data

As discussed in the previous chapter the IBCN is obtained from real-time images reconstructed from the navigator slice (see also Fig. 8.4). The minima of systolic contraction are determined in the IBCN signal and used to retrospectively reorder the k-space data of the image slice (see also Fig. 8.5). This allows for the final image reconstruction of cine images with high spatial and high temporal resolution.

9.3 Experiments

9.3.1 Numerical Simulations

A numerical phantom study using the SSE (see chapter 4) was carried out to evaluate how accurately the signal from two excited slices can be separated using GCaipi compared to radCaipi. The phantom used in these experiments consisted of a resolution grid on top of two ellipses representing blood pool and myocardium (Fig. 9.5). The location of the phantom was chosen such that the image content of the two slices obtained with a simulated dual-slice excitation pulse does not overlap. In contrast to previous studies the numerical phantom was static during the simulated data acquisition.

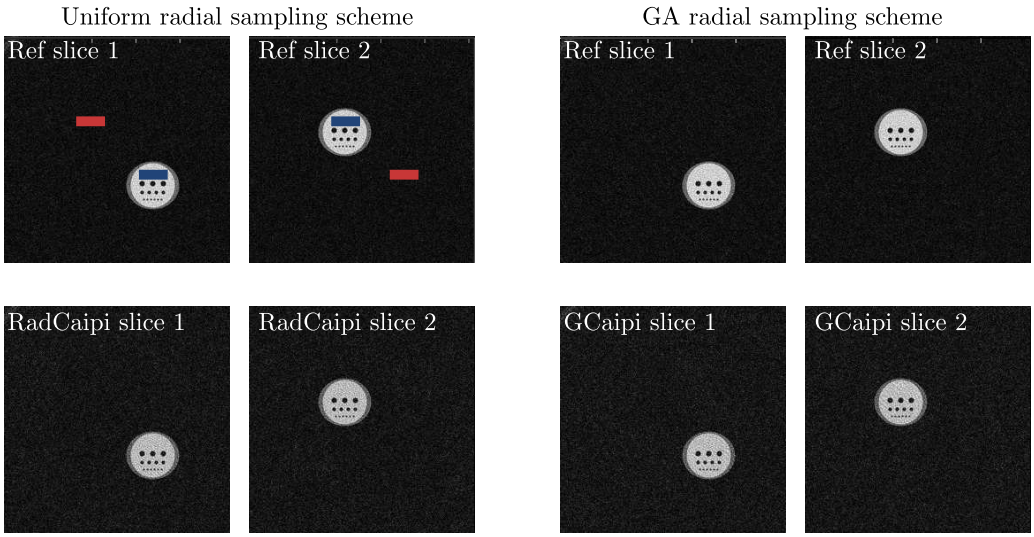

Figure 9.5: Phantom used for numerical simulations. Data acquisition was simulated for single slice acquisitions (Ref) of slice 1 and slice 2 and dual slice acquisition (radCaipi and GCaipi, respectively) using uniform and Golden Angle (GA) radial sampling schemes. The aSNR was calculated as the ratio between the mean signal of a high intensity region (blue rectangle) and the standard deviation of the background signal (red rectangle).

K-space data were obtained using radCaipi as presented in [175] and the proposed GCaipi approach. The size of the numerical phantom was 256 x 256 pixels and 256 k-space points were acquired along each radial line (N_r). In order to study the effect of undersampling on the signal separation, the number of obtained radial lines N_a was varied between 320 (i.e. number of radial lines fulfilling the Nyquist theorem for a fully sampled k-space) and 30 in steps of 2. Uneven values for N_a were not used because these would lead to a different number of radial spokes obtained with RF_0 and RF_π, respectively and therefore to incomplete signal cancellation. For each N_a the simulation was repeated 10 times and the obtained values for aSNR were averaged for the final analysis.

Data acquisition was also simulated using a uniform and Golden Angle radial acquisition scheme with a single-slice RF pulse with the same settings for N_r and N_a for comparison

Images were reconstructed using a non-uniform fast Fourier transform (NUFFT) [91]. Parallel imaging was not used for these simulations to avoid inhomogeneous noise enhancement and artefacts due to inaccurate coil sensitivity estimations.

Image quality achieved by radCaipi and GCaipi was assessed by comparing aSNR in images obtained with single-slice ($aSNR_{SL}$) and dual-slice ($aSNR_{DL}$) RF pulses

$$aSNR = \frac{I_S}{SD_N} \tag{9.1}$$

where I_S describes the mean signal in a high intensity region (i.e. blood pool) of the phantom and SD_N is the standard deviation of the background signal.

Differences between $aSNR_{SL}$ and $aSNR_{DL}$ can only be caused by any remaining artefacts which do not interfere destructively. Therefore, the ratio of these two parameters should provide a good indication of how accurately the two excited slices can be separated using radCaipi and GCaipi.

9.3.2 Phantom Studies

The slice profiles achieved with the modulated RF pulse RF_0 and RF_π were evaluated in phantom experiments. Therefore, CAIPIRINHA using the two RF pulses RF_0 and RF_π was implemented on a 1.5T MRI scanner (Philips Medical System, Best, The Netherlands). A 2D Cartesian MRI sequence was combined with additional SE gradients to achieve spatial encoding also along the SE direction. This allowed for an accurate visualisation and assessment of slice profiles with a FOV of 280 x 280 x 70 mm and resolution of 2 x 2 x 1.5 mm in FE, PE and SE direction, respectively.

The slice thickness was 8 mm and the distance between the two excited slices was set to 8, 24, and 48 mm. In order to verify the correct excitation achieved with RF_0 and RF_π, images were obtained using either RF_0 or RF_π. For comparison slice profiles were also obtained with an unmodulated single-slice RF pulse.

9.3.3 Volunteer Studies

Six short axis data sets were acquired with GCaipi in a healthy volunteer with the image slices distributed over the left ventricle and the navigator slice centred in the ventricle: balanced SSFP sequence, FOV: 320 x 320 mm, 2 mm in plane resolution, 8 mm slice thickness, 45° flip angle, TR/TE = 3.1/1.51 ms. Each slice was obtained in a 13.1 s breath-hold. Data was acquired with a 5-channel cardiac phased array coil. Written informed consent was obtained from the participant and the study was carried out following an approved protocol from our local hospital.

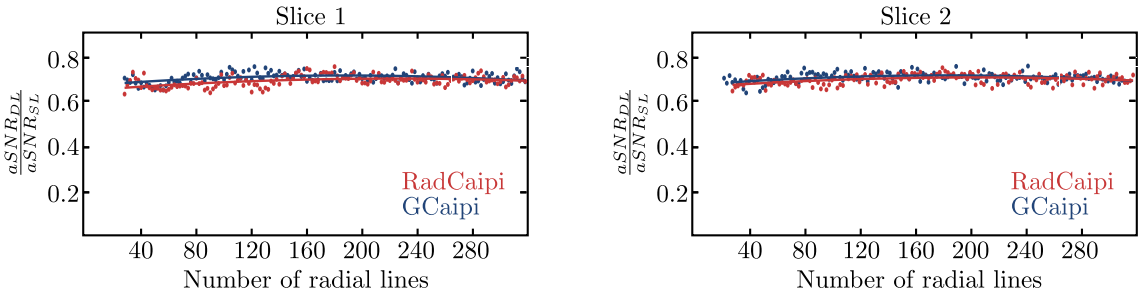

Figure 9.6: Ratio between aSNR achieved with a single-slice ($aSNR_{SL}$) and dual-slice ($aSNR_{DL}$) excitation pulse for a uniform radial sampling scheme (radCaipi) and Golden Angle radial trajectory (GCaipi). Results are shown for both slices excited with the dual-slice RF pulse.

For each slice an IBCN signal was obtained from real-time images reconstructed with a temporal resolution of 24.8 ms (i.e. sliding window approach, window shift of 8 radial lines). The accuracy of the obtained IBCN signal was determined as the standard deviation between the systolic minima and the R-peaks detected by the scanner in the external ECG signals according to equation (8.3). Based on the systolic minima of the IBCN signals the acquired k-space data of the image slice were retrospectively reordered. For each slice 30 cardiac phases were reconstructed yielding high temporal and high spatial resolution images.

9.4 Results

All simulations, phantom and volunteer experiments were carried out successfully.

Figure 9.6 depicts the ratio of aSNR between single-slice and dual-slice acquisitions for radCaipi and GCaipi as a function of different number of radial lines used for image reconstruction. Compared to a single-slice excitation the aSNR of both dual-slice techniques is approximately 30% lower. Nevertheless, the behaviour of radCaipi and GCaipi is comparable and there is also little dependency on the angular undersampling.

The measured slice profiles obtained with a single-slice excitation pulse and with RF_0 and RF_π are depicted in Fig. 9.7. The shape of the slice profiles is not altered due to the modulation with the cosine and sine functions. Nevertheless, the phase of the slice profiles shows a linear dependency relative to the centre between the

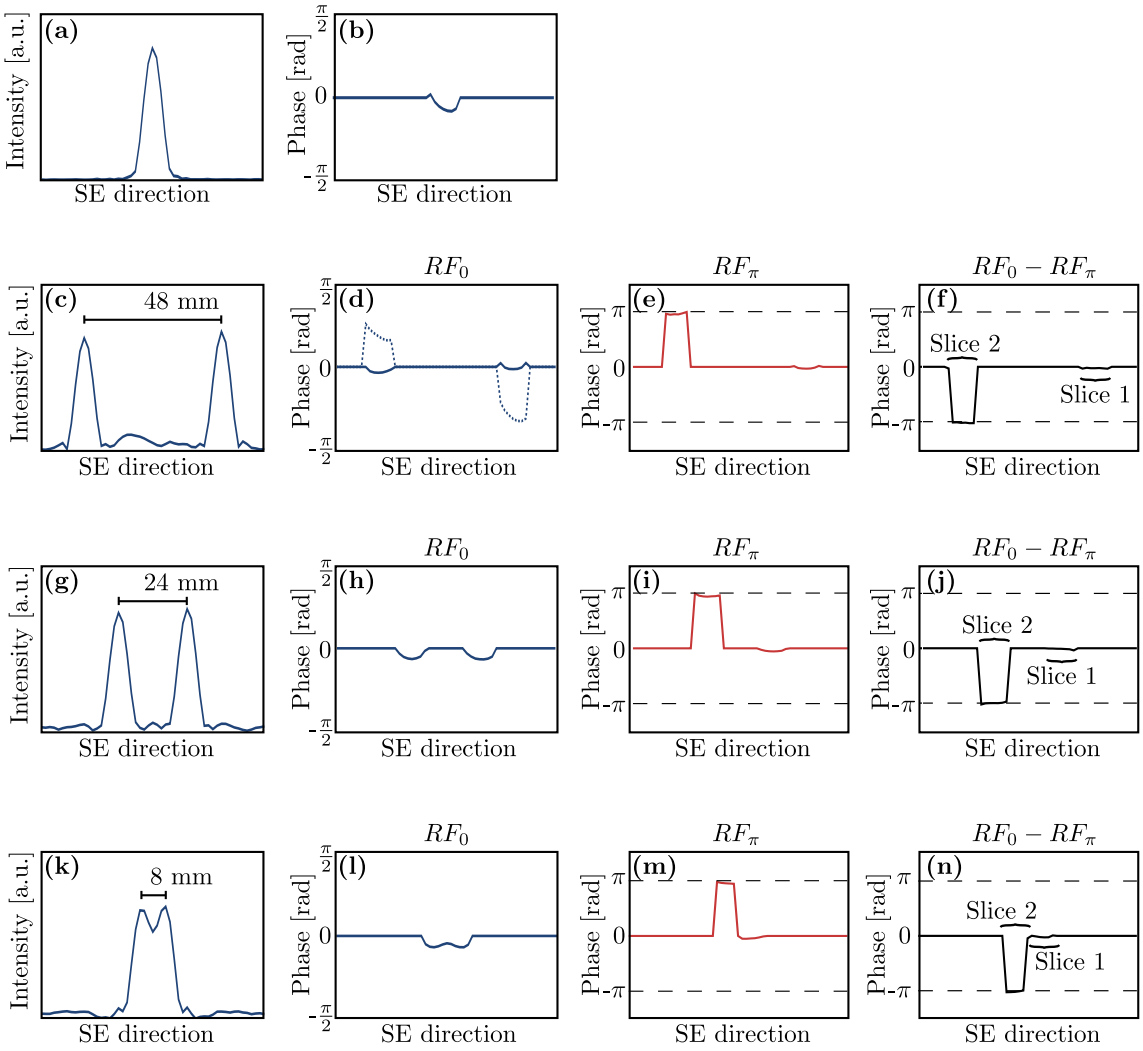

Figure 9.7: Measured slice excitation profiles achieved with a **(a,b)** single-slice excitation pulse and dual-slice excitation pulse with slices separated by **(c-f)** 48 mm, **(g-j)** 24 mm and **(k-n)** 8 mm. The slice thickness for all experiments was 8 mm. For each pulse the amplitude (a,c,g,k), the phase achieved with RF_0 (d,h,l), the phase achieved with RF_π (e,i,m) and the phase difference between RF_0 and RF_π (f,j,n) are shown as the mean over a region in the centre of the phantom. (d) The phase of the slice profiles (dotted line) shows a linear dependency relative to the centre between the two excited slices. By adapting the slice refocusing gradient for all excitation pulses this linear phase along the slice encoding direction was removed (solid lines in (d-f), (h-j) and (l-n). (f,j,n) The phase difference of RF_0 and RF_π is 0 for slice 1 (right) and π for slice 2 (left).

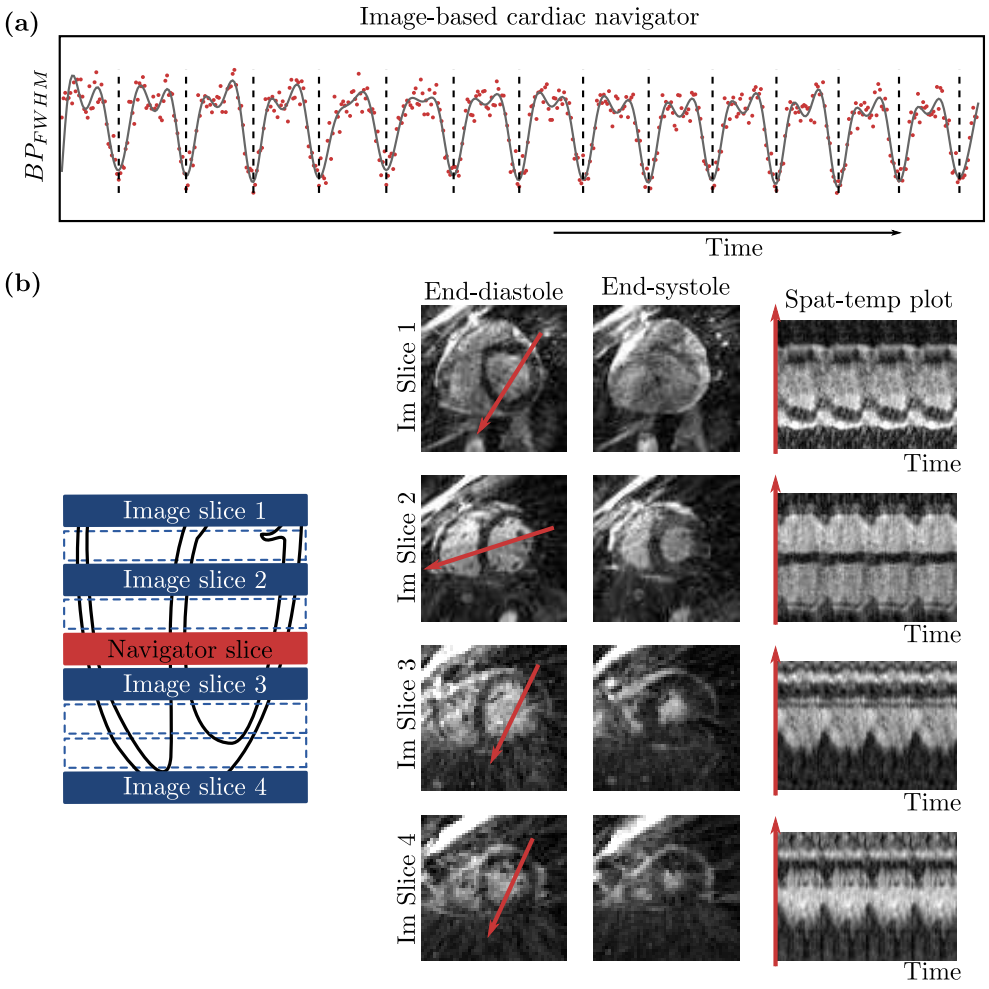

Figure 9.8: Results of volunteer study. **(a)** Image-based cardiac navigator signal (red dots: measured, grey line: low pass filtered signal). For each cardiac cycle the minimum of systolic contraction was accurately determined (dashed lines). **(b)** End-distolic and end-systolic images at four different slice locations. In addition spatial-temporal plots along the red arrows in the end-diastolic images are shown. BP_{FWHM} mean temporal change of FWHM of the LV blood pool.

two excited slices (Fig. 9.7b). This is due to the incomplete refocusing of the spins after the slice selection gradient [180]. The correct refocusing gradient depends on the magnetic centre of the RF excitation pulse. The cosine and sine modulations of RF_0 and RF_π change this magnetic centre and therefore also the refocusing gradient has to be adapted accordingly. The correct refocusing gradient was determined experimentally and applied to all following experiments.

The comparison between the phase of the slice profiles achieved with RF_0 and RF_π verifies the accurate phase alternation achieved for slice 2 and a constant phase for slice 1.

One IBCN signal of the volunteer study is depicted in Fig. 9.8a. The mean accuracy of the IBCN over all six slices was 16.58 ms with a standard deviation of 4.68 ms which is below the temporal resolution of the IBCN signal. Furthermore, the mean delay between systolic minima determined in the IBCN signal and the R-peak found by the scanner over all image slice locations was -37.62 $\pm$ 14.12 ms. This shows that the navigator slice yields a highly accurate IBCN signal independent of the position of the image slice. Retrospectively reordered cine images and spatial-temporal plots are shown in Fig. 9.8b.

9.5 Discussion

We have presented a method which obtains an image-based cardiac navigator from a separate navigator slice which is acquired in parallel to the image slice using a dual-slice excitation pulse. Data is obtained with a novel combination of CAIPIRINHA for a GA radial sampling scheme. Phantom studies have demonstrated that the signal of two simultaneously excited slice can be separated using GCaipi with a similar accuracy as previously presented methods. The slice profiles required for the dual-slice excitation have been successfully verified in phantom experiments. Volunteer studies have shown that the navigator slice yields a highly accurate gating signal independent of the location of the image slice. This allows for the retrospective combination of k-space data to reconstruct high temporal resolution cine images.

Our numerical simulations have shown that GCaipi provides an accurate separation of data excited with a dual-slice RF pulse similar to radCaipi. The aSNR

achieved with both dual-slice techniques is approximately 30% lower than with a single-slice approach. This is probably caused by signals which occur randomly and therefore do not interfere destructively. Therefore, any artefacts of one slice will also have in impact on the other slice after image reconstruction which would explain the strong decrease in aSNR. Yutzy et al. did not compare their proposed radCaipi approach to a single-slice excitation but only to a Cartesian CAIPIRINHA technique and did not discuss this effect.

The IBCN provided a highly accurate cardiac gating signal but it shows higher noise content then the results from the single-slice excitation in the previous study. In Fig. 9.8b the retrospectively reordered cine images clearly depict the LV and RV and the changes of the ventricles during the cardiac cycle are visible in the spatial-temporal plots. Nevertheless, the overall image quality is inferior to the results of the single-slice images shown in Fig. 8.7. This indicates that the dual-slice GCaipi approach presented here can still be improved. One possibility could be that the slice profiles of the modulated pulses are not selective enough. This is also indicated by the slice profiles shown in Fig. 9.7 where the modulated pulses lead to more signal outside of the desired slice region than the single-slice pulse.

Furthermore, Fig. 9.9 shows the results for two dual-slice acquisitions obtained in the same volunteer at the same location in the ventricle but with two different RF excitation pulses. In order to optimise T_R for bSSFP sequences, the standard single-slice pulse used for these experiments is as short as possible. The shape of the pulse is a single lobe without any zero-crossings with a duration of approximately 0.45 ms. Nevertheless, this reduces the accuracy of the slice excitation profile. By using an excitation pulse with one zero-crossing and a length of 0.8 ms the slice profile could be improved which leads to a significantly better IBCN signal and also increases the quality of the retrospectively reordered cine images. The TR and TE for the longer pulse are increased from 3.0 ms to 4.0 ms and 1.49 ms to 2.0 ms, respectively. The shape of the two pulses is also shown in Fig. 9.9. Future work will be focused on further optimising the slice excitation profiles in order to improve our method.

The dual-slice excitation pulses used for our experiments were created by modulating a single-slice excitation pulse with cosine and sine functions, respectively.

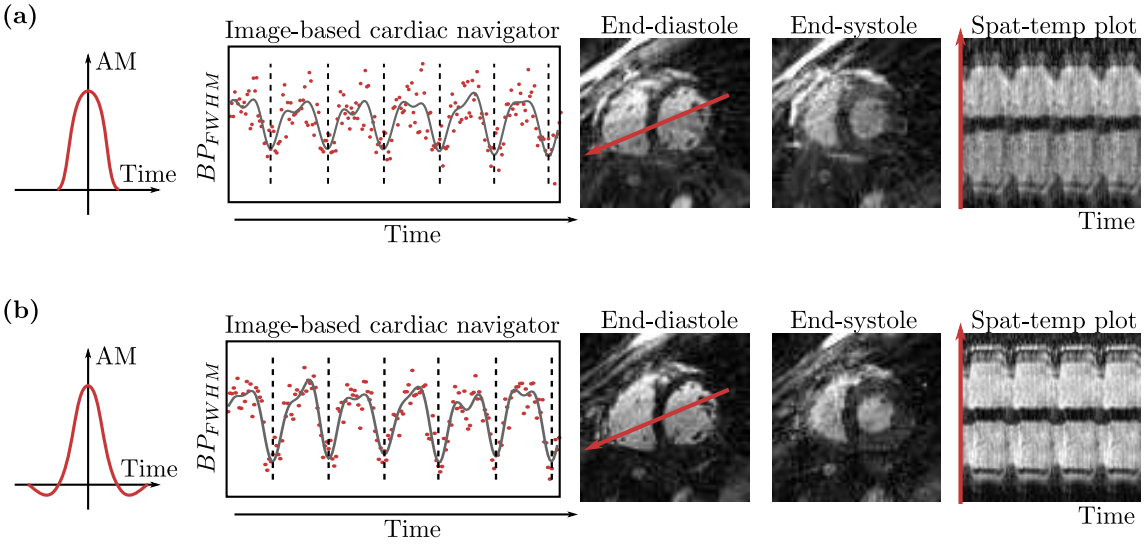

Figure 9.9: Data acquired with dual-slice excitation pulses based on two different single-slice excitation pulses $RF_S(t)$. **(a)** Standard RF excitation pulse for bSSFP sequences which consists of a single lobe and a duration of approximately 0.45 ms. **(b)** RF pulse with one zero-crossing and a duration of 0.8 ms which leads to a more accurate slice excitation. The IBCN signal, the retrospectively reordered cine images and the spatial-temporal plot along the line depicted in the end-diastolic images show strong improvements due to the more accurate slice excitation. AM amplitude modulation of RF pulse. BP_{FWHM} mean temporal change of FWHM of the LV blood pool.

Although this has been shown to lead to the desired slice profiles and GCaipi encoding, it is only applicable for symmetric excitation profiles (i.e. symmetric distance from the isocentre of the slice selection gradient, same slice thickness and same flip angle). A more flexible approach would be provided by using a Shinnar-Le Roux approach which would allow for the design of more advanced slice excitation profiles [178].

9.6 Conclusion

We have presented a new method which uses data from two excited slices to obtain both image and navigator information at different locations simultaneously. The image-based navigators obtained from the navigator slice showed high accuracies and little variation between different image slice positions. Although this technique is not yet fully developed to be used in patient scans, we believe it is a first step towards a highly efficient approach to do functional assessment also during arrhythmia.

Our approach yields a cardiac navigator signal which is obtained from common navigator images allowing for slice positions which do not yield a reliable signal themselves. Although we demonstrated the image-based navigation for cardiac function, it can be used in a wide range of applications.

10 Conclusion

In this thesis novel MRI acquisition techniques have been presented to characterise and compensate for irregular motion of the heart. These methods ensure excellent image quality with high isotropic resolution and short scan times even for subjects with challenging breathing patterns. In addition the effect of breathing on different regions of the heart has been analysed and compensated for with respiratory motion models. An approach which obtains a cardiac gating signal directly from the motion of the ventricles during the cardiac cycle has been shown to provide accurate functional images without the need of an external ECG. The presented methods have been successfully evaluated in numerical simulations, phantom, volunteer and patient studies.

A new high resolution 3D whole-heart acquisition scheme, RPE-PAWS, has been presented in chapters 4 and 5. It provides a highly efficient method to minimise respiratory motion artefacts and scan times have been reduced by 36% in volunteers with irregular breathing compared to a commonly used respiratory gating method. Furthermore, this approach allows for very high acceleration factors (e.g. 10) by exploiting the undersampling properties of radial encoding [72, 181] and reducing undersampling artefacts with an iterative reconstruction scheme [82]. This can allow for further scan time reductions by 25% without impairing image quality.

RPE-PAWS not only yields anatomical information but also provides additional respiratory motion information without an increase in scan time. In chapter 6

respiratory motion at different anatomical landmarks in the heart has been assessed and analysed for both volunteers and a patient. It has been shown that breathing motion can lead to displacements of up to 10 mm in the apex but also more than 6 mm in the atria. This displacement is similar to the thickness of the atrial wall and the size of the lesions created during ablation therapy. Therefore, in order to ensure accurate image guidance during ablation therapy, respiratory motion has to be taken into consideration. The respiratory motion models obtained with RPE-PAWS can reduce these displacement errors to below the image resolution of 1.5 mm. These motion models can be applied in image guided ablation procedures to update the position and shape of 3D cardiac MR data used for additional guidance.

The motion estimation has been carried out on highly undersampled images which can be strongly impaired by undersampling artefacts. Although it has been shown that a reliable and accurate motion estimation is possible even for very high undersampling factors, motion estimation could be improved by obtaining the affine parameters directly in k-space. This would also significantly shorten computational times.

The main limitations of RPE-PAWS are long reconstruction times due to the requirement of a non-Cartesian iterative SENSE reconstruction. Therefore, for the visualisation of myocardial scar tissue in heart failure patients presented in chapter 5 HybridPAWS, a modification of RPE-PAWS, has been used. It allows for the immediate and fast image reconstruction on the MR scanner without impairing scan efficiency compared to RPE-PAWS.

In chapter 8 a novel technique to assess cardiac function during free-breathing without the requirement of an external ECG has been presented. Information about cardiac motion is obtained from real-time data which leads to an image-based cardiac navigator signal with a temporal resolution of 24 ms. The presented method has been compared to a standard external ECG signal and has been shown to provide a cardiac gating signal with an accuracy below 20 ms. This allows for the reconstruction of high quality cine images. In addition to a cardiac navigator the presented method can also provide respiratory motion information.

The image-based cardiac navigator has been combined with a dual-slice excitation pulse in chapter 9. In addition to a standard imaging slice an additional navigator

slice is obtained in parallel without changing the acquisition time. This navigator slice provides high quality real-time images which yield cardiac gating signals independent of imaging slices. This allows for a synchronised multi-slice acquisition of the heart and ensures a reliable image-based cardiac navigator signal for any image slice location.

In conclusion, the approaches detailed in this thesis provide reliable and rapid acquisition methods which yield viable information for an accurate treatment planning and catheter guidance during ablation therapy. The complex structures of the atria, thin atrial wall and small ablation lesions require high isotropic resolution image information for guidance during the procedure. Any misalignment errors or inaccuracies due to respiratory motion have to be determined and compensated for. RPE-PAWS has been shown to yield high isotropic resolution 3D images with a significantly increased respiratory navigator efficiency for irregular breathing patterns. Additionally, respiratory motion information is obtained without an increase in scan time which allows for the assessment and minimisation of any misalignment errors due to respiratory motion. A new 3D high resolution DE-MRI method to visualise myocardial fibrosis which significantly improves scan efficiency for patients with irregular respiratory patterns has also been introduced.

Furthermore, a novel technique for functional assessment which yields a gating signal directly from cardiac functional information and does not require an external ECG has been presented. This method could provide novel methods to address irregular heart beats during cine MRI and help to improve the functional assessment of patients suffering from arrhythmia. In addition to the cardiac gating signal also respiratory motion information could be obtained which would allow for functional assessment during free-breathing.

The novel MRI acquisition schemes presented in this thesis cannot just be used for patients suffering from AF or AFL. They can improve the accuracy, outcome and procedure time of other percutaneous procedures such as cardiac catheterisation for congenital heart disease [182] or cardiac resynchronization therapy [154].

11 | Publications

The techniques presented in this thesis have already been published in part as articles in scientific journals:

C. Kolbitsch, C. Prieto, J. Smink, and T. Schaeffter, "Highly efficient whole-heart imaging using radial phase encoding - phase ordering with automatic window selection", *Magn Reson Med*, vol. 66, pp. 1008-18, 2011.

C. Kolbitsch, C. Prieto, C. Buerger, J Harrison, R. Razavi, J. Smink, and T. Schaeffter, "Prospective high-resolution respiratory-resolved whole-heart MRI for image-guided cardiovascular interventions", *Magn Reson Med*, vol. 68, pp. 205-13, 2011.

and discussed during presentations at scientific meetings:

C. Kolbitsch, C. Prieto, J. Smink, and T. Schaeffter, "Highly efficient isotropic whole-heart imaging using radial phase encoding PAWS", in *Proceedings of the 19th Annual Meeting of ISMRM, Montreal, Canada*, pp. 4358, 2011.

C. Kolbitsch, C. Prieto, C. Buerger, R. Razavi, J. Smink, and T. Schaeffter, "Prospective high resolution respiratory resolved whole-heart MRI for image-guided cardiovascular interventions", in *Proceedings of the 19th Annual Meeting of ISMRM, Montreal, Canada*, pp. 196, 2011.

R. Clough, C. Buerger, C. Kolbitsch, M. Henningsson, C. Prieto, and T. Schaeffter, "3D Aortic motion estimation for image-guided intervention", in *Proceedings of the 19th Annual Meeting of ISMRM, Montreal, Canada*, pp. 3740, 2011.

J. Burakiewicz, C. Kolbitsch, G. D. Charles-Edwards, and T. Schaeffter, "Reducing artefacts in inversion recovery prepared MRI caused by varying heart rate through real-time adaptation of the inversion time", in *Proceedings of the 19th Annual Meeting of ISMRM, Montreal, Canada*, pp. 4620, 2011.

Z. Chen, C. Kolbitsch, J. Smink, J. Harrison, V. O. Puntmann, E. Nagel, R. Razavi, A. Rinaldi, and T. Schaeffter, "Hybrid phase ordering with automatic window selection (HybridPAWS) improves respiratory-navigator efficiency during 3D late-gadolinium enhancement CMR in patients with chronic heart failure and irregular respiratory pattern", *J Magn Reson Imaging*, vol. 14(Suppl 1), pp. 256, 2012.

C. Kolbitsch, D. Giese, J. Smink, C. Prieto, and T. Schaeffter, "Cardiac function assessment without ECG using image-based navigation", in *Proceedings of the 20th Annual Meeting of ISMRM, Melbourne, Australia*, pp. 3849, 2012.

C. Kolbitsch, T. Schaeffter, J. Smink, and C. Prieto, "Image-based self-navigator using cardiac functional parameters for cine imaging", in *Proceedings of the 20th Annual Meeting of ISMRM, Melbourne, Australia*, pp. 602, 2012. (ISMRM merit award *Magna cum laude*)

D. Giese, C. Kolbitsch, A. Aitken, M. Buehrer, T. Schaeffter, and S. Kozerke, "Magnetic field monitoring of radial trajectories", in *Proceedings of the 20th Annual Meeting of ISMRM, Melbourne, Australia*, pp. 3849, 2012.

M. Usman, C. Kolbitsch, G. Vaillant, D. Atkinson, T. Schaeffter, P. G. Batchelor, and C. Prieto, "A frame work for non-rigid motion corrected compressed sensing for highly accelerated MRI", in *Proceedings of the 20th Annual Meeting of ISMRM, Melbourne, Australia*, pp. 72, 2012.

G. Vaillant, C. Prieto, C. Kolbitsch, G. Penny, and T. Schaeffter, "Intra-frame motion correction in dynamic radial MRI using the phase correlation method", in *Proceedings of the 20th Annual Meeting of ISMRM, Melbourne, Australia*, pp. 3414, 2012.

Glossary

(b)SSFP	(Balanced) Steady-State Free-Precession
aCNR	Apparent Contrast to Noise Ratio
aSNR	Apparent Signal to Noise Ratio
CT	Computer Tomography
CAD	Coronary Artery Disease
DE-MRI	Delayed Enhancement MRI
DCF	Density Compensation Function
ECG	Electrocardiogram
FFT	Fast Fourier Transform
FOV	Field of View
FT	Fourier Transform
FID	Free Induction Decay
FE	Frequency Encoding
FWHM	Full-Width Half-Maximum
GA, GR	Golden Angle
GR	Golden Ratio
GE	Gradient Echo
iFFT	inverse Fast Fourier Transform
iFT	Inverse Fourier Transform
iNFFT	Inverse Nonequispaced Fast Fourier Transform
IR	Inversion Recovery
T_I	Inversion Time
LA	Left Atrium

LCA	Left Coronary Artery
LV	Left Ventricle
M_z	Longitudinal Magnetisation
T_1	Longitudinal Relaxation Time
MR	Magnetic Resonance
MRI	Magnetic Resonance Imaging
MRS	Magnetic Resonance Spectroscopy
M2D	Multi-Slice 2D
NE	Navigator Efficiency
NFFT	Nonequispaced Fast Fourier Transform
NMR	Nuclear Magnetic Resonance
PSR	Peak to Sidelobe Ratio
PE	Phase Encoding
PSF	Point Spread Function
RPE	Radial Phase Encoding
RF	Radio Frequency
ROI	Region of Interest
RA	Right Atrium
RCA	Right Coronary Artery
RV	Right Ventricle
RMS Error	Root Mean Square Error
SENSE	Sensitivity Encoding
SNR	Signal to Noise Ratio
SE	Spin Echo
SS	Structure Sharpness
TRE	Target Registration Error
3D	Three-Dimensional
M_{xy}	Transversal Magnetisation
T_2, T_2', T_2*	Transversal Relaxation Times
TV	Tricuspid Valve
T_D	Trigger Delay
2D	Two-Dimensional
VS	Vessel Sharpness

Bibliography

[1] D. W. McRobbie, E. A. Moore, M. J. Graves, and M. R. Prince, *MRI From Picture to Proton*. Press Syndicate of the University of Cambridge, 2003.

[2] P. C. Lauterbur, "Image formation by induced local interactions. examples employing nuclear magnetic resonance.," *Nature*, vol. 242, pp. 190–191, Mar 1973.

[3] P. B. Roemer, W. A. Edelstein, C. E. Hayes, S. P. Souza, and O. M. Mueller, "The NMR phased array.," *Magn Reson Med*, vol. 16, pp. 192–225, Nov 1990.

[4] J. Hennig, A. Nauerth, and H. Friedburg, "RARE imaging: a fast imaging method for clinical MR.," *Magn Reson Med*, vol. 3, pp. 823–833, Dec 1986.

[5] D. Matthaei, J. Frahm, A. Haase, W. Hxnicke, and K.-D. Merboldt, "Three-dimensional flash MR imaging of thorax and abdomen without triggering or gating," *Magnetic Resonance Imaging*, vol. 4, pp. 381–386, 1986.

[6] D. K. Sodickson and W. J. Manning, "Simultaneous Acquisition of Spatial Harmonics (SMASH): fast imaging with radiofrequency coil arrays.," *Magn Reson Med*, vol. 38, pp. 591–603, Oct 1997.

[7] K. P. Pruessmann, M. Weiger, M. B. Scheidegger, and P. Boesiger, "SENSE: sensitivity encoding for fast MRI.," *Magn Reson Med*, vol. 42, pp. 952–962, Nov 1999.

[8] M. A. Griswold, P. M. Jakob, R. M. Heidemann, M. Nittka, V. Jellus, J. Wang, B. Kiefer, and A. Haase, "Generalized autocalibrating partially parallel acquisitions (GRAPPA).," *Magn Reson Med*, vol. 47, pp. 1202–1210, Jun 2002.

[9] M. Lustig, D. Donoho, and J. M. Pauly, "Sparse MRI: The application of compressed sensing for rapid MR imaging.," *Magn Reson Med*, vol. 58, pp. 1182–1195, Dec 2007.

[10] A. M. Blamire, "The technology of MRI–the next 10 years?," *Br J Radiol*, vol. 81, pp. 601–617, Aug 2008.

[11] D. J. Pennell, U. P. Sechtem, C. B. Higgins, W. J. Manning, G. M. Pohost, F. E. Rademakers, A. C. van Rossum, L. J. Shaw, and E. K. Yucel, "Clinical indications for cardiovascular magnetic resonance (CMR): Consensus panel report.," *Eur Heart J*, vol. 25, pp. 1940–1965, Nov 2004.

[12] O. M. Weber, A. J. Martin, and C. B. Higgins, "Whole-heart steady-state free precession coronary artery magnetic resonance angiography.," *Magn Reson Med*, vol. 50, pp. 1223–1228, Dec 2003.

[13] British Heart Foundation, "European cardiovascular disease statistics, 2008 edition."

[14] R. S. Oakes, T. J. Badger, E. G. Kholmovski, N. Akoum, N. S. Burgon, E. N. Fish, J. J. E. Blauer, S. N. Rao, E. V. R. DiBella, N. M. Segerson, M. Daccarett, J. Windfelder, C. J. McGann, D. Parker, R. S. MacLeod, and N. F. Marrouche, "Detection and quantification of left atrial structural remodeling with delayed-enhancement magnetic resonance imaging in patients with atrial fibrillation.," *Circulation*, vol. 119, pp. 1758–1767, Apr 2009.

[15] K. H. W. J. T. Tusscher and A. V. Panfilov, "Influence of diffuse fibrosis on wave propagation in human ventricular tissue.," *Europace*, vol. 9 Suppl 6, pp. vi38–vi45, Nov 2007.

[16] T. H. Everett and J. E. Olgin, "Atrial fibrosis and the mechanisms of atrial fibrillation.," *Heart Rhythm*, vol. 4, pp. S24–S27, Mar 2007.

[17] M. Haissaguerre, P. Jais, D. C. Shah, A. Takahashi, M. Hocini, G. Quiniou, S. Garrigue, A. L. Mouroux, P. L. Metayer, and J. Clementy, "Spontaneous initiation of atrial fibrillation by ectopic beats originating in the pulmonary veins.," *N Engl J Med*, vol. 339, pp. 659–666, Sep 1998.

[18] J. Dewire and H. Calkins, "State-of-the-art and emerging technologies for atrial fibrillation ablation.," *Nat Rev Cardiol*, vol. 7, pp. 129–138, Mar 2010.

[19] H. Vidaillet, J. F. Granada, P. o Huang Chyou, K. Maassen, M. Ortiz, J. N. Pulido, P. Sharma, P. N. Smith, and J. Hayes, "A population-based study of mortality among patients with atrial fibrillation or flutter.," *Am J Med*, vol. 113, pp. 365–370, Oct 2002.

[20] P. Kirchhof, M. Ozguen, S. Zellerhoff, G. Moennig, L. Eckardt, K. Wasmer, W. Heindel, G. Breithardt, and D. Maintz, "Diastolic isthmus length and 'vertical' isthmus angulation identify patients with difficult catheter ablation of typical atrial flutter: a pre-procedural MRI study.," *Europace*, vol. 11, pp. 42–47, Jan 2009.

[21] F. Morady, "Catheter ablation of supraventricular arrhythmias: state of the art.," *Pacing Clin Electrophysiol*, vol. 27, pp. 125–142, Jan 2004.

[22] F. Murgatroyd, A. D. Krahn, G. J. Klein, A. C. Skanes, and R. K. Yee, *Handbook of Cardiac Electrophysiology: A Practical Guide to Invasive EP Studies and Catheter Ablation.* ReMEDICA Publishing Limited, 2001.

[23] H. Oral, C. Pappone, A. Chugh, E. Good, F. Bogun, F. Pelosi, E. R. Bates, M. H. Lehmann, G. Vicedomini, G. Augello, E. Agricola, S. Sala, V. Santinelli, and F. Morady, "Circumferential pulmonary-vein ablation for chronic atrial fibrillation.," *N Engl J Med*, vol. 354, pp. 934–941, Mar 2006.

[24] R. Kato, L. Lickfett, G. Meininger, T. Dickfeld, R. Wu, G. Juang, P. Angkeow, J. LaCorte, D. Bluemke, R. Berger, H. R. Halperin, and H. Calkins, "Pulmonary vein anatomy in patients undergoing catheter ablation of atrial fibrillation: lessons learned by use of magnetic resonance imaging.," *Circulation*, vol. 107, pp. 2004–2010, Apr 2003.

[25] I. M. Robbins, E. V. Colvin, T. P. Doyle, W. E. Kemp, J. E. Loyd, W. S. McMahon, and G. N. Kay, "Pulmonary vein stenosis after catheter ablation of atrial fibrillation.," *Circulation*, vol. 98, pp. 1769–1775, Oct 1998.

[26] F. G. Cosio and J. Perea, "The continuing challenge of typical atrial flutter ablation: it is the anatomy! (again).," *Europace*, vol. 12, pp. 1518–1519, Nov 2010.

[27] A. D. McGavigan and J. M. Kalman, "Atrial anatomy and imaging in atrial fibrillation ablation," *J Cardiovasc Electrophysiol*, vol. 17, pp. S8 – S15, 2006.

[28] P. A. Noseworthy, Z. J. Malchano, J. Ahmed, G. Holmvang, J. N. Ruskin, and V. Y. Reddy, "The impact of respiration on left atrial and pulmonary venous anatomy: implications for image-guided intervention.," *Heart Rhythm*, vol. 2, pp. 1173–1178, Nov 2005.

[29] R. Razavi, V. Mathuranu, S. R. Hedge, and A. M. Taylor, *Clinical Cardiac MRI*. Springer Berlin Heidelberg, 2005.

[30] V. Y. Reddy, Z. J. Malchano, G. Holmvang, E. J. Schmidt, A. d'Avila, C. Houghtaling, R. C. Chan, and J. N. Ruskin, "Integration of cardiac magnetic resonance imaging with three-dimensional electroanatomic mapping to guide left ventricular catheter manipulation: feasibility in a porcine model of healed myocardial infarction.," *J Am Coll Cardiol*, vol. 44, pp. 2202–2213, Dec 2004.

[31] K. S. Rhode, M. Sermesant, D. Brogan, S. Hegde, J. Hipwell, P. Lambiase, E. Rosenthal, C. Bucknall, S. A. Qureshi, J. S. Gill, R. Razavi, and D. L. G. Hill, "A system for real-time XMR guided cardiovascular intervention.," *IEEE Trans Med Imaging*, vol. 24, pp. 1428–1440, Nov 2005.

[32] H. Saybasili, A. Z. Faranesh, C. E. Saikus, C. Ozturk, R. J. Lederman, and M. A. Guttman, "Interventional MRI using multiple 3D angiography roadmaps with real-time imaging.," *J Magn Reson Imaging*, vol. 31, pp. 1015–1019, Apr 2010.

[33] C. E. Saikus and R. J. Lederman, "Interventional cardiovascular magnetic resonance imaging: a new opportunity for image-guided interventions.," *JACC Cardiovasc Imaging*, vol. 2, pp. 1321–1331, Nov 2009.

[34] G. W. Lenz, E. M. Haacke, and R. D. White, "Retrospective cardiac gating: a review of technical aspects and future directions.," *Magn Reson Imaging*, vol. 7, no. 5, pp. 445–455, 1989.

[35] J. Liu, O. Wieben, Y. Jung, A. A. Samsonov, S. B. Reeder, and W. F. Block, "Single breathhold cardiac CINE imaging with multi-echo three-dimensional hybrid radial SSFP acquisition.," *J Magn Reson Imaging*, vol. 32, pp. 434–440, Aug 2010.

[36] D. C. Peters, D. B. Ennis, P. Rohatgi, M. A. Syed, E. R. McVeigh, and A. E. Arai, "3D breath-held cardiac function with projection reconstruction in steady state free precession validated using 2D cine MRI.," *J Magn Reson Imaging*, vol. 20, pp. 411–416, Sep 2004.

[37] R. C. Semelka, E. Tomei, S. Wagner, J. Mayo, G. Caputo, M. O'Sullivan, W. W. Parmley, K. Chatterjee, C. Wolfe, and C. B. Higgins, "Interstudy reproducibility of dimensional and functional measurements between cine magnetic resonance studies in the morphologically abnormal left ventricle.," *Am Heart J*, vol. 119, pp. 1367–1373, Jun 1990.

[38] G. L. Nayler, D. N. Firmin, and D. B. Longmore, "Blood flow imaging by cine magnetic resonance.," *J Comput Assist Tomogr*, vol. 10, no. 5, pp. 715–722, 1986.

[39] O. P. Simonetti, R. J. Kim, D. S. Fieno, H. B. Hillenbrand, E. Wu, J. M. Bundy, J. P. Finn, and R. M. Judd, "An improved MR imaging technique for the visualization of myocardial infarction.," *Radiology*, vol. 218, pp. 215–223, Jan 2001.

[40] C. Pappone, G. Oreto, F. Lamberti, G. Vicedomini, M. L. Loricchio, S. Shpun, M. Rillo, M. P. Calabro, A. Conversano, S. A. Ben-Haim, R. Cappato, and S. Chierchia, "Catheter ablation of paroxysmal atrial fibrillation using a 3D mapping system.," *Circulation*, vol. 100, pp. 1203–1208, Sep 1999.

[41] B. Hall, V. Jeevanantham, R. Simon, J. Filippone, G. Vorobiof, and J. Daubert, "Variation in left atrial transmural wall thickness at sites commonly targeted for ablation of atrial fibrillation.," *J Interv Card Electrophysiol*, vol. 17, pp. 127–132, Nov 2006.

[42] T. Niendorf, C. J. Hardy, R. O. Giaquinto, P. Gross, H. E. Cline, Y. Zhu, G. Kenwood, S. Cohen, A. K. Grant, S. Joshi, N. M. Rofsky, and D. K. Sodickson, "Toward single breath-hold whole-heart coverage coronary MRA using highly accelerated parallel imaging with a 32-channel MR system.," *Magn Reson Med*, vol. 56, pp. 167–176, Jul 2006.

[43] T. D. Nguyen, P. Spincemaille, M. D. Cham, J. W. Weinsaft, M. R. Prince, and Y. Wang, "Free-breathing 3-dimensional steady-state free precession coronary magnetic resonance angiography: comparison of four navigator gating techniques.," *Magn Reson Imaging*, vol. 27, pp. 807–814, Jul 2009.

[44] T. Tangcharoen, C. Jahnke, U. Koehler, B. Schnackenburg, C. Klein, E. Fleck, and E. Nagel, "Impact of heart rate variability in patients with normal sinus rhythm on image quality in coronary magnetic angiography.," *J Magn Reson Imaging*, vol. 28, pp. 74–79, Jul 2008.

[45] H. Sakuma, Y. Ichikawa, S. Chino, T. Hirano, K. Makino, and K. Takeda, "Detection of coronary artery stenosis with whole-heart coronary magnetic resonance angiography.," *J Am Coll Cardiol*, vol. 48, pp. 1946–1950, Nov 2006.

[46] H. Timinger, S. Krueger, J. Borgert, and R. Grewer, "Motion compensation for interventional navigation on 3D static roadmaps based on an affine model and gating.," *Phys Med Biol*, vol. 49, pp. 719–732, Mar 2004.

[47] A. P. King, R. Boubertakh, K. S. Rhode, Y. L. Ma, P. Chinchapatnam, G. Gao, T. Tangcharoen, M. Ginks, M. Cooklin, J. S. Gill, D. J. Hawkes, R. S. Razavi, and T. Schaeffter, "A subject-specific technique for respiratory motion correction in image-guided cardiac catheterisation procedures.," *Med Image Anal*, vol. 13, pp. 419–431, Jun 2009.

[48] A. Z. Faranesh, P. Kellman, and R. J. Lederman, "Roadmaps incorporating respiratory and cardiac motion for X-ray fused with MRI," in *Proceedings of Joint Annual Meeting ISMRM-ESMRMB, Stockholm, Sweden*, 2010.

[49] H. Ashikaga, T. Sasano, J. Dong, M. M. Zviman, R. Evers, B. Hopenfeld, V. Castro, R. H. Helm, T. Dickfeld, S. Nazarian, J. K. Donahue, R. D. Berger, H. Calkins, M. R. Abraham, E. Marban, A. C. Lardo, E. R. McVeigh, and H. R. Halperin, "Magnetic resonance-based anatomical analysis of scar-related ventricular tachycardia: implications for catheter ablation.," *Circ Res*, vol. 101, pp. 939–947, Oct 2007.

[50] D. C. Peters, J. V. Wylie, T. H. Hauser, K. V. Kissinger, R. M. Botnar, V. Essebag, M. E. Josephson, and W. J. Manning, "Detection of pulmonary vein and left atrial scar after catheter ablation with three-dimensional navigator-gated delayed enhancement MR imaging: initial experience.," *Radiology*, vol. 243, pp. 690–695, Jun 2007.

[51] F. Epstein, A. E. Arai, J. A. Feinstein, T. K. Foo, S. D. Wolff (Inventors), and General Electric Company (Assignee), "Retrospective ordering of segmented MRI cardiac data using cardiac phase." United States Patent US 5997883, 1999.

[52] D. E. Bohning, B. Carter, S. Liu, and G. M. Pohost, "PC-based system for retrospective cardiac and respiratory gating of NMR data.," *Magn Reson Med*, vol. 16, pp. 303–316, Nov 1990.

[53] A. D. Scott, J. Keegan, and D. N. Firmin, "Motion in cardiovascular MR imaging.," *Radiology*, vol. 250, pp. 331–351, Feb 2009.

[54] R. P. Lewis, S. E. Rittogers, W. F. Froester, and H. Boudoulas, "A critical review of the systolic time intervals.," *Circulation*, vol. 56, pp. 146–158, Aug 1977.

[55] T. Leiner, G. Katsimaglis, E. N. Yeh, K. V. Kissinger, G. van Yperen, H. Eggers, W. J. Manning, and R. M. Botnar, "Correction for heart rate variability improves coronary magnetic resonance angiography.," *J Magn Reson Imaging*, vol. 22, pp. 577–582, Oct 2005.

[56] E. M. Haacke, R. W. Brown, M. R. Thompson, and R. Venkatesan, *Magnetic Resonance Imaging - Physical Principles and Sequence Design*. John Wiley & Sons, Inc., 1999.

[57] M. A. Bernstein, K. F. King, and X. J. Zhou, *Handbook of MRI Pulse Sequences*. Elsevier Academic Press, 2004.

[58] R. Vink, "Nuclear magnetic resonance characterization of secondary mechanisms following traumatic brain injury.," *Mol Chem Neuropathol*, vol. 18, pp. 279–297, Apr 1993.

[59] J. Henning, "Echoes -how to generate, recognize, use or avoid them in MR-imaging sequences," *Concepts in Magnetic Resonance*, vol. 3, pp. 125–143, 1991.

[60] J. Henning, "Echoes -how to generate, recognize, use or avoid them in MR-imaging sequences," *Concepts in Magnetic Resonance*, vol. 3, pp. 179–192, 1991.

[61] A. Stadler, W. Schima, A. Ba-Ssalamah, J. Kettenbach, and E. Eisenhuber, "Artifacts in body MR imaging: their appearance and how to eliminate them," *Eur Radiol*, vol. 17, pp. 1242–1255, 2007.

[62] H. Y. Carr, "Steady-state free precession in nuclear magnetic resonance," *Physical Review*, vol. 112, pp. 1693–1708, 1958.

[63] K. Scheffler and S. Lehnhardt, "Principles and applications of balanced SSFP techniques.," *Eur Radiol*, vol. 13, pp. 2409–2418, Nov 2003.

[64] K. Scheffler, "A pictorial description of steady-state in rapid magnetic resonance imaging," *Concepts in Magnetic Resonance*, vol. 11, pp. 291–304, 1999.

[65] Y. Zur, S. Stokar, and P. Bendel, "An analysis of fast imaging sequences with steady-state transverse magnetization refocusing.," *Magn Reson Med*, vol. 6, pp. 175–193, Feb 1988.

[66] K. Scheffler and J. Henning, "Eddy current optimized phase encoding schemes to reduce artifacts in balanced SSFP imaging," in *Proceedings of the 11th Annual Meeting of ISMRM, Toronto, Canada*, p. 732, 2003.

[67] C.-M. Tsai and D. G. Nishimura, "Reduced aliasing artifacts using variable-density k-space sampling trajectories.," *Magn Reson Med*, vol. 43, pp. 452–458, Mar 2000.

[68] M. A. Bernstein, S. B. Fain, and S. J. Riederer, "Effect of windowing and zero-filled reconstruction of MRI data on spatial resolution and acquisition strategy.," *J Magn Reson Imaging*, vol. 14, pp. 270–280, Sep 2001.

[69] K. F. King and P. R. Moran, "A unified description of NMR imaging, data-collection strategies, and reconstruction.," *Med Phys*, vol. 11, no. 1, pp. 1–14, 1984.

[70] T. Koehler, "A projection access scheme for iterative reconstruction based on the golden section," in *Proceedings of IEEE Nuclear Science Symposium Conference Record*, vol. 6, pp. 3961–3965, 16–22 Oct. 2004.

[71] S. Winkelmann, T. Schaeffter, T. Koehler, H. Eggers, and O. Doessel, "An optimal radial profile order based on the golden ratio for time-resolved MRI.," *IEEE Trans Med Imaging*, vol. 26, pp. 68–76, Jan 2007.

[72] M. L. Lauzon and B. K. Rutt, "Effects of polar sampling in k-space.," *Magn Reson Med*, vol. 36, pp. 940–949, Dec 1996.

[73] J. G. Pipe, "Reconstructing MR images from undersampled data: data-weighting considerations.," *Magn Reson Med*, vol. 43, pp. 867–875, Jun 2000.

[74] A. C. Larson, O. P. Simonetti, and D. Li, "Coronary MRA with 3D undersampled projection reconstruction TrueFISP.," *Magn Reson Med*, vol. 48, pp. 594–601, Oct 2002.

[75] D. C. Peters, F. R. Korosec, T. M. Grist, W. F. Block, J. E. Holden, K. K. Vigen, and C. A. Mistretta, "Undersampled projection reconstruction applied to MR angiography.," *Magn Reson Med*, vol. 43, pp. 91–101, Jan 2000.

[76] K. Scheffler and J. Hennig, "Reduced circular field-of-view imaging.," *Magn Reson Med*, vol. 40, pp. 474–480, Sep 1998.

[77] C. Stehning, P. Boernert, K. Nehrke, H. Eggers, and O. Doessel, "Fast isotropic volumetric coronary MR angiography using free-breathing 3D radial balanced FFE acquisition.," *Magn Reson Med*, vol. 52, pp. 197–203, Jul 2004.

[78] O. Wieben, E. Brodsky, C. A. Mistretta, and W. F. Block, "Correction of trajectory errors in radial acquisitions," in *Proceedings of the 11th Annual Meeting of ISMRM, Toronto, Canada*, 2003.

[79] T. Schaeffter, S. Weiss, H. Eggers, P. Boernert, and V. Rasche, "Self-referencing multi-gradient-echo projection reconstruction," in *Proceedings of the 11th Annual Meeting of ISMRM, Toronto, Canada*, 2003.

[80] K. J. Lee, M. N. J. Paley, P. D. Griffiths, and J. M. Wild, "Method of generalized projections algorithm for image-based reduction of artifacts in radial imaging.," *Magn Reson Med*, vol. 54, pp. 246–250, Jul 2005.

[81] V. Rasche, D. Holz, and R. Proksa, "MR fluoroscopy using projection reconstruction multi-gradient-echo (prMGE) MRI.," *Magn Reson Med*, vol. 42, pp. 324–334, Aug 1999.

[82] R. Boubertakh, C. Prieto, P. G. Batchelor, S. Uribe, D. Atkinson, H. Eggers, T. S. Soerensen, M. S. Hansen, R. S. Razavi, and T. Schaeffter, "Whole-heart imaging using undersampled radial phase encoding (RPE) and iterative sensitivity encoding (SENSE) reconstruction.," *Magn Reson Med*, vol. 62, pp. 1331–1337, Sep 2009.

[83] C. Prieto, S. Uribe, R. Razavi, D. Atkinson, and T. Schaeffter, "3D undersampled golden-radial phase encoding for DCE-MRA using inherently regularized iterative SENSE," *Magn Reson Med*, vol. 64, pp. 514–526, 2010.

[84] V. Rasche, R. Proksa, R. Sinkus, P. Boernert, and H. Eggers, "Resampling of data between arbitrary grids using convolution interpolation.," *IEEE Trans Med Imaging*, vol. 18, pp. 385–392, May 1999.

[85] J. I. Jackson, C. H. Meyer, D. G. Nishimura, and A. Macovski, "Selection of a convolution function for Fourier inversion using gridding [computerised tomography application].," *IEEE Trans Med Imaging*, vol. 10, no. 3, pp. 473–478, 1991.

[86] J. G. Pipe and P. Menon, "Sampling density compensation in MRI: rationale and an iterative numerical solution.," *Magn Reson Med*, vol. 41, pp. 179–186, Jan 1999.

[87] D. Mitsouras, R. V. Mulkern, and F. J. Rybicki, "Fast, exact k-space sample density compensation for trajectories composed of rotationally symmetric segments, and the SNR-optimized image reconstruction from non-Cartesian samples.," *Magn Reson Med*, vol. 60, pp. 339–349, Aug 2008.

[88] H. Schomberg and J. Timmer, "The gridding method for image reconstruction by Fourier transformation.," *IEEE Trans Med Imaging*, vol. 14, no. 3, pp. 596–607, 1995.

[89] J. D. O'Sullivan, "A fast sinc function gridding algorithm for Fourier inversion in computer tomography.," *IEEE Trans Med Imaging*, vol. 4, no. 4, pp. 200–207, 1985.

[90] P. J. Beatty, D. G. Nishimura, and J. M. Pauly, "Rapid gridding reconstruction with a minimal oversampling ratio.," *IEEE Trans Med Imaging*, vol. 24, pp. 799–808, Jun 2005.

[91] J. Keiner, S. Kunis, and D. Potts, "Using NFFT3 - a software library for various nonequispaced fast Fourier transforms," *ACM Transactions on Mathematical Software*, vol. 36, pp. 19:1–19:30, Aug 2009.

[92] M. L. Lauzon and B. K. Rutt, "Polar sampling in k-space: reconstruction effects.," *Magn Reson Med*, vol. 40, pp. 769–782, Nov 1998.

[93] E. M. Haacke, E. D. Lindskogj, and W. Lin, "A fast, iterative, partial-Fourier technique capable of local phase recovery," *Journal of Magnetic Resonance*, vol. 92, pp. 126–145, 1991.

[94] K. P. Pruessmann, M. Weiger, P. Boernert, and P. Boesiger, "Advances in sensitivity encoding with arbitrary k-space trajectories.," *Magn Reson Med*, vol. 46, pp. 638–651, Oct 2001.

[95] K. T. Block, M. Uecker, and J. Frahm, "Undersampled radial MRI with multiple coils. Iterative image reconstruction using a total variation constraint.," *Magn Reson Med*, vol. 57, pp. 1086–1098, Jun 2007.

[96] P. Qu, K. Zhong, B. Zhang, J. Wang, and G. X. Shen, "Convergence behavior of iterative SENSE reconstruction with non-Cartesian trajectories.," *Magn Reson Med*, vol. 54, pp. 1040–1045, Oct 2005.

[97] E. N. Yeh, M. Stuber, C. A. McKenzie, R. M. Botnar, T. Leiner, M. A. Ohliger, A. K. Grant, J. D. Willig-Onwuachi, and D. K. Sodickson, "Inherently self-calibrating non-Cartesian parallel imaging.," *Magn Reson Med*, vol. 54, pp. 1–8, Jul 2005.

[98] J. Bogaert, S. Dymarkowski, and A. M. Taylor, eds., *Clinical Cardiac MRI: With Interactive CD-ROM (Medical Radiology / Diagnostic Imaging)*. Springer Berlin Heidelberg, 2005.

[99] J. P. Earls, V. B. Ho, T. K. Foo, E. Castillo, and S. D. Flamm, "Cardiac MRI: recent progress and continued challenges.," *J Magn Reson Imaging*, vol. 16, pp. 111–127, Aug 2002.

[100] K. Nehrke, P. Boernert, P. Mazurkewitz, R. Winkelmann, and I. Graesslin, "Free-breathing whole-heart coronary MR angiography on a clinical scanner in four minutes.," *J Magn Reson Imaging*, vol. 23, pp. 752–756, May 2006.

[101] T. S. Soerensen, H. Koerperich, G. F. Greil, J. Eichhorn, P. Barth, H. Meyer, E. M. Pedersen, and P. Beerbaum, "Operator-independent isotropic three-dimensional magnetic resonance imaging for morphology in congenital heart disease: a validation study.," *Circulation*, vol. 110, pp. 163–169, Jul 2004.

[102] R. M. Botnar, M. Stuber, P. G. Danias, K. V. Kissinger, and W. J. Manning, "Improved coronary artery definition with T2-weighted, free-breathing, three-dimensional coronary MRA.," *Circulation*, vol. 99, pp. 3139–3148, Jun 1999.

[103] M. H. Moghari, D. C. Peters, J. Smink, L. Goepfert, K. V. Kissinger, B. Goddu, T. H. Hauser, M. E. Josephson, W. J. Manning, and R. Nezafat, "Pulmonary vein inflow artifact reduction for free-breathing left atrium late gadolinium enhancement.," *Magn Reson Med*, vol. 66, pp. 180–186, Jul 2011.

[104] D. Maintz, M. Ozgun, A. Hoffmeier, R. Fischbach, W. Y. Kim, M. Stuber, W. J. Manning, W. Heindel, and R. M. Botnar, "Selective coronary artery plaque visualization and differentiation by contrast-enhanced inversion prepared MRI.," *Eur Heart J*, vol. 27, pp. 1732–1736, Jul 2006.

[105] K. S. Nayak, J. M. Pauly, D. G. Nishimura, and B. S. Hu, "Rapid ventricular assessment using real-time interactive multislice MRI.," *Magn Reson Med*, vol. 45, pp. 371–375, Mar 2001.

[106] E. R. McVeigh and E. Atalar, "Cardiac tagging with breath-hold cine MRI.," *Magn Reson Med*, vol. 28, pp. 318–327, Dec 1992.

[107] N. Al-Saadi, E. Nagel, M. Gross, A. Bornstedt, B. Schnackenburg, C. Klein, W. Klimek, H. Oswald, and E. Fleck, "Noninvasive detection of myocardial ischemia from perfusion reserve based on cardiovascular magnetic resonance.," *Circulation*, vol. 101, pp. 1379–1383, Mar 2000.

[108] K. S. Nayak and B. S. Hu, "Triggered real-time MRI and cardiac applications.," *Magn Reson Med*, vol. 49, pp. 188–192, Jan 2003.

[109] K. S. Nayak, J. M. Pauly, P. C. Yang, B. S. Hu, C. H. Meyer, and D. G. Nishimura, "Real-time interactive coronary MRA.," *Magn Reson Med*, vol. 46, pp. 430–435, Sep 2001.

[110] S. Kaji, P. C. Yang, A. B. Kerr, W. H. W. Tang, C. H. Meyer, A. Macovski, J. M. Pauly, D. G. Nishimura, and B. Hu, "Rapid evaluation of left ventricular volume and mass without breath-holding using real-time interactive cardiac magnetic resonance imaging system.," *J Am Coll Cardiol*, vol. 38, pp. 527–533, Aug 2001.

[111] D. C. Peters, M. A. Guttman, A. J. Dick, V. K. Raman, R. J. Lederman, and E. R. McVeigh, "Reduced field of view and undersampled PR combined for interventional imaging of a fully dynamic field of view.," *Magn Reson Med*, vol. 51, pp. 761–767, Apr 2004.

[112] G. M. Nijm, A. V. Sahakian, S. Swiryn, J. C. Carr, J. Sheehan, and A. C. Larson, "Comparison of self-gated cine MRI retrospective cardiac synchronization algorithms.," *J Magn Reson Imaging*, vol. 28, pp. 767–772, Sep 2008.

[113] A. C. Larson, R. D. White, G. Laub, E. R. McVeigh, D. Li, and O. P. Simonetti, "Self-gated cardiac cine MRI.," *Magn Reson Med*, vol. 51, pp. 93–102, Jan 2004.

[114] S. D. Roes, G. Korosoglou, M. Schaer, J. J. Westenberg, M. J. P. van Osch, A. de Roos, and M. Stuber, "Correction for heart rate variability during 3D whole heart MR coronary angiography.," *J Magn Reson Imaging*, vol. 27, pp. 1046–1053, May 2008.

[115] A. M. Weissler, W. S. Harris, and C. D. Schoenfeld, "Systolic time intervals in heart failure in man.," *Circulation*, vol. 37, pp. 149–159, Feb 1968.

[116] Y. Wang, S. J. Riederer, and R. L. Ehman, "Respiratory motion of the heart: kinematics and the implications for the spatial resolution in coronary imaging.," *Magn Reson Med*, vol. 33, pp. 713–719, May 1995.

[117] K. Nehrke, P. Boernert, D. Manke, and J. C. Boeck, "Free-breathing cardiac MR imaging: study of implications of respiratory motion–initial results.," *Radiology*, vol. 220, pp. 810–815, Sep 2001.

[118] G. Shechter, C. Ozturk, J. R. Resar, and E. R. McVeigh, "Respiratory motion of the heart from free breathing coronary angiograms.," *IEEE Trans Med Imaging*, vol. 23, pp. 1046–1056, Aug 2004.

[119] K. McLeish, D. L. G. Hill, D. Atkinson, J. M. Blackall, and R. Razavi, "A study of the motion and deformation of the heart due to respiration.," *IEEE Trans Med Imaging*, vol. 21, pp. 1142–1150, Sep 2002.

[120] P. G. Danias, M. Stuber, R. M. Botnar, K. V. Kissinger, R. R. Edelman, and W. J. Manning, "Relationship between motion of coronary arteries and diaphragm during free breathing:

lessons from real-time MR imaging.," *AJR Am J Roentgenol*, vol. 172, pp. 1061–1065, Apr 1999.

[121] C. Jahnke, I. Paetsch, S. Achenbach, B. Schnackenburg, R. Gebker, E. Fleck, and E. Nagel, "Coronary MR imaging: breath-hold capability and patterns, coronary artery rest periods, and beta-blocker use.," *Radiology*, vol. 239, pp. 71–78, Apr 2006.

[122] Y. M. Kadah, A. A. Abaza, A. S. Fahmy, A.-B. M. Youssef, K. Heberlein, and X. P. Hu, "Floating navigator echo (FNAV) for in-plane 2D translational motion estimation.," *Magn Reson Med*, vol. 51, pp. 403–407, Feb 2004.

[123] W. Lin, F. Huang, P. Boernert, Y. Li, and A. Reykowski, "Motion correction using an enhanced floating navigator and GRAPPA operations.," *Magn Reson Med*, vol. 63, pp. 339–348, Feb 2010.

[124] Z. W. Fu, Y. Wang, R. C. Grimm, P. J. Rossman, J. P. Felmlee, S. J. Riederer, and R. L. Ehman, "Orbital navigator echoes for motion measurements in magnetic resonance imaging.," *Magn Reson Med*, vol. 34, pp. 746–753, Nov 1995.

[125] A. Shankaranarayanan, M. Wendt, J. S. Lewin, and J. L. Duerk, "Two-step navigatorless correction algorithm for radial k-space MRI acquisitions.," *Magn Reson Med*, vol. 45, pp. 277–288, Feb 2001.

[126] S. Uribe, V. Muthurangu, R. Boubertakh, T. Schaeffter, R. Razavi, D. L. Hill, and M. S. Hansen, "Whole-heart cine MRI using real-time respiratory self-gating.," *Magn Reson Med*, vol. 57, pp. 606–613, Mar 2007.

[127] M. V. McConnell, V. C. Khasgiwala, B. J. Savord, M. H. Chen, M. L. Chuang, R. R. Edelman, and W. J. Manning, "Comparison of respiratory suppression methods and navigator locations for MR coronary angiography.," *AJR Am J Roentgenol*, vol. 168, pp. 1369–1375, May 1997.

[128] D. A. Feinberg, D. Giese, D. A. Bongers, S. Ramanna, M. Zaitsev, M. Markl, and M. Guenther, "Hybrid ultrasound MRI for improved cardiac imaging and real-time respiration control.," *Magn Reson Med*, vol. 63, pp. 290–296, Feb 2010.

[129] T. S. Sachs, C. H. Meyer, P. Irarrazabal, B. S. Hu, D. G. Nishimura, and A. Macovski, "The diminishing variance algorithm for real-time reduction of motion artifacts in MRI.," *Magn Reson Med*, vol. 34, pp. 412–422, Sep 1995.

[130] P. Jhooti, P. D. Gatehouse, J. Keegan, N. H. Bunce, A. M. Taylor, and D. N. Firmin, "Phase ordering with Automatic Window Selection (PAWS): a novel motion-resistant technique for 3D coronary imaging.," *Magn Reson Med*, vol. 43, pp. 470–480, Mar 2000.

[131] A. Nuval, T. D. Nguyen, R. Watts, and Y. Wang, "An improved real-time navigator gating algorithm for reducing motion effects in coronary magnetic resonance angiography," *J X-ray Sci Technol*, vol. 11, pp. 115–123, 2003.

[132] M. Hackenbroch, K. Nehrke, J. Gieseke, C. Meyer, K. Tiemann, H. Litt, O. Dewald, C. P. Naehle, H. Schild, and T. Sommer, "3D Motion Adapted Gating (3D MAG): a new navigator technique for accelerated acquisition of free breathing navigator gated 3D coronary MR-angiography.," *Eur Radiol*, vol. 15, pp. 1598–1606, Aug 2005.

[133] H. Langreck, B. Schnackenburg, K. Nehrke, P. Boernert, A. Wahl, I. Paetsch, A. Bornstedt, E. Fleck, and E. Nagel, "MR coronary artery imaging with 3D Motion Adapted Gating (MAG) in comparison to a standard prospective navigator technique.," *Journal of Cardiovascular Magnetic Resonance*, vol. 7, no. 5, pp. 793–797, 2005.

[134] V. N. Kolmogorov, R. Watts, M. R. Prince, R. Zabih, and Y. Wang, "Simultaneous Multiple Volume (SMV) acquisition algorithm for real-time navigator gating.," *Magn Reson Imaging*, vol. 21, pp. 969–975, Nov 2003.

[135] V. Kolmogorov, T. D. Nguyen, A. Nuval, P. Spincemaille, M. R. Prince, R. Zabih, and Y. Wang, "Multiprocessor scheduling implementation of the Simultaneous Multiple Volume (SMV) navigator method.," *Magn Reson Med*, vol. 52, pp. 362–367, Aug 2004.

[136] P. Jhooti, J. Keegan, and D. N. Firmin, "A fully automatic and highly efficient navigator gating technique for high-resolution free-breathing acquisitions: Continuously adaptive windowing strategy.," *Magn Reson Med*, vol. 64, pp. 1015–1026, Jun 2010.

[137] M. Weiger, P. Boernert, R. Proksa, T. Schaeffter, and A. Haase, "Motion-adapted gating based on k-space weighting for reduction of respiratory motion artifacts.," *Magn Reson Med*, vol. 38, pp. 322–333, Aug 1997.

[138] R. Sinkus and P. Boernert, "Motion pattern adapted real-time respiratory gating.," *Magn Reson Med*, vol. 41, pp. 148–155, Jan 1999.

[139] Y. P. Du, "Prospective navigator gating with a dual acceptance window technique to reduce respiratory motion artifacts in 3D MR coronary angiography.," *Int J Cardiovasc Imaging*, vol. 19, pp. 157–162, Apr 2003.

[140] P. G. Danias, M. V. McConnell, V. C. Khasgiwala, M. L. Chuang, R. R. Edelman, and W. J. Manning, "Prospective navigator correction of image position for coronary MR angiography.," *Radiology*, vol. 203, pp. 733–736, Jun 1997.

[141] R. L. Ehman and J. P. Felmlee, "Adaptive technique for high-definition MR imaging of moving structures.," *Radiology*, vol. 173, pp. 255–263, Oct 1989.

[142] Y. Wang and R. L. Ehman, "Retrospective adaptive motion correction for navigator-gated 3D coronary MR angiography.," *J Magn Reson Imaging*, vol. 11, pp. 208–214, Feb 2000.

[143] T. Schaeffter, V. Rasche, and I. C. Carlsen, "Motion compensated projection reconstruction.," *Magn Reson Med*, vol. 41, pp. 954–963, May 1999.

[144] M. L. Wood and R. M. Henkelman, "MR image artifacts from periodic motion.," *Med Phys*, vol. 12, no. 2, pp. 143–151, 1985.

[145] T. D. Nguyen, G. Ding, R. Watts, and Y. Wang, "Optimization of view ordering for motion artifact suppression.," *Magn Reson Imaging*, vol. 19, pp. 951–957, Sep 2001.

[146] G. H. Glover and J. M. Pauly, "Projection reconstruction techniques for reduction of motion effects in MRI.," *Magn Reson Med*, vol. 28, pp. 275–289, Dec 1992.

[147] A. Etienne, R. M. Botnar, A. M. C. V. Muiswinkel, P. Boesiger, W. J. Manning, and M. Stuber, ""Soap-Bubble" visualization and quantitative analysis of 3D coronary magnetic resonance angiograms.," *Magn Reson Med*, vol. 48, pp. 658–666, Oct 2002.

[148] J. Canny, "A computational approach to edge detection.," *IEEE T Pattern Anal*, vol. PAMI-8, no. 6, pp. 679–698, 1986.

[149] S. Holm, "A simple sequentially rejective multiple test procedures," *Scandinavian journal of statistics*, pp. 65–70, 1979.

[150] E. Spuentrup, M. Katoh, A. Buecker, W. J. Manning, T. Schaeffter, T.-H. Nguyen, H. P. Kuehl, M. Stuber, R. M. Botnar, and R. W. Guenther, "Free-breathing 3D steady-state free precession coronary MR angiography with radial k-space sampling: comparison with Cartesian k-space sampling and cartesian gradient-echo coronary MR angiography–pilot study.," *Radiology*, vol. 231, pp. 581–586, May 2004.

[151] P. Z. Larson, P. T. Gurney, and D. G. Nishimura, "Anisotropic field-of-views in radial imaging.," *IEEE Trans Med Imaging*, vol. 27, pp. 47–57, Jan 2008.

[152] T. S. Soerensen, D. Atkinson, T. Schaeffter, and M. S. Hansen, "Real-time reconstruction of sensitivity encoded radial magnetic resonance imaging using a graphics processing unit.," *IEEE Trans Med Imaging*, vol. 28, pp. 1974–1985, Dec 2009.

[153] P. N. Jordan and D. J. Christini, "Therapies for ventricular cardiac arrhythmias.," *Crit Rev Biomed Eng*, vol. 33, no. 6, pp. 557–604, 2005.

[154] S. G. Duckett, A. Chiribiri, M. R. Ginks, S. Sinclair, B. R. Knowles, R. Botnar, G. S. Carr-White, C. A. Rinaldi, E. Nagel, R. Razavi, and T. Schaeffter, "Cardiac MRI to investigate myocardial scar and coronary venous anatomy using a slow infusion of dimeglumine gadobenate in patients undergoing assessment for cardiac resynchronization therapy.," *J Magn Reson Imaging*, vol. 33, pp. 87–95, Jan 2011.

[155] D. Manke, P. Roesch, K. Nehrke, P. Boernert, and O. Doessel, "Model evaluation and calibration for prospective respiratory motion correction in coronary MR angiography based on 3-D image registration.," *IEEE Trans Med Imaging*, vol. 21, pp. 1132–1141, Sep 2002.

[156] C. Buerger, T. Schaeffter, and A. P. King, "Hierarchical adaptive local affine registration for fast and robust respiratory motion estimation.," *Med Image Anal*, Mar 2011.

[157] T. Maekelae, P. Clarysse, O. Sipilae, N. Pauna, Q. C. Pham, T. Katila, and I. E. Magnin, "A review of cardiac image registration methods.," *IEEE Trans Med Imaging*, vol. 21, pp. 1011–1021, Sep 2002.

[158] P. A. Yushkevich, J. Piven, H. C. Hazlett, R. G. Smith, S. Ho, J. C. Gee, and G. Gerig, "User-guided 3D active contour segmentation of anatomical structures: significantly improved efficiency and reliability.," *Neuroimage*, vol. 31, pp. 1116–1128, Jul 2006.

[159] C. Buerger, A. P. King, T. Schaeffter, and C. Prieto, "3D non-rigid motion modeling of the liver from undersampled golden-radial phase encoding (G-RPE) acquisitions," in *Proceedings of Annual Meeting ISMRM, Montreal, Canada*, 2011.

[160] K. T. Block, M. Uecker, and J. Frahm, "Suppression of MRI truncation artifacts using total variation constrained data extrapolation.," *Int J Biomed Imaging*, vol. 2008, p. 184123, Aug 2008.

[161] A. P. King, K. S. Rhode, R. S. Razavi, and T. R. Schaeffter, "An adaptive and predictive respiratory motion model for image-guided interventions: theory and first clinical application.," *IEEE Trans Med Imaging*, vol. 28, pp. 2020–2032, Dec 2009.

[162] T. S. Soerensen, C. Prieto, D. Atkinson, M. S. Hansen, and T. Schaeffter, "GPU accelerated iterative SENSE reconstruction of radial phase encoded whole-heart MRI," in *Proceedings of Joint Annual Meeting ISMRM-ESMRMB, Stockholm, Sweden*, p. 2869, 2010.

[163] K. C. Wu, R. G. Weiss, D. R. Thiemann, K. Kitagawa, A. Schmidt, D. Dalal, S. Lai, D. A. Bluemke, G. Gerstenblith, E. Marban, G. F. Tomaselli, and J. A. C. Lima, "Late gadolinium enhancement by cardiovascular magnetic resonance heralds an adverse prognosis in nonischemic cardiomyopathy.," *J Am Coll Cardiol*, vol. 51, pp. 2414–2421, Jun 2008.

[164] D. C. Peters, E. A. Appelbaum, R. Nezafat, B. Dokhan, Y. Han, K. V. Kissinger, B. Goddu, and W. J. Manning, "Left ventricular infarct size, peri-infarct zone, and papillary scar measurements: A comparison of high-resolution 3D and conventional 2D late gadolinium enhancement cardiac MR.," *J Magn Reson Imaging*, vol. 30, pp. 794–800, Oct 2009.

[165] R. J. Kim, D. J. Shah, and R. M. Judd, "How we perform delayed enhancement imaging.," *J Cardiovasc Magn Reson*, vol. 5, pp. 505–514, Jul 2003.

[166] T. D. Nguyen, P. Spincemaille, J. W. Weinsaft, B. Y. Ho, M. D. Cham, M. R. Prince, and Y. Wang, "A fast navigator-gated 3D sequence for delayed enhancement MRI of the myocardium: comparison with breathhold 2D imaging.," *J Magn Reson Imaging*, vol. 27, pp. 802–808, Apr 2008.

[167] D. C. Look and D. R. Locker, "Time saving in measurement of NMR and EPR relaxation times," *Rev. Sci. Instrum*, vol. 41, p. 250, 1970.

[168] M. Doneva, C. Stehning, K. Nehrke, and P. Boernert, "Improving scan efficiency of respiratory gated imaging using compressed sensing with 3D Cartesian Golden Angle sampling," in *Proceedings of Annual Meeting ISMRM, Montreal, Canada*, 2011.

[169] M. K. Laudon, J. G. Webster, R. Frayne, and T. M. Grist, "Minimizing interference from magnetic resonance imagers during electrocardiography.," *IEEE Trans Biomed Eng*, vol. 45, pp. 160–164, Feb 1998.

[170] T. A. Spraggins, "Wireless retrospective gating: application to cine cardiac imaging.," *Magn Reson Imaging*, vol. 8, no. 6, pp. 675–681, 1990.

[171] M. E. Crowe, A. C. Larson, Q. Zhang, J. Carr, R. D. White, D. Li, and O. P. Simonetti, "Automated rectilinear self-gated cardiac cine imaging.," *Magn Reson Med*, vol. 52, pp. 782–788, Oct 2004.

[172] J. Liu, P. Spincemaille, N. C. F. Codella, T. D. Nguyen, M. R. Prince, and Y. Wang, "Respiratory and cardiac self-gated free-breathing cardiac CINE imaging with multiecho 3D hybrid radial SSFP acquisition.," *Magn Reson Med*, vol. 63, pp. 1230–1237, May 2010.

[173] W. S. Kim, C. W. Mun, D. J. Kim, and Z. H. Cho, "Extraction of cardiac and respiratory motion cycles by use of projection data and its applications to NMR imaging.," *Magn Reson Med*, vol. 13, pp. 25–37, Jan 1990.

[174] M. S. Hansen, T. S. Soerensen, A. E. Arai, and P. Kellman, "Retrospective reconstruction of high temporal resolution cine images from real-time MRI using iterative motion correction.," *Magn Reson Med*, Dec 2011.

[175] S. R. Yutzy, N. Seiberlich, J. L. Duerk, and M. A. Griswold, "Improvements in multislice parallel imaging using radial CAIPIRINHA.," *Magn Reson Med*, vol. 65, pp. 1630–1637, Jun 2011.

[176] S. P. Souza, J. Szumowski, C. L. Dumoulin, D. P. Plewes, and G. Glover, "SIMA: simultaneous multislice acquisition of MR images by Hadamard-encoded excitation.," *J Comput Assist Tomogr*, vol. 12, no. 6, pp. 1026–1030, 1988.

[177] G. H. Glover, "Phase-offset multiplanar (POMP) volume imaging: a new technique.," *J Magn Reson Imaging*, vol. 1, no. 4, pp. 457–461, 1991.

[178] F. A. Breuer, M. Blaimer, R. M. Heidemann, M. F. Mueller, M. A. Griswold, and P. M. Jakob, "Controlled aliasing in parallel imaging results in higher acceleration (CAIPIRINHA) for multi-slice imaging.," *Magn Reson Med*, vol. 53, pp. 684–691, Mar 2005.

[179] D. Staeb, C. O. Ritter, F. A. Breuer, A. M. Weng, D. Hahn, and H. Koestler, "CAIPIRINHA accelerated SSFP imaging.," *Magn Reson Med*, vol. 65, pp. 157–164, Jan 2011.

[180] C. H. Cunningham and M. L. Wood, "Method for improved multiband excitation profiles using the Shinnar-Le Roux transform.," *Magn Reson Med*, vol. 42, pp. 577–584, Sep 1999.

[181] D. C. Peters, P. Rohatgi, R. M. Botnar, S. B. Yeon, K. V. Kissinger, and W. J. Manning, "Characterizing radial undersampling artifacts for cardiac applications.," *Magn Reson Med*, vol. 55, pp. 396–403, Feb 2006.

[182] R. Razavi, D. L. G. Hill, S. F. Keevil, M. E. Miquel, V. Muthurangu, S. Hegde, K. Rhode, M. Barnett, J. van Vaals, D. J. Hawkes, and E. Baker, "Cardiac catheterisation guided by MRI in children and adults with congenital heart disease.," *Lancet*, vol. 362, pp. 1877–1882, Dec 2003.